THÈSE DE DOCTORAT

de l'Université de recherche Paris Sciences et Lettres
PSL Research University

Préparée à l'Observatoire de Paris

A study of the emission processes of two different types of gamma-emitting Active Galactic Nuclei

École doctorale nº127

ASTRONOMIE ET ASTROPHYSIQUE

Spécialité ASTROPHYSICS

COMPOSITION DU JURY :

M Jacques Le Bourlot
Observatoire de Paris
Président

Mme Monica Orienti
INAF/IRA
Rapporteuse

M Pierre-Olivier Petrucci
IPAG
Rapporteur

Mme Isabel Márquez
IAA, CSIC
Membre du jury

Soutenue par
Maialen ARRIETA LOBO
le 14 Decembre 2017

Dirigée par
Catherine BOISSON
Andreas ZECH

l'Observatoire de Paris

PSL RESEARCH UNIVERSITY PARIS

ZURETZAT, AITA

Preface

Active Galactic Nuclei (AGN) are compact extragalactic objects that present accretion activity onto a supermassive black hole (10^6-10^{10} $M_\odot$). One of the most striking characteristics of AGN is the fact that the luminosity of the compact central object can outshine the whole host galaxy. Such extreme luminosities are ascribed to non-thermal radiative processes that dominate the emission from the central part of the AGN. These non-thermal radiative processes are thought to originate from relativistic plasma outflows, known as jets, ejected from the central engine, sometimes even into the intergalactic medium. The most extreme subclass of AGN, the blazar subclass, features relativistic jets that are oriented closely towards the line of sight of the observer, leading to a heavily enhanced radiation due to relativistic effects. Blazars can be further classified into BL Lacertae (BL Lac) and Flat Spectrum Radio Quasar (FSRQ) objects, and can be detected at TeV by ground-based Imaging Atmospheric Cherenkov Telescopes (IACTs).

While the Spectral Energy Distribution (SED) of BL Lacs can be accurately described by means of simple one-zone Synchrotron Self-Compton (SSC) models, this is not the case for other sources detected at gamma-ray energies, like FSRQs for example, where additional external photon fields such as the obscuring torus, the accretion disc, the X-ray corona or the Broad Line Region (BLR) are necessary to describe the observed radiation and broad-band SED. This seems also to be the case for a new class of gamma loud objects, the gamma-loud Narrow Line Seyfert 1 galaxies (NLS1s). So far, less than 10 NLS1s have been discovered at gamma-ray energies by the Large Area Telescope aboard the Fermi satellite. Indeed, gamma-loud NLS1 represent an exotic subsample of AGN whose GeV detection was unexpected due to their lower black hole masses and higher accretion rates w.r.t. blazars. Thus, there is great interest in studying the radiative mechanisms involved in such high energy emission.

After a brief introduction of the general characteristics of AGN and the unification paradigm in Chapter 1, this manuscript introduces ground-based TeV gamma-ray

astronomy, and also presents the High Energy Stereoscopic System (HESS) experiment as an example of IACTs in Chapter 2, with a brief mention to the Target of Opportunity (ToO) procedures implemented to swiftly trigger HESS observations when an extragalactic source enters an interesting enhanced activity state.

Afterwards, Chapter 3 introduces the radiative mechanisms necessary to explain the observed emission from gamma-loud AGN, along with the SSC model that is applied in Chapter 5. The numerical code that combines the aforementioned SSC model with additional external radiative fields (i.e. light from a multi-temperature accretion disc and corona scattered by the BLR and torus) that we have developed in order to model more complex SEDs is also presented.

Chapter 4 presents the HESS ToO program in more detail. As an example of the multi-wavelength observation campaigns that can be triggered when a blazar enters a flarings state, the July 2016 flare of PKS 1749+096 is presented, focusing on the Swift analysis that has been performed. A preliminary discussion on the source's variability is also provided.

Next, Chapter 5 focuses on the analysis and modeling of HESS data and available quasi-simultaneous multi-wavelength data from the HESS-detected BL Lac 1ES 2322−409. The SED of the source is interpreted through the simple one-zone SED. One of the initial motivations to model this source was its poorly constrained redshift. Applying the SSC model to two different redshift hypothesis constrains the physical parameters of the emission region.

Chapter 6 presents the results of the application of our external component model to three gamma-emitting NLS1s for quiescent and gamma-ray flaring states. Solutions for a disc- and BLR-IC dominated scenario and a torus-IC dominated scenario are provided for each of the states. We assume that the variability of the source can be accounted for by changes in the jet parameters. An alternative scenario where different accretion rates could explain the enhanced high-energy emission is also explored.

Finally, Chapter 7 summarizes the findings and conclusions from the present work.

Préface

Les Noyaux Actifs de Galaxie (Active Galactic Nuclei en anglais, AGN) sont des objets extragalactiques compacts qui présentent de l'activité d'accrétion dans un trou noir supermassive (10^6-$10^{10} M_\odot$). Une des caractéristiques la plus remarquable des AGN est le fait que la luminosité de l'objet compact central peut éclipser celui de la galaxie hôte. Telles luminosités extrêmes sont attribuées à des processus non-thermaux qui peuvent dominer l'émission provenant de la partie centrale de l'AGN. Ces processus radiatifs non-thermaux proviennent des écoulements de plasma relativistes connues comme jets, éjectés depuis l'AGN central que parfois arrivent même jusqu'au milieu intergalactique. La sous-catégorie la plus extrême des AGN, les blazars, présente des jets relativistes orientés très proches a la ligne de visée de l'observateur, ce qui génère de la radiation fortement augmentée dû a des effets relativistes. Les blazars peuvent être classifies en objets du type BL Lacertae (BL Lacs) et du type Flat Spectrum Radio Quasar (FSRQ) qui peuvent être detectés au sol par des Télescopes à Imagerie Tcherenkov Atmosphérique (Imaging Atmospherique Cherenkov Telescopes en anglais, IACTs).

Tandis que la distribution spectrale d'énergie (Spectral Energy Distribution en anglais, SED) des BL Lacs peut être décrite avec précision via des modèles une-zone Synchrotron Self-Compton (SSC), ce n'est pas le cas pour autres sources détectées aux énergies gamma, par exemple les FSRQs, pour lesquels des champs des photons externes complémentaires comme le tore, le disque d'accrétion, la couronne ou la Broad Line Region (BLR) sont nécessaires pour proprement décrire la radiation observée. Celle-ci semble être aussi le cas pour une nouvelle classe d'objets découverts récemment comme des émmeteurs gamma, les galaxies dites Narrow Line Seyfert 1 (NLS1). Jusqu'à présent, moins de 10 NLS1s ont été vues aux énergies gamma par le satellite Fermi. En conséquence, il s'agit d'une sous-catégorie exotique des AGN dont la détection gamma était inespérée suite à leurs trous noirs à petite masse et des taux d'accrétion plus grandes par rapport aux blazars. Il-y-a donc beaucoup d'intérêt a étudier les mécanismes radiatifs impliqués dans leur émission gamma.

Apès une introduction générale des AGN et leur paradigme d'unification dans le Chapitre 1, ce manuscrit introduit l'astronomie gamma au sol avec l'expérience HESS comme exemple des IACTs dans le Chapitre 2, avec une brève mention aux procédures Target of Opportunity (ToO) mises en place pour un déclenchement rapide des observations HESS des sources extragalactiques qui entrent dans des états d'émission augmentée.

Ensuite, nous présentons dans le Chapitre 3 les processus radiatifs nécessaires pour décrire l'émission observée des AGN émmeteurs du rayonnement gamma qui nous concernent, ainsi que le modèle SSC que nous appliquons dans le Chapitres 5. Le code numérique qui combine le modèle SSC simple avec les champs des photons externes complémentaires (c'est a dire le tore, le disque d'accrétion, la couronne et la BLR) que nous avons développé pour décrire des SEDs plus complexes est aussi présenté.

Le Chapitre 4 présent plus en détail le protocole ToO introduit dans le Chapitre 2, donnant un aperçu des procédures mises en place. Nous donnons comme exemple les observations multi-longueur d'onde réalisées en Juillet 2016 pendant le 'flare' de PKS 1749+096, et nous concentrons spécialement sur l'analyse des données Swift et a la variabilité observée dans ces données multi-longueur d'onde.

Le Chapitre 5 de cette thèse vise a l'analyse des données HESS, ainsi qu'aux données multi-longueur d'onde quasi-simultanées existantes, du BL Lac 1ES 2322−409 détecté par HESS. La SED de cette source est interprétée via un modèle simple SSC. Une des motivations initiales pour modèliser cette source était son redshift insuffisamment restreint. En appliquant le modèle SSC a deux hypothèses de redshift permet de contraindre les paramètres physiques de la zone d'émission.

La dernière partie de ce travail a consisté au développement d'un code numérique qui combine le précédemment mentionné modèle SSC avec des champs radiatifs externes complémentaires, consistant de la lumière provenant d'un disque d'accrétion multi-temperature, et une couronne éparpillées par la BLR et le tore, a fin de modéliser des SED plus complexes. Le code a été appliqué à trois NLS1s émetteurs des rayons gamma, pour des états de flux bas et hauts. Les résultats son présentés dans le Chapitre 6.

Le manuscrit finit avec le Chapitre 7 et nos conclusions principales sur le travail mené.

Contents

Acronyms

2MASS Two Micron All Sky Survey. 144, 170, 188, 193

AGN Active Galactic Nuclei. i–iv, xi, xv, 1, 2, 4–7, 10–20, 23–29, 31, 34–40, 42, 66, 73, 76, 79, 81, 84, 90, 94, 99, 101, 105, 123, 144, 162, 175, 187, 222, 223, 232–235, 237

ATOM Automatic Telescope for Optical Monitoring. 66, 132, 139, 140, 152, 161–163, 234

BAT Burst Alert Telescope. 131, 177

BBB Big Blue Bump. 10, 82, 98, 101, 103, 182, 185, 208, 224, 236

BDT Boosted Decision Tree. 72

BH Black Hole. 8, 9, 24, 30, 31, 34–36, 101, 174, 175, 178, 187, 212, 214, 216, 218, 219, 222–224, 227, 230, 235

BLR Broad Line Region. i–iv, xiii, xv, 12, 13, 18, 30, 36, 94, 98, 105–107, 109–122, 173, 182, 183, 185, 186, 195, 198, 200, 205, 207, 208, 210–214, 216, 217, 220–227, 229, 230, 232, 234–236, 270

BLRG Broad Line Radio Galaxy. 20

BLS1 Broad Line Seyfert 1. 34, 35

BPL Broken Power-Law. 87, 88, 112, 116

CSS Catalina Sky Survey. 161, 188

CT Charge Threshold. 73

EBL Extragalactic Background Light. 73, 76, 90, 91, 169

EIC External Inverse Compton. 37, 100, 105, 112–114, 116, 117, 119, 181, 205

FRI Fanaroff-Riley type I. xi, 20, 21, 23, 24, 30

FRII Fanaroff-Riley type II. xi, 20, 22–24, 30

FSRQ Flat Spectrum Radio Quasar. i, iii, 23, 24, 29–33, 37, 76, 77, 120, 121, 132, 175, 189, 219, 224, 225, 227, 228, 232, 236

FWHM Full Width Half Maximum. 13, 34, 187, 188, 201

GROND Gamma-Ray Optical/Near-infrared Detector. 145, 152, 161–166, 170

HBL High-energy peaked BL Lac. 31, 76, 77, 79, 86, 90, 91, 94, 123, 143, 154, 168, 171, 233, 234

HE High Energy. 17, 27, 28, 31, 50, 82–85, 164, 188

HEGRA High Energy Gamma Ray Array. xi, 47, 48

HESS High Energy Stereoscopic System. ii, iv, xi, xii, xv, 15, 17, 28, 43, 48, 59, 61–67, 73, 74, 76, 77, 91, 131–133, 139, 140, 143–145, 148, 150–152, 161–165, 170, 171, 233, 234, 263

IACT Imaging Air Cherenkov Telescope. i–iv, xi, 43, 48, 56–59, 61, 62, 66, 76, 223, 233, 236

IBL Intermediate-energy peaked BL Lac. 31, 76, 77, 123

IC Inverse Compton. ii, xiii, xv, 17, 30, 31, 36, 84–89, 94, 96, 98, 101, 103–105, 107–110, 112–120, 122, 165, 173, 182–186, 195, 196, 198, 199, 205, 207–209, 211–216, 220–226, 229, 230, 234–236

IR InfraRed. 20, 31, 176, 178, 179, 181, 182, 185, 198, 208, 224, 226, 230

LAT Large Area Telescope. xv, 31, 37, 131, 132, 139, 140, 152, 161–166, 170, 177, 179, 188, 190, 191, 203, 234

LBL Low-energy peaked BL Lac. 31, 32, 76, 77, 132

LC Light Curve. xiii, 164, 177, 179, 180, 191, 193, 203

LE Low Energy. 27, 84, 85

MJD Modified Julian Date. 133, 139, 151, 153, 156, 157, 159, 161–164, 176, 179, 180, 194

MVA Multi-Variate Analysis. 72, 150, 152, 170, 171

MWL Multi WaveLength. xii, xiii, 25, 66, 76, 131, 132, 137, 139, 140, 143, 150, 152, 154, 162–164, 166, 171, 176, 177, 190, 203, 204, 233–235

NLR Narrow Line Region. 13, 18

NLRG Narrow Line Radio Galaxy. 20

NLS Narrow Line Seyfert. 111, 117

NLS1 Narrow Line Seyfert 1. i–iv, xi, xv, 1, 27, 28, 34–37, 40, 42, 79, 86, 94, 173–178, 181, 187, 189, 201, 203, 205, 219, 220, 223, 225, 226, 228, 232, 233, 235–237, 270

NSB Night Sky Background. 64, 65, 71, 72

PCA Proportional Counter Array. 153

PMT Photo-Multiplier Tube. 57, 62, 64, 66, 67

QSO Quasi Stellar Object. 5

RASS Rosat All Sky Survey. 144

RL Radio Loud. 5, 6, 34–36

RQ Radio Quiet. 6

RXTE Rossi X-ray Timing Explorer. xii, xv, 124, 145, 152–158, 162, 163, 166, 170

SDSS Sloan Digital Sky Survey. 187–189

SED Spectral Energy Distribution. i–iv, xii, xiii, 16, 30–33, 36, 76, 79, 87, 88, 91, 92, 94, 123, 128, 143, 152, 154, 156, 159, 161, 164, 166, 170, 171, 173, 176–179, 184, 187, 189–191, 193, 198, 199, 202, 209, 219, 220, 224, 226, 228, 230, 232–234, 270

SMBH Super-Massive Black Hole. 1, 7, 8, 10, 12, 24, 26

SSC Synchrotron Self-Compton. i–iv, xii, xv, 79, 86–88, 90–94, 110, 123, 125, 126, 128, 129, 139, 143–145, 154, 164, 166, 168–171, 176–178, 181, 182, 185, 195, 198, 205, 206, 208, 212, 214, 221, 222, 225, 229, 230, 233–235

SSRQ Steep Spectrum Radio Quasar. 23, 24

SUMSS Sidney University Molonglo Sky Survey. 144, 169, 170

ToO Target of Opportunity. ii, iv, 76, 131–133, 137, 139, 140, 233, 234

UV Ultra-Violet. 10, 11, 13, 14, 20, 30, 31, 34, 83, 108, 121, 177, 178, 185, 195, 208, 216, 225, 226, 236

UVOT UltraViolet/Optical Telescope. xv, 134, 135, 138–140, 144, 145, 152, 158–160, 162–164, 166, 177, 179, 190–193, 234

VHE Very High Energy. 15, 17, 27, 31, 43, 47, 54, 61, 64, 76, 84, 90, 120, 121, 125, 129, 130, 132, 133, 139, 143, 144, 148, 152, 164, 168, 169, 171, 223, 235

WISE Wide-field Infrared Survey Explorer. xiii, 144, 152, 161, 163–166, 170, 179, 180, 188, 193, 226

XRT X-Ray Telescope. xv, 131, 136–140, 144, 145, 152, 157–159, 162–164, 166, 168, 177, 179, 188–191, 193, 202, 234

List of Figures

List of Tables

1 Active Galactic Nuclei

Active Galactic Nuclei (AGN) are amongst the most interesting astrophysics subjects nowadays. As the most powerful and compact sustained rate energy sources in the Universe, these extragalactic objects are intrinsically interesting. Remarkably enough, 10-20% of all energy radiated over the life of the Universe comes from AGN, whence they must have had a strong influence on the formation of its structure. Moreover, the fact that AGN are the most luminous objects in the sky make them extraordinary beacons of the very distant Universe, and hence their study can help us gain a better understanding of the cosmology of the Universe. But what do we exactly call an AGN?

For AGN we understand any galactic nucleus that presents indications of activity due to accretion onto a Super Massive Black Hole (SMBH, $M_{BH} \sim 10^7$-$10^9\ M_\odot$). The observational signatures of accretion activity one has to look for in the search for AGN include strong emission lines in the optical range, strong radio emission, broad-band continuum spectra and rapid variability, among others. Active galaxies represent around 1% of the total galaxies in the Universe, and the objects within the AGN class are fairly inhomogeneous, and sometimes differ greatly from one another in a certain characteristic.

This chapter gives a brief summary of the discovery of AGN [Section 1.1], along with a description of the basic components [Section 1.2]. We also present the AGN unification paradigm and the basics of the AGN classification that were motivated by the varied AGN zoo known so far [Section 1.3]. Special emphasis is put in the two gamma-emitting AGN subclasses that will be the main subjects of the present work, blazars and gamma-emitting NLS1 galaxies [Section 1.4] and their main observational characteristics [Section 1.5].

1.1 Overview of the history of AGN discovery

Going back in time for around a century, first observations of what we now call AGN were performed by Fath (Fath [Fat09]) at the Lick Observatory in California. At that time, there was great interest in clarifying whether the spiral nebulae were either relatively nearby, gaseous objects resembling the Orion nebula, or either far more distant recollections of unresolved stars. Fath himself was prone to think that these spirals showed a continuum spectrum in accord with a collection of stars rather than the bright-lined spectrum expected from gaseous nebulae.

With a self-made spectrograph specially designed to detect faint spectra, he realized that while most of the objects showed a continuum spectra with stellar absorption lines, there was one, NGC 1068 (also known as Messier 77), which also presented emission lines in its spectrum. He correctly identified the absorption lines as the integrated light of large numbers of stars, and recognized the emission lines as the characteristic emission lines of planetary nebulae. He did not consider that NGC 1068 could be a galaxy on its own though. Figure 1.1 shows the spectra he obtained for NGC 1068 and for the Andromeda galaxy as a comparison.

A couple of years later, Slipher [Sli17] confirmed these bright lines of NGC 1068 and its composite spectrum with spectra taken in 1913 at the Lowell Observatory, and additionally found a very large shift toward the red in the lines. He nonetheless discarded any kind of radial velocity explanation for this spread of the spectra.

Hubble's findings of Cepheid variable stars in spiral nebulae that were too distant to belong to the Milky Way proved the existence of such objects outside our galaxy (Hubble [Hub25]), confirming the theory that stated that the Universe was not limited to the Milky Way. In 1926, observing NGC 1068 again along with other extragalactic nebulae such as NCG 4050 and 4051, Hubble re-emphasized those features that resembled planetary-nebula-like emission lines in their spectra (Hubble [Hub26]).

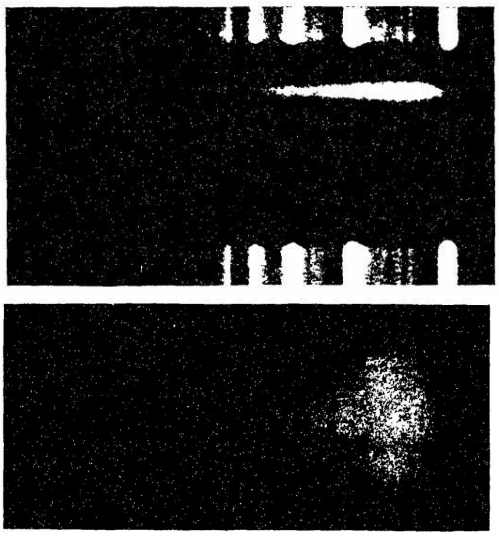

Figure 1.1 Spectra of NGC 1068 (**top**) and the Andromeda nebula (**bottom**) obtained by Fath [Fat09]. Andromeda was not yet known as a galaxy until Hubble's findings (Hubble [Hub25]).

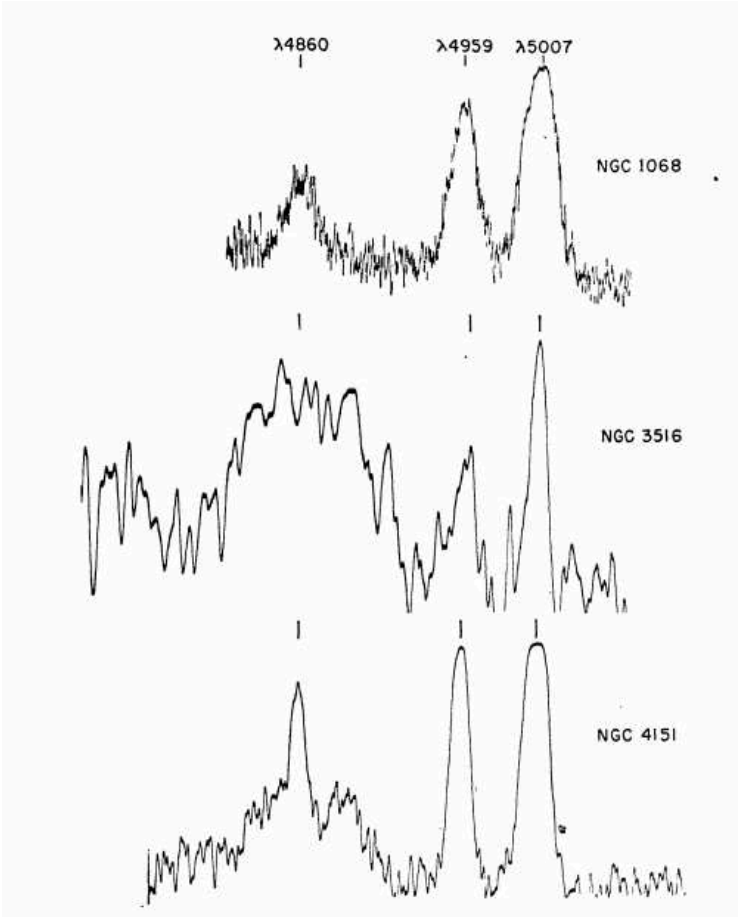

Figure 1.2 Microphotometer tracings of three emission lines in the three spiral nebulae NGC 1068, 3516 and 4151 obtained by Seyfert (Seyfert [Sey43]).

Somewhat later, in 1943, Seyfert observed these and some other galaxies, closely analysing the ones that presented relatively high-ionization nuclear emission lines (Seyfert [Sey43]). During his research, Seyfert obtained spectrograms of 6 galaxies (thought to be nebulae at that time) with nearly stellar nuclei showing emission lines superimposed on a normal solar-type spectrum (see Figure 1.2).

He discovered not only that these 'nebulae' invariantly had a highly luminous compact nucleus, but also that they showed much wider emission lines than the galaxies with low-ionization emission lines. The luminous, relatively small star-like nucleus spectrum is actually the main characteristic defining the most abundant type of AGN, the Seyfert galaxies, that will be introduced later on in this work.

Despite the enormous potential of his findings, Seyfert's research was not enough to put AGN in the focal point of astronomers. The necessary thrust would come in later years with the development of radio astronomy.

Indeed, the end of WWII meant that many radio engineers working at facilities that had so far been deployed for warfare purposes became idle. Hence, they decided to turn their efforts towards less belligerent aims like the study of astronomical radio sources.

During a survey of the Milky Way at 60 MHz by Hey et al. [Hey+46], the first discrete radio source was accidentally discovered: a small, fluctuating source in the Cygnus constellation. Bolton and Stanley [BS48] not only confirmed the discreteness of the source, but also set tight constraints on the angular size of the source (down to 8 arcminutes) via interferometry techniques. Alongside, they deduced a brightness temperature of around 4×10^6 K which would be fairly incompatible with a thermal origin of the radiation. It was Bolton [Bol48] who actually introduced the nomenclature Cyg A, Cas A, etc. with a study of 6 discrete radio sources.

These discoveries were closely followed by the optical identification of discrete radio sources by e.g. Bolton et al. [Bol+49] and Smith [Smi51]. Their deft measurements enabled Baade and Minkowski [BM54] to identify the optical counterparts of strong radio sources.

There were some radio sources which seemed difficult to identify to an optical counterpart, though. Some of them appeared to be simple galactic stars, with no absorption lines in their continuous spectra, but unidentifiable broad emission lines that did not match the wavelengths expected for star features were present. Called 'stellar radio sources', various trials were made to explain their characteristics as

bizarre stars, such as white dwarfs with anomalous abundance of the elements, but no consistent interpretation was obtained in such a way.

The decades of the 1950s and 1960s also saw the publication of extensive radio surveys, such as the Third Cambridge Catalogue (3C, Edge et al. [Edg+59]) or the Parkes surveys (PKS, Bolton et al. [Bol+64]; Price and Milne [PM65]; Day et al. [Day+66]). These extensive surveys enabled the classification of radio sources into Class I sources, associated to the Milky Way plane, and Class II sources, isotropically distributed and probably extragalactic (see e.g. Hanbury Brown [Han58]). Three Class II sources presented 12 arcsec upper limits on their size that implied brightness temperatures of 2×10^7 (Morris et al. [Mor+57]) which pointed them as extragalactic radio sources similar to Cyg A.

It was not until Schmidt [Sch63] singled out a number of well-known nebular emission lines in the 'stellar' radio source 3C 273[1] that the first light was cast on the nature of the aforementioned 'stellar radio sources'. In the position indicated by the radio source, Schmidt found two sources: a blue star and something that resembled a "jet". He found that the strong broad emission lines in the spectra of this bizarre blue star were actually the usual Hydrogen Balmer ones, only redshifted to an unparalleled degree, precisely to the (then) large redshift of $z = 0.158$.

The discovery of the large redshift of 3C 273 motivated Greenstein and Matthews to search for emission lines in the spectra of another similar radio source, 3C 48, finding a redshift of $z = 0.367$ (Greenstein and Matthews [GM63]). Being observed at such great distances implied that both 3C 273 and 3C 48 must be very luminous objects, with apparent luminosities reaching up to $\approx 10^{48} \mathrm{erg} \cdot \mathrm{s}^{-1}$. Accordingly, they could not possibly be stars - they were hence dubbed quasi stellar radio sources, 'quasars', AGN so luminous and distant that their host galaxy could not, at that time, be resolved on photometric images[2].

Some time later, 'quasi stellar radio quiet sources' or optically selected quasars were identified (Sandage [San65]). Designed 'quasi-stellar objects', (QSOs) at the beginning, the discrimination between the two classes is quite faded nowadays, considering both radio and optically selected objects simply 'quasars' by the majority of researchers.

Kellermann et al. [Kel+89] introduced the 'radio-loudness' parameter which is widely used nowadays in order to classify a source as radio loud (RL) or radio quiet

[1] One of the sources comprised in the aforementioned Third Cambridge Catalog.
[2] The star-like nucleus can be subtracted with high accuracy nowadays though, unveiling the surrounding galaxy.

(RQ) based on the ratio of the radio (5 GHz) and optical (B-band) spectral flux densities,

$$R = \frac{F_\nu(5\,\mathrm{GHz})}{F_\nu(B)}. \tag{1.1}$$

If the ratio is larger than 10, a source is classified as RL. As will be later introduced, we will only consider RL sources in this work, since their radio-loudness is a characteristic that is linked to their gamma-ray emission.

The discovery of RL and RQ quasars introduced the concept that different types of AGN were likely to present different appearances and features. A clear example is a subclass of RL quasars, known as 'blazars', *blazing quasi-stellar radio sources*, that presents extreme properties that clearly set them apart from other AGN types.

Some of the extreme properties of blazars include rapid optical variability at all wavelengths and on all kind of timescales. Moreover, some blazars present a smooth, featureless optical spectra whose origin is usually explained by means of the presence of a relativistic jet whose axis is closely aligned to the line of sight of the observer (Blandford and Rees [BR78]). The small angle of view between the jet and the Earth causes the emission from the jet to be heavily Doppler boosted, so its intensity is so strong that hampers the detection of the inner part of the AGN. Blazars and their relativistic jets will be discussed in more detail further on this work.

1.2 The cornerstones of AGN

Although different AGN subclasses might present different characteristics that might be explained, for instance, by means of orientation and inclination biases, as will later be explained, their basic structure is composed of a number of key components that will be presented in the following. A schematic view of the components and their position w.r.t. the central engine is shown in Figure 1.12.

1.2.1 The central engine

The origin of the high luminosities observed in Seyferts, quasars and AGN in general lies within a very small region (around less than a few tens of light days) close to the center of the object. So as to reach such luminosity levels, the amount of released energy must be much higher than the one that can be attained from thermonuclear reactions. The only mechanism consistent with the release of such energy levels is the gravitational force generated in a rotating accretion disc around a compact object of $M \approx 10^7 - 10^9 M_\odot$, which general relativity requires to be a SMBH. The potential gravitational energy of the matter spinning around the SMBH is transformed into thermal energy via friction and viscosity, creating an accretion disc around the central engine. For a review in the topic see e.g. Rees [Ree78], Rees [Ree84].

The term black hole is used to describe a sufficiently compact object that its event horizon, i.e. the furthest point a photon can reach before being swallowed by the gravitational potential of the black hole, has noticeable effects on the surrounding spacetime and matter. In other words, the event horizon sets the boundary around the black hole from which nothing, not even light, can escape. If an object was to go beyond the event horizon of a black hole and fall inwards, an external observer would see the light emitted by the object infinitely redshifted.

Different types of black holes yield different event horizons. For instance, in the case of a Schwarzschild (static) black hole, the event horizon is located at the Schwarszchild radius

$$R_S = \frac{2Gm}{c^2}. \tag{1.2}$$

which in units of the gravitational radius corresponds to $R_S = 2R_G$. For a one-solar-mass object the Schwarszchild radius is $R_S = 3\,\mathrm{km}$. However, general relativity states that the space-time around heavily compact objects is curved, so there cannot be a stable circular orbit in the vicinity of the event horizon: the last stable orbit or Innermost Stable Circular Orbit (ISCO) is actually located at a distance $R_{ISCO} = 3R_S$. Note that all these statements are valid for non-rotating black holes, i.e. the aforementioned Schwarszchild (static) metric. The horizon is much more complicated in rotating objects, and the last stable orbit is located closer to the central engine, as will be presented in the following subsection.

1.2.2 The accretion flow

The term *accretion* stands for matter falling onto some body, more precisely onto a compact object as far as the present work is concerned. The presence of a SMBH is closely linked to the existence of an accretion flow in the vicinity of the central compact object.

To illustrate the creation of such flow, let us consider matter being accreted onto a compact body of mass M and radius R. The potential energy of matter falling freely to a distance r from the compact object is

$$E_{acc} = \frac{GMm}{r} \tag{1.3}$$

where G is the gravitational constant and m is the mass of the infalling matter. When the accreting matter reaches the surface of the object at $r = R$, part of the kinetic energy of the free fall has to be radiated away as heat. The accretion luminosity of the compact object can then be defined as a function of the mass accretion rate of the BH $\dot{m} = \mathrm{d}m/\mathrm{d}t$ as

$$L_{acc} = \frac{GM\dot{m}}{R}\,. \tag{1.4}$$

Defining the accretion distance R in units of the Schwarzschild radius R_S (see Equation 1.2) so that $R = n\,R_S$, the accretion luminosity can be expressed as

$$L_{acc} = \frac{\dot{m}c^2}{2n} = \eta\,\dot{m}\,c^2\,. \tag{1.5}$$

Here, η is known as the efficiency of the accretion, defined as the fraction of the rest mass energy that is converted into radiation before succumbing to the gravitational field of the black hole.

The most compact astrophysical objects are indeed black holes, but they do not have a surface for the matter to fall onto. However, the accreting matter always possesses a certain amount of angular momentum that prevents it from falling directly onto the compact object. The accreting matter will hence rotate around the central engine. Collisions between particles in the direction parallel to the angular momentum will tend to sum to zero, while collisions in the orthogonal direction will tend to maintain

an average circular velocity, resulting in the cloud being flattened into a steady structure known as accretion disc. If the disc becomes sufficiently dense, viscosity within the disc will cause an outward transfer of angular momentum and will also heat the disc itself. In the geometrically thin but optically thick disc paradigm, the most studied one[3], most of the heat will radiate away from the disc surface before the matter falls into the black hole. In other words, infalling matter spirals across the accretion disc while it loses angular momentum via friction, becoming increasingly hotter (and hence radiating) until it reaches the event horizon and falls into the black hole.

The accretion efficiency η of a black hole accretion disc depends on the innermost stable circular orbit of the disc, R_{ISCO}, which is determined by the spin of the BH. The innermost stable orbit is different for static (Schwarzschild) and rotating (Kerr) BHs, whose R_{ISCO} are at $\mathrm{R}_{ISCO} = 6\ \mathrm{R}_G$ and $\mathrm{R}_{ISCO} = 1\ \mathrm{R}_G$ respectively. Hence, the accretion efficiency is also different for both types of BH, namely $\eta \sim 0.06$ for a Schwarzschild BH and $\eta \sim 0.42$ for a Kerr BH.

Another important quantity regarding accretion discs is the so-called **Eddington luminosity**, the luminosity at which the gravitational force inwards

$$F_G = \frac{GMm}{R^2} \tag{1.6}$$

balances with the radiation force outwards. To calculate the latter, let us recall the expression of the radiation pressure at a distance R,

$$P_{rad} = \frac{L}{c}\frac{1}{4\pi R^2}\,. \tag{1.7}$$

Radiation pressure is force per unit area, so the radiation force can be expressed as

$$F_{rad} = P_{rad}\,\kappa\, m \tag{1.8}$$

where κ is the opacity of the accreting material, i.e. the cross-sectional area per unit mass for radiation scattering. Assuming that in high energy astrophysics most of the accreting material is ionized hydrogen, and that the opacity can be considered to be given by the Thompson scattering cross-section σ_T, the cross-section will come

[3] It is indeed the paradigm that we consider in our external component model in Chapter 3.

from electrons, while the mass will lie on protons. Hence, we can approximate the opacity κ as $\kappa = \sigma_T/m_p$, and introducing this opacity in Equation 1.8, the radiation force can be expressed as

$$F_{rad} = \frac{P_{rad}\sigma_T m}{m_p} = \frac{L\sigma_T m}{cm_p}\frac{1}{4\pi R^2}. \tag{1.9}$$

Thus, balancing the gravitational force (Equation 1.6) and the radiation force (Equation 1.9), the Eddington luminosity is given by

$$L_{Edd} = 1.3 \times 10^{38}\frac{M}{M_\odot} \tag{1.10}$$

whence the Eddington luminosity only depends on the black hole mass, and sets an upper limit to the disc luminosity. That is, if the accretion disc was to produce a luminosity larger than the Eddington luminosity, the mass being accreted would feel a radiation pressure that will equate the gravitational potential and stop the accretion process, lowering the disc luminosity to the Eddington level, in a self-regulating process: we have a natural feedback process with a limiting accretion rate. If we equal the accretion luminosity in Equation 1.5 to the Eddington luminosity, we get the limiting Eddington mass accretion rate

$$\dot{M}_{Edd} = \frac{4\pi G M m_p}{\eta c \sigma_T}. \tag{1.11}$$

The UV excess seen in the spectra of many Seyfert galaxies, also known as the "UV bump" or Big Blue Bump (BBB), is the observational proof of the presence of a cold accretion disc in the vicinity of the black hole that can be be fitted by a blackbody with a temperature of 23 000 K-30 000 K (Malkan and Sargent [MS82], Malkan [Mal83]).

In low-mass, high accretion rate AGN, the Wien tail of an standard accretion disc can extend into the soft X-ray regime. On the contrary, accretion discs of SMBHs are not expected to emit much keV X-ray radiation since they are relatively cold. Thus, the observed and well documented AGN X-ray emission that reaches up to hundreds of keV requires a component other than an accretion disc to be generated. Back in 1988 Guilbert and Rees [GR88] and Lightman and White [LW88] predicted the presence of a strong iron line and a broad high energy bump in the X-ray spectra of Seyfert galaxies that originate from the reprocessing of the soft X-ray flux intercepted by

cold matter. Such features were first confirmed by e.g. Pounds et al. [Pou+90], Piro et al. [Pir+90], Matsuoka et al. [Mat+90]. Observations also showed that the X-ray spectrum can be well approximated by a simple power law up to $\sim 150\,\mathrm{keV}$ (e.g. Turner and Pounds [TP89]). Furthermore, when high-energy X-ray observations are available, an exponential cutoff is observed in the spectrum of Seyferts in the range 100-150 keV (Fabian et al. [Fab+15]) and the radiative spectrum can be expressed as

$$F_X(\nu) \propto \nu^{-\alpha_X} \exp[-\nu/\nu_C], \;\; \alpha_X \in [0.7 - 0.9] \tag{1.12}$$

where ν_C is the cutoff frequency.

The rapid variability found by Kunieda et al. [Kun+91] requires the cold matter to be located close to the X-ray emitting region. Moreover, luminosities that are (if smaller) comparable to those of the accretion disc, point towards the X-ray emission region being located not very far away from the central engine itself. One of the suitable scenarios that can account for these observational characteristics is the hot ($\sim 10^9\,\mathrm{K}$) corona scenario where a significant fraction of the accretion disc is comptonized into an optically thin, X-ray emitting corona (Haardt and Maraschi [HM91], Haardt and Maraschi [HM93]). Making a parallelism with the Solar corona, in this scenario both above and below the accretion disc there is a region filled by very hot electrons (w.r.t. those in the accretion disc). The X-ray corona is thought to dominate X-ray emission in non-blazar sources. For a recent review on the X-ray emission from AGN, see Reynolds [Rey16].

There is also evidence of a second comptonization region, optically thicker and cooler than the corona, in the accretion flow of some AGN. The signature of this additional emission region is an excess of soft X-ray emission above the power law of the corona, whence its name “soft excess” originates. This soft-excess can for instance be modeled as a thermal black body with a constant temperature profile (see e.g. Gierliński and Done [GD04]).

Thus, the continuum emission of the accretion flow can be described through a combination of an accretion disc emitting mostly at UV/optical frequencies, a comptonization region producing the soft-excess and another comptonization region (the corona) producing harder X-rays.

1.2.3 The broad and narrow line regions

Spectra of some AGN present broad lines that are originated within a region located at a distance of around 100 light-days from the central engine known as the Broad Line Region (BLR). The BLR is thought to be a high-density gas (with electron densities $n_e \geq 10^9\,\mathrm{cm}^{-3}$) composed by individual clouds moving in Keplerian orbits around the SMBH. The high-density of the clouds would mean that collisions would suppress forbidden transitions.

The width of the broad lines greatly varies from object to object. Typical values lie within the 1000 to 10 000 $\mathrm{km\,s}^{-1}$ range, widths too large to be due to thermal motions. As a reference, a temperature of $T \sim 10^4\,\mathrm{K}$ yields a velocity of $v = 10\,\mathrm{km\,s}^{-1}$, so the temperatures required to obtain the widths observed in the broad lines would need to be extremely (and unrealistically) high. If the widths cannot have a thermal origin, bulk motions are necessary to observe such Doppler shifts. Considering that these bulk motions are most probably determined by the central engine, and that the BLR reprocesses photons from the continuum radiation source, i.e. the accretion disc, the BLR provides an unmatched insight on the innermost regions of the AGN.

In fact, the most successful method for direct measurements of the black hole mass of an AGN is the so-called reverberation mapping technique (see e.g. Peterson [Pet93], Blandford and McKee [BM82]). Using high-cadence spectrophotometric monitoring, the reverberation mapping approach measures the time-delay between variations in the continuum flux and the echo of such variations in the broad emission line flux. This delay gives a benchmark of the BLR size which in combination with the velocity width of the emission line enables the deduction of a virial estimate of the mass of the central engine. A scaling factor is applied in order to account for the BLR geometry and kinematics. Up to now, dozens of successful black hole mass measurements have been performed via reverberation mapping (e.g., Peterson [Pet98], Peterson [Pet04], Du et al. [Du+16]).

A useful quantity that can be derived from reverberation mapping measurements is the relation between the radius of the BLR and the luminosity of the AGN, the $r - L$ relation (e.g. Kaspi et al. [Kas+00], Bentz et al. [Ben+09]). For instance, considering the Lyman Alpha line, the size of the BLR is proportional to the square

root of the disc luminosity in units of $10^{45}\,\mathrm{erg\,s^{-1}}$(e.g. Ghisellini and Tavecchio [GT09])

$$R_{BLR} \sim 10^{17} L_{disc,45}^{1/2}\,\mathrm{cm}. \tag{1.13}$$

Here the underlying assumption of most of the disc being able to ionize the atoms in the BLR has been made. Indeed, through the $r - L$ relation, one can obtain an estimate of the mass of the black hole by measuring the continuum luminosity and the velocity width of a broad-line of the same spectrum. Although much simpler than the time-consuming reverberation mapping campaigns, the application of the $r - L$ correlation to infer additional quantities is partly biased due to such studies having been carried out mainly for radio quiet AGN, that is, sources where synchrotron radiation from the jet at optical/UV frequencies is negligible w.r.t. the emission from the continuum radiation source (i.e. the accretion disc).

The high correlation between the variations of emission line fluxes and continuum fluxes indicate that the lines are indeed caused by the accretion disc photoionizing the BLR clouds. An important quantity is how much of the continuum radiation from the central region of the AGN ionizes the BLR. Considering the clouds to be opaque, the amount of radiation they absorb can be approximated as a covering factor that represents the fraction of the sky covered by BLR clouds as seen by the central engine. The covering factor can be estimated by comparing the luminosity from all emission lines an that of the continuum emission.

The spectra of some AGN also present narrow emission lines that originate from a region of ionized, low-density gas (with electron densities $n_e \leq 10^3 - 10^6\,\mathrm{cm^{-3}}$) known as the Narrow Line Region (NLR). Narrow lines have Full Width Half Maximums (FWHM) of $\sim 300 - 500$ km s^{-1}, still much larger than the widths originated by thermal broadening, but narrower than the widths seen in broad lines. Another difference w.r.t. the BLR is that electron densities in the NLR are small enough so as not to collisionally suppress forbidden lines, as mentioned before. For the narrow lines, the distances are around 100 pc, much larger distances than the BLR.

1.2.4 The obscuring torus

The central engine of an AGN is surrounded by a region composed by individually optically thick dusty clouds scattered in a toroidal structure (e.g. Krolik and Begelman [KB88]). The presence of a torus that provides anisotropic obscuration is fundamental for the paradigm of the unification theory in which different AGN spectral classes are mostly via differences in the viewing angle, as will later be explained in Section 1.3. Its presence is nowadays a certainty, since Jaffe et al. [Jaf+93] achieved direct imaging of the torus two decades ago (see Figure 1.3).

Starting at around a 10 pc distance from the central engine, the outermost region of the torus reaches out to some hundred parsecs. As for the radiation processes involved, the accretion disc optical and UV photons heat up the inner part of the torus which in turn emits infrared radiation due to blackbody absorption and re-emission.

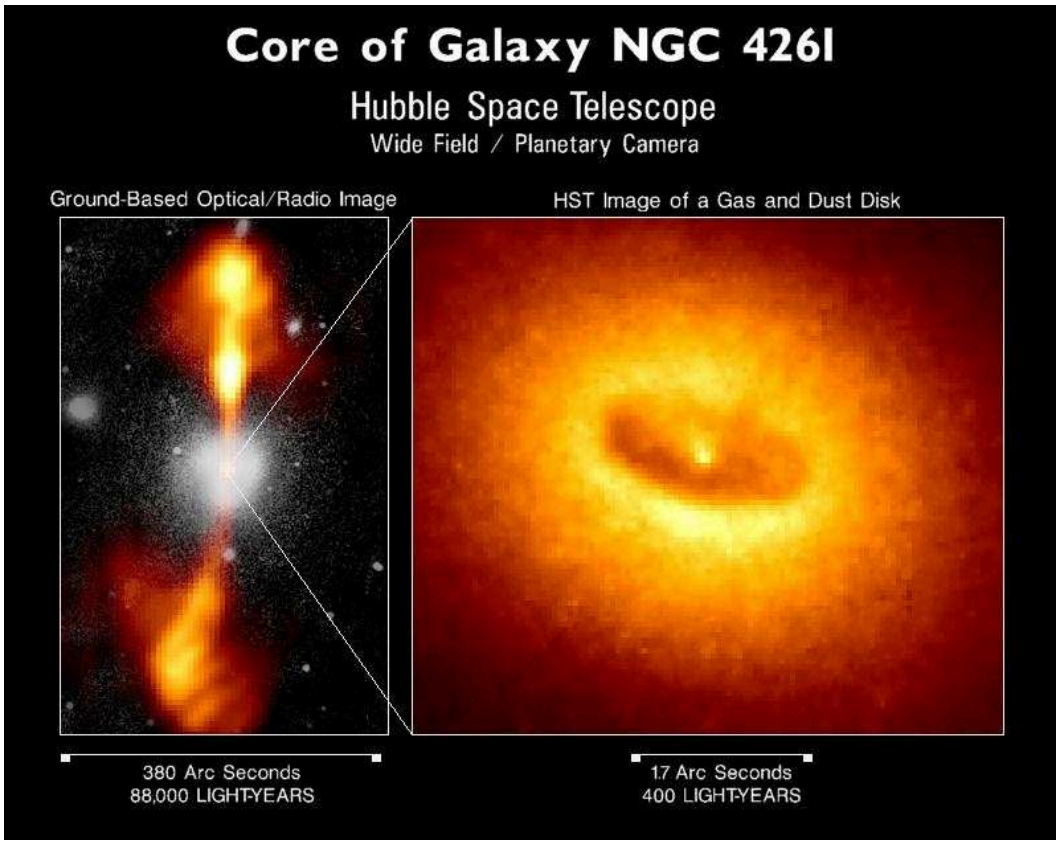

Figure 1.3 Close-up on the obscuring torus of the galaxy NGC 4261. From Jaffe et al. [Jaf+93].

1.2.5 The relativistic jet

Some accretion discs produce highly collimated particle (plasma) flows that are accelerated away from the central engine at velocities close to the speed of light. Known as relativistic jets, such outflows are thought to be generated when the accretion flow couples with the magnetic field of the black hole, and magneto hydrodynamics simulations point towards the magnetic field playing an important role in jet formation and posterior collimation.

The first relativistic jet from an AGN to be observed (at optical wavelengths) was that of M87 by H.D. Curtis in 1917 (see Figure 1.4 for M87 and its jet as seen by the Hubble Space Telescope). 40 years later, the development of radioastronomy opened a new window for better understanding the nature of jets, and consequently of AGN. Although jets were initially mostly seen at radio frequencies, emission from jets has nowadays been detected at different wavelengths, even at Very High Energies (VHE) by the High Energy Stereoscopic System (HESS, Chapter 2), as shown in Figure 1.5.

Nowadays we know that AGN jets can be long and smooth or short and stubby, and range from straight shapes to curved shapes, with a varying presence of knots within. Although the majority of those knots show apparent superluminal velocities [Section 1.5.3], some of them present either subluminal movement or even static behaviour. With respect to the cases where superluminal velocities are measured, we do know that the angle towards the observer needs to be of a few degrees.

The processes by which such energetic outflows are generated and by which the particles are accelerated up to relativistic velocities are still a mystery though. The most extended theory postulates that the plasma is accelerated through stochastic shock acceleration: particles traveling across the shocks gain kinetic energy. The jet reaches its end when its kinetic energy is balanced to the kinetic energy of the intergalactic medium. High angular resolution observations show evidence of jets extending from the sub-pc up to even the mega-pc scale.

Jets carry an important fraction of the AGN power away from the nucleus. Interferometry studies show how varied the speeds and energy carried by the jets are. For instance, Seyfert 1 galaxies present slower and fainter jets than blazar type objects, whose jets are the highly energetic and collimated. Moreover, blazar jets are known to be very variable within small time scales at all wavelengths. All these facts undoubtedly make jets one of the most spectacular characteristics of active galaxies, and one of the best sources for their study.

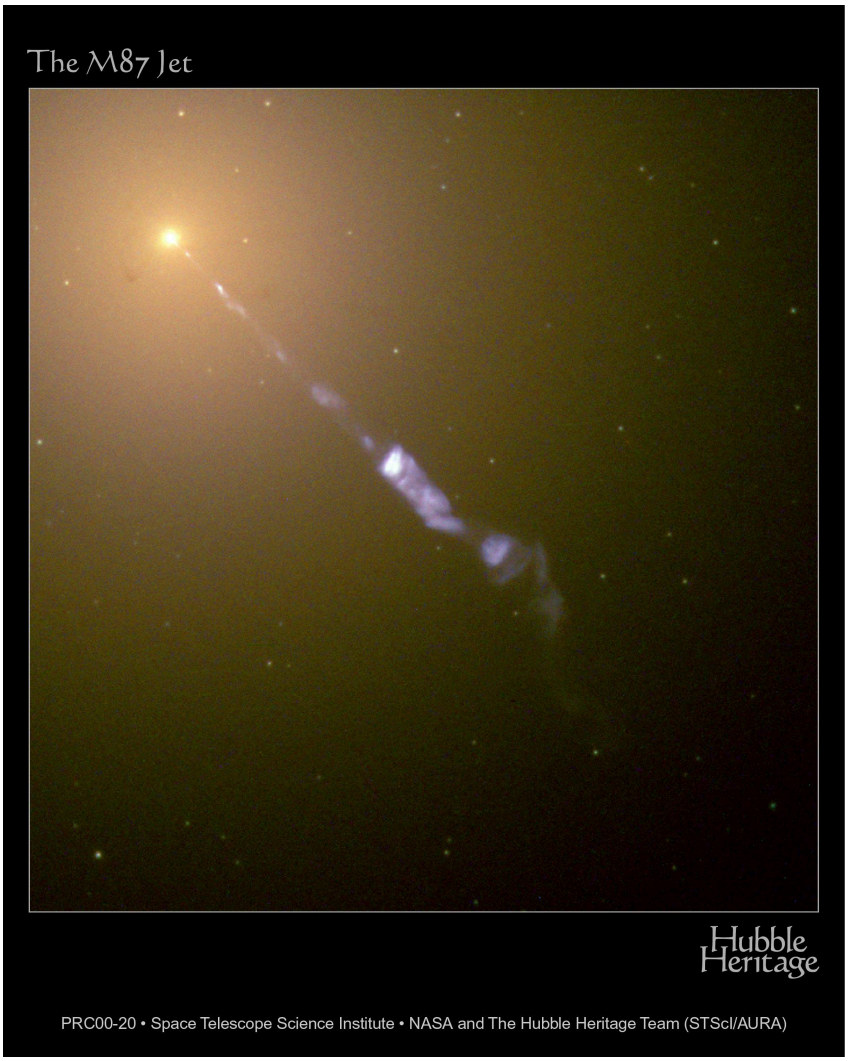

Figure 1.4 M87 as seen by the Hubble Space Telescope. The jet is clearly visible at optical wavelengths.

At radio frequencies, the inner region of the jet, the nucleus, is optically thick. That means the majority of the radiation created by the source is self-absorbed by the source itself. Here lies the difficulty of observing and extracting information from the center of the engine that powers the jet. As we travel further away from the nucleus along the relativistic jet, regions of enhanced emission known as components or knots are observed.

By studying the Spectral Energy Distribution (SED) of AGN, we know that the majority of the energy they release comes under the form of synchrotron radiation (see Section 3.1.1) from the interaction between relativistic charged particles within the relativistic outflow and the surrounding magnetic field. The nature of synchrotron radiation generates a stratification of the jet regarding the amount of emitted energy

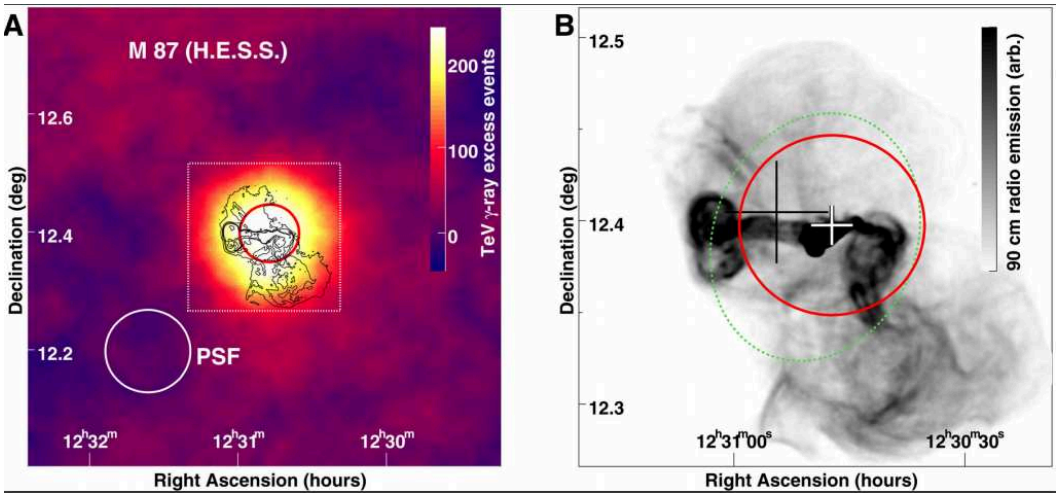

Figure 1.5 Sky map as well as the position and extension limit of the TeV gamma-ray emission from M87. **Left:** Smoothed TeV gamma-ray excess map as measured by HESS. **Right:** The 90 cm radio data measured with the Very Large Array, together with the TeV position. The black cross marks the position and statistical error of the gamma-ray source reported by HEGRA. From Aharonian [Aha06].

and the frequency at which it is emitted: the innermost regions of the jet not only do emit more radiation, but the emitted radiation is more energetic. The relativistic plasma emits at lower energies as it cools down along the jet.

Apart from synchrotron radiation, another dominant radiation mechanism within jets is the Inverse Compton (IC, Section 3.1.4) scattering of low-energy photons by highly relativistic particles[4]. The environment within the jet is a mixture of highly relativistic particles and a radiation field. Since the average photon energies of the radiation field lie well below the energies of the relativistic particles, the presence of IC processes that result in the generation of High Energy (HE) and even VHE photons is major. The radiative processes mentioned here will be presented in more detail in Section 3.1.

Although there are many unknown aspects regarding the physics of relativistic jets in AGN, we do know that jets are bond to dominate the emission over a large part of the electromagnetic spectrum, which means that the observed radiation will be heavily relativistically beamed. Such beaming needs to be accounted for if we are to study the underlying physical processes involved in relativistic jets, an ubiquitous phenomenon happening all over the Universe in systems accreting onto compact

[4]The nature of the highly relativistic particles is still cause of debate. One of the major uncertainties with respect to AGN jets lies on their composition, that is, whether the jet has a purely leptonic or a hybrid lepto-hadronic composition. For the purposes of the present work, only leptonic jets are considered.

objects, e.g. microquasars, gamma-ray bursts and obviously AGN. In the present work, we focus precisely on the jets from the latter type of object.

1.3 Unified schemes of AGN

From the discovery of radio-loud and radio-quiet quasars (see Section 1.1), it was clear that AGN come in a wide variety of types and flavours. Indeed, it seemed that although these compact objects might share a given characteristic, they could be completely different regarding another one. These observational differences motivated the development of AGN unification schemes that account for the highly anisotropic emission from the inner parts of the AGN.

Concerning the radio point of view, the basic classification is the radio-loud and radio-quiet AGN dichotomy. In fact, radio-loud AGN probably do contain a normal, radio-quiet AGN within, plus a seemingly unrelated radio emission from the relativistic jets.

Starting from radio-quiet AGN, Antonucci [Ant93] proposed a further classification based on optical spectroscopy[5]. In this paradigm, Type 2 AGN present permitted and forbidden lines from the NLR in their spectra. In addition to these narrow lines, Type 1 AGN present permitted lines from the BLR and a strong, featureless continuum in comparison to their broad-line emission. The lack of broad forbidden lines suggests the broad line gas is extremely dense, as mentioned in Section 1.2.3, thus non-electric-dipole transitions are quenched by collisions. Figure 1.6 and Figure 1.7 present the spectra of a Type 1 Seyfert and a Type 2 Seyfert respectively. Note that if the nuclear luminosity of the AGN is low, we have Type 1 and Type 2 Seyfert galaxies (because the host galaxy is visible), whereas high luminosity AGN would be Type 1 and Type 2 quasars.

This spectroscopic classification also seems to yield different X-ray properties between Type 1 and Type 2 AGN. The latter usually presents strong keV emission, while X-rays have been detected only for a few objects that historically had been classified as

[5]This classification was based on the approach proposed by Khachikian and Weedman [KW74].

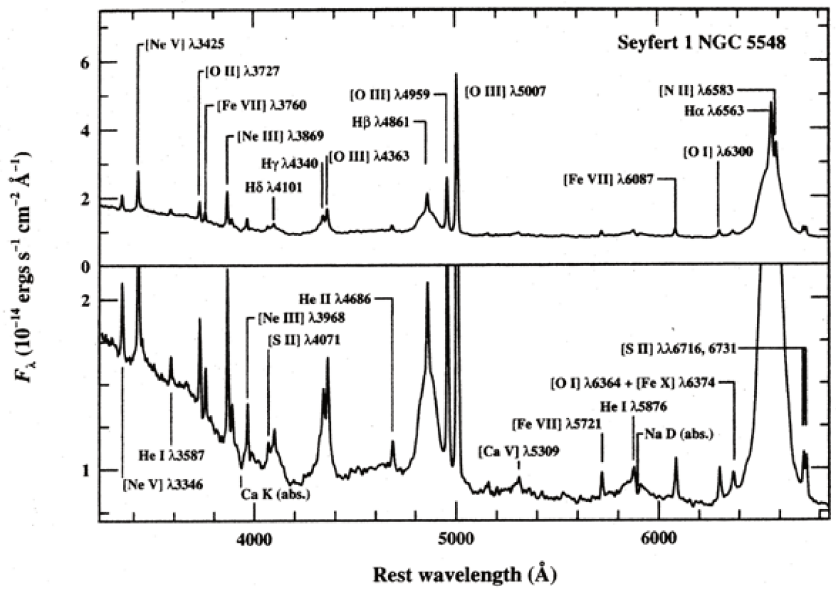

Figure 1.6 Optical spectrum of Seyfert 1 NGC 5548. Strong absoption features of the host galaxy and broad and narrow emission liens of the Seyfert are identified. Lower panel shows an expanded ordinate axis. FWHM of the broad components is about $5900\mathrm{km}\cdot\mathrm{s}^{-1}$, whereas for narrow lines it is $400\mathrm{km}\cdot\mathrm{s}^{-1}$. Credits: A.V. Filippenko.

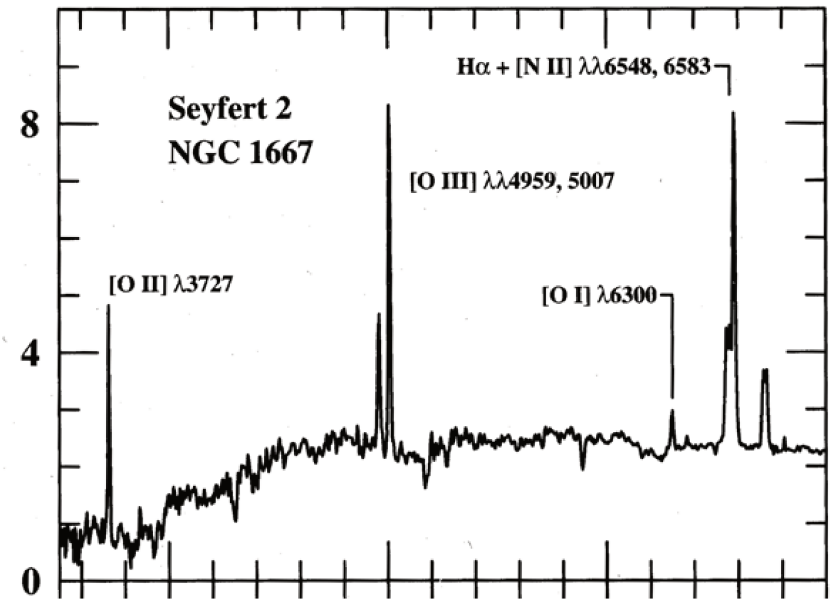

Figure 1.7 Optical spectrum of Seyfert 2 NGC 1667. Most important emission lines are pinpointed in the spectrum (Ho et al. [Ho+93]). Some strong absorption lines that arise in the host galaxy rather than the AGN itself are also identified. X-axis and y-axis represent wavelength in Å and F_λ in erg cm^{-2} s^{-1} Å^{-1} respectively. This spectrum can be compared with the spectrum of the Seyfert 1 NGC 5548, in Figure 1.6. Credits: A. V. Filippenko.

Type 2s. This subset of X-ray bright AGN with weak or undetectable broad lines are called narrow-line X-ray galaxies.

All the above mentioned considerations suppose that radio-quiet AGN can be classified depending on whether they have broad lines and featureless continua or not. The underlying question is why do Type 2 AGN not present these features. Either they do not have them intrinsically, either they are obscured for an observer in Earth at least. The fact that polarized observations of Type 2 AGN reveal a Type 1 nucleus is a strong hint towards the obscuration scenario, where Type 1 AGN would be seen face-on, right into the nucleus, while Type 2 would be edge-on AGN with an obscuring body (i.e. the torus) between the nucleus and the observer, as illustrated in Figure 1.8.

Regarding radio-galaxies, they can be classified into Type 2 radio galaxies (a.k.a. Narrow-Line Radio Galaxies, NLRG) and Type 1 radio galaxies (a.k.a. Broad Line Radio Galaxies, BLRG) from the spectroscopic point of view. NLRGs can be further divided into Fanaroff-Riley I galaxies (FRI) if their radio emission is core-dominated, and Fanaroff-Riley II galaxies (FRII) if the emission is dominated by the two hot-spots at the edges of the lobes, and represent the shock front between the relativistic jet and the intergalactic medium. Figure 1.9 and Figure 1.10 show images of a core-dominated FRI and a lobe-dominated FRII respectively. FRII seem to have IR, optical and UV properties similar to radio-quiet AGN, which is probably the case of FRIs too, but the anisotropic radiation from the core drenches these components.

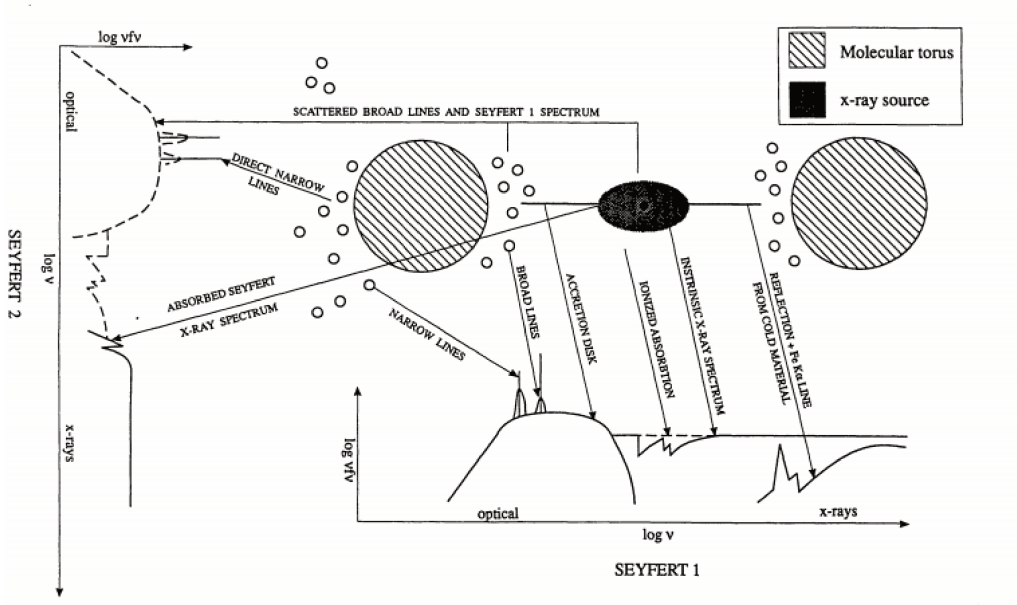

Figure 1.8 Schematic view of emission spectra observed in Seyfert 1 and Seyfert 2 galaxies, from Mushotzky et al. [Mus+93]

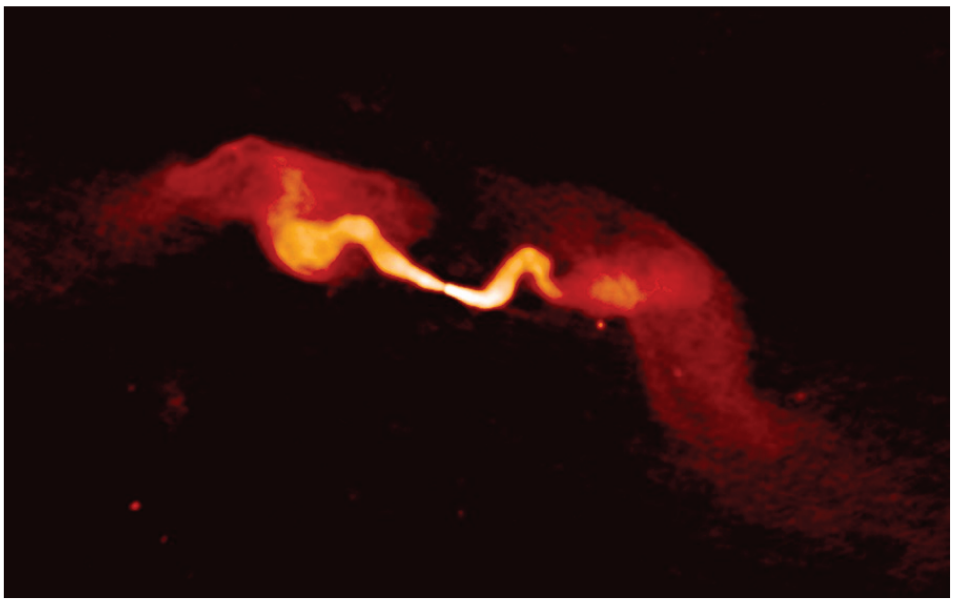

Figure 1.9 The FRI galaxy 3C31. The radio emission is clearly core-dominated, in opposition to Cygnus A in Figure 1.10. Image courtesy of NRAO/AUI.

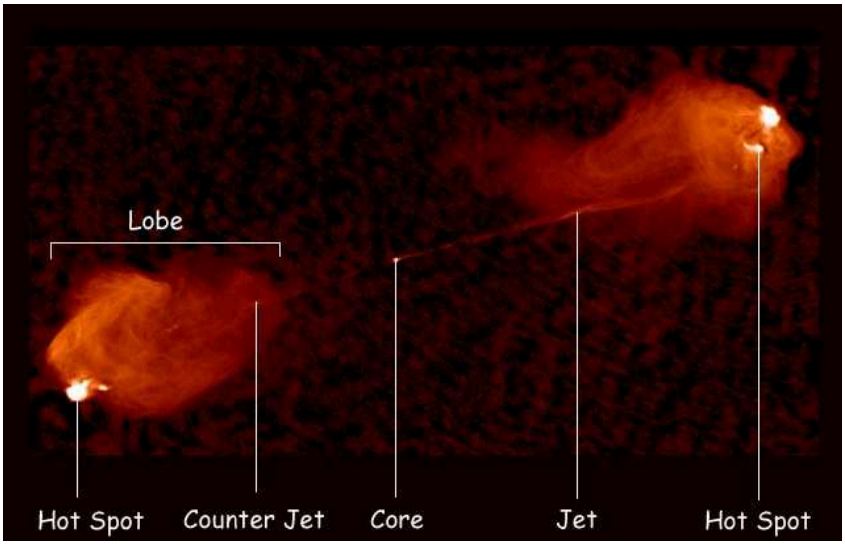

Figure 1.10 The archetypal FRII galaxy Cygnus A as seen by the VLA. The radio emission is lobe-dominated in FRII galaxies. Image courtesy of NRAO/AUI.

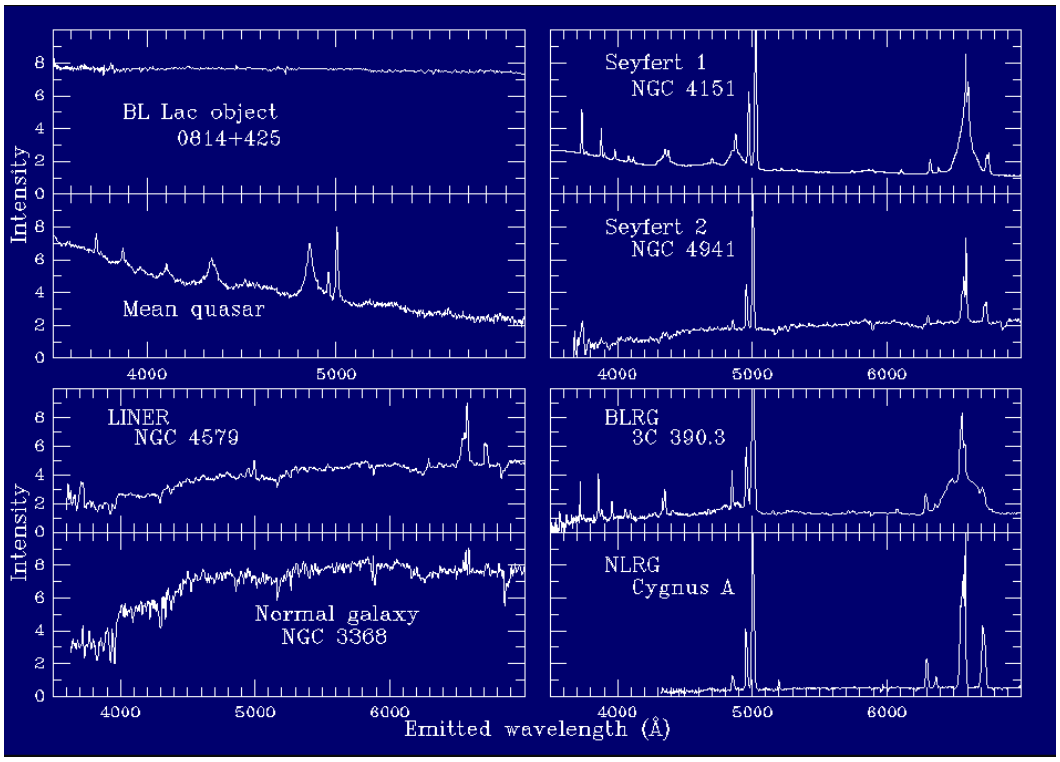

Figure 1.11 Summary of optical spectra of different types of AGN. The BL Lac object and BLRG spectra are from Lawrence et al. [Law+96]. The mean quasar composite spectrum was generated by Francis et al. [Fra+91]. The normal-galaxy NGC 3368 credit goes to Kennicutt [Ken92], while NGC 4579 and NGC 4941 are presented in Keel [Kee83]. Finally, the Cygnus A spectrum comes from Owen et al. [Owe+90]. Image credit: William Keel.

Radio(-loud) quasars can also be further classified into Steep Spectrum Radio Quasars (SSRQs) and Flat Spectrum Radio Quasars (FSRQs) depending on their spectral index[6] at a few GHz, $\alpha = 0.5$ being usually the threshold value. This distinction also reflects the size of the radio emitting region. Considering that synchrotron radiation has a relatively steep spectrum ($\alpha_r \sim 0.7$) for extended emission regions associated to the radio-lobes, and a somewhat flatter spectrum for nuclear, compact emission, SSRQs are mostly lobe dominated FRII AGN, while the nuclear radio emission in FSRQs overrides the extended one, positioning them closer to FRI galaxies.

[6] AGN broad-band spectra are power-laws, the observed flux density roughly being $F_\nu \propto \nu^{-\alpha}$, where the spectral index is $\alpha \sim 1$.

The brief AGN classification summary we have so far presented already gives the impression of a somewhat overwhelming variety of galaxies, sub-classifications and nomenclatures, that regardless of their differences concerning a certain characteristic fall within the AGN class. Thus, the need for a unification scheme that describes all the different types of galaxies comprised within the AGN division along with the variations of the parameters observed for each type of galaxy is easily understandable.

The main concept behind the unified schemes is the highly anisotropic nature of the emission from the inner parts of the AGN. The currently accepted paradigm includes a central engine, possibly a SMBH, surrounded by an accretion disc and fast-moving clouds. The clouds are thought to be under the influence of the strong gravitational field of the BH, emitting Doppler-broadened optical spectral lines due to the radiation they receive from the thermal emission from the accretion disc as introduced in Section 1.2.3. The width of the lines, caused by Doppler broadening, is linked to the distance between the line and the central engine. Thus, narrow lines are originated within the farthest emission regions, and broad lines point towards regions closer to the SMBH.

In addition to the BH, the disc and the clouds, an absorbing material, usually pictured as a torus, obscures the central part of the AGN. Therefore, for transverse lines of sight only narrow line emitting clouds are seen (Type 2 AGN), while near infrared to soft X-ray nuclear continuum from the accretion disc and broad lines from clouds close to the engine are only seen when the galaxy is face-on (Type 1 AGN). The last main element of the unification scheme is a relativistic jet, roughly perpendicular to the accretion disc, which produces strong anisotropy and enhanced continuum emission, the so-called relativistic beaming. Such relativistic jet requires a strong magnetic field which collimates the outflow. The jet is also a discriminating variable to classify the AGN as radio loud or radio quiet based on its presence or absence - a jetted AGN will invariantly be a radio loud AGN. These main AGN components have been presented in Section 1.2. Table 1.1 summarizes the main characteristics of the AGN components.

This axisymmetric description of AGN yields widely different observational properties depending on viewing angles. For instance, BL Lacs are thought to be FRIs with jets at relatively small ($\theta \leq$ 20-30°) angle to the line of sight, while FSRQs are FRIIs oriented at small ($\theta \leq 15°$) angles, SSRQs being at the angles between those of FSRQs and FRIIs. Blazars then are the AGN subclass whose jet is closely oriented with regards to the line of sight. Consequently, an unification model that considers

intrinsic, isotropic features to unify fundamentally identical but apparently different AGN types is more than necessary.

Considering the fact that AGN emit radiation over the whole electromagnetic spectrum, a multi-wavelength (MWL) approach is fundamental if we are to understand the different emission mechanisms originating in different regions of the AGN. MWL campaigns ideally include different instruments that will simultaneously (or over the same time-span) cover the whole energy range of the electromagnetic spectrum, from radio to gamma-rays. MWL observations are thus crucial to study the radiation fields from the different components within the AGN unification theory framework, and thus enable the reconstruction and understanding of the energy spectra of the underlying particle distributions. Such understanding will foster the accuracy of unification schemes by casting more light into the behaviour and intrinsic characteristics of AGN.

In the next section, we will describe in more detail the role that jets play on particle acceleration up to relativistic velocities as well as the link between jets as particle accelerators and the observed gamma-ray emission in jetted AGN.

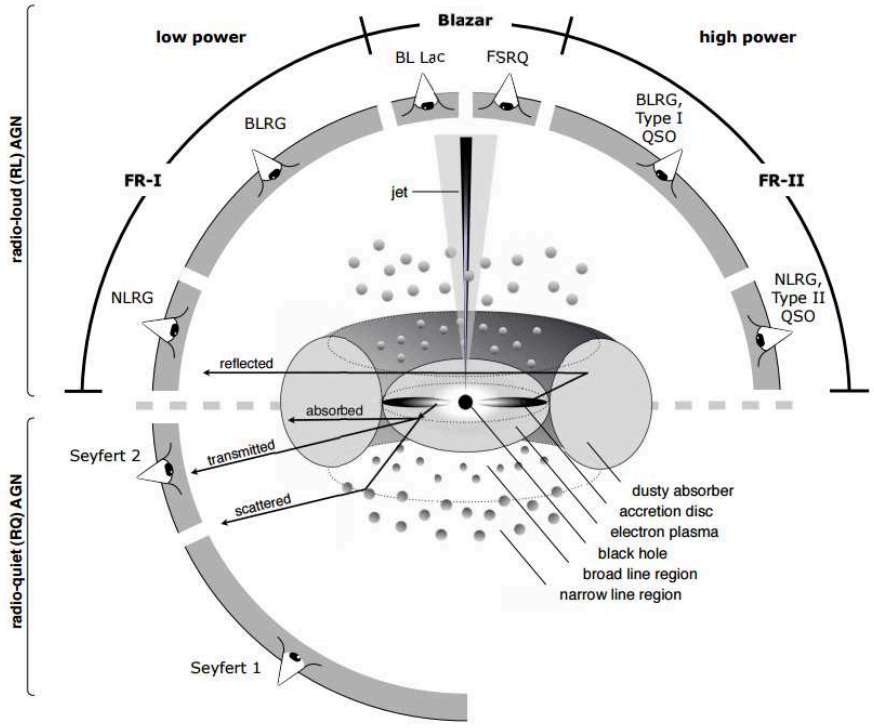

Figure 1.12 AGN unification theory scheme. From Beckmann and Shrader [BS12]

SMBH	$M \sim 10^7$-$10^9\ M_\odot$
Accretion Disc	$r \sim 10^{-3}\mathrm{pc}$ $n \sim 10^{15}\mathrm{cm}^{-3}$ $kT \sim 50\mathrm{eV} \cdot \mathrm{r}^{-3/4}$ $v \sim 0.3\,c$ at inner edge
BLR	$r \sim 0.01 - 0.1\mathrm{pc}\ (\sim \text{light days})$ $n \sim 10^{10}\mathrm{cm}^{-3}$ $v \sim 1000 - 5000\mathrm{km} \cdot s^{-1}$ $T \sim 10^4 K$
NLR	$s \sim 100 - 1000\mathrm{pc}$ $n \sim 10^3 - 10^6\mathrm{cm}^{-3}$ $v \sim \text{few } 100\mathrm{s\,km} \cdot \mathrm{s}^{-1}$
Torus	$r \sim 1 - 10\mathrm{s\,pc}$ $n \sim 10^3 - 10^6\mathrm{cm}^{-3}$ $T \longrightarrow \text{cold}$

Table 1.1 Physical characteristics of unified AGN model components that had been presented as the AGN cornerstones in Section 1.2. See e.g. Antonucci [Ant93] for a review on the topic.

1.4 AGN at gamma-ray energies

Ever since the very first jet studies at radio frequencies, astronomers inferred that jet radio emission is dominated by synchrotron radiation [Section 3.1.1] from (at least) GeV-energy particles. The fact that relativistic jets are some of the most extreme phenomena observed in the Universe coupled with gamma-rays only originating in extreme environments positioned jets at very likely sites of gamma-ray creation.

In addition to presenting AGN as powerful particle accelerators, this section presents the main characteristics of the two gamma-ray detected AGN types in which the present work is centered, blazars and gamma-emitting NLS1s.

1.4.1 AGN as particle accelerators

For astronomical sources, the energies of the observed gamma-ray radiation (starting from the rest mass energy of an electron, i.e. 511 keV, up to TeV) cannot be obtained from nuclear decay, which is the mechanism by which low energy (LE) gamma-rays are obtained in nuclear laboratories. Such energies cannot be generated by thermal emissions of hot celestial objects either: there is nothing hot enough in the Universe - apart from the Big Bang itself - to emit such energetic gamma-rays. Therefore, HE gamma-rays probe the existence of a *non-thermal* Universe: there have to be other mechanisms that allow the concentration of large amounts of energy onto a single quantum of radiation. In fact, TeV radiation is one of the less ambiguous proofs of particles being accelerated up to VHE, since at least a TeV electron/particle is required to yield a TeV photon through the inverse Compton process (see Section 3.1.4).

Initial particles are accelerated up to such high energies via the **Fermi acceleration mechanisms** (see, e.g. Bell [Bel78a], Bell [Bel78b]). Fermi acceleration, also known as **diffusive shock acceleration**, is the acceleration that charged particles undergo when they are repeatedly reflected, usually by a magnetic mirror. This type of acceleration is thought to be the primary mechanism by which particles gain non-thermal energies in astrophysical shock waves, and it plays a very important role in many astrophysical models. Different acceleration scenarios yield different spectral shapes and indexes for the accelerated particles, which is why it is paramount to

have accurate observational descriptions of AGN so that relevant conclusions can be derived.

It is now widely believed that Fermi acceleration processes are responsible for the production of non-thermal power-law particle distributions in AGN. Apart from shock and turbulence acceleration, magnetic reconnection and direct electric fields found in the vicinity of the central engine are also likely to contribute to the overall acceleration of particles. Moreover, relativistic reconnection processes could also play their part in accelerating the particles, since this type of mechanism could account for the non-thermal emission properties such as rapid HE variability that are often observed in AGN.

All in all, the study of HE gamma-rays is thought to be one of the best ways to study cosmic particle accelerators, since due to their neutral nature they travel in a straight line directly from the source. Unlike cosmic rays, gamma-ray photons are not electromagnetically charged, so they do not suffer from interactions in the full-of-magnetic-fields interstellar medium. Hence their trajectory remains unchanged along all the way from the source to the very first interaction, either with a satellite such as Fermi, or with the Earth's atmosphere, initiating an extensive air shower [Section 2.2] that can be detected by ground-based detectors like HESS [Section 2.5].

As a side note, we would like to mention that the neutrino could be another type of messenger that carries information about the source. Unfortunately, neutrinos hardly interact with matter, so they are extremely difficult to detect. However, experiments such as IceCube in the South Pole are active in the search for this type of messenger, and this field of research will benefit from more advanced facilities such as the Cubic Kilometre Neutrino Telescope (Km3NET) that will hopefully cast more light on the issue.

In this work, and as previously mentioned, we will focus on two types of AGN that show indications of particle acceleration up to gamma-ray energies: blazars and gamma-loud NLS1 galaxies. Their main characteristics will be further developed in the following subsections.

1.4.2 Blazars

Before the launch of the Compton Gamma Ray Observatory (CGRO) satellite, gamma-rays from AGN were thought to originate from energetic protons accelerated in shocks within the accretion disc. However, the lower-energy counterparts of CGRO-detected gamma-ray sources turned out to be blazars. What is more, the observed fast variability along with the intensity of the gamma-ray emission suggested that gamma-radiation moved at relativistic speed and that the emission needed to be produced further away than the accretion disc, i.e. within the jet.

Briefly introduced in Section 1.1, blazars are the most extreme and powerful type of AGN. They present beamed continuum emission caused by a relativistic jet oriented closely to the line of sight, which results in heavily Doppler boosted observed radiation (see Section 1.5.1), and the bulk of their radiative output is emitted in the gamma-ray range (Ghisellini et al. [Ghi+98]). Blazars are the beamed population of jetted AGN. Although most AGN show continuum variability, blazars present the most rapid, large amplitude variability at very short timescales. Some of their main characteristics are a flat radio spectrum and a broad-band spectrum dominated by non-thermal radiation that originates both the polarized optical and radio emission and the rapid variability (see e.g. Strittmatter et al. [Str+72]; Stein et al. [Ste+76]; Moore and Stockman [MS81]).

The blazar class can be further divided into BL Lacs and FSRQs. Within the AGN unification scheme paradigm, the main difference between both types is the presence of significant emission-line equivalent widths in the optical spectra of the former, and lack thereof in the case of the latter ($EW < 5$Å, see e.g. Angel and Stockman [AS80]). However, some BL Lac-classified objects, for instance the archetypal BL Lacertae, have been found to have broad lines in their spectra (e.g. Madejski et al. [Mad+99]). In fact, although the presence or absence of emission lines in the optical spectra is used as the first classification filter, other differences between BL Lacs and FSRQs do exist. For example, BL Lacs are located much closer than FSRQs - the redshift distribution of FSRQs peaks at around $z = 1.0$, while BL Lacs are mostly found in the local Universe (e.g. Massaro et al. [Mas+09a]). In the framework of the previously presented unification theory, one of the plausible explanations is the so-called *blazar evolutionary sequence*, which suggests that FSRQs are young AGN that eventually evolve into BL Lac objects as the central engine consumes the interstellar gas (e.g. Cavaliere and D'Elia [CD02], Maraschi and Tavecchio [MT03]). For a recent review on the topic see Foschini [Fos17]. The redshift distribution could

be biased though, due to the fact that the featureless optical spectra of BL Lacs hampers the determination of their redshift.

Another difference lies in their luminosity - FSRQs appear to be more luminous than BL Lac objects (Padovani [Pad92]). As presented in Section 1.3, the unification model paradigm explains this divergence from the difference in jet structure observed in FRI and FRII radio galaxies: bright FSRQs are FRII galaxies seen in the direction of the jet, while BL Lacs are fainter FRI galaxies (Urry and Padovani [UP95]).

The SED of both blazar types spans a frequency range over 20 orders of magnitude in frequency, from radio frequencies up to gamma- rays. In the case of BL Lacs, the observed emission is dominated by the radiation fields linked to the relativistic jet that yields an SED featuring two bumps: a low-energy component, and a high-energy component dominated by hard gamma-rays. The first hump is commonly attributed to synchrotron radiation [Section 3.1.1] and thus known as the **synchrotron bump**, while the high-energy bump is linked to IC processes and thus known as the **Inverse Compton bump**. One of the most extended theories pictures that the synchrotron photons originated by the interaction between the tangled magnetic field and the electron population within the blob are actually the seed photons that are scattered up to the observed gamma-ray energies in a process known as the synchrotron self-Compton process [Section 3.1.5]. Conversely, the FSRQ subtype features more complex broad-band emission spectra that requires radiation from external photon fields such as the accretion disc or the dusty torus to be accounted for.

In fact, some of the differences between FSRQs and BL Lacs could be due to changes in the accretion flow. BL Lacs accrete at low Eddington rates, so the accretion flow is in the hot, advection-dominated regime that implies faint UV emission. This type of disc is known as Advection Dominated Accretion Flow (ADAF) disc. The faint UV emission cannot provide sufficient ionization for the BLR clouds to emit strong broad lines. On the other hand, FSRQs accrete close to the Eddington limit, which enables the existence of a UV-bright disc that ionizes the BLR that is at the origin of the observed enhanced external Compton emission in this type of object. This enhanced IC emission is the reason why the SED of FSRQs is more Compton-dominated than that of BL Lacs, meaning that the ratio of Compton to synchrotron luminosities is larger in FSRQs than in BL Lacs.

In FSRQs, the BH mass can be determined through standard scaling factors (reverberation mapping techniques, Section 1.2.3) that reveal quite large masses of the order of $M_{BH} \geq 10^8$ $M_\odot$ (Ghisellini and Tavecchio [GT15]). Despite the inherent challenge for BH mass determination due to the lack of broad lines in their spectra,

recent studies of host galaxy characteristics have found similar masses for BL Lacs (e.g. Plotkin et al. [Plo+11], Falomo et al. [Fal+03]).

In this regard, BL Lacs and FSRQs form a "blazar sequence" of increasing accretion power onto similar mass BHs that also illustrates variations and shifts in luminosity peak frequencies that result in SEDs that vary according to the observed bolometric luminosity. The blazar sequence is illustrated in Figure 1.13, both the original and the revisited one.

The luminosity of the low-energy bump of FSRQs peaks at IR/optical wavelengths, while the position of the peak in BL Lacs can vary from IR/optical up to UV/X-ray frequencies (see e.g. Abdo et al. [Abd+10b]). What is more, BL Lacs can be further classified in different subtypes based on the position of their synchrotron peak. Thus there are Low frequency-peaked BL Lac (LBL) objects, Intermediate frequency-peaked BL Lac (IBL, peak right at visible/UV wavelengths) objects and High frequency-peaked BL Lac (HBL) objects (Giommi and Padovani [GP94], Padovani and Giommi [PG95]).

LBLs are generally brighter than HBLs, indicating a luminosity-dependent SED evolution, with luminosities increasing as the synchrotron peak energy decreases. Low-power lineless HBLs have synchrotron and Compton bumps that peak at high frequencies, with corresponding luminosities that are about equal. FSRQs feature aforementioned Compton-bump dominances and compose the high-luminosity part of the blazar sequence.

The fact that the position of the synchrotron peak shifts depending on the BL Lac type also shifts the energies of the observed X-ray radiation. Accordingly, X-ray emission can also be used to classify BL Lacs. For instance, the X-ray spectra of LBLs is harder than that of HBLs (index generally smaller than 2.0), since in the former the slope already corresponds to the raising of the IC bump. On the other hand, Fermi-Large Area Telescope (LAT) observations[7] showed that just the opposite happens at gamma-ray frequencies. Indeed, given that the spectra is measured after the IC peak, HBLs are characterized by a harder spectral index smaller than 2.0, while LBLs' are smaller (Abdo et al. 2010b). Figure 1.14 shows the SED of a typical GeV FSRQ and a typical TeV BL Lac object.

[7] The Fermi-LAT Third AGN catalog (3LAC) now lists about 1600 HE sources, while at VHE (very high energy, > 100 GeV) energies the detection of around 70 AGN is currently summarized in the TeVCat catalog. Most of these sources are of the blazar type. See Section 2.5.8 for more details.

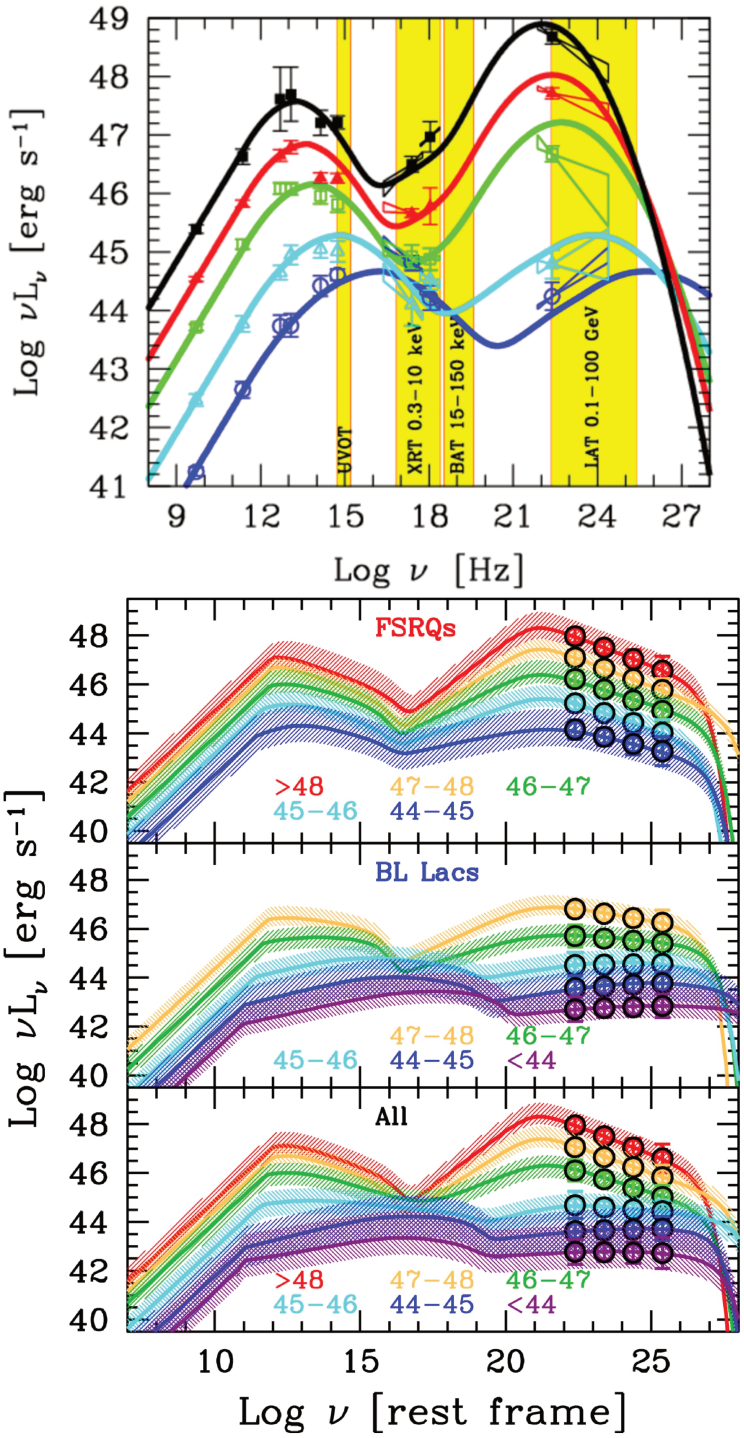

Figure 1.13 The original blazar sequence (**top**, adapted from Fossati et al. [Fos+98], Donato, D. et al. [Don+01]) and the revisited one (**bottom**, Ghisellini et al. [Ghi+17]). The original one was constructed with the 126 blazars belonging to complete (flux limited) radio and X-ray samples of blazars at those times. The blue SED corresponds to low-power lineless BL Lacs whose synchrotron and Compton bumps peak at high frequencies, with similar luminosities. On the opposite side of the diagram we have powerful FSRQs in black, whose Compton bump clearly dominates the low-energy bump. Yellow vertical stripes correspond to the observing bands of *Swift* and *Fermi*/LAT. The new phenomenological sequence shows LBLs only (top panel), BL Lacs (middle panel) and for all sources (bottom panel).

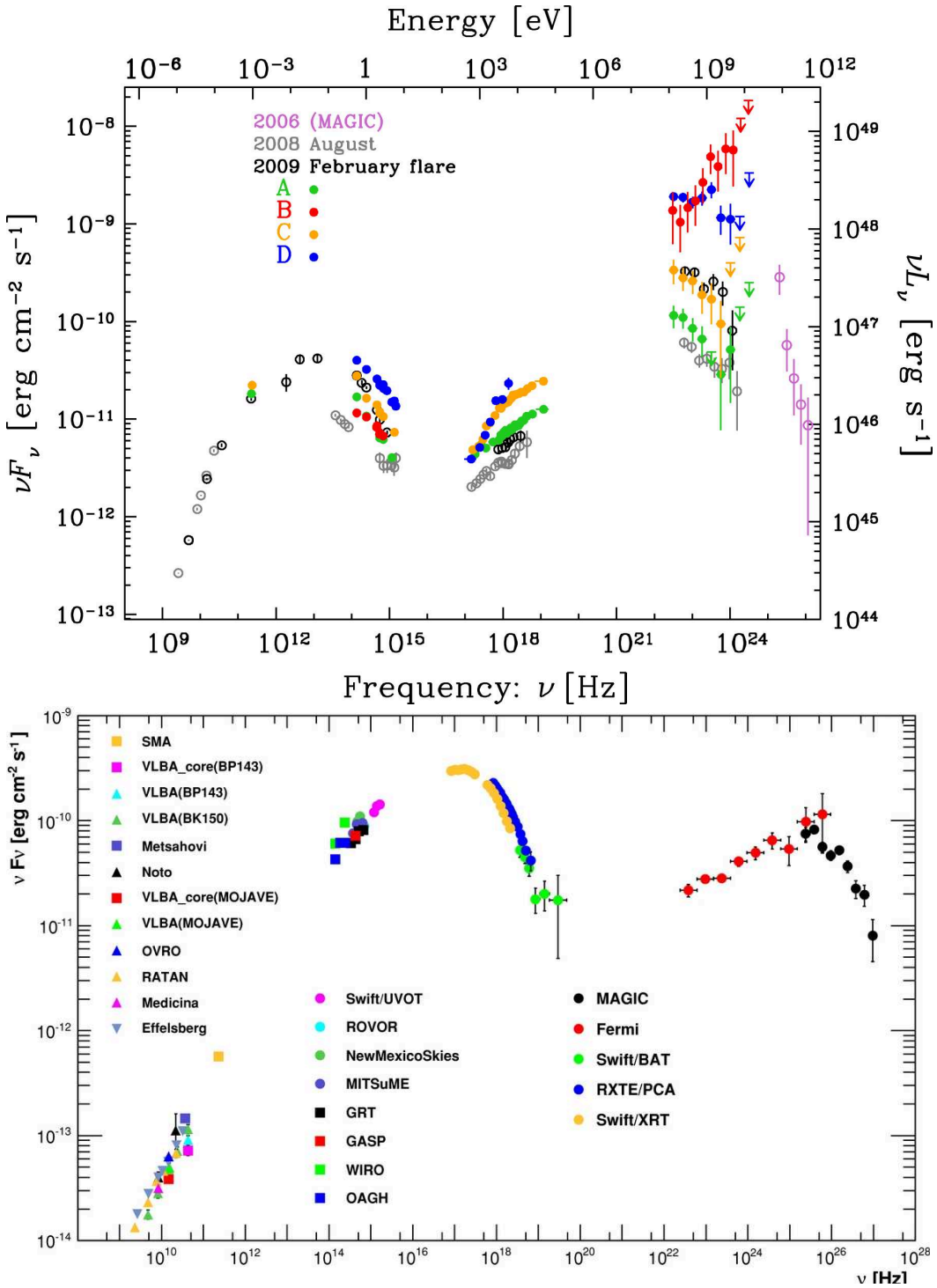

Figure 1.14 SED of 3C279, a typical GeV FSRQ (**top**, Hayashida et al. [Hay+15]) and Mrk 421 a typical TeV BL Lac (**bottom**, Abdo et al. [Abd+11]).

1.4.3 Narrow Line Seyfert 1 galaxies

The presence of a relativistic jet that dominates the radio emission of a source automatically characterizes an AGN as radio-loud. The lack of such strong jets in Seyferts, apart from making them radio-quiet, allows the central regions of the active nucleus to be observed, unveiling details impossible to see in strongly beamed jetted AGN. In the present work, we are interested in the Narrow Line Seyfert 1 (NLS1) subtype of Seyfert galaxies, the gamma-loud NLS1 subsample to be precise.

It was Osterbrock and Pogge [OP85] who first classified as NLS1s the galaxies that present a nuclear spectrum that resembles that of Seyfert 1 galaxies (i.e. strong Fe-II and relatively weak [O III] w.r.t. the Balmer lines), but whose permitted line widths are much narrower than those of Seyfert 1s. Indeed, for a source to be classified as NLS1, its spectrum needs to have narrow permitted lines only slightly broader than the forbidden lines, a ratio [O III]/Hβ < 3 and FWHM(Hβ)$\leq$ 2000 km s^{-1} (see e.g. Osterbrock and Pogge [OP85], Goodrich [Goo89]). The small FWHM(Hβ) velocities seen in NLS1 would point towards a low-mass BH accreting at a high Eddington ratio.

Concerning X-rays, NLS1s are characterized by a strong optical/UV/X-ray continuum (Khachikian and Weedman [KW74]; Osterbrock [Ost89]) and a remarkable soft X-ray excess (0.5 keV-2 keV), and they present variability at small time scales (Veron-Cetty et al. [Ver+04]). What is more, their spectral indexes are quite hard ($\Gamma \sim 1.8$) and they present large widths typical of the Fe-Kα line (Leighly [Lei99]). These X-ray characteristics that set NLS1s apart from other Seyfert types are mainly due to their high Eddington coefficients ($L/L_{Edd} \sim$ 0.1-1, Boroson and Green [BG92]; Boller et al. [Bol+96]) and their low BH masses with regards to Seyfert 1s ($M_{BH} \sim$ 10^6-10^7 M$_\odot$, Grupe and Mathur [GM04]), confirming the results indicated by the observed low velocity widths mentioned before. However, recent works question the low BH mass of a subsample of NLS1s (see e.g. Baldi et al. [Bal+16a], Calderone et al. [Cal+13]), as will be discussed later on the present work.

Initially it was thought that low-mass AGN like NLS1s could not possibly be RL (see Equation 1.1). This idea was nonetheless challenged by the actual detection of RL low-mass AGN (Ho [Ho02], Yuan et al. [Yua+08]). Regarding NLS1s, a dedicated search for strong radio emission from 128 NLS1 galaxies (Komossa et al. [Kom+06]) showed that only 7% of all NLS1 galaxies are radio-loud ($R > 10$) compared to 15% in quasars, and only 2.5% exceed $R > 100$. These fractions are much lower than

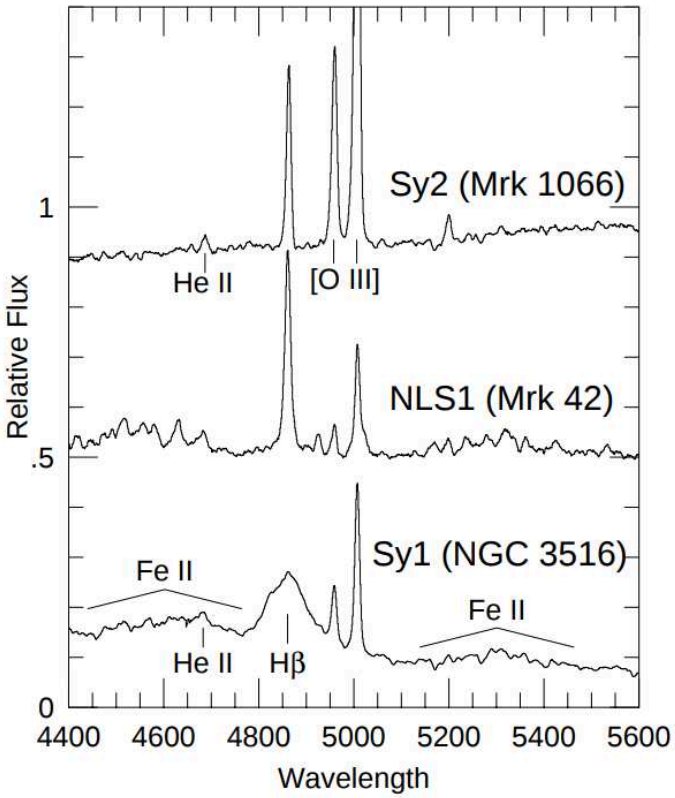

Figure 1.15 Example of optical spectra around the Hβ region of the Seyfert 2 galaxy Mrk 1066 (**top**), the NLS1 Mrk 42 (**middle**) and the Seyfert 1 NGC 3516 (**bottom**) from Pogge [Pog11]. The the Hβ line is more intense than the [O III] line for the NLS1, from which the [O III]/Hβ < 3 classification benchmark originates.

among Broad-Line Seyfert 1 (BLS1) galaxies, where percentages of 20% and 13% respectively where found.

Recently, Rakshit et al. [Rak+17a] published a catalog of around 11000 NLS1 sources, which is definitely promising for studying the global characteristics of this class of AGN. Rakshit et al. [Rak+17a] found only 5% of the NLS1s to be RL. In a later publication (Rakshit et al. [Rak+17b]), they presented some early conclusions extracted from the study of their sample, specially with regards to the comparison between NLS1 and their broad line counterparts BLS1 galaxies. From the large sample they analyzed, they confirmed that NLS1s have larger FeII, smaller BH masses and larger Eddington ratios than BLS1s. NLS1s also present a steeper soft excess and lower variability amplitudes than their broad-line counterparts.

All these findings show that, in addition to Seyfert 1-like characteristics, a very small subsample of NLS1s, the RL-NLS1 subsample, also presents blazar-like observational properties as the aforementioned radio-loudness, flat radio spectrum, high brightness temperatures between 10^{10} K-10^{14} K (D'Ammando, F. et al. [D'A+13], Angelakis

et al. [Ang+15], Fuhrmann et al. [Fuh+16]), strong Doppler boosting and one-sided relativistic jets.

Another striking discovery that confirmed the presence of relativistic jets in some NLS1 was the detection of gamma-ray emission by the Fermi collaboration (Abdo et al. [Abd+09a]) from a sub-sample of RL-NLS1 galaxies, henceforth gamma-loud NLS1 or gamma-emitting NLS1. The small black hole masses of 'standard' NLS1s[8] and the fact that their galaxy host type is mostly spirals with high incidence of bars and star formation (see e.g.Deo et al. [Deo+06]; Ohta et al. [Oht+07]; Sani et al. [San+10]; Caccianiga et al. [Cac+14]) made this discovery completely unexpected, although blazar-like characteristics of some NLS1s had already been reported by Yuan et al. [Yua+08]. This discovery questions the idea of relativistic jets being only found in giant elliptical galaxies (see for instance Kotilainen et al. [Kot+98a], Kotilainen et al. [Kot+98b]). It may be worth noticing that a handful of powerful radio galaxies have been found to be hosted in spirals, all of them with BH masses larger than $10^8 M_\odot$ (e.g. Morganti et al. [Mor+11], Singh et al. [Sin+15]). All the so-far detected gamma-loud NLS1 sources are gathered in Table 1.2.

We must underline that that host galaxy morphologies of gamma-loud NLS1 and Seyferts are generally not well known. An exception is the remarkable NLS1s galaxy 1H 0323+342, which is hosted by a one-armed spiral or ring galaxy (Zhou et al. [Zho+07]; Antón et al. [Ant+08]). For more details on 1H 0323+342, see Section 6.1. On the other hand, GranTeCan observations of the gamma-loud NLS1 FBQS J1644+2619 indicate that its host is an elliptical galaxy (D'Ammando et al. [D'A+17]). Apparently, though, the elliptical galaxy-jet paradigm would be an observational bias, and galaxies could in principle host relativistic jets irrespective of their morphological types.

All in all, it appears that NLS1s are very much blazar-like objects with BH masses two orders of magnitude lower than blazars and with much larger accretion rates. Whether these differences and similarities are a matter of orientation, or whether NLS1s are AGN with rapidly growing BHs remains an open question. Either way, the study of gamma-emitting NLS1 galaxies definitely opens a new window into the nature of jets in highly accreting environments. Indeed, gamma-emitting NLS1s could play a major role on increasing our knowledge of jet powering and launching mechanisms. Ghisellini et al. [Ghi+14] found a correlation between jet power and accretion disc luminosity, with jet powers around ten times larger than accretion disc luminosities, indicating that the jet launching mechanism must be very efficient and

[8] As we have previously mentioned, recent works have found RL-NLS1s to have BH masses larger than those expected for standard NLS1 galaxies.

directly linked to the accretion flow. The fact that gamma-emitting NLS1s accrete at high rates and present signatures of blazar-like jets, and that they have so far only been found in the local Universe ($z < 0.8$, Zhou et al. [Zho+06]) makes them suitable candidates to explore this path.

Name	3FGL Fermi Name	RA	Dec	z	Ref.
1H 0323+342	J0325.2+3410	155.7268	-18.7565	~ 0.0629	[1]
B2 0954+25A	J0956.6+2515	205.5113	+50.9816	0.707 48	[2]
FBQS J1644+2619	J1644.4+2632	046.2067	-38.4001	0.144 05	[2]
PKS 1502+036	J1505.1+0326	002.2266	+50.2544	0.408 86	[3]
SBS 0846+513	J0849.9+5108	167.6063	+39.1351	0.583 45	[3]
PKS 2004-447	J2007.8-4429	355.3310	-31.8499	~ 0.24	[4]
PMN J0948+0022	J0948.8+0021	236.5895	+38.7133	0.583 84	[2]
PKS J1222+0413	J1222.4+0414	284.8190	+66.0655	0.964 21	[2]
B3 1441+476	J1443+4725	083.2986	+60.1754	0.703 14	[2]
NVSS J124634+023808	?	300.0061	+65.4800	0.362 25	[2]

Table 1.2 Fermi-LAT detected gamma-loud NLS1 sources and their 3FGL Fermi name (column 2), Galactic J2000 coordinates (columns 3 and 4), redshift value and corresponding reference (columns 5 and 6). References are: [1] Zhou et al. [Zho+07], [2] Ahn and et al. [Ae13], [3] Adelman-McCarthy [Ade09] and [4] Massaro et al. [Mas+09b].

As far as their broad-band emission is concerned, the SED of NLS1s is different from the double-bumped spectrum observed in most BL Lac objects, since characteristics corresponding to components other than the relativistic jet are often observed in their energy distribution, i.e. the torus, accretion disc and BLR for example, along with the corresponding IC radiation. The model components that will be considered for the description of the broad-band emission of three selected gamma-loud NLS1 are presented in Chapter 3. The fact that EIC processes are required to explain the high-energy emission observed in gamma-loud NLS1s shows the similarities between them and the second blazar subclass, FSRQs. Interestingly, the UV bump may be observable during some particular states of FSRQs (D'Ammando [D'A11]). In the previous section, we mentioned the "blazar sequence" of increasingly accreting objects of similar masses. Considering the similarities between FSRQs and gamma-loud NLS1s, one of the major open questions regarding the latter is whether they form the low-mass, high accretion rate tail of this sequence.

Last, we would like to say a word about the variability of gamma-loud NLS1s, since flaring gamma-ray states will be afterwards considered for modeling purposes. The numerous outburst episodes documented for this particular type of AGN have clearly shown that they are quite variable objects at most wavelengths, displaying even

intra-night variability (see e.g. Abdo et al. [Abd+09b], Calderone et al. [Cal+11], Foschini et al. [Fos+12], D'Ammando and Orienti [DO13], Wajima et al. [Waj+14]). Such violent variability is an additional common feature that gamma-loud NLS1s share with their (apparently) higher mass counterparts, blazars, and will be the focus of the dedicated study in Chapter 6.

1.5 Observational properties of jetted AGN

The relativistic effects taking place in the jetted AGN subclasses that we have introduced in the previous section cause observed quantities such as the apparent velocity, the apparent luminosity or the brightness temperature to be related to the AGN rest frame through the Doppler factor δ, the Lorentz factor Γ and the angle to the line of sight θ. This section gives a brief description of some of the most significant observed quantities.

1.5.1 Relativistic beaming or Doppler boosting

One of the common characteristics of gamma-loud AGN is the Doppler boosting suffered by the radiation via relativistic beaming due to the jet being oriented at small viewing angles towards the observer. The matter outflow ejected from jetted AGN moves at ultra-relativistic speed, causing the observed quantities to be enhanced w.r.t. the intrinsic ones. Both quantities can be related by the relativistic Doppler factor defined as

$$\delta = \frac{1}{\Gamma(1 - \beta \cos\theta)} \tag{1.14}$$

where β is the velocity in units of the speed of light $\beta = v/c$, and θ is the viewing angle. The $1/\Gamma$ term is the usual special relativity term given by the Lorentz factor

$$\Gamma = \frac{1}{\sqrt{1 - \beta^2}}, \tag{1.15}$$

while the $1/(1 - \beta\cos\theta)$ term is the usual Doppler factor term. The usual Doppler factor term becomes very large for small viewing angles, thus compensating for the special relativity term $1/\Gamma$. On the contrary, for orthogonal trajectories the predominant factor is the usual special relativity one.

1.5.2 Apparent luminosity

The detection of luminosities much larger than the intrinsic ones is due to the the beaming effect caused by relativistic jet of the AGN being closely aligned with the line of sight. The relation between the intrinsic and observed luminosities is given by

$$L_{obs} = \delta^n L_{int}. \tag{1.16}$$

Here L_{int} is the intrinsic luminosity in the frame of the AGN while the exponent n represents the effects of K correction and Doppler boosting, and controls the sharpness of the peak of the aspect curves[9]. It depends both on the Doppler boost exponent p and on the spectral index of the radiation α, $n = p + \alpha$. Sources with flat spectra have $\alpha = 0$, while the p parameter lies usually between 2 and 3. A smooth jet would have $p = 2$, while an isolated optically thin source would yield $p = 3$ (e.g. Cohen et al. [Coh+07]).

1.5.3 Apparent superluminal motion

The relativistic velocity composition law states that the sum of two velocities will never be greater than the speed of light, and that regardless of a succesive increase in the velocity of an object, its velocity will never surpass that of light. The expression for the sum of two velocities u and v is derived from the time and space transformation equation, and it reads

$$u' = \frac{u + v}{1 + \frac{uv}{c^2}}. \tag{1.17}$$

Einstein's theory of relativity sets the velocity of light as an insurmountable limit for any object. In some astrophysical phenomena, such as the relativistic jets in some AGN, superluminal velocities have been measured though. If we consider matter moving from the point A at an instant t_1 to the point B at an instant t_2 following

[9] Aspect curve: Curve that shows the possible observable parameters for a source with known intrinsic values. It lies on the observation planes, that is, (β_{app}, L) axis.

a straight trajectory with a constant speed v, where $v < c$, the time taken for the matter to cross the distance AB is simply

$$t_2 - t_1 = \frac{AB}{v} \tag{1.18}$$

but an earthling observer placed in C, who has no conscience of his viewing angle θ, sees the object in C after a time $t_1 + AC/c$ where AC/c is the time taken by the light to go from A to C. Given that $AC = AB\cos\theta$, we know that the observer measures an apparent time which, considering that the apparent distance is $d_{app} = AB\sin\theta$, yields an apparent velocity of

$$v_{app} = \frac{d_{app}}{t_{app}} = \frac{AB\sin\theta}{\left(\frac{AB}{v} - \frac{AB\cos\theta}{c}\right)} = \frac{v\sin\theta}{1 - \frac{v\cos\theta}{c}} \tag{1.19}$$

The apparent velocity can be greater than the speed of light depending on the values of θ and v. To illustrate this better, if we define the velocity in units of the speed of light $\beta = v/c$, we calculate the angle for which the apparent velocity is at its maximum, and the apparent velocity is

$$\beta_{app} = \frac{\beta}{\sqrt{1-\beta^2}} = \Gamma\beta. \tag{1.20}$$

In the case where the Lorentz bulk factor is $\Gamma \gg 1$, the velocity is $\beta \approx 1$ and the apparent velocity of an object can be larger than the speed of light. This is certainly the case when the matter moves at great speed towards the observer under a very small viewing angle θ. Apparent superluminal motion is observed in AGN relativistic jets, where features within seem to move faster than light.

Regarding observational data, apparent velocities up to $50\,\mathrm{c}$ have been found in blazars (Homan [Hom12]), while for gamma-loud NLS1s, superluminal motion has been found for SBS 0846+513 (with apparent velocities $7.7 - 9.7\,\mathrm{c}$, D'Ammando et al. [D'A+12]) and 1H 0323+342 (range of apparent velocities from $0.93 - 6.92\,\mathrm{c}$, Fuhrmann et al. [Fuh+16]) but not for PKS 1502+036 (D'Ammando et al. [D'A+16]).

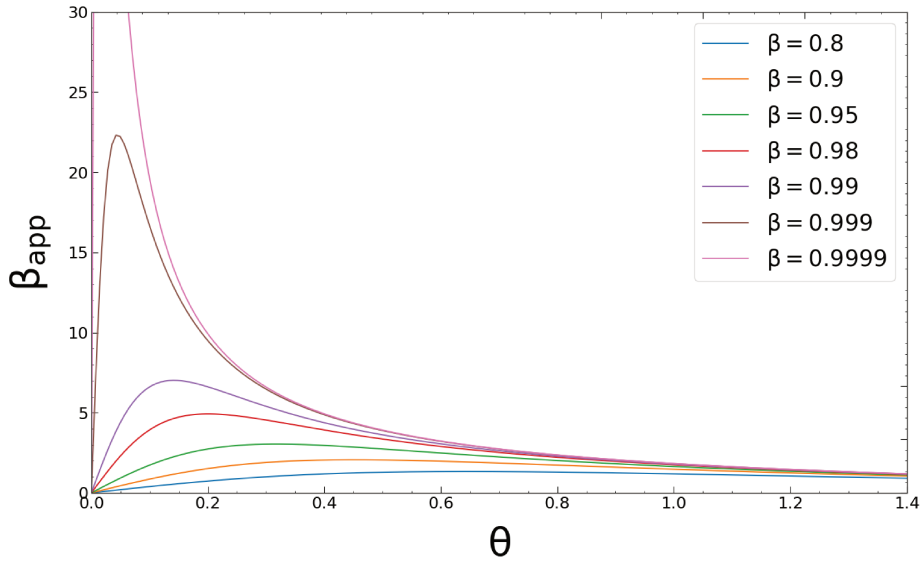

Figure 1.16 Plot of the apparent velocity β_{app} versus the viewing angle θ for different values of $\beta = v/c$.

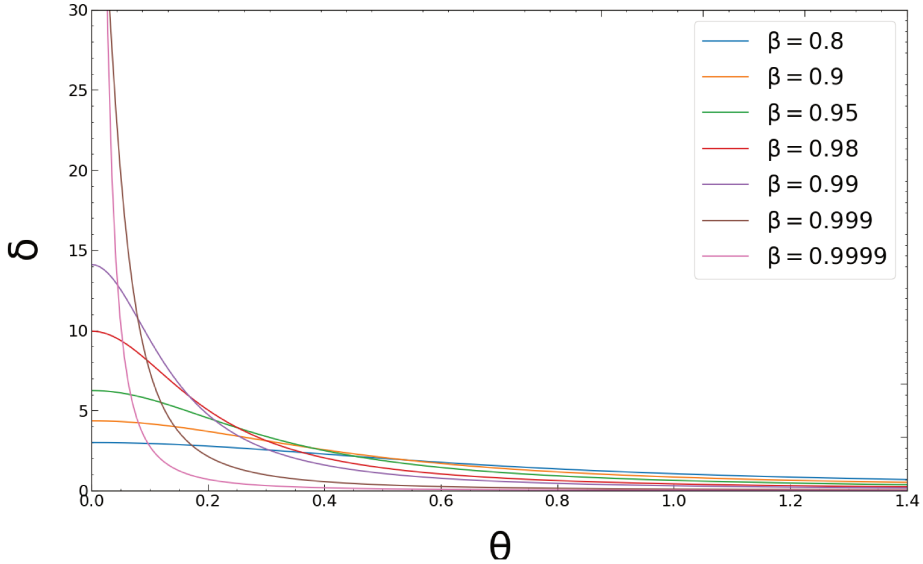

Figure 1.17 Plot of the Doppler boosting factor δ versus the viewing angle θ for different values of $\beta = v/c$.

1.5.4 Brightness temperature

The brightness temperature of an object is the temperature that would characterize it if it radiated as a blackbody. However, it can also be used to make estimations of the temperatures of any radiating object, regardless of the process being thermal or non-thermal.

Indeed, the extremely high brightness temperatures measured in relativistic jets point towards a non-thermal origin of the radiation. By considering the limits set by physical arguments on the brightness temperature, one can infer the value of the Doppler factor δ by arguing that the excess brightness temperature observed is purely due to Doppler boosting effects.

In NLS1s, moderate brightness temperatures (and hence Doppler factors) are observed, which suggests mildly relativistic jets. The core brightness temperature is found to be in the $T_B = 10^{8.4}$-$10^{11.4}$ K range (Gu et al. [Gu+15]), smaller than the classic blazar population for whom $T_B \approx 10^{11}$-10^{13} K (e.g. Kovalev et al. [Kov+05]).

To summarize this section, the aforementioned observational properties of jetted AGN are gathered in Table 1.3.

Intrinsic	Formula	Observed	Formula
Lorentz factor	$\Gamma = (1-\beta^2)^{-1/2}$	Doppler beaming	$\delta = \Gamma^{-1}(1-\beta\cos\theta)^{-1}$
Jet bulk velocity	$\beta = v/c$	Apparent velocity	$\beta_{app} = \Gamma\beta$
Luminosity	L_{int}	Apparent luminosity	$L_{obs} = \delta^n L_{int}$
Brightness temperature	T_B^{INT}	Brightness temperature	$T_{VLBI} = \delta T_B^{INT}$ $T_{var} = \delta^3 T_B^{INT}$

Table 1.3 Intrinsic and observed properties of jetted AGN. See text for more details. Adapted from Ros [Ros08].

2 Ground-based VHE astrophysics: The HESS experiment

In this Chapter, we first present the time-line of the long path followed to arrive to the current state-of-art of ground-based Very High Energy (VHE) gamma-ray observatories [Section 2.1]. Then we provide detailed explanations of extensive air-shower development [Section 2.2] and the Cherenkov effect that accompanies them [Section 2.3]. Last, the High Energy Stereoscopic System (HESS) collaboration telescopes are presented, along with the overall specificities of data analysis procedures, as an example of the current generation of Imaging Atmospheric Cherenkov Telescopes (IACTs) [Section 2.5].

2.1 A look into the past

The first theoretical step towards the current state-of-art of ground-based VHE observatories was taken by Oliver Heaviside in 1889 (Heaviside [Hea89]) when he described the movement of an electron traveling through a transparent medium with a velocity higher than the speed of light, always in the scenario of the 'ether' that enabled the transport of electromagnetic waves. According to his findings, the movement of such electrons would be followed by a specific conical emission. However, the community did not show much interest in these discoveries.

The first report of actually observing the bluish radiation from gamma-rays generated within liquids containing radioactive radium particles is thought to have been made by Marie Sklodowska-Curie around 1910. In any case, in the writings of her daughter Eve it is clear that both Marie and Pierre Curie were acquainted with the blue glow from decaying radioactive materials seen in the dark (Curie [Cur41]). Marie Sklodowska-Curie did not specifically carry out research on this effect though, and she cataloged it as some sort of luminescence.

French scientist Mallet pioneered the studies of this 'luminiscence' phenomenon, describing the observed characteristics of the effect. He found the bluish light had a continuum spectrum, which was against the fluorescence explanation due to the lack of the emission lines and bands expected in the case of fluorescence (Mallet [Mal26], Mallet [Mal28] and Mallet [Mal29]).

But it was the PhD research accomplished by Pavel Cherenkov under the guidance of Sergei Vavilov that was groundbreaking, although as many times in history it was not well accepted by the community at the time of publication. Given that at that time there was no detector for Cherenkov light yet, he spent most of his research time in a dark cellar looking at faintly glowing liquid vessels. In this grim environment, he found out that the light emission remained despite greatly changing the temperature and pressure of the liquids, confirming Mallet's findings of the continuum spectrum. When he published these results in 1934 (Cherenkov [Che34]), his supervisor Vavilov rejected coauthoring the paper, and instead wrote his own interpretation of his student's findings, attributing the observed continuum spectrum to *bremsstrahlung* radiation from electrons, that is, that the bluish light was radiation from Compton electrons created by the gamma rays being slowed down in the liquid (Vavilov [Vav34]).

In spite of what probably was a discouraging moment in his career, Cherenkov continued his research, and three years later he proved the anisotropy of the radiation, showing that the light was emitted only in a small cone in the forward direction of the emission, as predicted by Heaviside. Nature rejected to publish this discovery and it was not until he submitted a short letter to Physical Review Letters that his results were publicly presented to the community (Cherenkov [Che37]).

Meanwhile, Ilya Frank and Igor Tamm had created a theoretical explanation of the observed phenomenon that is the current description of the Cherenkov radiation phenomenon (Tamm and Frank [TF37]). According to Tamm and Frank, a charged particle moving in a transparent, dielectric medium of refraction index n with a velocity $v > c/n$ will polarize the medium asymmetrically along its path, as illustrated in Figure 2.1. After the passage, the medium relaxes by emitting anisotropic radiation in the forward direction. Cherenkov, Tamm and Frank's discoveries were awarded the Nobel Prize in 1958.

Their findings meant that the theoretical and observational framework was understood, but it was still unclear whether the Cherenkov radiation could also be observed in the atmosphere, or whether it was limited to liquid environments. In 1952, Patrick Blackett estimated from the night sky and aurorae that at least 10^{-4} part of air shower elementary particles should be producing Cherenkov radiation

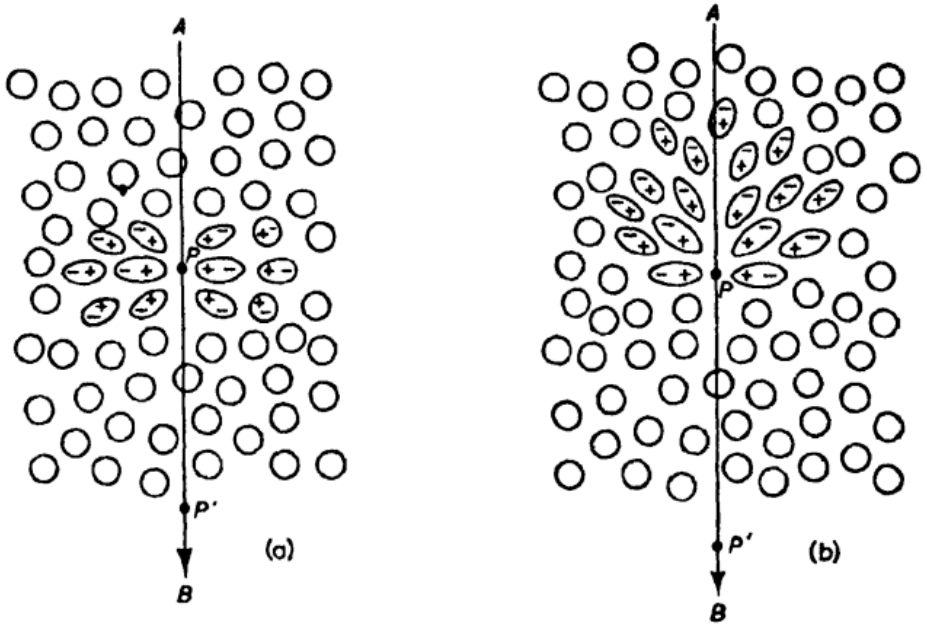

Figure 2.1 Polarization of surrounding particles by a charged particle moving (a) relatively slowly; (b) at relativistic speed. The figure illustrates the effect of an electron traveling through a dielectric, transparent medium. If the electron moves relatively slowly, the atoms composing the medium that are close to the passage of the electron are be distorted by the electric field of the later, and become elementary dipoles. Thus, the medium is polarized. Due to the complete symmetry (both in azimuth and in the axis direction) of the polarization field around the charged particle, there is no resultant dipole and hence no radiation is observed. However, an electron traveling with a speed comparable to that of light in the medium, although still symmetric in the azimuthal direction, the polarization field is no longer symmetric along the axis. This generates a resultant dipole field, briefly set up by the charged particle at each element along its path, which will radiate to return to the non-excited state. The emitted radiation is spread over the band of frequencies corresponding to the Fourier transforms of the pulse. From Jelley 1958.

(Blackett [Bla48]). Shortly after transmitting his findings regarding atmospheric Cherenkov radiation to Jelley and Galbraith, who were in turn conducting research on Cherenkov emission in water environments, Jelley and Porter constructed the first atmospheric Cherenkov detector. Made up of a 25 cm parabolic mirror fixed to a dustbin with a photomultiplier at its focus, the telescope soon started counting 2-minute spaced pulses. By operating this telescope along with a Geiger counter that measured air showers, they confirmed that they were indeed measuring Cherenkov pulses coming from air showers. These discoveries that set off the era of atmospheric air Cherenkov detectors were published by Galbraith and Jelley in Nature in 1953 Galbraith and Jelley [GJ53].

Almost contemporaneously, Natasha Nesterova and Alexander Chudakov had measured the lateral distribution of Cherenkov light in the Pamir mountains, at an altitude above 3800 m from sea level, confirming the existence of Cherenkov light pulses (Nesterova and Chudakov [NC55]). Notice that both Jelley-Galbraith's and Chudakov-Nesterova's experiences were able to detect atmospheric showers, but not to detect the specific emission from a source.

In 1958, Philip Morrison published a paper in which he suggested that the fact that gamma-rays are more directly related to nuclear and high-energy processes than optical or radio emission without the complete loss of source information that accompanies high-energy particles could be exploited to open a new window in astronomy (Morrison [Mor57]). He remarked that the energy range from "a few tenths of MeV to a few hundred of MeV" contained the "most direct information with the least objectionable background, and to be relatively accessible to observation". He pointed out balloon observatories beneath $25\,\mathrm{g\,cm^{-2}}$ of air to be the most suitable observational tools. In the same paper, he also made a tentative of pointing out suitable gamma-ray source candidates, amongst which the Crab nebula, whose expanding gas shell he thought should contain radioactive debris from the explosion.

At the 1959 ICRC conference, Giuseppe Cocconi gave an overoptimistic estimate of the flux of TeV gamma-ray photons expected from the Crab nebula (3 orders of magnitude larger than the actually observed one!, Cocconi [Coc60]). Later on, Alexander Chudakov and collaborators built an array of 4 telescopes in the Crimean Peninsula with the idea that the detection techniques implemented in the Pamir mountains could be suitable for the gamma-ray sky search. However, their 4-year experience did not find any excess emission from the Crab Nebula[1], nor from other bright radio sources that seemed good gamma-ray candidates (Chudakov

[1]The signal upper limit from the direction of the Crab Nebula for a total of ≈ 5.5 h of observation was around $5 \times 10^{-11}\,\mathrm{ph\,cm^{-2}\,s^{-1}}$ for the threshold of $\approx$ 4-5 TeV. The integral flux of the Crab Nebula

et al. [Chu+63]). The conclusion was that Cocconi's assumption of the relativistic electrons from the Crab originating in proton collisions could not be correct, and that some other particle acceleration mechanisms must take place at the heart of the Nebula. Obviously, the non-detection also refuted Cocconi's optimistic flux estimation of the Crab.

Things were pretty quiet in the ground-based gamma-ray astronomy development field until 1966, when Trevor Weekes joined Giovanni Fazio and colleagues' project to develop a multi-faceted 10m Cherenkov telescope at Mount Hopkins (Arizona, US), the Whipple telescope. It was Weekes and Tuver who, in 1977, suggested the implementation of a stereoscopic imaging system that would enable a much more robust background suppression (Weekes and Turver [WT77]). One of the main objectives was to reject shower images in which the axes were not aligned with the supposed gamma-ray source. Two telescopes located 100 m apart should show Cherenkov images with the axis pointing at the source. In 1981, Turver and Weekes coined the "third generation detector" term, who would consist of an array of four 10-15 m telescopes deploying stereoscopy techniques (Turver and Weekes [TW81]).

In the years to come, the Whipple team measured signal levels from the Crab slightly below 5 σ. It was not until 1985 when Michael Hillas came up with a new and special parametrization of the measured shower images (Hillas [Hil85], to be presented further into the Chapter) that enabled the measurement of a 9σ level from the Crab three years later, definitely inaugurating the ground-based VHE astronomy era. Two years later, in 1992, the first detection of gamma-rays from the extragalactic source Markarian 421 was made by Punch et al. [Pun+92]. Contrary to the apparent steady emission from the Crab, the gamma-ray emission from Markarian 421 was highly variable.

A couple of years later, the High Energy Gamma Ray Array (HEGRA, 1987-2000) was the first experiment to be designed and handled by a big group of collaborators. An air shower detector of 250 scintillators was coupled to several muon detectors at an altitude of 2200 m on the La Palma island. Eventually, a grid of 7×7 large hemispherical photomultipliers that observed the whole sky along with 5 small imaging Cherenkov telescopes were added to the array. Figure 2.2 shows a sketch representing the setup of the experiment. The HEGRA-CT array was the first implementation of the stereoscopic systems dreamed of by Turves and Weekes, the first of

above 4 TeV is $\approx 2.5 \times 10^{-12}\,\mathrm{ph\,cm^{-2}\,s^{-1}}$. This means that the flux limit set by Chudakov and his colleague was ≈ 20 times higher than the flux from the source.

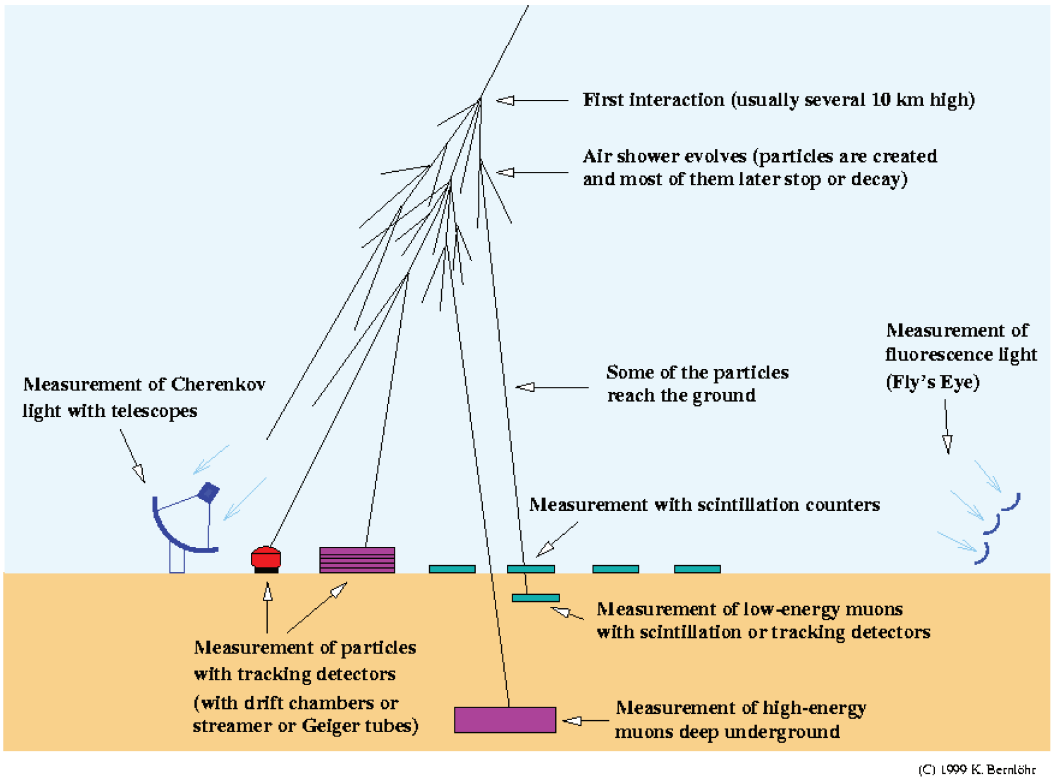

Figure 2.2 Schematic view of the HEGRA-CT observatory. Credits: K. Bernlohr.

the 'third generation' detectors, a.k.a. Imaging Atmospheric Cherenkov Telescopes (IACTs).

Figure 2.3 represents a rough summary of the gamma-ray astronomy time-line, from its debut to the implementation of the third-generation telescopes. Before diving into the characteristics of the current generation of ground-based Cherenkov detectors, let us detail more the processes of atmospheric air showers and the Cherenkov radiation in the following sections, to ensure an enhanced understanding of the HESS experiment minutia.

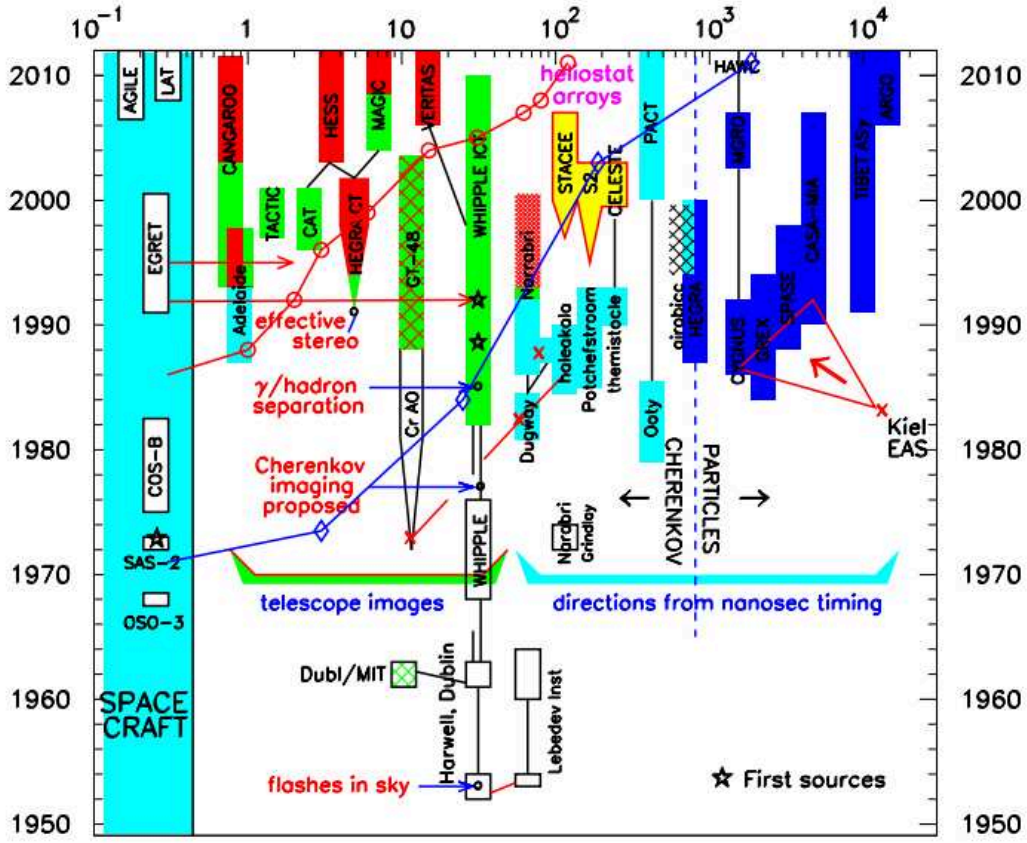

Figure 2.3 Partial gamma-ray astronomy time-line, from A.M. Hillas [A.M13]. The turquoise rectangle on the left represents the space-based facilities. The central region (up to the blue dashed line) illustrates Cherenkov light observations, while the rightmost part illustrates air shower particle detector development. In the Cherenkov part, white panels represent detectors using pulse counting with light collectors. Green panels show facilities where Cherenkov images were taken with a single telescope. Red panels represent stereoscopic focusing telescope systems. The turquoise ones show arrays of Cherenkov detectors using fast timing for source-location, while dark blue ones represent shower particle detectors. Finally, yellow panels represent converted solar power farms. Black connecting lines show continuity of personnel, red connecting line show strong influences. Stars mark the first clear source detections. Red crosses mark influential early Cygnus X-3 claims. The scale at the top corresponds to the number of known sources discovered from ground (red circles joined by line) or space (blue diamonds joined by line). Note that not all experiments are shown.

2.2 Extensive air showers

When a gamma-ray enters the Earth's atmosphere, it interacts via pair-production with the electric field of an atmospheric atom. The process of pair production is the creation of an elementary particle and its antiparticle from a neutral boson, usually by a photon, as illustrated in Figure 2.4.

Pair production of either electron and positron, muon and anti-muon or tau and anti-tau particles will happen provided that the photon is energetic enough so as to create the pair (thus carry, at least, twice the rest mass energy of the particles $E_0 > m_e\,c^2$, e.g. 511 keV for electrons) and that the energy and momentum can both be conserved. This last condition implies that pair production cannot take place in free space, where momentum and energy cannot be conserved at the same time.

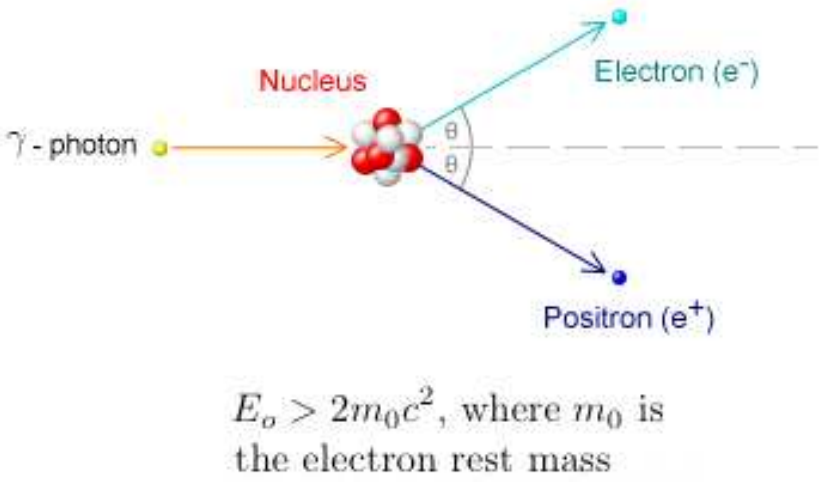

Figure 2.4 An electron and a positron are created via pair production when a very HE photon encounters an atom or a molecule. From `http://www.relativitycalculator.com/energy_doppler.shtml`.

If the energy of the incident gamma-ray, and hence of the created electron-positron pair, is large enough the process of electron-positron pair generation over the first radiation length is followed by *bremsstrahlung*[2] emission over the next radiation length, which will eventually decay into another electron-positron pair until they reach the energy threshold. The whole process, from the incident particle entering the atmosphere until the last of the secondary set of particles and photons is generated, is known as **extensive atmospheric cascade** or **shower** (top panel of Figure 2.5).

[2]Electromagnetic radiation created when a charged particle is depleted by another charged particle.

Gamma-rays are not the only initial particles that can set off such cascades, though. Indeed, depending on the particle that originated the shower, **electromagnetic showers** (initiated by leptons or gamma-rays) and **hadronic showers** (initiated by a proton or another cosmic-ray nucleus, see bottom panel of Figure 2.5) can be differentiated .

The development of electromagnetic cascades is dominated by three physical processes: electron-positron pair production, *bremsstrahlung* (electron/positron braking), and electron/positron energy losses through ionization. Any given shower will continue until the particles reach a critical energy where at which the *bremsstrahlung* and ionization rates are equal. Below this critical energy, ionization rather than *bremsstrahlung* becomes the predominant energy-loss process. A rough estimate of this threshold energy is $E_c = 800\,\mathrm{MeV}/(Z + 1.2)$. For the atmosphere, the corresponding value is $E_c \approx 85\,\mathrm{MeV}$.

To get an idea of the orders of magnitude of shower development, let us recall the definition of the electromagnetic radiation length X_0, which represents the amount of matter traversed by a particle until a certain level of energy is reached. For a layer of atomic number Z and mass number A, the length is defined as (Heitler [Hei54])

$$\frac{1}{X_0} = 4\,\alpha\,r_e^2\,\frac{N_A}{A}\,Z^2 \ln\left(183\,Z^{-1/3}\right)\mathrm{g\,cm^{-2}} \tag{2.1}$$

In the atmosphere, the radiation length is $\approx 37\,\mathrm{g\,cm^{-2}}$. The energy losses generated by *bremsstrahlung* can be expressed as a function of the thickness of the atmosphere $X = \int_h^\infty \rho\,(h)\,\mathrm{d}h$ that the electron or photon has traversed:

$$E\,(X) = E_0 \exp\left(-\frac{X(1+b)}{X_0}\right) \tag{2.2}$$

where $b = \frac{1}{18\mathrm{Ln}(183/\mathrm{Z}^{1/3})}$. If $b \ll 1$, a gamma-ray photon will undergo a pair creation process after the distance $R = X_0\mathrm{Ln}2$ known as radiation length, which is also the distance at which each electron losses half of its energy to a new gamma-ray. In other words, after traveling a distance R, half of the energy of an electron will be transferred to a *bremsstrahlung* photon, while a gamma-ray photon will transfer all its energy onto an electron-positron pair, $E_{e^-} = E_{e^+} = \frac{E_0}{2}$. Then, after another R radiation length, the electron-positron pair loses half of its energy by radiating a photon of energy $\frac{E_0}{4}$. The whole process is illustrated in Figure 2.6. Thus, after a

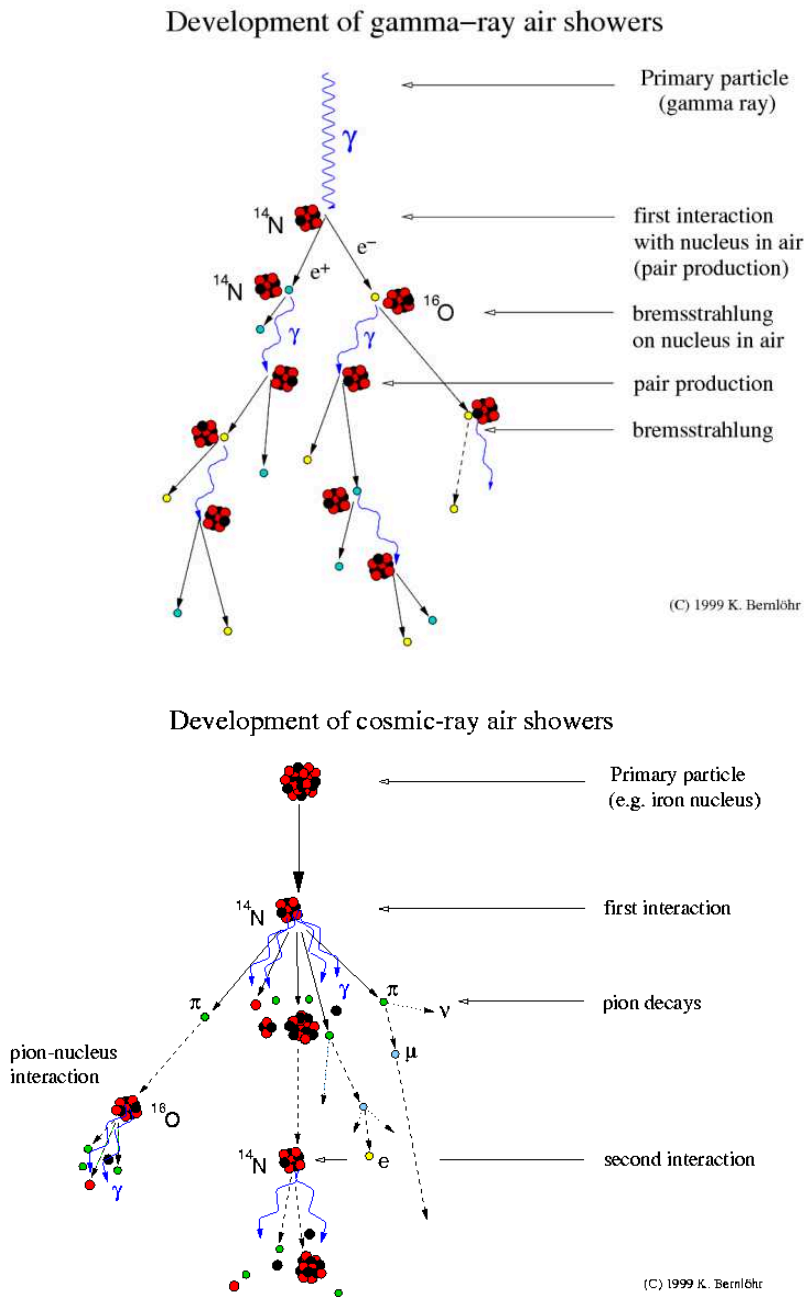

Figure 2.5 Scheme of a gamma-ray shower (**top**) and hadronic shower (**bottom**). Image credit: K. Bernlöhr.

distance nR, a total number 2^n of gamma-rays, electrons and positrons is created, whose average energy is $\frac{E_0}{2^n}$. An average photon-initiated shower consists of $\frac{2}{3}$ charged particles and $\frac{1}{3}$ photons.

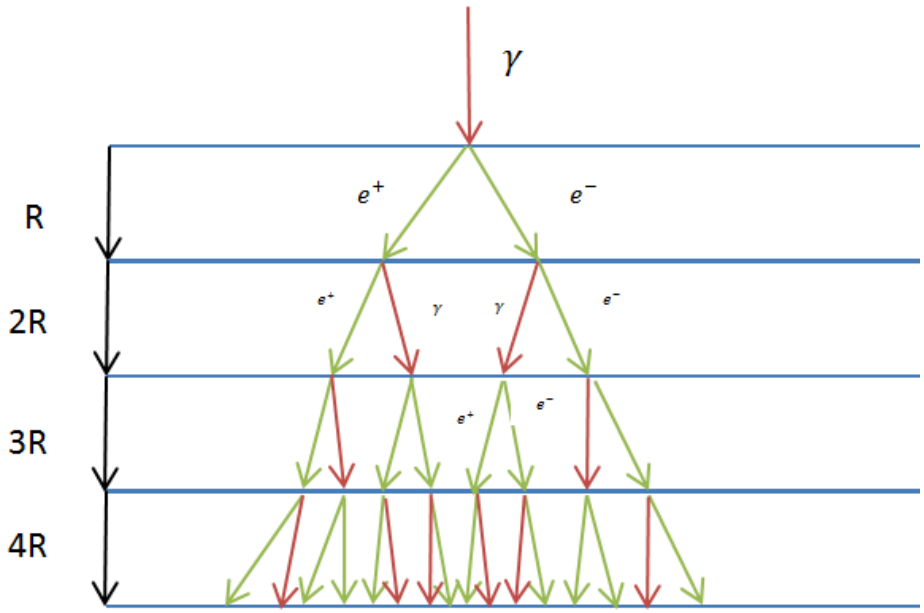

Figure 2.6 Electromagnetic shower caused by a gamma-ray entering the Earth's atmosphere. The initial photon creates an electron-positron via pair production after traveling a radiation length R. Each of these charged particles will create a photon, and the process will continue until the threshold energy level is reached.

This simple model permits the determination of the traverse depth at which the maximum of the cascade development is reached

$$X_{max} = X_0 \mathrm{Ln} \frac{E_0}{E_c} \tag{2.3}$$

where E_c is the aforementioned critical energy at which ionization losses become dominant. Considering a hydrostatic atmosphere, its density can be expressed in terms of the altitude h, $\rho = \rho_0 \exp(-h/h_0)$ where $\rho_0 = 1.2\,\mathrm{kg\,m^{-3}}$ and $h_0 \approx 8.4km$[3], so the traverse depth as a function of altitude is

$$X(h) = \rho_0\, h_0 \exp \frac{-h}{h_0} \tag{2.4}$$

[3] $h_0 = RT/gM$.

which is equivalent to a maximum shower altitude of

$$h_{max} = h_0 \,\mathrm{Ln}\left(\frac{\rho_0\, h_0}{X_0 \,\mathrm{Ln}\,(E_0/E_c)}\right). \tag{2.5}$$

Electromagnetic cascades not only transform a VHE gamma-ray into a very large number of fast moving charged particles, but also spread them over a vast area. Varying atmospheric conditions and incident particle energies mean that Cherenkov light cones have different characteristics, with shower-heights ranging from 6 km-20 km, and, consequently, different aperture angles. What is more, electromagnetic showers are rather collimated and present smaller transverse dispersion than hadronic showers, which have several components and hence become wider (Figure 2.7). This is one of the properties used for gamma-hadron discrimination in ground-based gamma-ray detectors, as will later be explained in more detail.

Both leptonic and hadronic cascades generate charged particles that move at highly relativistic speed through the atmosphere, exciting the surrounding medium and thus generating Cherenkov light photons [Section 2.1, Section 2.3] that accompany the shower and can be easily detected by ground-based telescopes. Let us stress that Cherenkov radiation and *bremsstrahlung* are totally unrelated: the latter is emitted by *the electron* when it collides with atoms within the medium, while the former corresponds to radiation emitted *by the medium* when the charged particles crosses it. Next, we will discuss the Cherenkov effect in more detail.

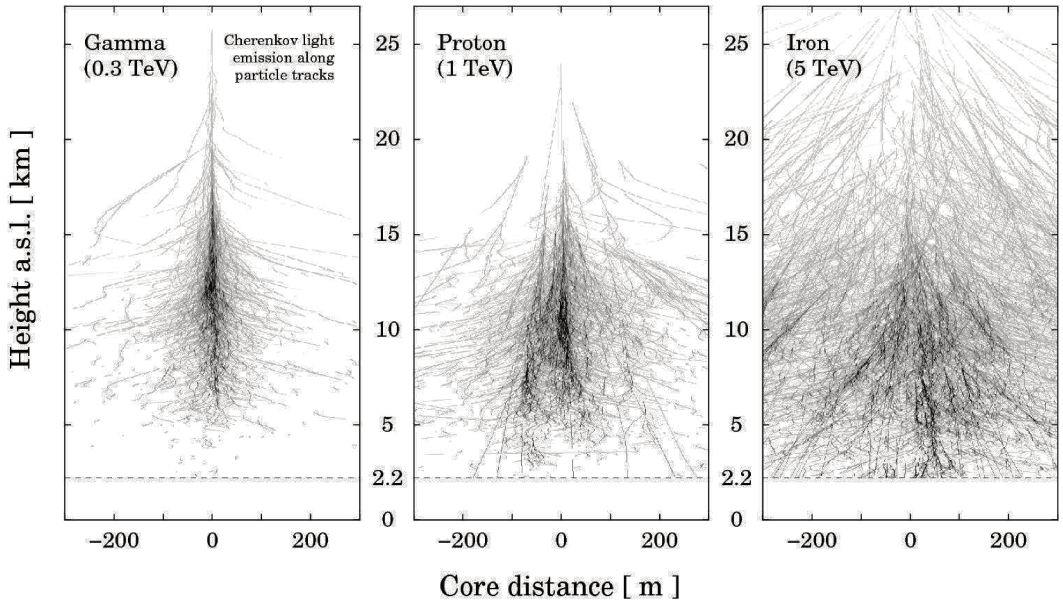

Figure 2.7 Simulations of extended air shower track simulation for different primary particles. Gamma-rays (**left**) create narrower showers that are more aligned with the direction of the incoming photon than hadronic showers (**middle, right**). From Bernlöhr [Ber08].

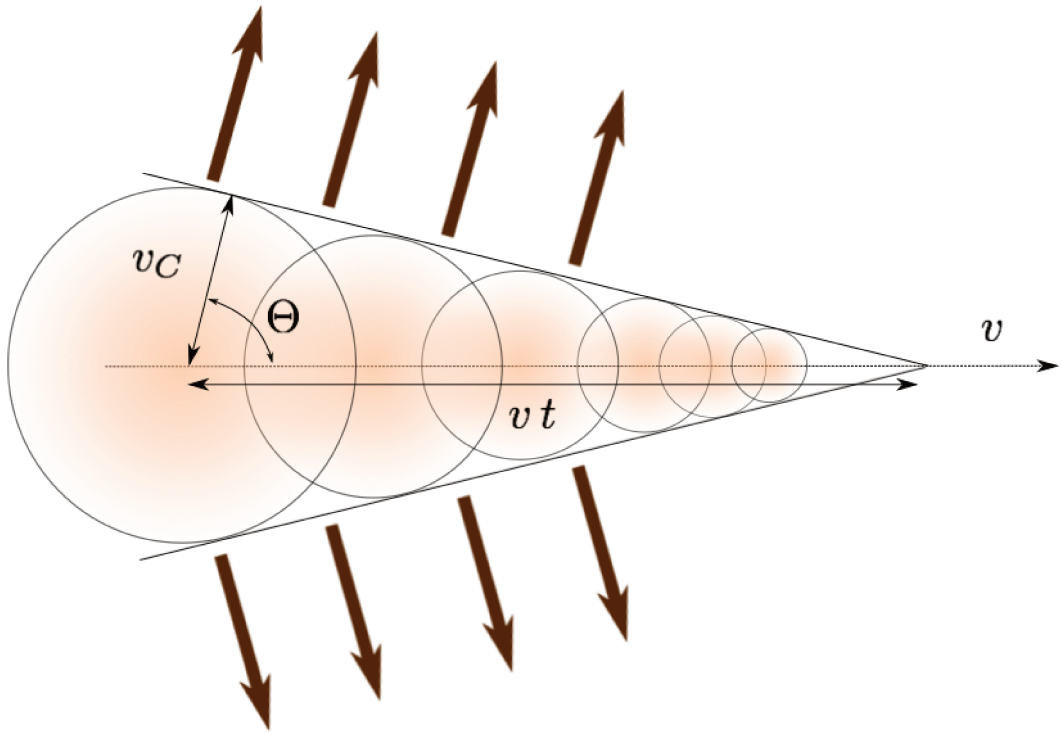

Figure 2.8 Sketch showing the propagation of the Cherenkov conical shock generated by a relativistic particle. Details are given in the text.

2.3 The Cherenkov effect

As introduced in Section 2.1, the Cherenkov effect consists in the generation of a characteristic radiation when charged particles interact with the surrounding environment at a velocity greater than the velocity of light in the medium. The particles generated in a shower have an initial velocity greater than the speed of light in the atmosphere, which results in a conical shock wave made up of the bluish Cherenkov light.

To characterize the opening angle of the Cherenkov emission, let us assume the relativistic particle is traveling at a fraction of the speed of light $v = \beta\, c$, while the velocity of the emitted Cherenkov photons is dependent on the refraction index of the medium at a wavelength λ, $v_C = c/n(\lambda)$ (see Figure 2.8). After a traveling time t, the opening angle, a.k.a. Cherenkov angle[4] can thus be expressed as

$$\cos\Theta = \frac{1}{\beta\, n(\lambda)}\,. \tag{2.6}$$

For a relativistic particle of charge Z and speed v traveling down the atmosphere, the number of emitted Cherenkov photons per length and wavelength unit is

$$\frac{\mathrm{d}^2 N}{\mathrm{d}x\mathrm{d}\lambda} = \frac{2\pi\alpha Z^2}{\lambda^2}\left(1 - \frac{1}{\beta^2 n^2(\lambda)}\right) \tag{2.7}$$

where α the fine structure constant $\alpha = \frac{e^2}{4\pi\epsilon_0\hbar c} \approx 1/137$.

As introduced in Section 2.2, cosmic rays entering the atmosphere also generate cascades and thus the accompanying Cherenkov radiation, but the pattern of a cosmic-ray shower is different to the pattern of a gamma-ray shower, which helps distinguishing one from the other. In fact, roughly only 1% of the showers are gamma-ray initiated. The origin of the remaining showers are cosmic rays, and represent the major background noise source in ground-based gamma-ray astronomy, whose latest generation of detectors, the IACTs, will be introduced next.

[4] First predicted by Heaviside and confirmed by Cherenkov [Section 2.1].

2.4 The current generation of IACTs

The absorption suffered by gamma-rays when they enter the atmosphere is a problem for direct gamma-ray detectors, which have to be flown in a balloon or a satellite (e.g. the Energetic Gamma Ray Experiment Telescope, EGRET, or the Fermi-Large Area Telescope) to a height where the influence of the atmosphere is minimized. This type of detector observes the positron-electron pairs created by the incoming primary astronomical gamma-rays after their interaction with a much denser environment (the detector in this case), and reconstructing the direction, time of arrival and energy of the gamma-rays in the energy range from a few MeV to around hundreds of GeV (at least in theory, since statistics above a few tens of GeV are limited in practice). In contrast, and as introduced in Section 2.1, the main advantage of IACTs is that they use the atmosphere as a part of the detector, acting as a calorimeter.

Gamma-ray detecting IACTs collect Cherenkov light that accompanies the particle shower by focusing the Cherenkov photons at the focal plane of a large set of mirrors, where the photons are collected by cameras composed of very sensitive Photo Multiplier Tubes (PMTs). Then, fast data acquisition systems are used to record the signal, with sampling rates of around 1 GHz. This way, an image of the projection of the air shower on the detection plane is recorded, which is afterwards used for energy and orientation reconstruction and background rejection purposes.

In fact, IACTs do not only detect Cherenkov light-pools caused by cosmic gamma-rays, but also an important cosmic-ray background caused by hadrons, electrons and muons that needs to be rejected before further analysis. As a matter of fact, the majority of events that reach the telescopes are originated by diffuse cosmic-ray hadrons that produce showers featuring characteristic secondary particles, such as nucleons, pions, K mesons, secondary gamma-rays from $\pi^0 \rightarrow \gamma\gamma$ decay, muons originated from the decay of charged mesons, and atmospheric neutrinos from the decay of charged pions, K mesons or muons (Figure 2.5). These secondary showers mask the desired signal from the gamma-ray-initiated showers. Simulations such as the one illustrated in Figure 2.7 show that cascades with gamma-ray origins have a smaller angular distribution and an ellipsoidal shape that aligns itself with the direction of the incoming gamma-ray, whereas cosmic-ray induced showers present broader and not-so-well aligned profiles.

Several other characteristic features also enable the discrimination of hadronic and gamma-ray showers. For instance, hadronic showers are more irregular and contain

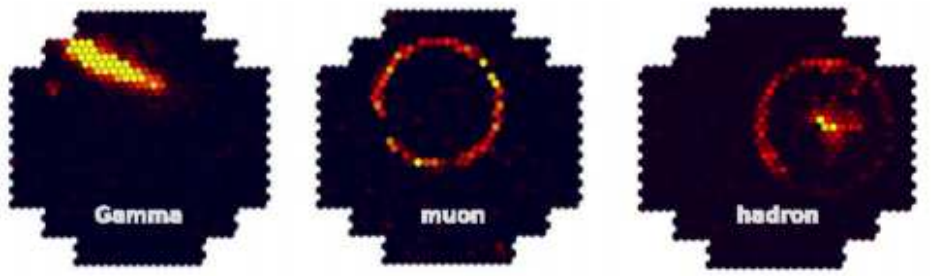

Figure 2.9 Different shower images created by different cosmic particles reaching IACTs. In contrast to the elliptical shape created by a genuine gamma-ray reaching the telescope, face-on muon showers present a characteristic ring-shape, while hadronic showers the shapes captured by the cameras are quite irregular.

several electromagnetic sub-showers initiated by disintegration of neutral pions. Hence, images in cameras often exhibit several separated clusters.

Electron-originated background contamination reaches the telescopes too. This type of particle creates electromagnetic cascades that quite resemble the gamma-ray showers, but the primary depth of electron cascades is shorter, i.e. the altitude at which the first interaction with the atmosphere happens is higher. This primary depth difference provides a good benchmark for gamma-electron rejection. What is more, electrons present spectral indexes of around 3.3, which means their contribution to the total background noise is only significant at very low energies ($\sim$ tens of GeV).

Additionally, the decay of charged pions generates atmospheric muons that are detected as single events in IACTs. If seen face-on, the Cherenkov image from a muon cascade has a very distinctive ring-shape, which obviously enables their discrimination (middle panel of Figure 2.9). However, if the Cherenkov light from a muon cascade reaches the cameras with an inclined position, the shower image quite resembles that of a gamma-ray. Stereoscopy techniques are very useful to discard this type of muon events.

The total number of Cherenkov light photons created in a gamma-ray shower is roughly proportional to the initial gamma-ray photon energy ($\simeq 50\,000\,\mathrm{ph\,GeV^{-1}}$, see Equation 2.7). Although Cherenkov photons are emitted all along the air shower at different heights and times, the light pool arrives to the ground-based detectors almost simultaneously (within few nanoseconds), because the particles and the light propagate with almost the same velocity.

Due to the fact that the Cherenkov light is very faint, the detectors need to be extremely sensitive in order to detect such dim emission, meaning that clean detections

can only be made on dark, moonless nights, which reduces the observation period of this type of telescope. What is more, although the number of events in the low energy range is larger than in the high energy range, low energy gamma-rays that reach the atmosphere produce even fainter Cherenkov light, so individual telescopes with large mirror areas are fundamental in order to detect the fainter light cones. Conversely, the mirrors used for IACTs do not need to be as high-quality as the ones in optical telescopes, since Cherenkov telescopes image the light of the pool instead of the actual astronomical source.

As for the collection area, for IACTs it is roughly the area of the light pool at the detector altitude, which can reach up to 50 000 m^2 for gamma-ray detection. Given that a single IACT would only see a part of the electromagnetic cascade from a given angle, the combination of images of the same shower captured by different telescopes located within the Cherenkov light pool enables the reconstruction of not only the initial direction, but also the energy of the initial particle. This multiple-telescope stereoscopy technique, foreseen by Weekes and Turver [WT77] [Section 2.1] and illustrated in Figure 2.10, provides the observer with a number of different snapshots of the same shower, enabling a better reconstruction of the trajectory and energy of the incident photon. Stereoscopic techniques also provide better constraints on the asymmetry of hadronic showers, which results in better background determination and muon rejection that improve the actual detection of gamma-ray photons.

A good example of a stereoscopic IACT array is the HESS experience, which features 5 IACTs located in the Khomas highland of Namibia (Figure 2.11), one of whom has a larger collection area for better low energy gamma-ray detection. A detailed description of the experience is presented in the following section.

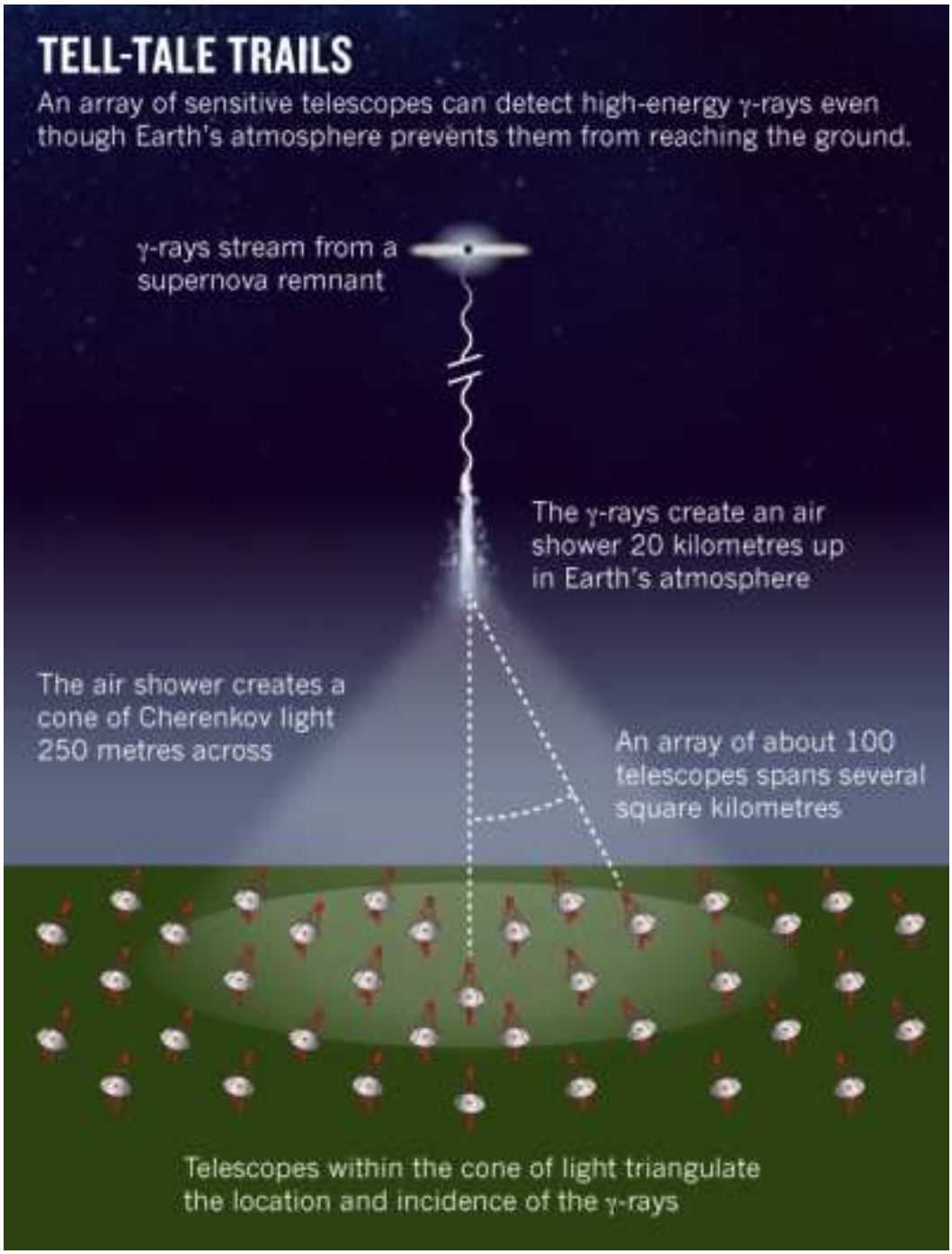

Figure 2.10 Schematic detection of a gamma-ray coming from a source, a supernovae remnant concretely. The Cherenkov light is detected by the telescopes located inside the projection of the light cone. Image credit: Eugenie Samuel Reich.

2.5 The HESS experiment

Named after Victor Hess, whose discovery of cosmic-rays in 1912 (F. Hess [FH12]) awarded him the Nobel Prize in 1936, the High Energy Stereoscopic System (HESS) is a gamma-ray observatory involving 35 institutions from 12 countries located in the Khomas Highland of Namibia, 1800 m above sea level. The Namibian plains were chosen to build the instrument due to the high quality of the sky over that part of the world, mainly thanks to the low background luminosity levels that characterize such isolated locations, and the dry atmosphere and low cloud coverage. In addition, the position of the observatory is close to the tropic of Capricorn, which allows optimal observation of the inner regions of the Galactic Plane.

Figure 2.11 The five IACTs composing the HESS observatory next to the Gamsberg mountain in Namibia. Image credit: HESS collaboration.

The HESS experience saw its first light in 2001, when the installation of the first telescope was completed. Since then, the experience has provided invaluable observations of the Universe in the VHE band. The experience features 5 IACTs dedicated to VHE gamma-ray astronomy in the energy range from ~ 30 GeV to hundreds of TeV. The assembly of the initial 4-small-telescope stage, or the HESS-I phase, was completed in 2003, while the HESS-II phase begun on the 28th September 2012 with the inauguration of the 28-meter telescope.

2.5.1 The telescopes

Located in the corners of a 120-metre-side square, the HESS-I telescopes' structure is an altazimuthal mount made of steel that allows observations in any position of the firmament, since telescopes can be pointed to any direction in the sky in less than 2 minutes, thus enabling observations of transient phenomena.

Composed of 380 spherical mirrors of 60 cm of diameter aligned with the spheroid defined by the mount, the dish of the telescopes has a total diameter of 13 m, and an area of 107 m^2. The mirrors are arranged in a Davies-Cotton mount, i.e. a spherical reflector composed of a number of mirrors that have the same focal distance f as the whole telescope and are arranged on a sphere of radius $2f$. The segmented spherical mirrors focus incident light into a camera built of 960 PMTs.

The fifth telescope (also known as CT5) is located in the center of the square created by the other 4 smaller telescopes. CT5 is the largest IACT so far built[5]. Such a large telescope was added to the array in order to lower the detection threshold of the system to around 30 GeV, and hence increase the sensitivity of the array at low-energies. A lower threshold in energies means an overlap between HESS-II and Fermi data, i.e. a continuous spectral coverage ranging from hundreds of MeV up to a couple of TeV for the brightest objects.

Unlike the phase I telescopes, CT5 is a parabolic telescope, i.e. the mirrors are arranged on a paraboloid, and the focal length of the mirror facets varies with the distance from the optical axis, in order to minimize dispersion. The dish is made up of 875 hexagonal mirrors of 90 cm of diameter, building up a total surface of 614 m^2. The camera mounted on CT5 provides a much higher resolution, 2048 pixels with a 0.07 degree field of view each, resulting in a total field of view of 3.2 degrees.

In the HESS-II camera, PMTs are grouped into drawers which also contain the electronics. However, the HESS-II camera is much larger - it contains 2048 PMTs in 128 drawers. The photomultiplier pixels of the camera have the same physical size, but due to the larger focal length shower images are much better resolved. See Table 2.1 for a comparison of HESS-I and HESS-II telescope characteristics.

[5] CT5 is even the largest mirror telescope ever built in general, awaiting the E-ELT (European-Extremely Large Telescope) to be superseded.

	HESS-I	HESS-II
Number of mirrors	382	875
Shape of mirrors	Round	Hexagonal
Diameter of mirrors	60 cm	90 cm
Total mirror area	108 m^2	614 m^2
Focal length	15 m	36 m
PMTs	960	2048
Drawers	60	128
Pixel size	42 mm $\simeq$ 0.16 °	42 mm $\simeq$ 0.07°
Total field of view	5 °	3.2 °
Camera body dimension width (cm) $\times$ height (cm) $\times$ depth(cm)	$160 \times 160 \times 150$	$227 \times 240 \times 184$
Weight	800 kg	2.8 tons

Table 2.1 Summary of the most important differences between HESS-I and HESS-II telescopes.

2.5.2 The cameras

The cameras of the HESS telescopes implement fine pixelization for optical imaging of the electromagnetic shower along with fast electronics for optimal background rejection.

As briefly mentioned in the previous section, PMTs are arranged in sub-units or drawers that also host the power supplies and trigger, readout and control electronics. A Winston cone is placed in front of each PMT and is used as a light concentrator to reject photons coming from an angle greater than $30°$ with respect to the PMT's normal. Winston cones limit the field of view of the PMT to the actual size of the mirror, reducing albedo noise from the ground.

The cameras feature really fast electronics, adapted to Cherenkov light flashes (let us recall that they last for nanoseconds), and the detector field of view is $3.2°$ for CT5 and $5°$ for HESS-I[6] The ngular resolution of the system depends on the off-axis position of the source and the elevation angle of the telescope.

The signal from each PMT is split into a trigger channel and two acquisition channels, the high gain and low gain channels respectively, to reduce the saturation of the signal[7]. After amplification, the signal is sent to an analogue memory and to the trigger system designed to identify spatial structures that could correspond to air showers in the camera. The trigger system helps reduce the rate of accidental events induced by the Night Sky Background (NSB) light[8], as we will see next.

[6] A larger field of view is required to capture showers up to VHE completely, since more energetic initial particles result in larger Cherenkov pools.

[7] The high gain channel is used to detect signal charges up to 200 photoelectrons, while the low gain channel covers the range from 15 to 1600 photoelectrons Aharonian et al. [Aha+04]

[8] The glow of the night sky comprises contributions from a number of sources, e.g. the diffuse night-sky background due to star-light scattered in the atmosphere, light from stars themselves, scattered light from the rising or dawning moon, the moon itself or the Zodiacal light (sun-light scattered around the ecliptic).

2.5.3 The trigger system

The trigger system featured in the HESS array is a system that allows the rejection of NSB signal with regards to the actual Cherenkov images. Due to the necessity of reconstructing the parameters of the initial shower, events triggering less than two telescopes are automatically discarded.

The trigger system is dual. The first level or local level features an internal trigger system within each camera that uses correlation between neighbouring pixels to reduce the influence of NSB. Cameras are divided into 38 overlapping sectors of 64 pixels each, and a trigger decision will not be taken unless the signal in a number of pixels S_2 inside the same sector of the camera exceeds a given threshold S_1, which for normal operations $S_1 = 4$ photoelectrons and $S_2 = 3$ pixels. Hence, the single camera trigger rate is around 1.4 kHz.

On a second level, coincidences between different telescopes are considered to both reduce triggering due to muons or localized showers and to ensure a stereoscopic view of showers, which greatly improves the reconstruction precision and the rejection capability of the system. Accordingly, when one of the cameras is triggered, it sends a signal to the central trigger, which in turn delays the signal from different telescopes according to the pointing conditions.

In addition, the central trigger makes trigger decisions based on the number of telescopes triggered in the same shower. The central trigger system sends a confirmation to the telescope to continue processing the analogue signal, provided that simultaneous observations of the same shower took place. Should this not be the case, the system proceeds to the next event.

2.5.4 The environment

Apart from the IACTs, several smaller instruments are installed in the HESS array to ensure proper monitoring of the atmosphere and the instrument behaviour. For instance, the *flat-fielding LED*, composed of flashing LEDs and isotropic diffusers and installed on the center of the dish is used to cross-calibrate the response of PMTs.

Close to the 5 IACTs, the *Automatic Telescope for Optical Monitoring* (ATOM), a Cassegrain reflector[9] with a primary mirror diameter of 75 cm and a focal length of 600 cm, is an optical telescope dedicated to the observation of variable gamma-ray sources in the visible (B,V,R and I filters) and to the monitoring of AGN. ATOM enables quasi-simultaneous Multi-WaveLength (MWL) observations, and therefore this complimentary instrument is highly important for blazar physics because it provides a follow-up in visible light of the TeV targets, providing alerts for flares when a scheduled source shines above a predefined threshold.

Another supplementary set-up is the *atmospheric monitoring system*, required for the array operation since it allows the reduction of systematic effects at the analysis level. This monitoring provides information to the shift crew on site about the quality of the sky and safety of operations. Monitoring cloud coverage and wind speed allows the observer to stop the observations and put the camera in safe state before rain. The system gives quantitative criteria to estimate the quality of the sky and decide which data are hampered by bad weather. The equipment involves one radiometer per telescope, installed on the telescope mount and pointing towards the same field of view as the telescope, that measures the temperature of the sky and monitors the clouds crossing the field of view. In addition, the scanning radiometer makes full sky images of cloud coverage, and the weather station provides measurements of temperature, pressure, humidity, wind speed and direction.

In addition, the HESS observatory also comprises a LIDAR (LIght Detection And Ranging), which makes measurements of the aerosol composition of the atmosphere as a function of the altitude. For more details on the LIDAR, see Bregeon et al. [Bre+16].

[9] A Cassegrain reflector is a combination of a primary concave mirror and a secondary convex mirror, often used in optical telescopes and radio antennas.

2.5.5 Calibration runs

Calibration runs are required to correctly calibrate the images of the Cherenkov showers, and some observing time is necessarily spent on this. In the HESS experience, different calibration techniques are carried out through different run types:

- ***Pedestal runs***, performed with the lid of the camera closed for the measurement of the electronic output in absence of Cherenkov light.
- ***Single photo-electron runs***, performed via the measurement of the light emitted by dedicated calibration LED pulsers located in front of the PMTs of the camera in order to establish their response.
- ***Flat-field runs***, which measure the signal from LED flashers mounted on the telescope dishes, illuminating the camera homogeneously. A laser located in the dish of each telescope can emit an homogeneous signal over the whole camera so that the response of different channels can be calibrated.

In addition to the above mentioned calibration runs, pointing runs are also taken on a regular basis by observing a number of stars to determine whether their positions are correctly accounted for.

2.5.6 Shower reconstruction

After data taking and calibration adjustments, and previous to any physics analysis, data need to be reconstructed. The aim is to on the one hand reconstruct the direction, energy and impact parameter of the primary particle, and on the other to provide discrimination for background events from cosmic rays.

First, we present the Hillas description of the parameters of the ellipse seen in the cameras, which was the first reconstruction technique to be developed. Then we present the different, more complex data analysis chains that have been developed within the HESS collaboration. A special emphasis is put on the Model++ chain, since is the chain with which we performed the analysis of 1ES 2322−409 presented in Chapter 5.

The Hillas analysis algorithm

In 1985, Hillas [Hil85] suggested that recorded images of atmospheric showers could be reduced to a few parameters with the aim of approximately modeling the image seen by the detectors as a 2D ellipse. Indeed, the **Hillas parametrization** assumes that gamma-ray showers are elliptical in shape in the focal plane of the camera, while an irregular, non-elliptical shape would point towards a hadronic origin of the shower.

The parametrization of the ellipse is obtained via the length L and width W of ellipse, the size (total image amplitude), the nominal distance d (angular distance between center of camera and center of gravity of the image), the azimuthal angle of the image center of gravity φ and the orientation angle of shower α (see Figure 2.12 for a sketch of the ellipse). First and second moments, along with variances and covariances, are used to define intermediate variables. To determine these parameters, only the pixels taking part in the shower image are considered.

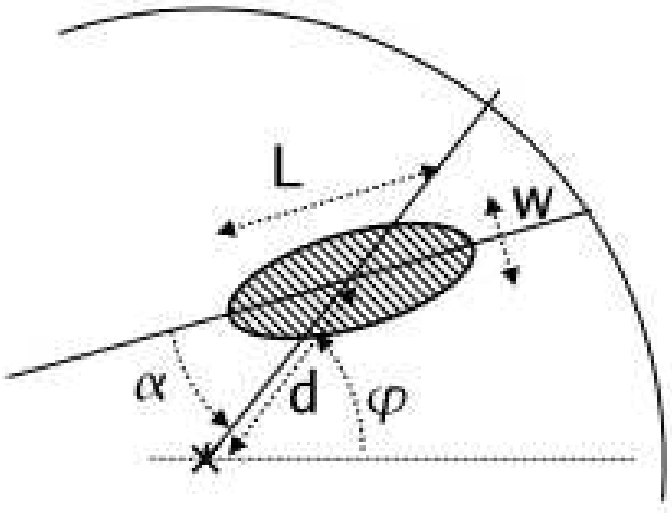

Figure 2.12 Schematic view of the ellipse generated by a cosmic gamma-ray in the camera. The parameters that define the ellipse are shown in the cartoon. From De Naurois [DN06].

The stereoscopic reconstruction imaging technique is a simple geometric reconstruction of showers. Source detection is given by the intersection of the major axis of the shower images superimposed in the cameras (see Figure 2.13). As for the shower impact point, it is calculated via the geometrical intersection of the planes in the sky

containing the telescopes and the shower track. Shower energy is estimated from the weighted average of each single telescope's energy reconstruction.

In single telescope observations, shower direction is also estimated from Hillas parameters but the choice of symmetrical parametrization of the shower leads to degenerate solutions on each side of the image center of gravity along the main axis. This issue could be solved by the addition of parameters such as the skewness or the kurtosis.

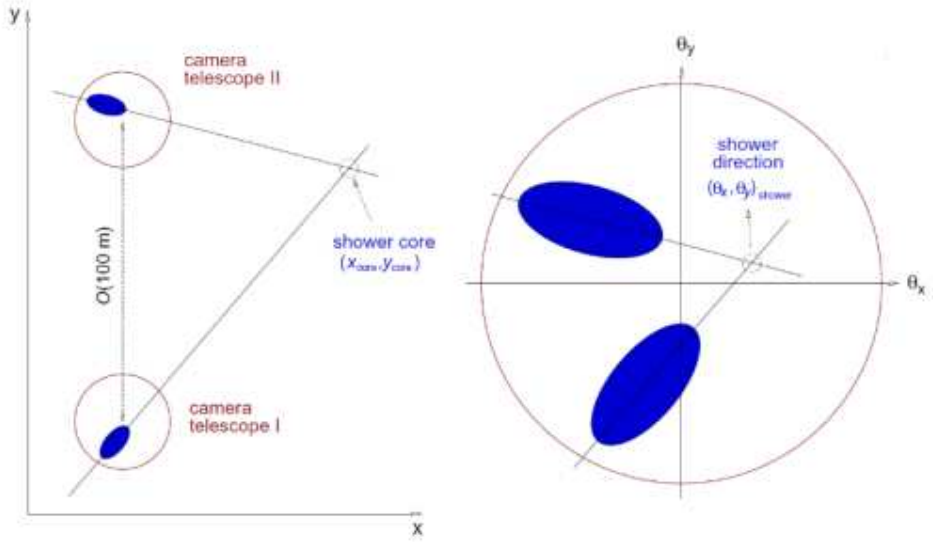

Figure 2.13 Stereoscopic reconstruction of an air shower. The shower core is given by the intersection of the two shower directions given by the major axes of the ellipses seen by different telescopes. The superposition of both camera images onto a single camera coordinate system, one can reconstruct the direction of the original shower. Credit: Heike Prokoph.

Apart from allowing the reconstruction of shower parameters, Hillas parameters can also help to discriminate gamma-rays from the much more numerous hadrons. For this purpose, the most important variables are the ***Scaled Width*** and ***Scaled Length***, which are almost uncorrelated for gamma-induced showers. These variables can be easily combined in stereoscopic analysis through the mean of those variables on different telescopes, yielding the ***Mean Scaled Width*** and ***Mean Scaled Length*** variables.

Look up tables are used to reconstruct the energy of primary particles as a function of image amplitude and impact parameter. Such tables allow the numerical inversion of the relations between the true primary energy, the impact parameter and the measured signal intensity, and are constructed from simulations.

The Model 3D analysis algorithm

The method created by Lemoine-Goumard et al. [Lem+06] is a 3D generalization of the Hillas parametrization reconstruction, based on the assumption of a 3D elliptical shape of the photo-sphere that is adjusted to the observed images simultaneously in all telescopes (see Figure 2.14). This makes this method only applicable to stereoscopic data. In this algorithm, showers are modeled as Gaussian photo-spheres that are used to predict the light collected in each pixel. The comparison between actual and predicted images, done through log-likelihood methods, allows for the reconstruction of 8 shower parameters, including the mean altitude, impact point and impact direction of the shower, the luminosity of the shower or the 3D image amplitude.

The major advantage of the 3D Model reconstruction over the Hillas reconstruction is that the relation between the actual image amplitude in the telescopes and the total shower luminosity is encoded in an unequivocal way. The best estimation of the primary energy of the incident particle is the luminosity of the Gaussian photosphere. Besides, the altitude of the photosphere gives another estimation of the energy of the shower, since high-energy showers penetrate deeper into the atmosphere than low-energy showers.

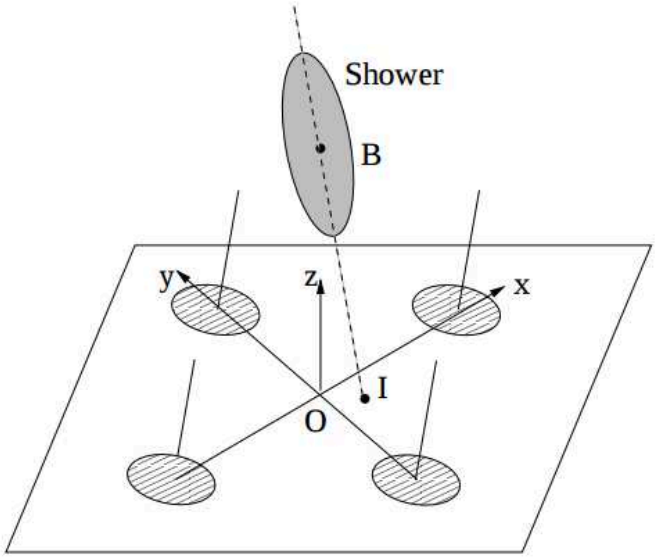

Figure 2.14 3D view of an air shower. From Lemoine-Goumard et al. [Lem+06].

The Model++ analysis algorithm

The Model++ reconstruction technique is a gamma-ray likelihood reconstruction procedure based on the comparison of actual shower images with predictions obtained from a semi-analytical model. Model++ is the improved version of the Model technique by de Naurois and Rolland [dR09], with additional discriminating variables that provide better gamma-hadron discrimination.

The semi-analytical model generates shower images based on different Cherenkov light distributions, which in turn are determined by the longitudinal, lateral and angular distribution of the charged particles of the cascade. These distributions are derived from Monte Carlo techniques (for different zenith angles, interaction depth and energy and impact parameters) and parametrized to yield an analytic description of the shower, i.e. the shower model.

To obtain the corresponding best-fit values of the image parameters (direction, impact, depth of first interaction and primary energy), the model shower images are compared to the actual images through a log-likelihood minimization procedure (that accounts for the Poisson nature of the detected number of photons in each pixel) assuming that the incident particle is a gamma-ray. The NSB contribution of each pixel is also modeled. For the minimization procedure, the intensity in each pixel of the camera image is compared with the intensity predicted by the model. The fitting procedure considers all the pixels of the camera, and thus does not require any type of prior image cleaning procedure.

Background rejection is done by comparing the actual log-likelihood and the expected one, to inspect the compatibility of the recorded events with the hypothesis of a gamma-ray originated shower.

For better gamma-hadron discrimination, additional variables are put in place. For instance, the pixels that contribute to the goodness-of-fit and have a predicted amplitude larger than 0.01 p.e. are gathered into the *ShowerGoodness* variable that is more sensitive than the goodness-of-fit to incongruities between the real images and the predicted ones. Remarkably enough, the Model++ reconstruction yields a factor ≈ 2 better sensitivity compared to standard Hillas reconstruction.

Multi-variate analysis methods

There are additional analysis chains within the collaboration that implement Boosted Decision Tree (BDT) Multi-Variate Analysis (MVA) algorithms for photon-hadron discrimination purposes. Some of them are presented here:

- **Paris-MVA, Becherini et al. [Bec+11]:** uses Hillas and 3D model variables, resulting in a significant improvement on sensitivity. Initially developed for the study of faint sources, i.e. luminosities of 1% of the Crab nebula, Paris-MVA implements parameters from Hillas and 3D Model algorithms, along with the use of BDTs for gamma-hadron discrimination. Paris-MVA sensitivity is 1.2 to 1.8 times higher than the sensitivity of the best of the traditional Hillas algorithms. This algorithm is also the most robust against NSB variations. **APC-MVA** (Khelifi et al. [Khe+15]) is an updated version of the BDT approach from Becherini et al. [Bec+11] based on the same event parameters but including improvements in the BDT training process and the use of gamma-background discrimination cuts optimized for different templates of sources. APC-MVA is the principal analysis chain used for 1ES 2322−409, for which we performed the quality cross-check analysis through the Model++ chain (see Chapter 5).

- **ImPACT, Parsons and Hinton [PH14]:** the Image Pixel-wise fit for Atmospheric Cherenkov Telescopes algorithm can be seen as the mixture of Model++ and Paris-MVA. ImPACT is based on a BDT multi-variate discrimination, while the maximization of the function is quite similar to the one implemented in Model++. This method does not use any analytic model for the reconstruction. The expected intensity distributions for the pixels of the camera are created merely via Monte Carlo simulation of showers.

2.5.7 Data analysis

Once the data have been properly calibrated, three are the main steps for HESS data analysis of point-like sources: the run selection, the computation of the significance of the source, and the spectral analysis of the source. An additional step, the morphology analysis, is also possible for extended sources, but will not be presented here since the present work focuses on point-like sources. In this section, each step will be briefly described, with the aim of clarifying the process that has been implemented for the HESS analyses of the source presented in Chapter 5.

An initial selection of runs that will be afterwards analyzed is performed to get an homogeneous data set by discarding observations affected by bad weather and/or technical problems. The weather quality is estimated by a radiometer installed on each telescope [Section 2.5.4], while the image quality is estimated according to the fraction of broken pixels on the camera and based on trigger rates.

More than a single configuration of cuts can be applied within the different analysis chains. The main difference between the applicable configurations is the Charge Threshold (CT) contained in the gamma-ray image. For instance, the Model++ analysis chain enables three different configurations, a *loose* configuration with CT = 40 photoelectrons, a *standard* cut with CT = 60 and a *faint* cut where CT = 80. Since the CT defines the low-energy threshold of the reconstructed spectrum, and faint showers are related to low-energy photons mostly, *loose* analysis configurations are adapted to soft-spectrum sources, e.g. AGN and particularly distant AGN whose spectrum is soft due to Extragalactic Background Light (EBL) absorption (see Section 3.2 for details). It is important to keep in mind that this type of cut is much more permissive, resulting in a worse photon-hadron discrimination. It follows that *faint* configurations suit hard spectrum sources best. Anyway, analyses with standard cuts are first required for a positive detection of a source, while the cuts are eventually adapted to the type of source.

After the gamma-hadron separation, background determination is one of the trickiest steps of the HESS reconstruction. The first step of hadron-like shower rejection is achieved by the goodness-of-fit variable in the Model++ chain, for instance.

A second step towards a correct signal estimation consists of the subtraction of background noise caused by gamma-like events that might still linger in the field of view after gamma-hadron separation. For that purpose, two different region types are considered in the field of view of the camera: ON and OFF regions. For a better background rejection, HESS telescopes do not point exactly at the target

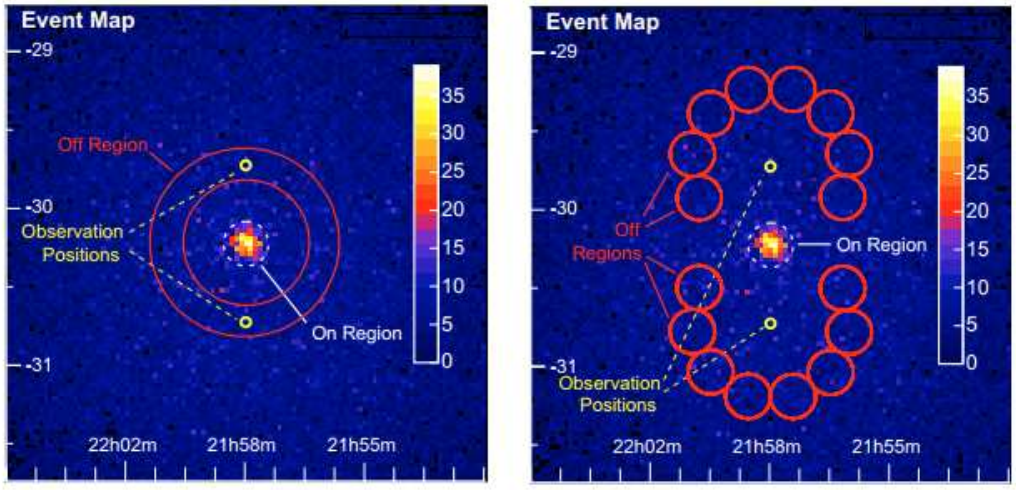

Figure 2.15 Schematic illustration of the ring-background model (left) and the reflected-background model (right) implemented in HESS. From Berge et al. [Ber+07]

source. Instead, the position of the aimed source is shifted by $\sim 0.5°$ with regards to the center of the field of view of the instrument. This means that the acceptance gradient of the telescopes has to be taken into account for the event reconstruction. The acceptance of a camera is given by the sensitivity of the instrument that varies rapidly as a function of the offset with respect to the center of the field of view. Up to first order, the acceptance of the camera at a given point depends only on the radial distance from the point to the center of the camera, i.e. azimuthal symmetry.

On the one hand, an ON region of a radius $\sim 0.1°$ is centered in the presumed position of the source. Note that the true radius of the ON region depends on the type of cuts that has been applied for the analysis. This is the region from which an estimate of the true gamma rays is obtained.

On the other hand, one or more OFF regions are considered in the zones of the field of view where no gamma ray excess is presumed, and the background noise is determined from these regions. As for the determination of OFF regions, a bunch of different methods can be deployed. Here, we just present the most widely used ones within the collaboration (see Figure 2.15).

Within the ***multiple background region method***, a number of OFF regions are selected, all of them being of the same size of and radially equidistant to the ON source. Moreover, if the case is given that any other gamma ray source is in the field of view of the source of interest, a security-radius is set around each of those extra sources, preventing them from being considered for the background determination. The number of events within ON and OFF regions is normalized by an α factor representing the ration of the exposures of the regions.

The second OFF region determination method we will mention is the ***complete ring region method***, implemented only for sky map generation. As the name suggests, the OFF region consists of a ring surrounding the ON region. Since the OFF region is at a distance for which the acceptance will not be the same as for the source region, the aforementioned radial acceptance differences need to be taken into account.

The signal is extracted by comparing the number of events in the ON region (N_{ON}) to the number of events in the control OFF region (N_{OFF}). The OFF region methods we have described above are designed to minimize the differences in the acceptance between ON and OFF regions. However, if the instrument response varies between both regions, an additional factor that gives the expected number of background events in the ON region given the background events in the OFF region is required, $\overline{N_{ON}} = \kappa\overline{N_{OFF}}$. The signal excess is defined as the difference between the events in the ON region and the normalized events in the OFF region, i.e. $N_{excess} = N_{ON} - \alpha N_{OFF}$. The significance of the detection is given by the approach by Li and Ma [LM83] that takes into consideration de Poisson nature of the distribution in case of poor statistics.

After all these steps have been performed, one can proceed to the high level analysis of the data, for example to perform a spectral analysis of the emission.

So as to compute the spectrum of the source, a so-called *forward folding technique* is implemented. This technique assumes that the measured spectrum can be expressed as the convolution of the parametrized intrinsic spectral shape and the Instrument Response Function. That is, if one knows the performance of your instrument (through the resolution $\mathscr{R}(E_{rec}, E_{true}|\delta, \Phi, \epsilon)$ and acceptance $\mathscr{A}(E_{true}|\delta, \Phi, \epsilon)$ functions where δ, Φ and ϵ are the zenith angle, the off-axis angle and the optical efficiency respectively) and assume a parametrized spectrum for the source $\Phi\left(E_{true}|\vec{\alpha}\right)$ (power-law, broken power-law, curved power-law, etc.), the expected number of gamma-rays for a reconstructed energy bin $[E_{rec,1}, E_{rec,2}]$ can be calculated:

$$n_\gamma = \int_{E_{rec,1}}^{E_{rec,2}} \mathrm{d}E_{rec} \int_0^\infty \mathrm{d}E_{true} \mathscr{R}(E_{rec}, E_{true}|\delta, \Phi, \epsilon) \times \mathscr{A}(E_{true}|\delta, \Phi, \epsilon) \times \Phi(E_{true}|\vec{\alpha}) \tag{2.8}$$

This expected gamma-ray excess can be compared to the actual detected gamma-rays extracted from the ON region after background subtraction, in order to obtain the best fit parameters of the assumed intrinsic spectral shape, as well as the significance of the fitting procedure, through the log-likelihood minimization introduced earlier.

2.5.8 AGN and HESS

Due principally to the EBL absorption of the most energetic photons emitted by AGN, the number of AGN detected at VHE by IACTs remains rather small. Figure 2.16 shows the TeV skymap of the so far detected 205 VHE sources, which are indeed clearly dominated by galactic sources.

The extragalactic subsample is clearly dominated by blazars, with 48 High-frequency-peaked BL Lacs (HBLs, 18 discovered by HESS), 8 Intermediate-frequency peaked BL Lacs (IBLs), 2 Low-frequency-peaked BL Lacs (LBLs, 1 discovered by HESS) and 6 FSRQs (2 discovered by HESS) detected up to now. The most distant source with known redshift detected at TeV is the FSRQ S3 0218+35 ($z \sim 0.96$, Yonehara, A. et al. [Yon+08]).

Observations carried out with the current generation of IACTs have enabled ground-based gamma-ray astronomers to characterize the SED of the majority of the VHE-detected AGN, moving forward towards a better comprehension of the emission processes behind the observed radiation.

Each year, proposals for the observation of well-known and interesting extragalactic VHE sources are written and discussed by the members of the HESS collaboration, to build the schedule of the sources that will be observed on a daily basis.

Apart from this 'normal' procedure, Target of Opportunity (ToO) procedures are also put in place to allow rapid scheduling of time-sensitive observations. The extragalactic ToO program closely monitors a variety of MWL facilities with the ultimate aim of rapidly triggering HESS observations when a source enters a high state on another given wavelength. The ToO monitoring task may also launch a MWL follow up campaign if a source enters a flaring state. This type of joint MWL observational campaigns are incredibly useful to provide us with simultaneous observational datasets that could potentially be modeled afterwards. An example of such a MWL campaign is presented in Chapter 4.

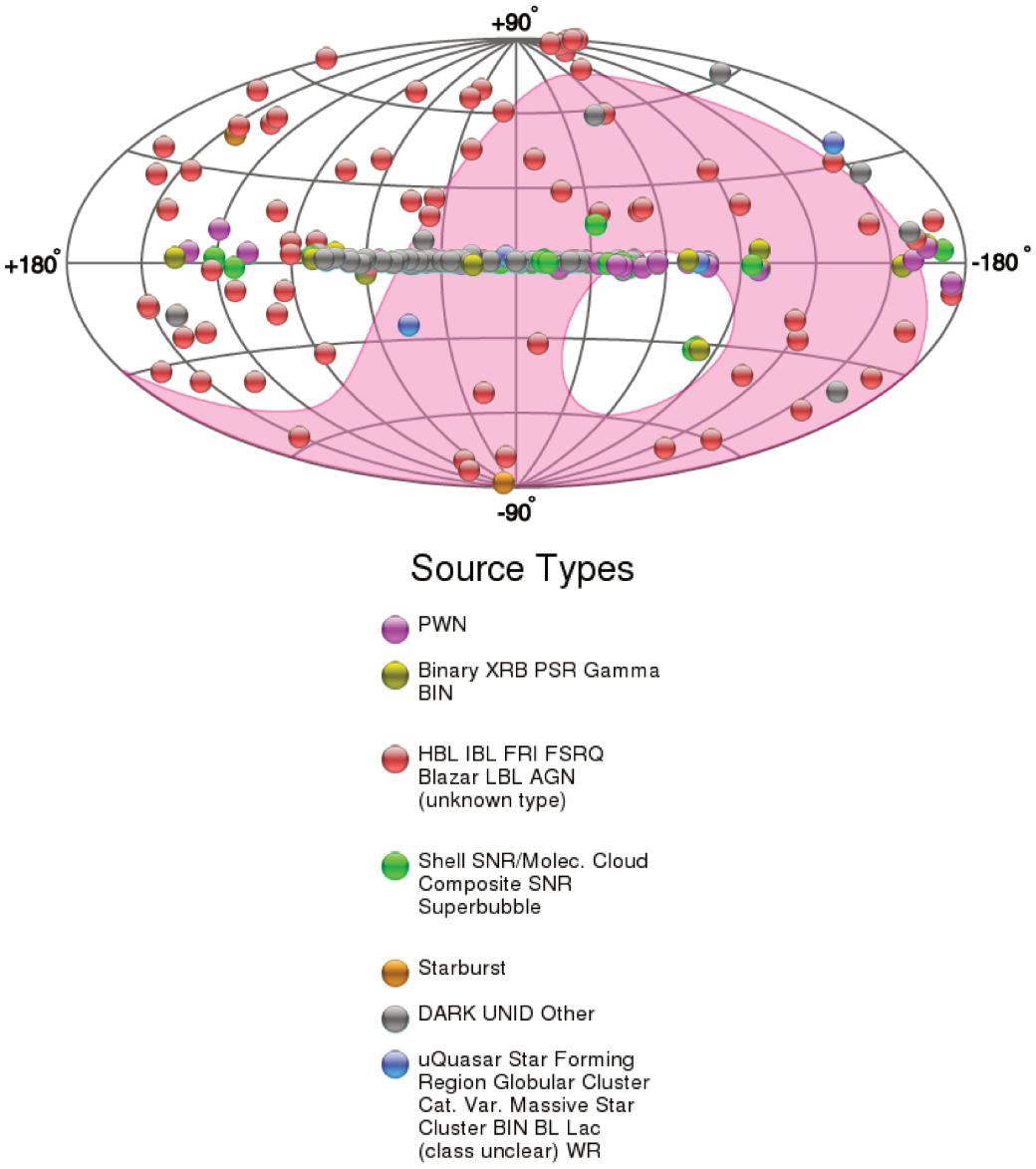

Figure 2.16 TeVCat Skymap in Galactic coordinates of TeV sources as of July 2017 (source: TeVCat). Purple points correspond to Pulsar Wind Nebulae (PWN), yellow points to X-Ray Binaries (XRB) and PulSaRs (PSR) and red points to various types of blazars. The majority of the TeV-detected sources are located along the galactic plane. Regarding extragalactic blazar-type sources, a total of 6 FSRQs, 48 HBLs, 8 IBLs and 2 LBLs have so fat been detected at these extreme energies. The colored region shows the part of the sky that is accesible to HESS.

3 Gamma-loud AGN modelisation

In this Chapter, the main radiative processes that are at the origin of the observed emission from jetted Active Galactic Nuclei (AGN) are introduced [Section 3.1]. Once the different interactions that generate the broad-band emission explained, the simplest model that is usually applied to High-frequency-peaked BL Lac (HBL) type objects, known as the Synchrotron Self-Compton (SSC) model, is presented along with the constraints that can be set upon different model parameters through a number of observables [Section 3.2]. Afterwards, we present the formalism of the numerical model that we have developed to take into account the additional external photon fields required to model sources with more complex Spectral Energy Distribution (SED), e.g. gamma-loud Narrow Line Seyfert 1 (NLS1) galaxies, along with the corresponding constraints and a quantitative exploration of their parameter space [Section 3.3.1]. Indeed, this Chapter sets the theoretical framework on which we base the studies that will be afterwards presented in Chapter 5 and Chapter 6. Last, a brief overview of some of the alternative models applied by other authors to jetted AGN is given [Section 3.4].

3.1 Radiative processes in AGN

The aim of this section is to give a brief insight on the main non-thermal and thermal radiation processes ascribed to one or more components of the AGN that are at the origin of the observed SED of blazars and NLS1s. In addition, the radiative processes that are implemented in the ground-based gamma-ray detectors presented in Chapter 2 are explained more thoroughly.

3.1.1 Synchrotron radiation

Synchrotron emission is a type of non-thermal radiation generated by charged particles (usually electrons) spiraling around magnetic field lines at a velocity close to the speed of light. Since the electrons are always changing direction, they are in effect accelerating and emitting photons.

Although particularly important at radio frequencies, depending on the energy of the electron and the strength of the magnetic field synchrotron emission can also occur at visible, ultraviolet and X-ray wavelengths. The radiation emitted is confined to a narrow cone pointing in the direction of the motion of the particle, in a process called *beaming*. It is also polarized in the plane perpendicular to the magnetic field, with the degree and orientation of the polarization providing information about the magnetic field of the source.

The spectrum of synchrotron emission results from summing the emission spectra of individual electrons (Figure 3.1). As the electron spirals around the magnetic field, it emits radiation over a range of frequencies peaking at ν_0, the critical frequency. The longer the electron travels around the magnetic field, the more energy it loses, the narrower the spiral it makes, and the longer the wavelength of the critical frequency.

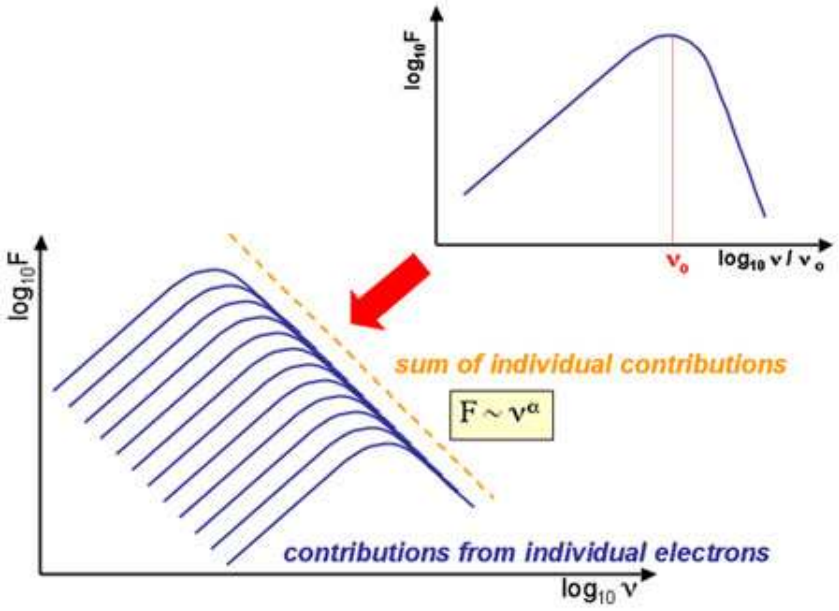

Figure 3.1 The sum of the spectra of electrons following a power law distribution over different frequencies, the characteristic spectrum of synchrotron radiation is observed to have a power law shape. Credit: Swinburne University.

In many cases, synchrotron radiation is emitted from electrons whose energy has a power law distribution. By summing the spectra from the individual electrons we find that synchrotron emission has a characteristic spectrum where flux steadily declines with frequency according to the relation $F \sim \nu^{\alpha}$, where α is known as the spectral index for the object and is linked to the index of the electron power law distribution n, $\alpha = (n-1)/2$.

Synchrotron radiation resulting from the interaction of the relativistic charged particles from the jet and the tangled magnetic field accounts for most of the non-thermal radio emission observed in AGN. Moreover, synchrotron photons are the seed photons for the synchrotron self-Compton process that will be presented briefly in Section 3.1.5 and in more detail in Section 3.2.

Last, we would like to mention that if the region where synchrotron photons are created becomes sufficiently dense, the re-absorption of synchrotron radiation by the synchrotron electron themselves will become important, and cause a sharp cutoff at lowest radio frequencies, modifying the observed spectra from a source. This effect, known as *synchrotron self-absorption* will be farther discussed in Section 3.2 and in the application of the models in Chapter 5 and Chapter 6.

3.1.2 Blackbody radiation

Black body radiation originates from bodies acting as *perfect absorbers*: bodies that are black, i.e.that absorb all the light, which in turn implies they are also *perfect emitters*, due to emission and absorption being closely linked. Blackbodies are the most efficient radiators both for thermal plasmas and incoherent radiation processes[1].

The spectral radiance of a perfectly absorbing blackbody that radiates at a temperature T is given by the following expression:

$$B_{\nu}(T) = \frac{2}{c^2} \frac{h\nu^3}{\mathrm{e}^{\frac{h\nu}{kT}} - 1} \tag{3.1}$$

[1] Coherent radiation: radiative process where the phases of two (or more) waves representing the radiation differ by a known constant.

whose peak frequency is $h\nu_{peak} = 2.82\ kT$, whereas that of the νB_ν distribution is located at $h\nu_{peak} = 3.93\ kT$. Moreover, higher temperatures yield larger intensities for all frequencies, so if $T_2 > T_1$, then $B_\nu(T_2) > B_\nu(T_1)$ for all ν.

The integral over frequencies of the blackbody spectral radiance is proportional to T^4

$$\int_0^\infty B_\nu(T)d\nu = \frac{\sigma_{SB}}{\pi}T^4 \tag{3.2}$$

where σ_{SB} is the Stefan-Boltzmann constant[2].

The spectral energy density is given by

$$u_\nu(T) = \frac{4\,\pi}{\mathrm{c}}\,B_\nu\,(T)\,. \tag{3.3}$$

As we will see later in the Chapter, the emission from the torus and the optical/ultraviolet Big Blue Bump (BBB) external photon fields in our multi-component model is assumed to radiate as black bodies [Section 3.3].

3.1.3 The Compton effect

The inelastic scattering[3] of a High Energy (HE) photon by a stationary free charged particle (usually an electron) when $\hbar\omega \gg m_e c^2$ is known as *Compton Scattering*. The incident photon transfers part of its energy to the charged particle, resulting in a lower energy photon and a higher energy particle.

[2] Stefan-Boltzmann constant: $\sigma_{SB} = (5.670\,367 \pm 0.000\,013) \times 10^{-8}\,\mathrm{W\,m^{-2}\,K^{-4}}$ (SI) $\approx 5.6704 \times 10^{-5}\,\mathrm{erg\,cm^{-2}\,s^{-1}\,K^{-4}}$ (CGS).

[3] In inelastic scattering processes, the wavelength of the scattered photon is different from that of the incident photon.

The energies of the initial and the scattered photon are related by the following expression:

$$\lambda_f - \lambda_i = \lambda_c(1 - \cos\theta) \tag{3.4}$$

where λ_f is the wavelength of the scattered photon, λ_i the wavelength of the incident photon, $\lambda_c = h / m_e c$ is the *Compton wavelength* and θ the scattering angle (see Figure 3.2).

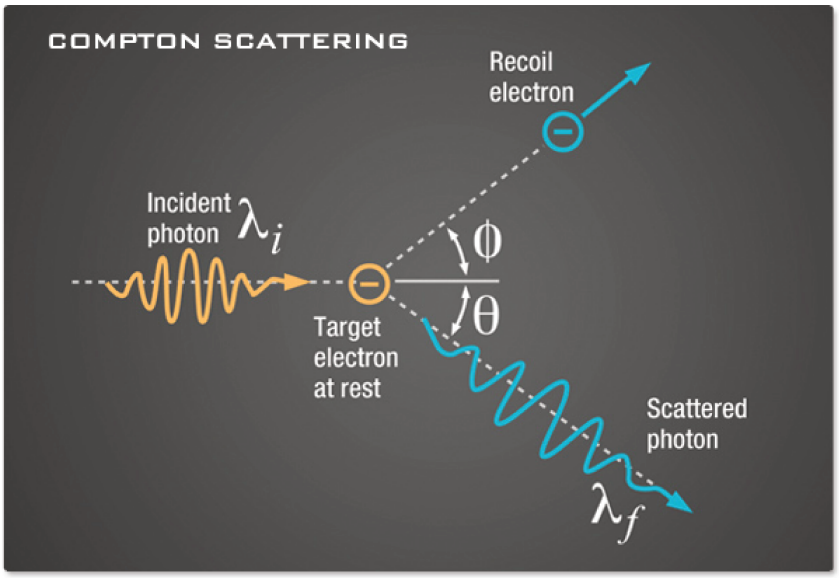

Figure 3.2 Electron scattering via Compton effect.

3.1.4 The Inverse Compton effect

The *Inverse Compton scattering* (IC) effect is the scattering of a Low Energy (LE) photon by a HE charged particle (e.g. a relativistic electron, see Figure 3.3). As a result of IC processes, LE photons can be up-scattered to HE or Very High Energy (VHE) by the electrons. Indeed, in astrophysical IC processes, the energy gained by the up-scattered photon can be much larger than the energy lost by the HE photon. As an example, the comptonization of soft photons (optical/UV) from the accretion disc by a corona of hot electrons is thought to be at the origin of the observed ubiquitous X-ray emission in HE (see Section 3.3 for more details).

As an estimate of the energy that a photon can gain via IC processes, if we consider a photon of initial energy ϵ_i, the average energy of the scattered photon ϵ_f in the Thomson regime ($\epsilon_i \ll m_e\,\mathrm{c}^2$) is

$$\epsilon_f \simeq \gamma^2 \epsilon_i \tag{3.5}$$

The fact that the energy of the photons scattered by ultra-relativistic electrons is $\sim \gamma^2$ times the energy of the initial LE photon is very important in high energy astrophysics. Electrons with Lorentz factors $\gamma \sim$ 100-1000 can be found in different astronomical sources (i.e. jets of AGN), so LE photons can be scattered up to very much higher energies.

On the other hand, in the Klein-Nishina regime where $\epsilon_i \gg m_e\,\mathrm{c}^2$, the average energy of the scattered photon is

$$\epsilon_f \simeq \gamma m_e \mathrm{c}^2 \tag{3.6}$$

so the boosting will not be as powerful as in the Thomson regime.

Let us consider a relativistic electron of $\gamma \sim 1000$ in the Thomson regime. According to Equation 3.5, the scattered radiation energy is roughly 10^6 times the energy of the incoming LE photon. Therefore, an optical photon with $\nu_0 = 10^{14}$ Hz will become gamma-rays with frequency $\nu = 10^{20}$ Hz (around 1.6 MeV), so the inverse Compton scattering is a very effective method to create HE photons.

In the multi-component model that will be presented later, inverse Compton scattering of LE seed photons from the external photon fields such as the torus or the accretion disc processes plays a major role for the description of the HE tail of the spectrum.

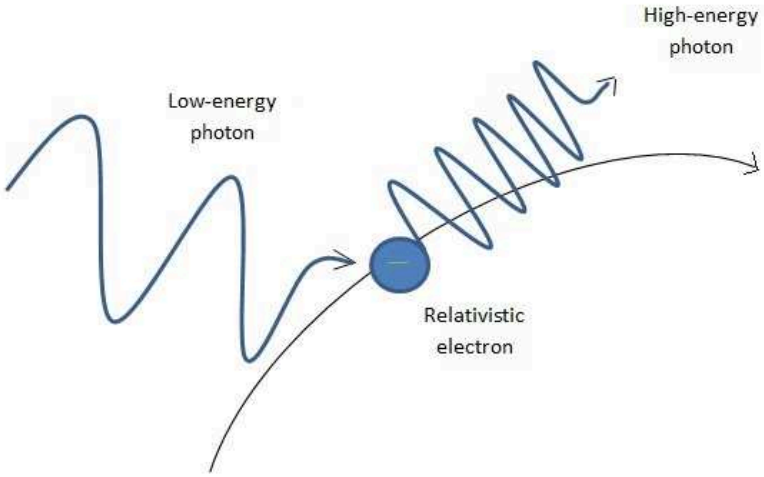

Figure 3.3 Illustration of IC scattering. The interaction between a relativistic electron an a LE photon originates aHEphoton due to the energy transference from the electron to the photon.

3.1.5 The synchrotron self-Compton process

A relativistic electron population within a magnetized region will produce synchrotron radiation as illustrated in Section 3.1.1, which will eventually fill the magnetized region with synchrotron photons. Shall these synchrotron photons interact with the original electron population via IC, a radiation process known as the Synchrotron Self-Compton process (SSC) will take place: the original electron population first creates synchrotron radiation, and then up-scatters it towards higher energies.

SSC processes are thought to be at the origin of the high energy bump of BL Lac emission. In this work, we have applied the simple SSC model that is presented in Section 3.2 to a HBL type source (see Chapter 5). Moreover, the multi-component model was developed from a simple SSC model, so it also features this radiative component that indeed is sometimes quite predominant for some of the NLS1 sources that we model (see Chapter 6).

3.2 One-zone leptonic Synchrotron Self-Compton models

In this section, we present the simplest model for TeV blazar broad-band modeling, the so-called one-zone stationary homogeneous SSC model introduced in Section 3.1.5, and the constraints that can be set upon its parameters though a number of observables. This simple model is afterwards applied to the source 1ES 2322−409 in Chapter 5.

The one-zone stationary homogeneous SSC model was developed soon after the discovery of X-ray and gamma-ray emission from quasars, aiming at establishing a theoretical framework for the observed radiative processes (see e.g. Gould [Gou79], Coppi and Blandford [CB90]). This scenario considers that radiation is produced in a single zone of the relativistic jet. Note that in this scenario, the relativistic jet is considered to be of leptonic origin, i.e. composed by electrons or pairs. The

single emission zone filled with relativistic electrons is approximated as a sphere of radius R_{src}, a.k.a. the blob, with a tangled magnetic field B. The blob moves through the relativistic jet at a small angle θ towards the observer. Accordingly, the observed radiation will be strongly beamed and affected by relativistic effects (see Section 1.5.1).

The interaction between the relativistic electrons and the magnetic field results in the electron population emitting synchrotron radiation [Section 3.1.1] in the frequency range from radio to X-rays, forming the first, low-energy bump observed in the SED of BL Lacs [Section 1.4.2]. The up-scattering of those same synchrotron photons to high and very high energies (up to gamma-ray energies, from 100 GeV to 1 TeV) by means of IC processes [Section 3.1.4] accounts for the second, high energy bump of the SED. A detailed description of the model can be found in Katarzyński et al. [Kat+01].

In this SSC scenario, ultra-relativistic particles are injected and can cool freely (via both synchrotron and inverse Compton scattering process) within the plasma blob. However, if the acceleration zone can be dissociated from the radiative one, two different electron energy distributions need to be considered: the injected distribution and the cooled distribution. The former is the result of the acceleration mechanisms, while the latter results from the cooling of particles (see e.g. Saugé and Henri [SH06]). Although the majority (including the present work) of simple, one-zone leptonic SSC models are steady-state, i.e. the observed emission is considered to stem from a stationary part of the distribution, rapidly varying emission can only be fully comprehended by means of time-dependent modeling (see e.g. Kirk et al. [Kir+98], Chiaberge and Ghisellini [CG99], Boutelier et al. [Bou+08]).

The observed stationary blazar spectral shape requires a relativistic electron population that steepens with energy, which can be represented by a Broken Power-Law (BPL) spectrum with a sharp cut-off at high energies

$$N(\gamma) = \begin{cases} K\gamma^{-n1} & if\ \gamma < \gamma_b \\ K\gamma_b^{n2-n1}\gamma^{-n2} & if\ \gamma > \gamma_b \end{cases} \tag{3.7}$$

provided that $n_1 < 3$ and $n_2 > 3$ (Katarzyński et al. [Kat+01]). Note that other models describing the electron distribution can also be considered within the models, see e.g. Massaro et al. [Mas+04].

These approximations enable the model to be completely described with just 7 parameters, i.e. the magnetic field intensity B (in Gauss), the radius of the emitting region R (in cm), the Doppler factor δ, the BPL indexes n_1 and n_2, the electron break energy γ_b[4] and the normalization factor K (in cm^{-3}) at $\gamma = 1$. The parameters are summarized in Table 3.1.

Parameter	Value
Bulk Doppler factor	δ
Magnetic field intensity	B
Radius of emitting region	R_{src}
Normalization at $\gamma = 1$	K
BPL index before break	n_1
BPL index after break	n_2
Minimum energy Lorentz factor	γ_{min}
Break energy Lorentz factor	γ_b
Maximum energy Lorentz factor	γ_{max}

Table 3.1 SSC model parameters. See text for more details.

On the other hand, the broad-band SED provides us with 6 observable quantities that are then used to determine the model parameters above mentioned, namely the indexes α_1 and α_2, the frequencies of the synchrotron and IC peaks ν_s and ν_c, and the peak luminosities $L_s(\nu_s)$ and $L_c(\nu_c)$. This leaves us with 6 observables for a 7 free parameter model. The remaining parameter can be constrained via the minimum variability time scale t_{var}, defined as

$$R \leq c\delta(1+z)^{-1}t_{var}\,. \tag{3.8}$$

In order to relate observables and parameters, one needs to know that the dominant synchrotron power in the SSC scenario is emitted by electrons with Lorentz factors γ_b corresponding to the break energy. Likewise, photons at an observed synchrotron frequency ν_s (where the transformation from the observer's frame to the blob's frame

[4]The peak synchrotron power is emitted by electrons with break energy $E_b = \gamma_b mc^2$.

is given by $\nu_s = \delta\,\nu'_s$) dominate the energy density of the target photons, while the IC power in the Thomson limit will be dominated by photons at the frequency

$$\nu_c = \frac{4}{3}\gamma_b^2 \nu'_s \delta \tag{3.9}$$

produced in the scattering between electrons at the break (γ_b) and photons with frequency ν'_s (see the approach by Tavecchio et al. [Tav+98]). That is, electrons of power γ_b will interact with the dominant target photon population at ν_s.

In addition, we know that the expression of the average synchrotron frequency emitted by an electron of Lorentz factor γ_b is

$$\nu_s = 3.7 \times 10^6 \gamma_b^2 B \frac{\delta}{1+z}. \tag{3.10}$$

Isolating γ_b from (3.9) and substituting it into (3.10), one gets

$$B = \frac{1}{2.8 \times 10^6} \frac{1+z}{\delta} \frac{\nu_s^2}{\nu_c} \tag{3.11}$$

which shows that, for fixed ν_s and ν_c, the magnetic field B and Doppler factor δ are inversely proportional.

Another relation to farther constraint the model parameters from observables is the relation between the ratio of the total luminosity of the synchrotron peak L_s to the total luminosity of the IC peak L_c and the ratio of the radiation energy density and the magnetic field energy density inside the source,

$$\frac{L_c}{L_s} = \frac{U'_{sync}}{U'_B}. \tag{3.12}$$

Considering that the total luminosity L_i (where $i = s,\ c$) can be expressed through the peak luminosity $L_i(\nu_i)$ so that $L_{s,c} = f(\alpha_1, \alpha_2)\nu_{s,c}L_{s,c}(\nu_{s,c})$ where

$$f(\alpha_1, \alpha_2) = \frac{1}{1-\alpha_1} + \frac{1}{\alpha_2 - 1} \tag{3.13}$$

and that the expression for the radiation energy density is

$$U'_{syn} = \frac{L_s}{4\pi R^2 c \delta^4}, \tag{3.14}$$

(3.11) can be rewritten as

$$\frac{L_c}{L_s} = \frac{2\nu_s L_s(\nu_s) f(\alpha_1, \alpha_2)}{R^2 c \delta^4 B^2}. \tag{3.15}$$

Finally, if we express the source size as a factor of the variability time scale given by (3.8), the second relation between the magnetic field intensity B and the Doppler factor δ is obtained:

$$B \geq \frac{1+z}{\delta^3} \left[\frac{2(\nu_s L_s(\nu_s))^2 f(\alpha_1, \alpha_2)}{c^3 t_{var} \nu_c L_c(\nu_c)} \right]^{1/2}. \tag{3.16}$$

The constraints set by the variability time scale, peak frequencies and peak luminosities can be graphically represented to estimate what is the permitted magnetic field and Doppler factor parameter space, as will be illustrated in Chapter 5 for the HBL 1ES 2322−409, and focus the search for valid solutions to a narrower range. However, one-zone synchrotron-self-Compton model solutions are inevitably degenerate, since the number of free parameters is higher than the number of observables. It is common practice in blazar modeling to choose a single set of values for the model parameters that provide a good description of the observed data without exploring the whole available parameter space.

Nevertheless, there are numerical algorithms that enable narrowing down the range of possible solutions. For example, Cerruti et al. [Cer+13a] developed a numerical algorithm that allows them to find the whole set of solutions from the information that can be extracted from the detection of a BL Lac object at GeV and TeV bands. Results from the application of the Cerruti et al. [Cer+13a] algorithm to 1ES 2322−409 will be presented in Chapter 5.

Regarding multi-wavelength data, note that the SSC homogeneous models are self-absorbed at radio frequencies (see Section 3.1.1), and therefore they cannot explain the radio emission from the source. Such radio emission is ascribed to the extended component of the jet (see Figure 3.4, Figure 3.5 and Figure 3.6), while the radiative components of the simple one-zone SSC model that has been described above are

linked to the compact component of the jet. Again, this is one of the simplest models we can apply to blazar modeling, which does not necessarily mean that it is a wrong or inaccurate description of the object being fit, it just means that contributions from other components than the blob within the jet might sometimes be required.

At the opposite end of the broad-band spectrum, the interaction between very energetic gamma-rays and the Extragalactic Background Light (EBL) causes the VHE spectra of jetted AGN to be absorbed by the time it arrives to ground-based detectors, and hence needs to be accounted for to determine the intrinsic spectrum when modeling the SED of a TeV blazar.

In fact, the Universe becomes opaque for gamma-rays with energies above a few hundred GeV, due to the photon-photon interactions between the gamma-rays and the light from all sources through cosmic history. The low-energy and high-energy photon interaction generates pairs and lower energy photons. Thus, the intrinsic spectrum of a gamma-ray source is modified by EBL absorption because the optical depth depends on energy, $\tau_{\gamma\gamma}(E, z)$. Thus, the observed spectrum becomes

$$F_{obs} = F_{int} \exp[-\tau_{\gamma\gamma}(E, z)]. \tag{3.17}$$

Although the EBL absorption might seem a drawback, the spectra detected by ground-based Cherenkov telescopes [Chapter 2] can be used to set upper limits on the EBL. For TeV SED modeling, a given EBL spectrum is assumed and the absorbed spectrum is compared to the one observed by imaging atmospheric Cherenkov telescopes. For the modeling of 1ES 2322−409 carried out in the present work [Chapter 5], we considered the EBL spectrum from Franceschini et al. [Fra+08]. For recent HESS collaboration results and estimates of the EBL determination, see H. E. S. S. Collaboration et al. [H. +17e].

Figure 3.4, Figure 3.5 and Figure 3.6 show examples that illustrate the validity of one-zone leptonic SSC models especially for HBL type sources. The effect of the EBL absorption is shown at TeV energies, where the solid lines represent the EBL-absorbed model, while the dashed lines correspond to the intrinsic model without correcting for absorption.

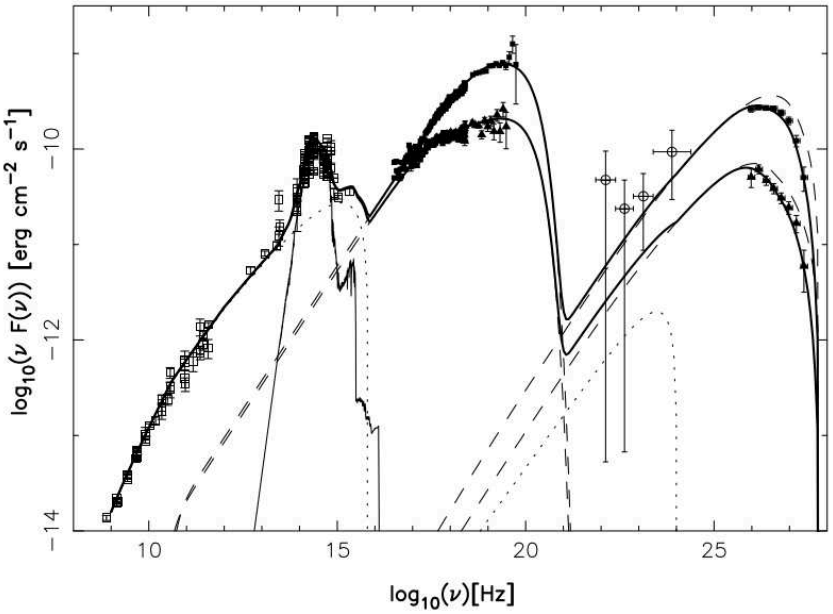

Figure 3.4 SSC models for Mrk 501 from Katarzyński et al. [Kat+01], where two different states of the source were modeled. The different lines correspond to the different components of the model. The bumps at intermediate and high energies are ascribed to synchrotron and SSC emission. The extended part of the jet contributes to the SED at radio frequencies At optical wavelengths, the contribution of the host galaxy can be seen.

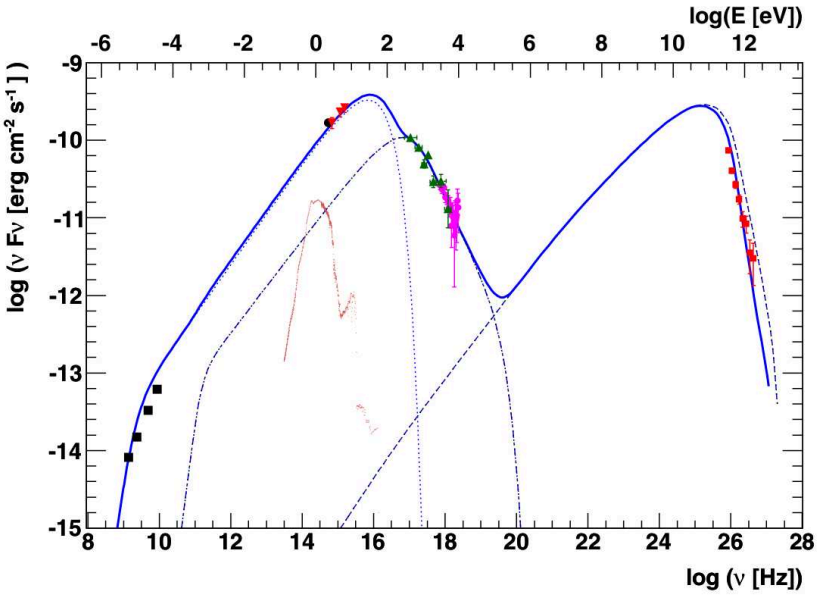

Figure 3.5 SSC models for PKS 2155-304 from H.E.S.S. Collaboration et al. [H.E+12]. The different lines represent the different components of the model. The X-ray and gamma-ray bumps are interpreted respectively as the synchrotron and SSC emission from a single population of relativistic electrons within the blob, while the extended jet contributes to the SED at radio frequencies.

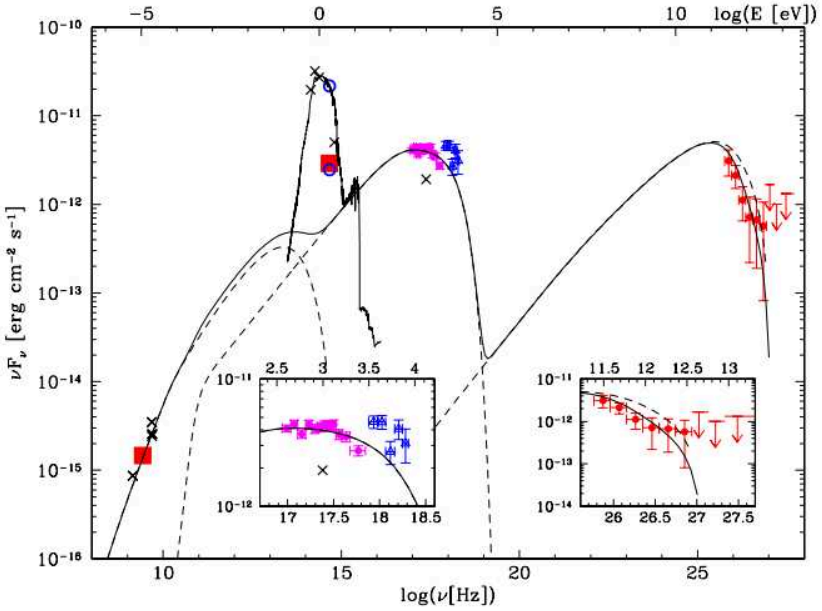

Figure 3.6 SSC models for RGB J0152+017 from Aharonian et al. [Aha+08]. Different lines represent different components of the model. The contribution of the dominating host galaxy is shown at optical wavelengths. Radio data were assumed to originate within the extended region, described by a separate synchrotron model for the extended jet.

3.3 External components for AGN modelisation

Simple SSC modeling scenarios have proved their worth to model the emission mechanisms of the HBL blazar type of AGN. However, this is not the case if we consider other types of AGN such as gamma-loud NLS1 galaxies whose double-bumped SED also presents emission features that require additional external components to be described.

In the present work, we have considered the contribution from several external photon fields at different wavelengths, namely the infrared emission from a torus, the optical/ultraviolet emission from an accretion disc and the X-ray emission from a hot corona. In addition, the corresponding IC emission components, namely IC-scattered torus and disc photons and Broad Line Region (BLR) photons contribute to the overall high energy emission at different levels, as we will show in Chapter 6. Figure 3.7 illustrates the edge-on view of the AGN and its external fields, while Figure 3.8 illustrates the distances to each of the external components. Figure 3.9 shows the different direct and IC components that we consider in our numerical model.

Figure 3.7 Schematic view of the external photon fields considered throughout this work.

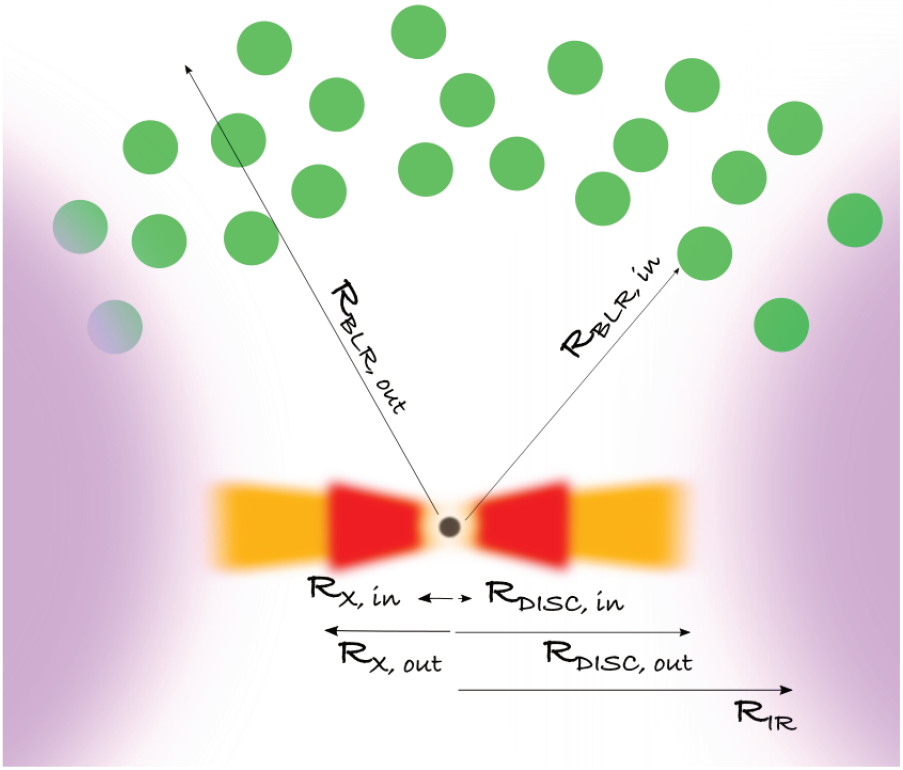

Figure 3.8 Schematic view of the distances of the external photon fields considered throughout this work.

3.3.1 Formalism for Compton scattering of different photon fields

In this Section, we present the details of the procedure that we followed in order to calculate the spectral distribution of the different external photon fields that are featured in the multi-component numerical model we have developed. The formalism is based on Dermer and Menon [DM09].

To calculate the spectral flux νF_{ν}^{IC} of the IC scattered high-energy photons, we first transform the electron distribution to the stationary frame (i.e. the source frame), and then the photon field is Compton-scattered.

The Compton spectral luminosity $\epsilon_s L_C(\epsilon_s, \Omega_s)$ of a one-zone system can be defined by the Compton emissivity $j_C(\epsilon_s, \Omega_s)$[5]

$$\epsilon_s \, L(\epsilon_s, \, \Omega_s) \, = \, V_B \, \epsilon_s \, j_C(\epsilon_s, \, \Omega_s) \tag{3.18}$$

where ϵ_s and Ω_s are the energy in units of $m_e \, \mathrm{c}^2$ and the solid angle in the source frame respectively, and V_B is the volume of the blob within the jet

$$V_B = \frac{4}{3} \pi R_{src}^3 \, . \tag{3.19}$$

Considering the head-on approximation of the Compton kernel[6], the Compton emissivity can be expressed as

$$\epsilon_s \, j_C(\epsilon_s) \, = \, \frac{3}{4} \, c \, \sigma_T \, \epsilon_s^2 \int_{\epsilon_s}^{\infty} \mathrm{d}\epsilon \frac{u(\epsilon)}{\epsilon^2} \int_{\gamma_{min}}^{\gamma_{max}} \mathrm{d}\gamma \, \frac{n_e(\gamma)}{\gamma^2} \, \mathrm{F}_C(\mathrm{q}, \Gamma_e) \tag{3.20}$$

where $u(\epsilon)$ is the energy density of the photon field at the energy ϵ, and F_C is given by

$$\mathrm{F}_C(\mathrm{q}, \Gamma_e) \, = \, 2 \, \mathrm{q} \ln \mathrm{q} + (1 \, + 2 \, \mathrm{q}) \, (1 \, - \, \mathrm{q}) \, + \, \frac{1}{2} \frac{(\Gamma_e \, \mathrm{q})^2}{1 \, + \, \Gamma_e \, \mathrm{q}} (1 \, - \, \mathrm{q}) \tag{3.21}$$

[5] **Note on notation:** quantities marked with a s refer to the scattered quantities, primed quantities refer to the comoving frame and unmarked ones to the observer's frame.

[6] In the "head-on" approximation, $\epsilon \ll 1 \ll \gamma$, and photons are scattered in approximately the same direction as the incident electrons (see e.g. Reynolds [Rey82], Dermer and Schlickeiser [DS93]

and

$$\mathrm{q} \equiv \frac{\epsilon_s/\gamma}{\Gamma_e\,(1\,-\,\epsilon_s\,\gamma)}, \qquad \Gamma_e \equiv 4\gamma\,\epsilon\,. \tag{3.22}$$

Substituting Equation 3.19 and Equation 3.20 into Equation 3.18, the Compton spectral luminosity can be expressed as

$$\epsilon_s\,L(\epsilon_s,\,\Omega_s)\;=\;\pi\,R_{src}^3\,c\,\sigma_T\,\epsilon_s^2\int_{\epsilon_s}^{\infty}\mathrm{d}\epsilon\frac{u(\epsilon)}{\epsilon^2}\int_{\gamma_{min}}^{\gamma_{max}}\mathrm{d}\gamma\,\frac{n_e(\gamma)}{\gamma^2}\,\mathrm{F}_C(\mathrm{q},\Gamma_e). \tag{3.23}$$

The νF_ν spectrum is defined as

$$\nu F_\nu = f_\epsilon = \frac{\epsilon_s L(\epsilon_s,\Omega_s)}{4\pi d_L^2} \tag{3.24}$$

where d_L is the luminosity distance of the source.

Plugging the Compton spectral luminosity Equation 3.23 into Equation 3.24, considering the full Compton cross section and the energy field of the source, $\epsilon \rightarrow \epsilon^*$ and also that the transformed stationary-frame electron distribution can be expressed in terms of the particle distribution in the comoving frame

$$N(\gamma,\,\Omega)\;=\;\delta_D^3\,N(\gamma',\,\Omega') \tag{3.25}$$

the final expression for the Compton scattered component from isotropically distributed electrons in the comoving frame of a uniform blob is

$$\nu F_\nu^{EC} = \frac{R_{src}^3 c\sigma_T\epsilon_s^2\delta_D^3}{4d_L^2}\int_{\epsilon_s}^{\infty}d\epsilon\frac{u(\epsilon)}{\epsilon^2}\int_{\gamma_{min}}^{\gamma_{max}}d\gamma\frac{n_e'(\gamma')}{\gamma^2}F_C(q,\Gamma_e) \tag{3.26}$$

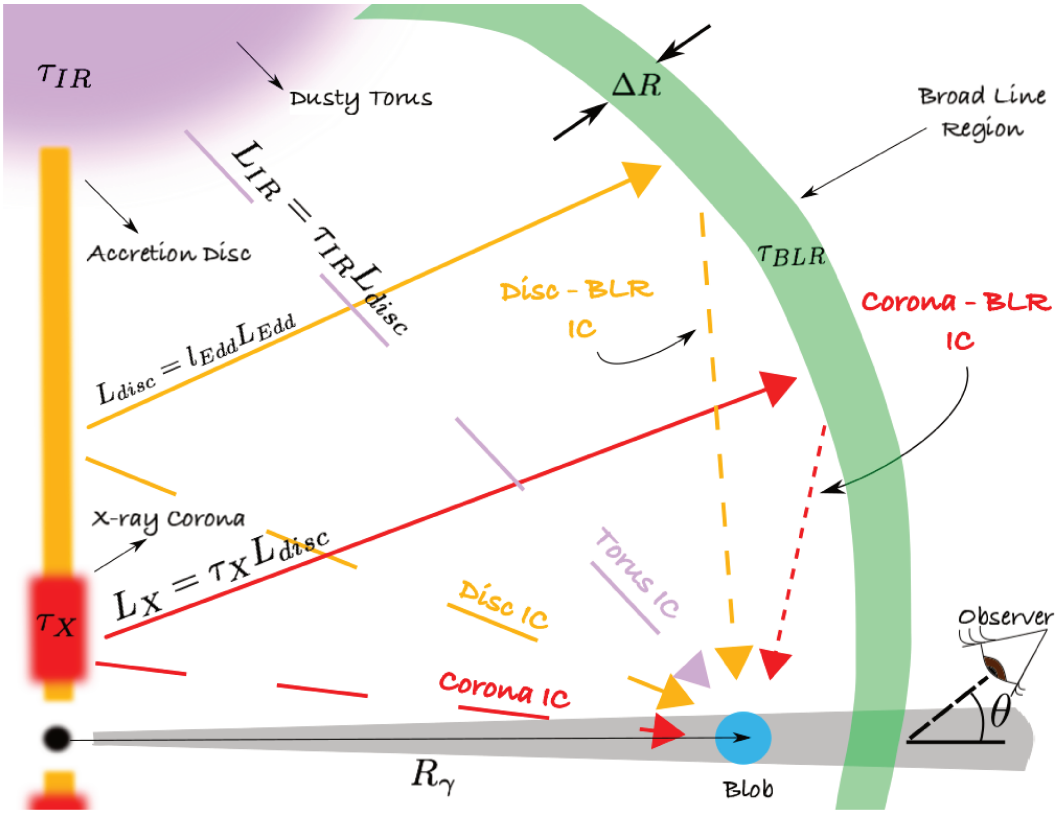

Figure 3.9 Schematic view of all external photon fields and some of the radiation fields that we consider in the model. Note that direct radiation from the torus, disc (i.e. BBB)and corona are not depicted. Long dashed lines represent the torus, BBB and corona photons that interact with the blob through IC processes, while the small dashed lines represent the disc and corona photons (lines) scattered by the BLR that interact with the blob.

3.3.2 The torus

As introduced in Section 1.3 and Section 1.2.4, the high dependency on the viewing angle of the AGN unification model requires the presence of an obscuring body commonly pictured as a dusty torus that will radiate in the infrared regime due to accretion disc photons heating the dust particles within.

Direct emission

Here, we consider the radiation from the torus as coming from a punctual source of radius R at a luminosity distance d_L. In our approach, the luminosity of the torus is considered to be isotropic and a fraction of the total nuclear luminosity given by the dust coverage of the torus τ_{IR} so that

$$L_{IR} = \tau_{IR}\, L_D \tag{3.27}$$

where L_D is the total luminosity of the accretion disc. The spectral luminosity of the torus can be approximated by a thermal black body distribution normalized to the torus luminosity L_{IR}

$$\epsilon L_{IR}\,(\epsilon) = \frac{15\, L_{IR}}{\pi^4} \frac{(\epsilon/\Theta_{IR})^4}{\exp\left[\epsilon/\Theta\right] - 1} \tag{3.28}$$

in units of $\mathrm{erg\,s^{-1}}$, where Θ_{IR} is the thermal energy normalized to $m_e\,\mathrm{c}^2$ units

$$\Theta_{IR} = \frac{k_b\, T_{IR}}{m_e\, c^2}. \tag{3.29}$$

and T_{IR} is the peak temperature of the distribution (see e.g. Dermer and Menon [DM09]). The $15\,/\,\pi^4$ factor comes from the integration of the black body intensity over all frequencies.

Considering the spectral luminosity given by equation (3.28), the $\boldsymbol{\nu\, F_\nu}$ spectrum for the dusty torus in the observer's frame is

$$\nu F_\nu^{IR} = \frac{15\, L_{IR}}{4\,\pi^5\, d_L^2} \frac{(\epsilon/\Theta)^4}{\exp\left[\epsilon/\Theta_{IR}\right] - 1} \tag{3.30}$$

Torus-IC emission

To describe the External Inverse Compton (EIC) processes where relativistic electrons from the blob up-scatter infrared dusty torus photons, we consider that the energy density of the torus $u_{IR}(\epsilon)$ from the general EIC formula (Equation 3.26) can be defined as

$$u_{IR}\left(\epsilon\right) \sim u_{IR,\,0} \frac{\epsilon^3}{\exp\left[\dfrac{\epsilon}{\Theta_{IR}}\right] - 1}. \tag{3.31}$$

where Θ is given by (3.29). Furthermore, in this scenario

$$u_{IR,0} = \frac{15\, L_{IR}}{4\,\pi^5\, c \Theta_{IR}^4\, R_{IR}^2}. \tag{3.32}$$

This leads to the following black body/thermal energy density for the dusty torus

$$u_{IR}(\epsilon) \sim \frac{15\, L_{IR}}{\pi^2\, R_{IR}^2\, \mathrm{c}\, \Theta_{IR}^4} \frac{\epsilon^3}{\exp\left[\dfrac{\epsilon}{\Theta_{IR}}\right] - 1}, \tag{3.33}$$

The radius of the torus R_{IR} can be estimated as the sublimation radius (e.g. Sikora et al. [Sik+09]), and is proportional to the square root of the disc luminosity in units of 10^{45},

$$R_{IR} = 3.5 \times 10^{18} \sqrt{\frac{L_D}{10^{45}}} \left(\frac{T_{IR}}{10^3}\right)^{-2.6}. \tag{3.34}$$

Plugging Equation 3.33 into the integral over energies in Equation 3.26, one gets the spectral energy density of the IC on the dusty torus photons.

3.3.3 The accretion flow

Due to its angular momentum, the accreting matter falling into the gravitational potential of the central BH will start orbiting the engine and eventually create an accretion disc [Section 1.2.2].

In our model, we approximate the ultraviolet excess or BBB as a multi-temperature black body, and the X-ray spectrum as a power-law hot corona. We would like to remark that the description of the accretion disc that we consider could be somewhat simplistic for sources where the soft-excess is visible and would require more complex models (see e.g. Done et al. [Don+12], Landt et al. [Lan+17]). This is not necessarily the case for the sources that we consider in this work, though.

The type of disc (BBB) we consider is the optically thick, geometrically thin accretion disc first considered by Shakura and Sunyaev [SS73]. In the AGN unification paradigm, a corona made up of thermally comptonized hot electrons is located above and below the accretion disc, and it is thought to be at the origin of the power-law-like X-ray spectra observed in many sources (as introduced in Section 1.2.2). The treatment of the corona in the model is fairly similar to the one given to the accretion in Section 3.3.3, except for the power-law energy distribution versus multi-temperature black body.

Direct emission from the disc (BBB)

The radiant surface-energy flux of an optically thick, geometrically thin Shakura-Sunyaev disc is given by

$$\frac{d\epsilon}{dAdt} = \frac{3GM\dot{m}}{8\pi R^3}\varphi(R) \tag{3.35}$$

where $\varphi(R) = 1 - \beta_i(R_i/R)^{1/2}$. Here, β_i is the fraction of angular momentum captured by the black hole at the innermost stable orbit R_{ISCO}, with values $0 \leq \beta_i \leq 1$. The disc radiant luminosity can be obtained by integrating Equation 3.35 over all radii (see Eq. 6.136 in Dermer and Menon [DM09]) and takes the form

$$L_{Disc} = \frac{3\,G\,M\,\dot{m}}{2\,R_i}\left(1 - \frac{2\,\beta_i}{3}\right). \tag{3.36}$$

If the matter does not have time to radiate a significant fraction of its energy, one would have $\beta \simeq 1$. In that case, the efficiency is $\eta_{Edd} = \frac{1}{12}$. Throughout this work, we consider these standard values for our model.

In order to obtain the spectral shape of a multi-temperature accretion disc, we divide the disc (which we assume to extend from an inner radius of $3R_S$ to an outer radius of $500\,R_S$) into circular slices, so that we can calculate the contribution of every single one of such annulus of inner radius r_i and outer radius r_o to the overall spectral distribution of the source. Accordingly, from Equation 3.36, we can define the black body temperature expression for each annulus the following way

$$T_D = \sqrt[4]{\frac{3\,G\,M_{BH}\,\dot{m}\left(1 - \beta_i\sqrt{\frac{r_i}{r_c}}\right)}{8\,\pi\,\sigma_{SB}\,r_c^3}}, \tag{3.37}$$

where $r_c = (r_i + r_o/2)$. Considering that the disc luminosity can be expressed in terms of the Eddington luminosity (Equation 1.10) as follows

$$L_{Disc} = l_{Edd}L_{Edd}, \tag{3.38}$$

the mass accretion rate $\dot{m}$ can be defined as

$$\dot{m} = 1.4 \times 10^{26} \, \frac{l_{Edd} \, M_{BH}}{\eta_{Edd}} \, . \tag{3.39}$$

The specific energy density per solid angle of each annulus is then

$$u\left(\nu, \Omega\right) = \frac{2\,h}{\mathrm{c}^3} \frac{\nu^3}{\exp\left[\dfrac{h\,\nu}{k_B\,T_D}\right] - 1.0} \, . \tag{3.40}$$

Considering that the relation between the specific energy density per solid angle and the specific intensity per solid angle is $I(\nu, \Omega) = \mathrm{c}\, u(\nu, \Omega)$, if we integrate over all angles, keeping in mind that in our case we only consider a semi-sphere so the integral over the solid angle is $\int \mathrm{d}\Omega = \pi$, the specific intensity becomes

$$I\left(\nu\right) = \frac{2\,\pi\,h}{\mathrm{c}^2} \frac{\nu^3}{\exp\left[\dfrac{h\,\nu}{k_B\,T_D}\right] - 1.0} \, , \tag{3.41}$$

the specific luminosity of an annulus between the radii r_i and r_o for all solid angles is

$$L_\nu(\nu) = \pi\left(r_o^2 - r_i^2\right) \frac{2\,\pi\,h}{\mathrm{c}^2} \frac{\nu^3}{\exp\left[\dfrac{h\,\nu}{k_B\,T_D}\right] - 1.0} . \tag{3.42}$$

Then, we integrate over frequencies to get the total disc luminosity. Last, we consider the disc as an isotropic point source, and we transform the luminosity into the flux density on the observer's frame via Equation 3.24.

Disc-IC emission

In our framework, we also consider that the multi-temperature disc (BBB) photons interact with the relativistic blob, originating another IC radiative component. Like-

wise for the direct emission from the disc, here we slice the accretion disc in rings, and we calculate the intensity for each of the rings, followed by the corresponding IC calculations that yield the IC spectrum.

The fact that each of the annuli is viewed under different angles by the relativistic blob (i.e. the jet emission) means that each of the rings receives a different amount of Doppler deboosting b_D which for the disc takes the form of

$$b_D = \Gamma(1 - \beta\,\mu_D) \tag{3.43}$$

where $\mu_D = \cos\theta_D$ is the angle of each annulus with respect to the jet axis (see e.g. Ghisellini and Tavecchio [GT09]). For a blob located at a distance R_γ from the base of the jet, and a disc annulus at a distance r from the blob and r_c from the base of the jet in the plane of the disc, the μ_D magnitude takes the form of

$$\mu_D = \cos\theta_D = \frac{R_\gamma}{r}. \tag{3.44}$$

Here, r has been calculated applying simple trigonometry, so $r = \sqrt{R_\gamma^2 + r_c^2}$.

The intensities in the comoving frame of the blob transform as $I'(\nu', \Omega') = b_D^3\, I(\nu, \Omega)$, and the transformation for the solid angle is

$$\mathrm{d}\Omega' = \frac{\mathrm{d}\Omega}{b_D^2} \quad \xrightarrow{\mathrm{d}\Omega = 2\,\pi\,\mathrm{d}\mu} \quad \mathrm{d}\Omega' = 2\,\pi\,\frac{\mathrm{d}\mu}{b_D^2}\,. \tag{3.45}$$

Translating all these considerations into the expression of the spectral intensity in the blob's frame, one gets

$$I'_D(\nu') = \frac{4\,\pi\,b_D\,h}{\mathrm{c}^2}\,\frac{\nu^3}{\exp\left[\dfrac{h\,\nu}{k_B\,T_D}\right] - 1.0}\,\mathrm{d}\cos\theta_D\,. \tag{3.46}$$

Once we have the complete expression for the spectral intensity in the blob's frame, we can proceed to the calculation of the IC processes, and afterwards transform the multi-temperature accretion disc IC spectrum into the observer's frame.

Disc BLR-IC emission

In addition to the EIC emission from accretion disc photons, in the model we also consider external processes involving the ionization of the BLR of the AGN by accretion disc photons (see Section 1.2.3). For this purpose, the target photon field is considered to involve different emission lines (i.e. Lyα, CIV, MgII, CIII, NV, OVI and the broad feature, see Table 3.2), whose contribution is calculated following the approach presented in Cerruti et al. [Cer+13b].

Different from what we do for the dusty torus in Section 3.3.2 where we consider the temperature of the black body to calculate the energy distribution of the torus, in the case of the BLR the strength of each line is fixed considering the ratio-estimation featured in Telfer [Tel01]. These line-strengths are expressed as the ratio of the line flux and the Lyα line flux, which is the most dominant one. For the sake of accuracy, line-widths from other sources, e.g. Francis et al. [Fra+91], Vanden Berk et al. [Van+01], were compared to the ratios provided by Telfer [Tel01], finding them all compatible.

Line	Energy (eV)	Flux
Lyα	10.20	100.0
CIV	8.0	52.0
MgII	4.43	22.3
CIII	6.53	13.2
Broad Feature	7.75	30.2
NV	10.0	22.0
OVI	12.04	19.1

Table 3.2 Emission lines considered for the BLR-IC modeling, along with their energies and intensities. Line-intensities are expressed as a ratio of the line flux and the Lyα line flux, which is the strongest one.

The model assumes a spherically symmetric BLR of inner radius R_{in} and outer radius $R_{out} \sim 3R_{in}$, where R_{in} is derived from reverberation mapping constraints (Equation 1.13). The electron number density of the BLR follows a power-law radial density distribution with an index ζ

$$n_{\rm BLR}(\zeta, R) = n_0 \left(\frac{R}{R_{in}}\right)^{\zeta} . \tag{3.47}$$

We choose to fix the spectral index to $\zeta = -2$, which means that most of the material of the BLR clouds is close to its inner radius, so most of the ionization of the BLRs happens at $R \simeq R_{in}$, and the luminosity of the radiation will be fainter towards the outer edge of the BLR.

The Thomson depth of the BLR, $\tau_{\rm BLR}$, is defined as the integral of the electron number density within the BLR times the Thomson cross-section

$$\tau_{\rm BLR} = \sigma_T \int_{R_{in}}^{R_{out}} dR\, n_{\rm BLR}(R) \tag{3.48}$$

which if $R_{in} \ll R_{out}$ and in the $\zeta < -1$ regime we choose takes the form

$$\tau_{\rm BLR} \simeq \sigma_T n_0 \frac{-R_{in}}{\zeta + 1}, \quad \zeta < -1\,. \tag{3.49}$$

Since we fix the ζ index and the inner radius of the BLR, the Thomson depth of the BLR only depends on the n_0 normalization of the electron distribution.

The BLR Thomson-scatters accretion disc photons, and the energy density of the BLR radiation for gamma-ray emission regions located at a distance R_γ below the BLR ($R_\gamma < R_{in}$) can be approximated as follows (Finke and Dermer [FD10])

$$u_{\rm BLR}(R, R_\gamma < R_{in}) \simeq \frac{\sigma_T\, L_{Disc}}{4\,\pi\,{\rm c}} \int_{R_{in}}^{R_{out}} \frac{dR}{R^2}\, n_{\rm BLR}(R)\,. \tag{3.50}$$

For $\zeta < -1$ electron number density spectral indexes, the expression can be further approximated as

$$u_{\rm BLR}(R_\gamma < R_{in}) \simeq u_0 \frac{1}{R_{in}^2} \frac{\zeta + 1}{\zeta - 1} \tag{3.51}$$

where u_0 is the energy density defined as

$$u_0 = \frac{\tau_{BLR}\, L_{Disc}}{4\,\pi\,{\rm c}}\,. \tag{3.52}$$

From Equation 3.50 we can see that for fixed ζ and τ_{BLR} (both input parameters of the model), the energy distribution of the BLR is independent of the distance between the emission region and the central engine.

For a gamma-ray emitting region located within the BLR ($R_{in} < R_\gamma < R_{out}$), and considering the approach in Finke and Dermer [FD10], the energy density takes the form of

$$u_{\rm BLR}(R, R_{in} < R_\gamma < R_{out}) \simeq \frac{\sigma_T \, L_{Disc}}{4\,\pi\,{\rm c} R_\gamma} \int_{R_{in}}^{R_{out}} \frac{dR}{R}\, n_{\rm BLR}(R) \tag{3.53}$$

which for electron number densities with $\zeta < -1$ can be expressed as

$$u_{\rm BLR}(R_{in} < R_\gamma < R_{out}) \simeq u_0 \frac{1}{R_\gamma\, R_{in}} \left(\frac{R_\gamma}{R_{in}}\right)^{\zeta} \frac{\zeta+1}{\zeta}. \tag{3.54}$$

Thus, when the blob is within the BLR, the energy density depends on the distance R_γ between the emission region and the central engine, which indeed is a free parameter of the model.

The energy densities of the lines $u_{\rm L}$ can be expressed as a function of the energy density $u_{\rm BLR}(\zeta, R)$

$$u_{\rm L} = \frac{u_{\rm BLR}(\zeta, R)\Delta_L}{100} \tag{3.55}$$

where Δ_L is the ratio of the intensity of a given line to the Lyα line (third column in Table 3.2). For an external monochromatic line spectrum being up-scattered, the energy density in the source frame becomes

$$u_{\rm L}(\epsilon_L) \equiv u(\epsilon) = u\delta(\epsilon - \epsilon_L), \tag{3.56}$$

where ϵ_L is the energy of a given line (second column in Table 3.2). Based on Equation 3.26, the expression for the disc-BLR IC component becomes

$$\nu F_\nu^{EIC,BLR} = \frac{R_{\rm SRC}^3\, {\rm c}\, \sigma_T\, u_{\rm L}\, \delta_D^3}{4 d_L^2} \left(\frac{\epsilon_s}{\epsilon_L}\right)^2 \int_{\gamma_{min}}^{\gamma_{max}} d\gamma \frac{n_e'\,(\gamma')}{\gamma^2}\, F_C(q,\, \Gamma_e)\,. \tag{3.57}$$

Direct emission from the corona

In our model, we consider the existence of a UV and X-ray emitting hot corona both below and above the disc, originated by the comptonization of some of the accretion disc photons and extending from around $3\,R_S$ to $60\,R_s$. Similar to the torus, the luminosity of such corona can be expressed as a fraction of the disc's luminosity

$$L_X = \tau_X\, L_{Disc} \tag{3.58}$$

whereas the spectrum of this luminosity in the comoving frame can be approximated by a power-law with an exponential cut-off

$$L_X \propto \nu^{-\alpha_X} \exp\left[\frac{-\nu}{\nu_c}\right] \tag{3.59}$$

where ν_c is the cut-off frequency value, which for is set to an energy value of $E_c = 150\text{keV}$, i.e. $\nu_c = 150e/h$, e and h being the electron charge value and Planck's constant respectively. The spectral distribution in the observer's frame is obtained by applying Equation 3.24. Note that the corona is considered to radiate starting at around the frequency corresponding to the accretion disc spectrum peak luminosity.

Corona-IC emission

For the IC emission of the X-ray corona photons, we follow the same procedure as for the multi-temperature accretion disc: we slice the corona in rings, and we calculate the intensity for each of the rings, followed by the corresponding calculations that yield the IC spectrum. Similar to the accretion disc, we need to take into account that each of the annuli is viewed under different angles by the relativistic blob (i.e.

the jet emission), receiving a different amount of Doppler deboosting b_X which in the case of the corona is defined as

$$b_X = \Gamma(1 - \beta\mu_X) \tag{3.60}$$

The expression of the spectral intensity of the corona in the blob's frame,

$$I'_X(\nu') \propto \mathrm{c}\,\nu'^{-\alpha_X} \exp\left[\frac{-\nu'}{b_X \nu_c}\right] \cos\theta_X. \tag{3.61}$$

Given that the frequency transformation from the corona frame to the blob's frame in this framework is $\nu' = b_X\,\nu$, one can write Equation 3.61 as a function of the corona frequency ν

$$I'_X(\nu') \propto \mathrm{c}\,(b_X\nu)^{-\alpha_X} \exp\left[\frac{-\nu}{\nu_c}\right] \cos\theta_X. \tag{3.62}$$

The normalization factor for the previous expressions can be obtained by integrating over the whole range of frequencies. Once we have the corresponding normalization, we can apply the IC calculation routines and transform the consequently obtained intensities from the blob's comoving frame to the observer's frame.

Corona BLR-IC emission

Radiation from the corona will Compton-scatter the BLR clouds creating a spectrum that features both lines and a continuum power-law (Tavecchio and Ghisellini [TG08]). The lines emitted by the BLR when illuminated by the X-ray corona will be different and much fainter w.r.t. those emitted when the disc photons ionize the clouds (i.e. the lines in Table 3.2). The model does not take into account these faint lines, but only the power-law continuum part of the spectrum.

The formalism to obtain the energy density of the BLR in this case is the same as for the disc BLR-IC interaction. The only change is the u_0 'normalization' factor of the $u_{BLR}(R)$ expressions in Equation 3.51 and Equation 3.54 (which in the case

of the corona we name $u_{0,X}$ and $u_{X,BLR}(R)$). When photons from the corona Compton-scatter the BLR clouds, instead of the u_0 given by Equation 3.52 one has

$$u_{0,X} = \frac{\tau_{X,BLR}\,\tau_{BLR}\,L_X}{4\,\pi\,\mathrm{c}} \tag{3.63}$$

where L_X is given by Equation 3.58. Note that an additional $\tau_{X,BLR}$ factor that illustrates the efficiency of the Compton scattering is introduced, whose value is around $\tau_{X,BLR} \sim 1\%$ (Ghisellini and Tavecchio [GT09]). Thus, in our model the energy density of the corona BLR-IC radiative component takes the spectral form

$$u_{X,BLR} \sim u_{X,\mathrm{BLR}}(R)\,\nu^{-\alpha_X}. \tag{3.64}$$

The normalized expression of Equation 3.64 is substituted in Equation 3.26 to calculate the overall spectral flux of the corona BLR-IC interaction.

3.3.4 Constraints on the multi-component EC model

Table 3.3 summarizes the parameters of the multi-component model we have implemented. Note that the emission region parameters are the same as for the one-zone SSC model (see Table 3.1 for the corresponding parameters), so we only show the additional one, i.e. the distance to the emission region R_γ.

Component	Parameter	Value
Black Hole	Mass	$M_{BH} \sim 10^7 - 10^9$ M$_\odot$
Emission region	Distance	$R_{src} < R_\gamma < R_{out}^{BLR}]$
Torus	Temperature	T$_{IR} \sim$ 1200 K-1300 K
	Distance	$\mathrm{R}_{IR} = 3.5 \times 10^{18} \sqrt{\frac{L_D}{10^{45}}} \left(\frac{T_{IR}}{10^3}\right)^{-2.6}$ cm
	Covering factor	$\tau_{IR} \sim 0.1 - 0.3$
Big Blue Bump	Inner radius	$\mathrm{R}_{IN} = 3R_S$
	Outer radius	$\mathrm{R}_{OUT} = 500R_S$
	Accretion efficiency	$\eta_{Edd} = \frac{1}{12}$
	Eddington ratio	$l_{Edd} \sim 0.5 - 1.0$
Corona	Inner radius	$\mathrm{R}_{IN} = 3R_S$
	Outer radius	$\mathrm{R}_{OUT} = 60R_S$
	Reprocessing factor	$\tau_X \sim 0.01 - 0.5$
Broad Line Region	Distance	$\mathrm{R}_{BLR} \simeq 10^{17} L_{disk,45}^{1/2}$ cm
	Width	ΔR = 3 R$_{BLR}$
	Density profile	$\zeta = -2$
	BLR optical depth	$\tau_{BLR} \sim 10^{-4} - 0.1$

Table 3.3 Constraints on the multi-component model parameters for gamma-loud NLS sources.

3.3.5 Exploring the parameter space of the multi-component EC model

To conclude the presentation of our multi-component model, we will illustrate in the following pages the changes generated by the variation of the most relevant parameters of the model on the EIC components for a BPL electron distribution.

These are the initial parameters for all models considered in the following section:

Blob-in-jet		External fields	
Parameter	Value	Parameter	Value
δ	11	T_{torus}	1300 K
K	2.5×10^6 cm^{-3}	τ_{torus}	0.1
B	0.1 G	M_{BH}	0.25×10^9 $M_\odot$
R_{src}	8.35×10^{16} cm	l_{Edd}	0.3
n_1	2.5	τ_{BLR}	0.1
n_2	3.5	R_{IN}^{BLR}	1×10^5 R_G
γ_{min}	100	R_{OUT}^{BLR}	3×10^5 R_G
γ_b	700	R_γ	5×10^4 R_G
γ_{max}	4×10^4		

We start with changes provoked by variations in the parameters that describe the electron distribution. Thereafter, we continue with the parameters that are linked to the external photon fields themselves. Note that the differences introduced by parameters that act as simple scaling factors (i.e. τ_{IR}, τ_X, τ_{BLR}) are not presented, since their effect is straightforward to determine.

The variation on the parameters is characterized by different colors which are explained in the legend of each figure. For reference purposes, both direct torus and direct disc components are also shown, regardless of their invariance towards the parameter changes.

Each component is plotted with different line style: dash-dotted ('-.') for the direct torus component, solid ('-') for the direct disc component, dotted (':') for the torus IC component, dashed ('–') for the disc IC component, and custom dash-dotted ('-::') for the BLR IC component.

Minimum energy of the electron distribution - γ_{min}

Figure 3.10 illustrates what happens to EIC components for minimum Lorentz factor γ_{min} values of 100, 700 and 1300 . Larger minimum electron energy distribution values push all EIC component peaks towards higher energies.

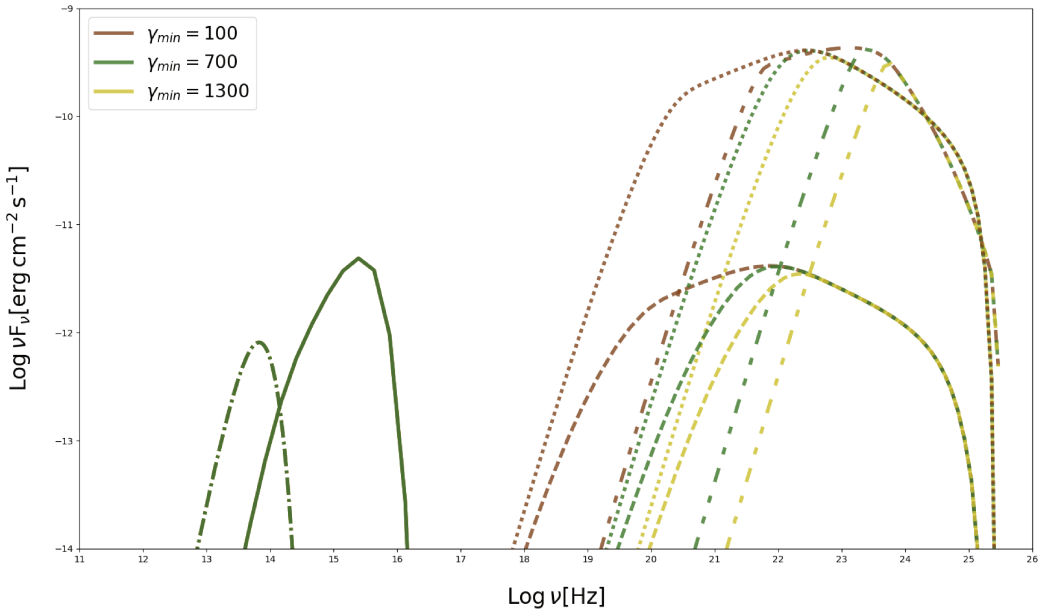

Figure 3.10 Effect on the EC components of arbitrarily changing the γ_{min} parameter. Dash-dotted ('-.') lines represent the direct torus component, solid ('-') lines the direct disc component, dotted (':') lines the torus IC component, dashed ('–') lines the disc IC component, and custom dash-dotted ('-::') lines the BLR IC component.

Maximum energy of the electron distribution - γ_{max}

Larger maximum electron energy distribution values generate EIC components that reach higher energies. Figure 3.11 shows the changes generated by γ_{max} values of 1.5×10^3, 8×10^4 and 1.5×10^6. Note that while the difference between $\gamma_{max} = 1500$ and $\gamma_{max} = 8 \times 10^4$ is quite noticeable, this is not the case for $\gamma_{max} = 8 \times 10^4$ and $\gamma_{max} = 1.5 \times 10^6$. Such a large increase of the parameter value barely increases the maximal span of energy attained by the components. This could be due to the fact that with increasing values of γ_{max} we reach the Klein-Nishina regime [Section 3.1.4] where the photons are not so strongly upscattered. Another reason might be that larger n_2 values hamper the injection of more electrons in the emission region.

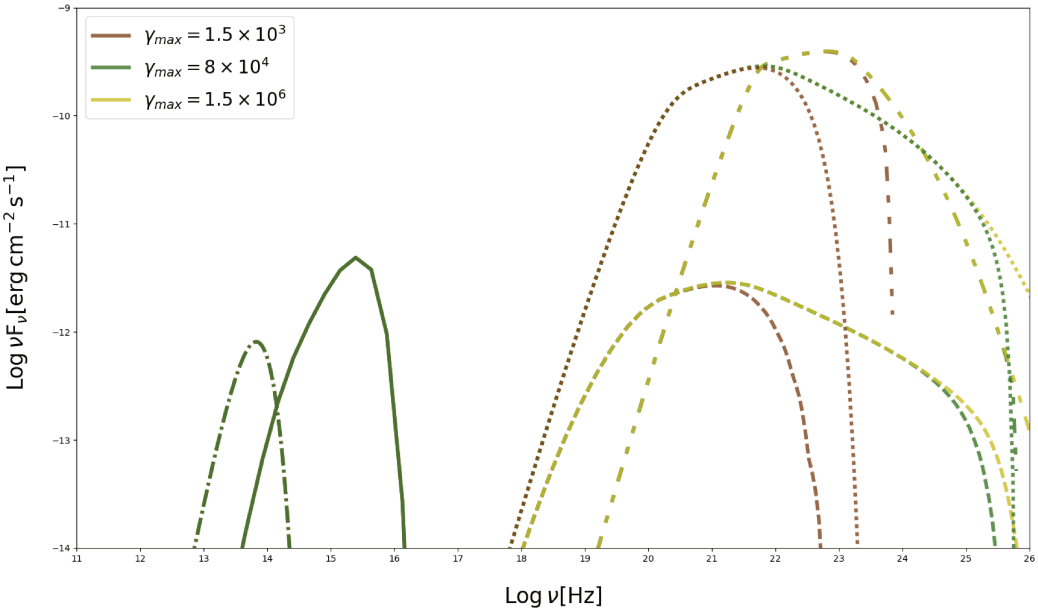

Figure 3.11 Effect on the EC components of arbitrarily changing γ_{max}. Dash-dotted ('-.') lines represent the direct torus component, solid ('-') lines the direct disc component, dotted (':') lines the torus IC component, dashed ('–') lines the disc IC component, and custom dash-dotted ('-::') lines the BLR IC component.

Break energy of the electron distribution - γ_b

Introducing a shift in the break energy shifts the peak of each of the components, which implies a major change in the shape of the distributions. If we were to calculate the total of all the model components, larger γ_b values would imply an IC peak located at higher energies. Figure 3.12 illustrates the changes generated by γ_b values of 400, 700 and 1100.

Larger break energy values imply an electron distribution with a longer cooling timescale, because we add electrons at higher energies when the break energy is shifted towards higher energies.

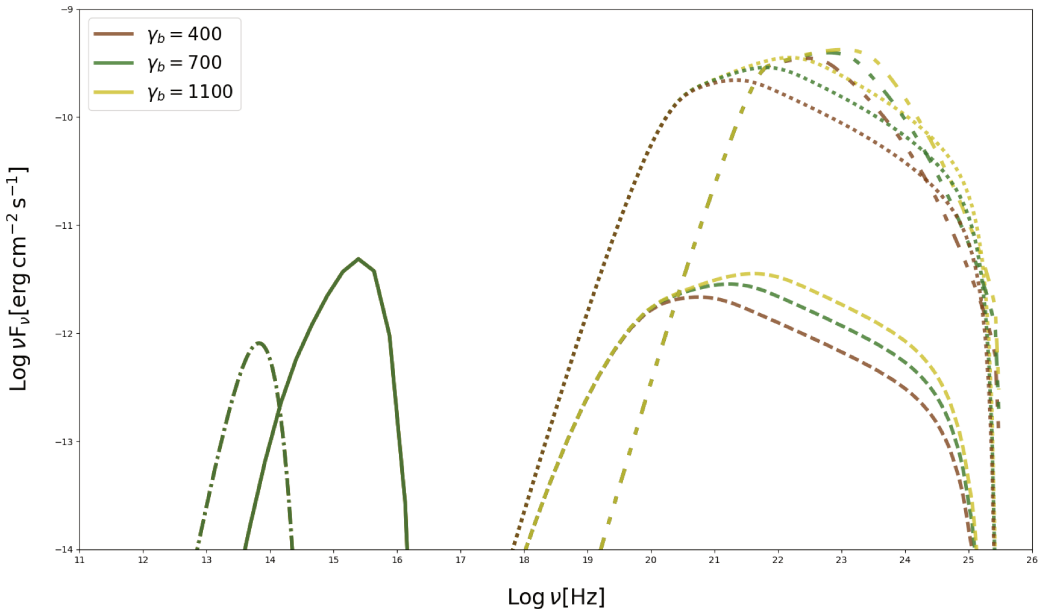

Figure 3.12 Effect on the EC components of arbitrarily changing γ_b. Dash-dotted ('-.') lines represent the direct torus component, solid ('-') lines the direct disc component, dotted (':') lines the torus IC component, dashed ('–') lines the disc IC component, and custom dash-dotted ('-::') lines the BLR IC component.

First slope of the electron distribution - n_1

From Figure 3.13, one can see that larger values (i.e. softer distribution) of the first slope of the BPL distribution decrease the Compton dominance of the EIC components. Indeed, the variation of the n_1 parameter causes changes in the luminosities of the components, since the electron population within the emission region changes. The spectral shape of the EIC components also changes, subtly for some of the components, and in a more notorious way for the dashed BLR-IC component.

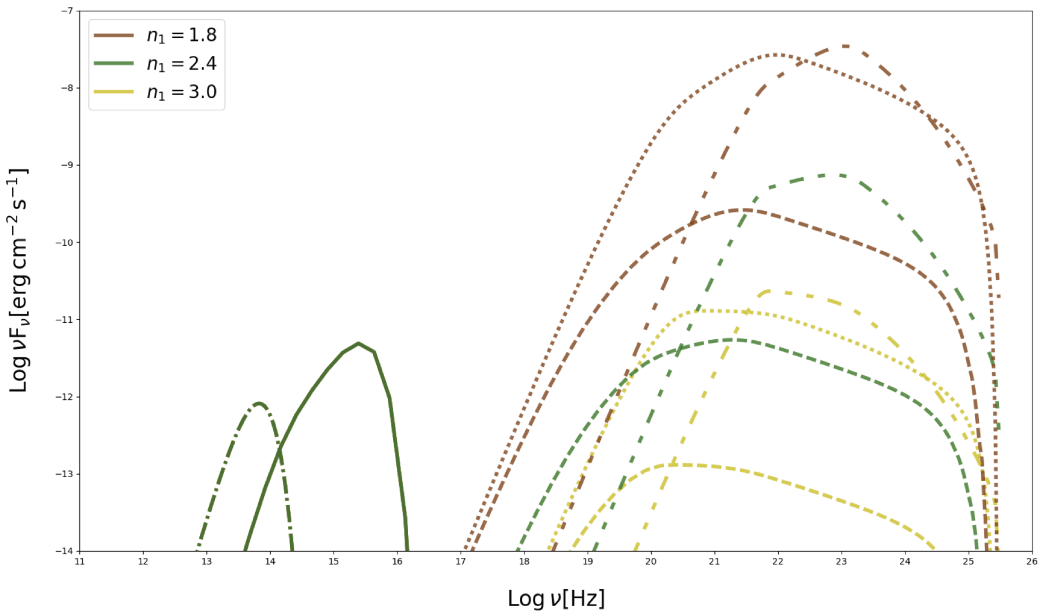

Figure 3.13 Effect on the EC components of arbitrarily changing n_1. Dash-dotted ('-.') lines represent the direct torus component, solid ('-') lines the direct disc component, dotted (':') lines the torus IC component, dashed ('–') lines the disc IC component, and custom dash-dotted ('-::') lines the BLR IC component.

Second slope of the electron distribution - n_2

If the slope of the electron distribution after the energy break is increased, one obtains an increasingly sharper shape of the EIC components, as shown in Figure 3.14. Also, the maximum energy of each component is slightly diminished, which for the disc-IC component (dashed '–' lines) is quite noticeable. As we will see when we apply the models to gamma-loud NLS sources, the spectral differences of GeV spectra between the quiescent and flaring states cause n_2 to be one of the parameters that changes most in our models.

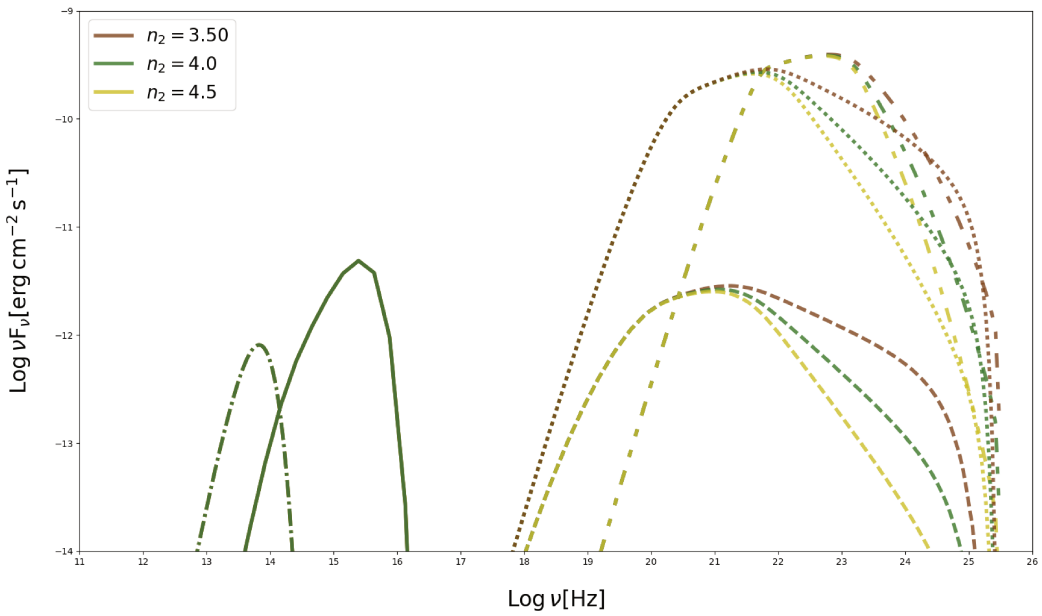

Figure 3.14 Effect on the EC components of arbitrarily changing n_2. Dash-dotted ('-.') lines represent the direct torus component, solid ('-') lines the direct disc component, dotted (':') lines the torus IC component, dashed ('–') lines the disc IC component, and custom dash-dotted ('-::') lines the BLR IC component.

Black hole mass - M_{BH}

Larger black hole masses yield more luminous accretion discs (see Figure 3.15), as could be inferred from Equation 3.36. However, the opposite behaviour is observed for the disc and BLR IC components, due to the fact that these components are inversely proportional to the gravitational radius (which is directly proportional to the black hole mass). Thus, larger black hole masses yield less luminous disc and BLR-IC components.

On the other hand, the torus luminosity is also proportional to the disc luminosity, so its direct radiation also increases with the black hole mass. However, the corresponding torus-IC component is invariant w.r.t. a more luminous disc. This is due to the fact that the dependence of the radius of the torus on the disc luminosity (Equation 3.34) cancels out the dependence of the torus energy density on the same luminosity Equation 3.32.

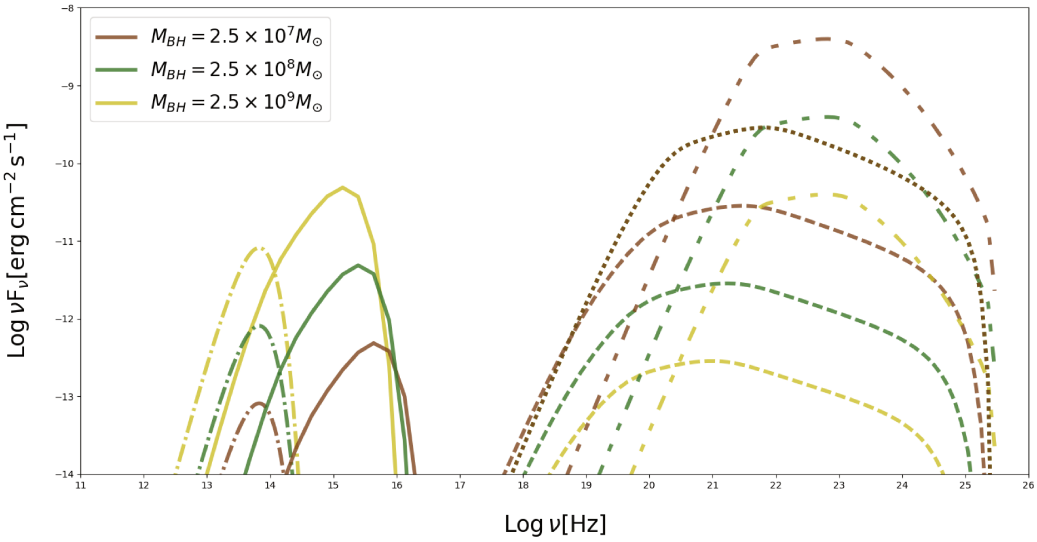

Figure 3.15 Effect on the EC components of arbitrarily changing M_{BH}. Dash-dotted ('-.') lines represent the direct torus component, solid ('-') lines the direct disc component, dotted (':') lines the torus IC component, dashed ('–') lines the disc IC component, and custom dash-dotted ('-::') lines the BLR IC component.

External radius of the accretion disc - R_{disc}^{out}

The size of the accretion disc is not a parameter that is given as an input for the code, but is instead hard-coded to a value of $R_{disc}^{out} \sim 500 R_S$. However, we were interested in seeing how a smaller accretion disc affects the model components. For this purposes, we created discs that featured $R_{disc}^{out} \sim 200\, R_S$ and $300\, R_S$, whose distributions are presented along with that of the default $R_{disc}^{out} \sim 500 R_S$ in Figure 3.16. Though not major, a difference in the low-end of the accretion disc component is introduced when the size of the disc varies - larger discs radiate down to lower energies. The same trend is also reflected in the disc EIC component. The torus and BLR EIC components are much less affected, since they are proportional to the integrated disc luminosity, value that does not greatly vary when we change the disc dimensions.

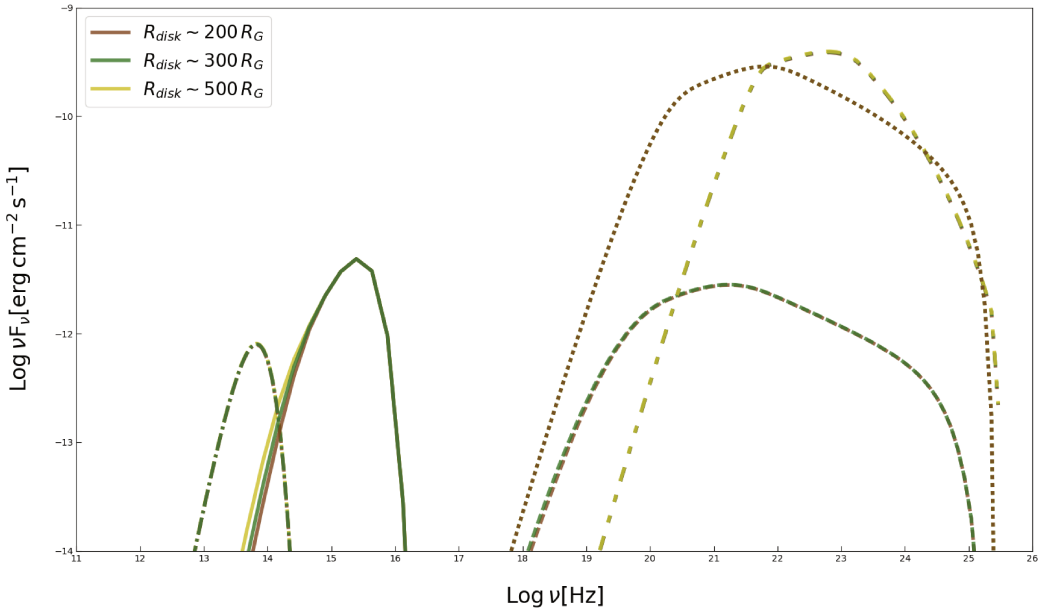

Figure 3.16 Effect on the EC components of arbitrarily changing R_{disc}^{out}. Dash-dotted ('-.') lines represent the direct torus component, solid ('-') lines the direct disc component, dotted (':') lines the torus IC component, dashed ('–') lines the disc IC component, and custom dash-dotted ('-::') lines the BLR IC component.

Distance to the dissipation region - R_γ

The changes generated by a blob located either very close to the central engine ($R_\gamma = 1 \times 10^3\, R_G$), farther away from it ($R_\gamma = 5 \times 10^4\, R_G$), in the middle of the BLR ($R_\gamma = 2 \times 10^3\, R_G$) and at the very end of the BLR ($R_\gamma = 3 \times 10^5\, R_G$) are presented in Figure 3.17. As expected, closer emission regions generate disc components that contribute more to the overall energy distribution: the farther the blob, the less they contribute. The same trend is observed for the BLR component. This is due to the fact that the BLR is described in a way that its ionization decreases with distance, i.e. the inner part of the BLR is the one that contributes the most to the radiation, while its contribution diminishes when we are located in its farther edge. However, no main difference is observed within solutions that feature different R_γ so long as they are either *below* ($R_\gamma < R^{in}_{BLR}$) or within ($R^{in}_{BLR} \leq R_\gamma \leq R^{out}_{BLR}$) the BLR.

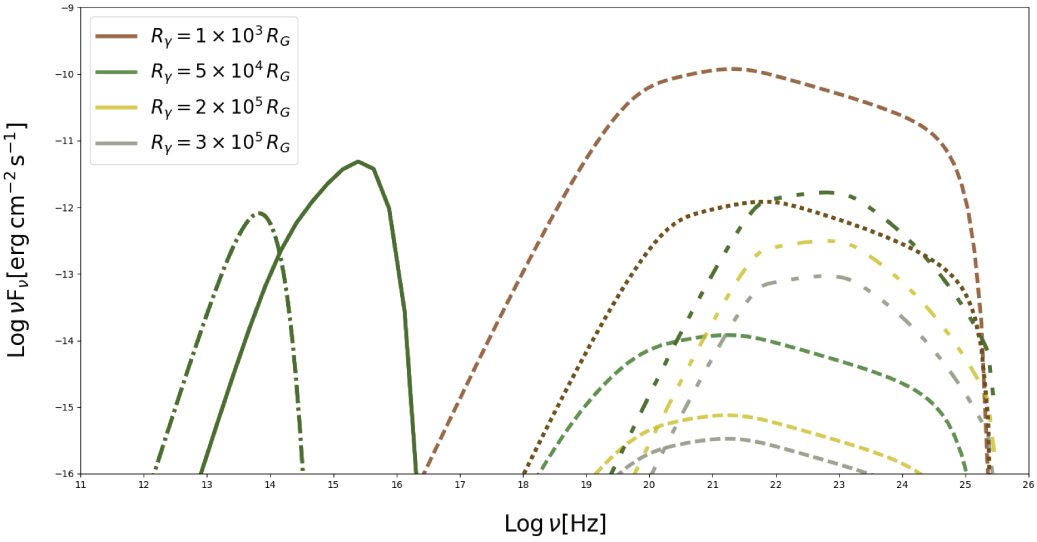

Figure 3.17 Effect on the EC components of arbitrarily changing R_γ. Dash-dotted ('-.') lines represent the direct torus component, solid ('-') lines the direct disc component, dotted (':') lines the torus IC component, dashed ('–') lines the disc IC component, and custom dash-dotted ('-::') lines the BLR IC component.

The location of the gamma-ray emitting region is the matter of quite a debate. The fast variability observed in gamma-loud objects points towards a compact emission region. Assuming the emission region occupies the whole cross-section of the jet, due to the conical nature of the latter, the emission region should in principle not be located much farther away than the BLR. However, the lack of absorption features in the spectra of objects detected up to VHE (i.e. FSRQs) indicate the emission should

be taking place outside the BLR, since an emission region close to the accretion disc and its high energy density of UV photons would be a major source of opacity for VHE photons. The fact that gamma-ray flares seem to be correlated with the ejection of superluminal components from blazar cores would also indicate emission regions located at a few parsec scales. For a sample of 217 blazars, Ghisellini and Tavecchio [GT15] showed that the emission region of 191 FSRQs was within the BLR. On the other hand, there is also some evidence of flaring events happening at different distances from the central engine within the same object (Figure 3.18). The latter argument will not be considered in this work, but the former two (i.e. emission region within the BLR and outside the BLR, for disc-dominated and torus-dominated scenarios respectively) will be developed in Chapter 6.

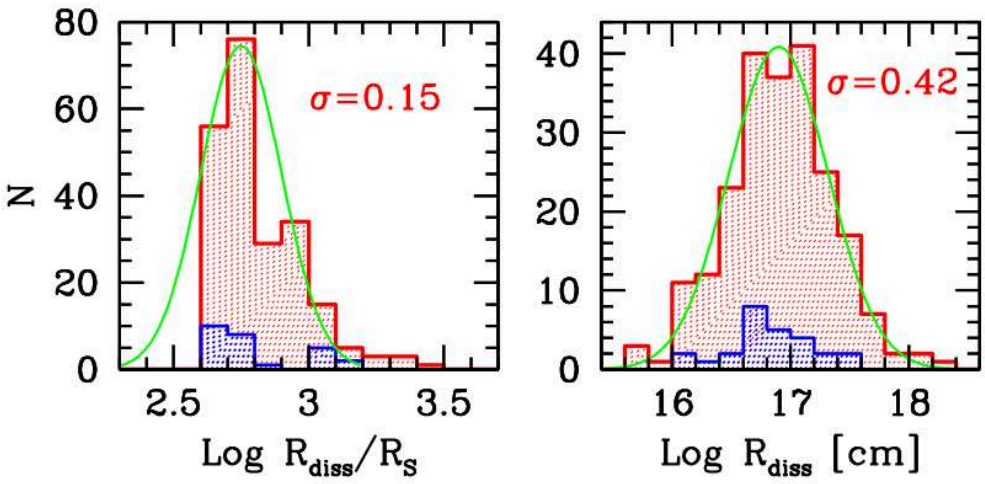

Figure 3.18 Distribution of the location of the emitting region (i.e. its distance from the black hole) in units of the Schwarzschild radius (**left**) and in cm (**right**) from Ghisellini and Tavecchio [GT15]. Red and blue hatched areas correspond to the FSRQs and BL Lacs from their sample, while the green line represents the distribution of the distances, σ being the width of each distribution.

Inner radius of the BLR - R^{in}_{BLR}

We also tested the influence of varying the inner radius of the BLR by keeping its width constant ($R^{out}_{BLR} = 3 \times R^{in}_{BLR}$) and the emission region in the middle of it ($R_\gamma = 2 \times R^{in}_{BLR}$).

In other words, we shifted the position of the whole BLR from $R^{in}_{BLR} = 10^4\, R_G$ by two orders of magnitude to see what the effect was. As can be seen in Figure 3.19, a farther located BLR (and thus a farther emission region according to the choices we made for comparison purposes) diminishes the contribution of the disc-IC component. A further BLR would also suffer from less ionization from the disc photons, so that its luminosity descends too. Note that the position of each component does not vary since γ_b is again constant.

Let us remark that the position of the BLR is constrained by the $r - L$ relation obtained from reverberation mapping studies, so that a farther BLR would only be possible in the case of more luminous accretion discs. The comparison we make here only aimed at exploring the approximate changes that a farther BLR would cause.

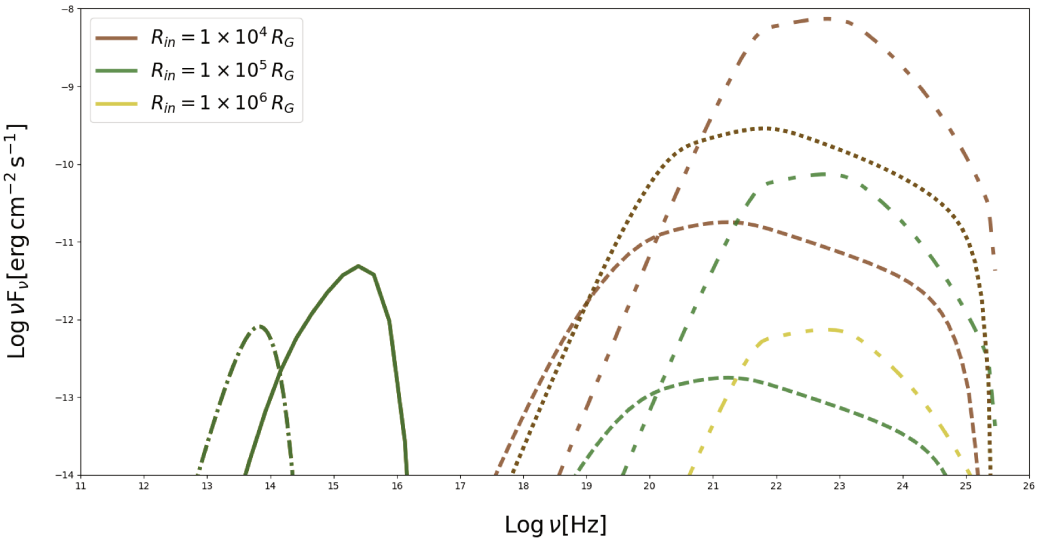

Figure 3.19 Effect on the EC components of arbitrarily changing R^{in}_{BLR}. Dash-dotted ('-.') lines represent the direct torus component, solid ('-') lines the direct disc component, dotted (':') lines the torus IC component, dashed ('–') lines the disc IC component, and custom dash-dotted ('-::') lines the BLR IC component.

3.4 Other models for gamma-loud AGN SED modelisation

Ever since first multi-wavelength observations of blazars enabled the determination of a compact zone moving close to the jet base at a relativistic speed, producing the characteristic 2-humped SED in the so-called SSC scenario, different, increasingly complex numerical scenarios have been developed with the aim of characterizing the emission zone. Thus, we would like to end the Chapter with a brief review of some of the other models and scenarios for gamma-loud AGN that exist nowadays. Some of them introduce variations on the one-zone SSC scenario, others consider a hadronic particle population instead of a leptonic one, and others contemplate different scenarios of particle acceleration. This brief exposition will present only a number of the existing models, and it is by no means exhaustive.

3.4.1 SSC models

Blob-in-jet model

One-zone SSC models cannot describe the lowest energy range of gamma-loud AGN SED, which is generally ascribed to the radio emission from the extended jet. This emission is considered through a model of conic stratified jet also emitting SSC radiation in the "blob-in-jet" scenario by Katarzyński et al. [Kat+01] and Katarzyński et al. [Kat+03].

This model neglects the interactions between the compact and the extended jet components, though, assuming that the jet power is weak. However, this might not be the case for sources other than HBLs, and the interaction between the jet components can become dominant. Hervet et al. [Her+15] developed a model that takes into account the base of the extended radio jet, and showed that such scenario can properly describe the SED of IBLs such as AP Librae (Figure 3.21).

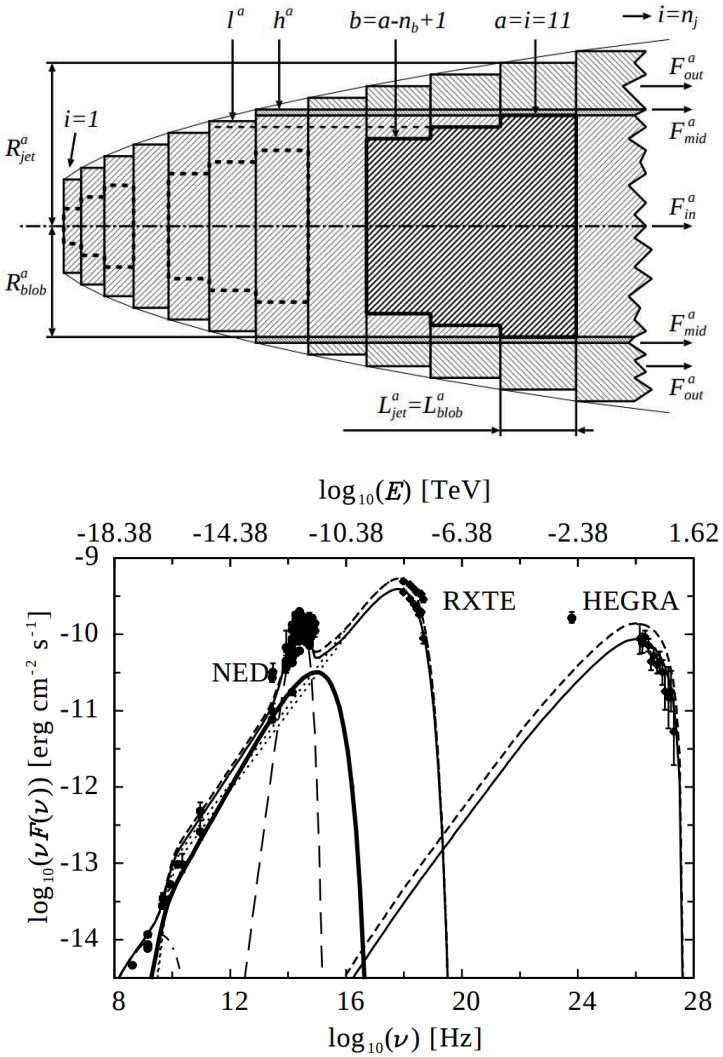

Figure 3.20 **Top:** Geometry of the jet and evolution of the blob geometry from Katarzyński et al. [Kat+03]. **Bottom:** Temporal evolution of the spectral energy distribution of Mrk 421 from the radio frequencies up to TeV by applying the above stratified jet model. Katarzyński et al. [Kat+03] applied the model to two high states of the source, one corresponds to the lowest of the two high energy states observed by RXTE in February 2000 (solid lines), and the other to the highest state from Krawczynski et al. [Kra+01] (dotted lines). The bold-solid line shows the synchrotron emission of the jet, the long-dashed line shows the thermal emission of the host galaxy, and the dashed-dotted line shows the radiation of the extended radio structure.

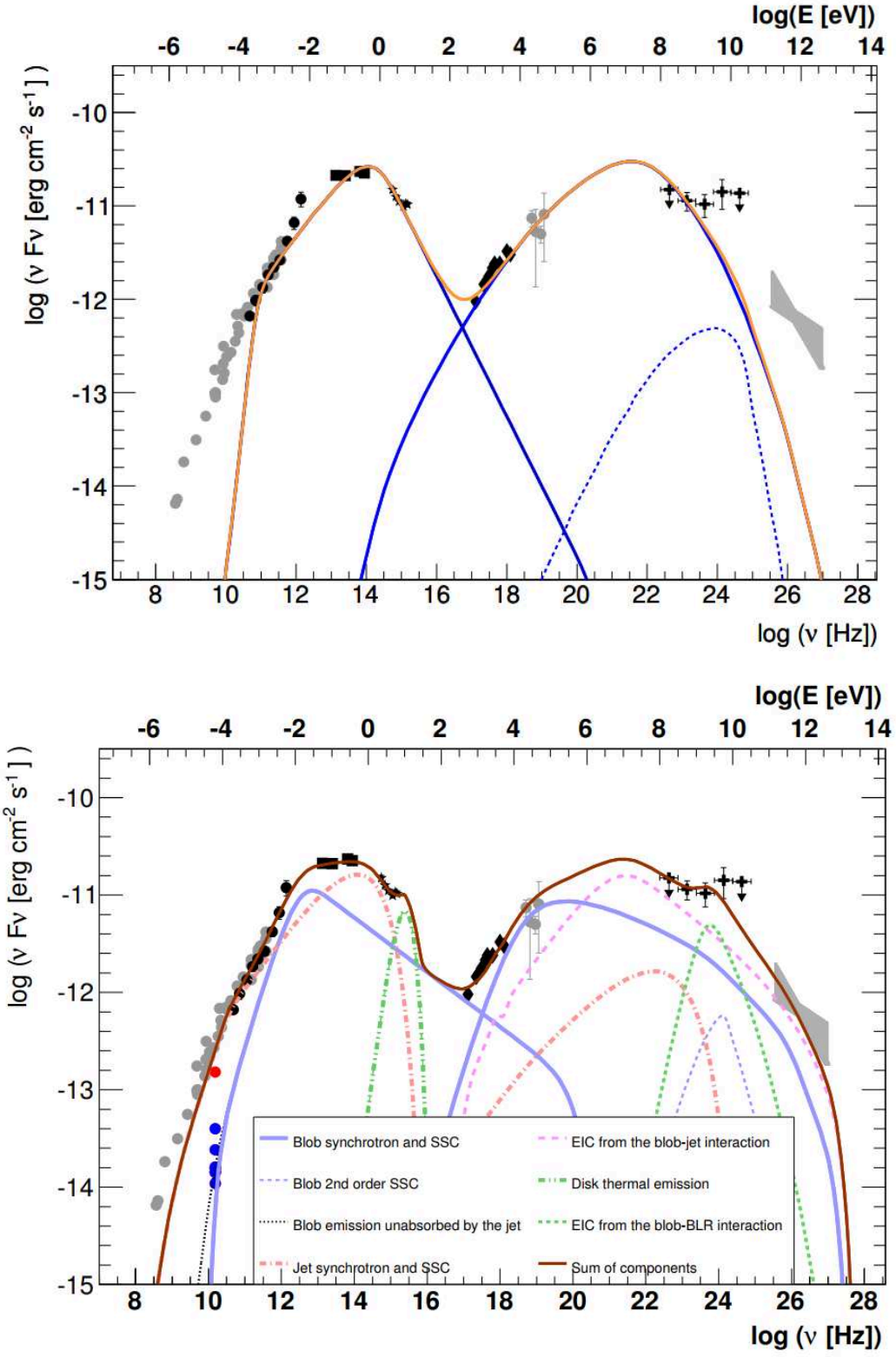

Figure 3.21 **Top:** SSC model of AP Librae from Hervet et al. [Her+15], where they showed that SSC scenarios are unable to reproduce the observedVHE fluxes. The solid blue lines represent the synchrotron component and SSC component of the model, while the dashed blue line corresponds to the second order SSC component. The total model is shown as an orange solid line. **Bottom:** Multi-component SSC modeling via the model developed by Hervet et al. [Her+15]. Different model components are explained in the panel within the figure.

Multi-blob model

Models that consider a spherical shell composed of several SSC blobs (see Figure 3.22) and defined by the total section of the jet that propagates at the base of the jet instead of a single blob traveling along the jet axis were conceived to explain the high and very high emission from radio-galaxies (Lenain et al. [Len+08]).

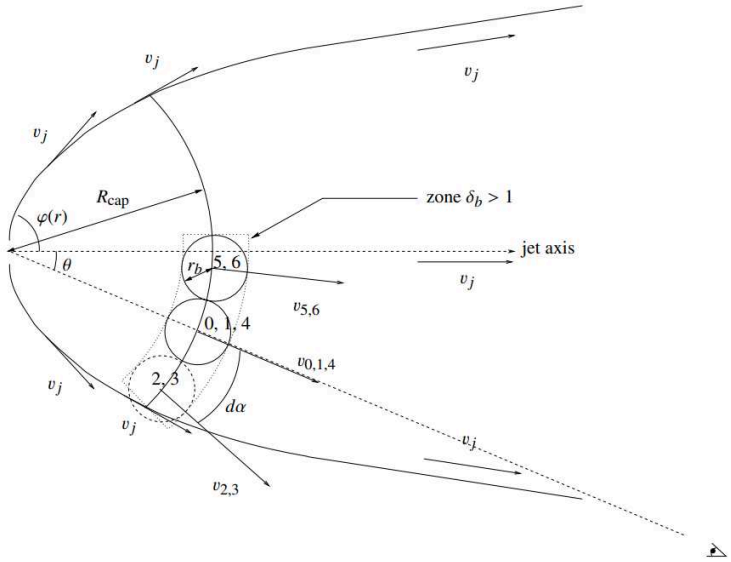

Figure 3.22 Scheme of the side view of the multi-blob model by Lenain et al. [Len+08].

In fact, radio galaxies were not expected to be observed at high energies, due to the large opening angles between their jets and the observer ($\theta \leq 1°$). Such large viewing angles should in principle not provide a strong enough Doppler boosting to account for the observed radiation. In the multi-blob model proposed by Lenain et al. [Len+08], though, some part of the shell will follow a direction closely aligned with the observer's direction and hence undergo the required relativistic beaming.

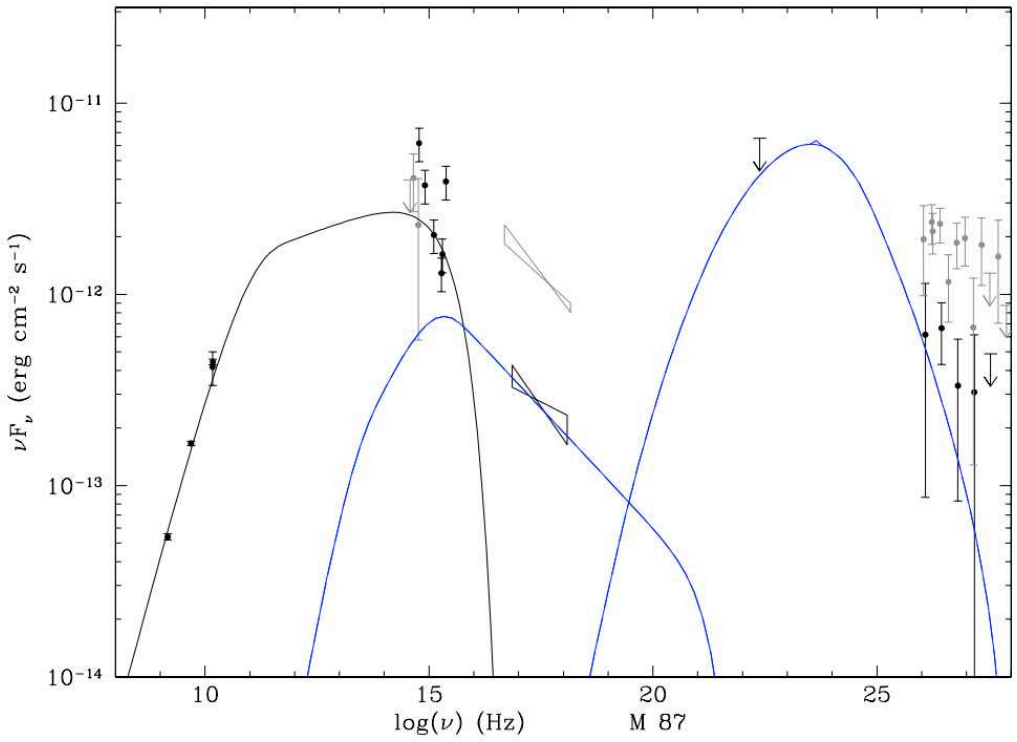

Figure 3.23 Multi-blob modeling of M 87 by Lenain et al. [Len+08]. Data that bring direct constraints to the model are shown in black, while less constraining data are depicted in gray. The black line corresponds to the model of the extended inner jet by Katarzyński et al. [Kat+01] and Katarzyński et al. [Kat+03], and the blue lines correspond to the radiation from the multi-blob scenario.

3.4.2 Hadronic models

Although it is well established that the observed synchrotron emission at low frequencies is originated by a leptonic population, the origin of the high energy emission in blazars is still a matter of debate. So far, we have considered a purely leptonic SSC scenario (with the possible addition of external photon fields), but frameworks where the hadronic component of the jet becomes dominant can also explain the gamma-ray emission.

In hadronic scenarios, the low part of the SED is attributed to synchrotron radiation from electrons that are accelerated along protons, while high energy emission can either originate from proton-synchrotron emission or from secondary emission from proton-photon (through photon-meson or Bethe-Heitler processes) or proton-proton interactions. Indeed, as proposed by Mannheim and Biermann [MB92] or Mannheim [Man93], if a significant fraction of the jet power is transformed into relativistic proton acceleration in a sufficiently magnetized environment, the threshold for pγ pion production will be reached, generating synchrotron-supported pair cascades.

The fact that extreme objects like ultra high-frequency peaked BL Lacs push the parameters of simple one-zone SSC models to the limit (e.g. Doppler factors of $\delta \sim 100$) could indicate the need for the presence of a major non-thermal proton population, which in turn might explain or answer the myriad of open questions about cosmic ray acceleration.

Models like the one developed by Cerruti et al. [Cer+15] that was preceded by other studies (e.g. Bottcher et al. [Bot+13]) have casted more light on whether such models yield less extreme parameters. They have also managed to describe the SED of objects such as PKS 2155-304 or Cen A (see figures Figure 3.24 and Figure 3.25 for models by Zech, A. et al. [Zec+17] based on Cerruti et al. [Cer+15]).

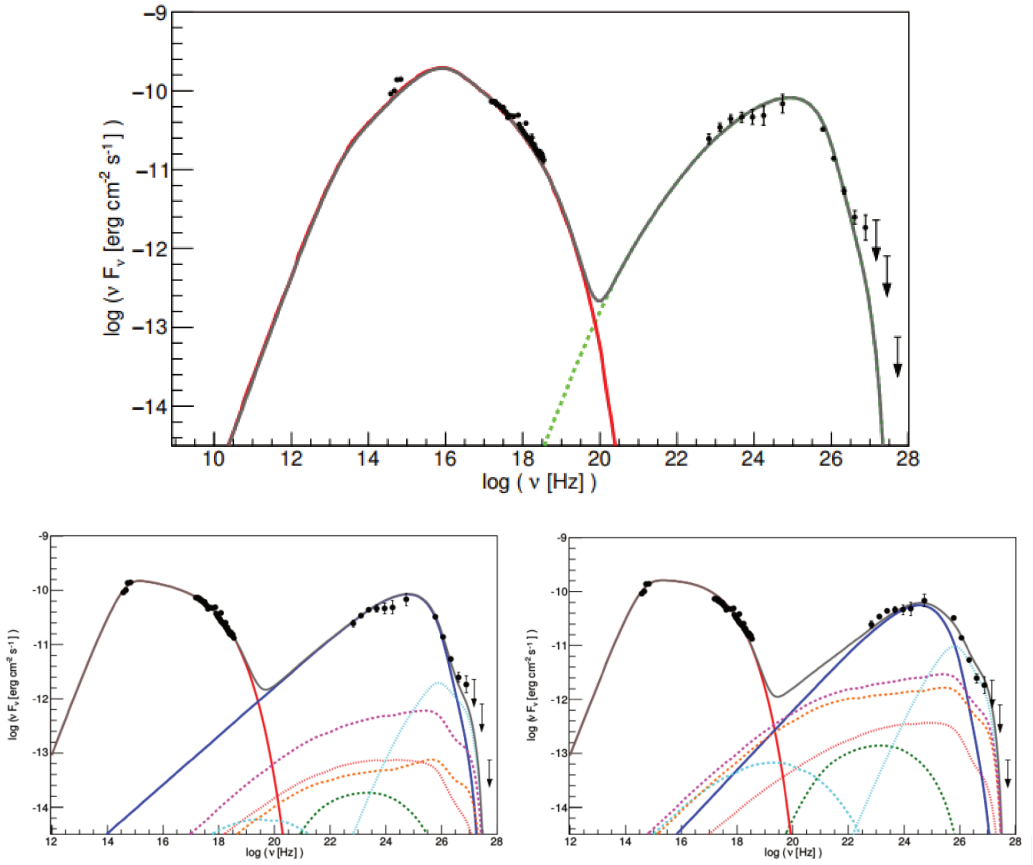

Figure 3.24 **Top:** Simple SSC model of PKS 2155-304 by [Zec+17]. **Bottom:** Hadronic modeling of PKS 2155-304 by Zech, A. et al. [Zec+17]. On the left figure the TeV energy range is dominated by proton synchrotron emission, while on the right muon-synchrotron emission is predominant. The simple one-zone SSC model solution provides a worse description of the VHE tail of the spectrum than the hadronic models.

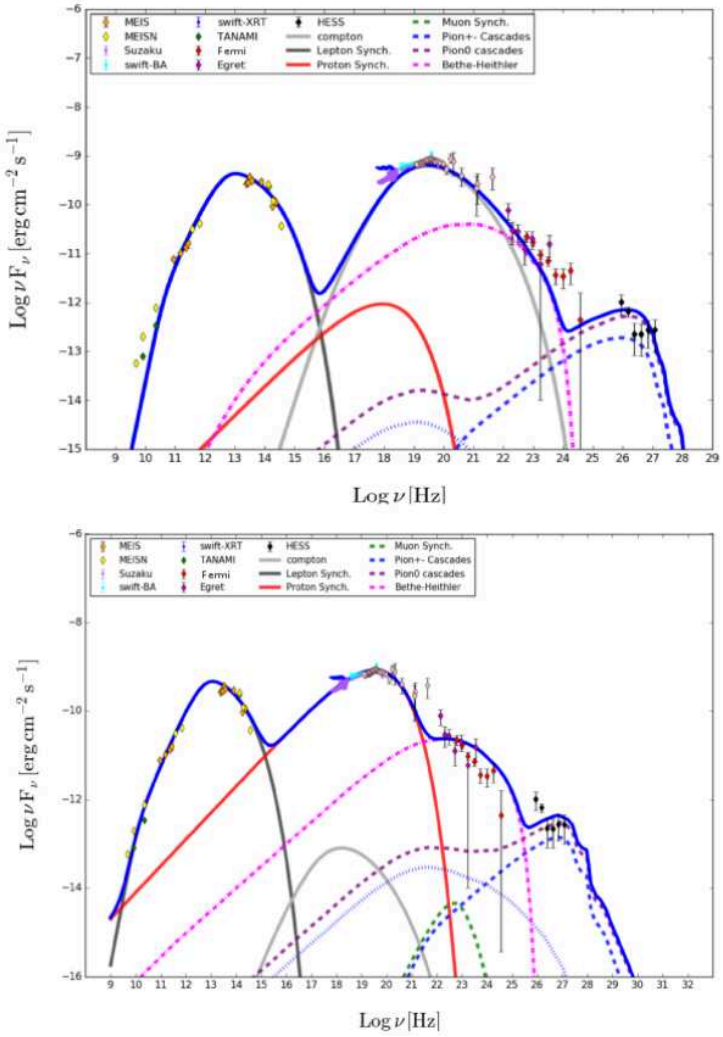

Figure 3.25 Two different hadronic one-zone models for Cen A from [Cer+17]. The top model is a VHE scenario up to MeVs, but at higher energies the synchrotron from secondary pairs from p-γ interactions between the protons and the primary synchrotron radiation from the electrons become dominant. The bottom model ascribes X-rays to proton-synchrotron emission, while the origin of GeV and TeV comes again from secondary pairs.

4 HESS ToO observations of PKS 1749+096 during its July 2016 flare

In Section 2.5.8 we introduced the Target of Opportunity (ToO) protocol implemented within the HESS collaboration. In this Chapter, we will describe the procedure in more detail, as well as presenting an overview of the achievements of the observations that were triggered in the 2016 campaign. Then, an example of the duties performed within this task force of the collaboration is given under the form of the Swift data analysis for the flare of PKS 1749+096 during its July 2016 flare that triggered a ToO campaign. A final word on the importance of this type of Multi-WaveLength (MWL) campaigns closes the Chapter.

4.1 The procedure

The length of each HESS observation shift ($\sim$ 28 days) is split into two ToO monitoring shifts, during which the corresponding shifter (known as trigger monitoring person) examines MWL data from a number of different facilities to search for interesting features in the data. If enhanced activity that fulfills some preset criteria is observed, an alert system that informs the shifters at the HESS site in Namibia of the need of scheduling observations for the given source is activated.

The main sources of information that are used by the ToO group include e.g. the monitoring of public data from the First G-APD Cherenkov Telescope (FACT, Anderhub et al. [And+13]), automatic, daily analysis of Fermi-Large Area Telescope (Fermi-LAT) data, follow-up of publicly available data from Swift X-Ray Telescope (XRT) and Burst Alert Telescope (BAT), private alerts from other MWL partners such as MAGIC (Major Atmospheric Gamma-ray Imaging Cherenkov Telescope, Lorenz

and Martinez [LM05]), VERITAS (Very Energetic Radiation Imaging Telescope Array System, Weekes [Wee03]) and HAWC (High-Altitude Water Cherenkov Observatory, Smith and HAWC Collaboration [SHC07]) within the context of Memoranda of Understanding, and also public alerts from the Astronomer's Telegram. Data from the Automatic Telescope for Optical Monitoring (ATOM) telescope on site [Section 2.5.4] are also carefully monitored in search for optical flaring activity.

Around 60 hours of total HESS observing time were dedicated to blazar ToO activities during the 2016 campaign. Some of the most remarkable results include the HESS detection of the BL Lac PKS 1749+096 ($z = 0.322$, Hewitt and Burbidge [HB89]), the detection of intensified gamma-emission from the BL Lac PKS 0447-439 ($z = 0.343$, Rovero et al. [Rov+13]) or the obtention of Very High Energy (VHE) emission upper limits of the FSRQs CTA 102 ($z = 1.037$, Schmidt [Sch65]) and PKS 2022-07 ($z = 1.388$, Drinkwater et al. [Dri+97]). We point the reader towards Schüssler et al. [Sch+17] for further details.

Participants of the ToO monitoring task perform different activities within the working group. The writer carried out MWL shifter duties, as well as performing Swift data analyses for several sources. The Swift analysis of July 2016 data from the ToO event triggered by the flaring Fermi-LAT activity of PKS 1749+096 is presented in the following.

4.2 An example: The July flare of PKS 1749+096

Also known as OT 081, PKS 1749+096 (spectroscopic redshift of z = 0.322, Hewitt and Burbidge [HB89], RA = 17:51:32.81855, Dec = +09:39:00.7288 J2000) is a LBL object that went into a flaring state on July 9th 2016 at GeV energies, reaching up to a daily averaged gamma-ray flux of $F_{E>100\,\mathrm{MeV}} = (1.0 \pm 0.2) \times 10^{-6}\,\mathrm{ph\,cm^{-2}\,s^{-1}}$ (statistical uncertainty only, Becerra Gonzalez et al. [Bec+16]), around 20 times the average flux from the 3FGL catalog.

Such enhanced gamma-emission was followed by an optical outburst that peaked during the interval between 2016 July 16th and 20th at a magnitude $R \sim 14.9$, as reported in Balonek et al. [Bal+16b]. The gamma-ray outburst set off high-urgency

follow-up ToO Swift observations between 2016 July 17 and July 20, as reported in Ciprini et al. [Cip+16]. Unfortunately, moon constraints made simultaneous HESS observations of PKS 1749+096 impossible. However, observations started on July 22nd for a duration of 6 nights, obtaining around 12 hours worth of observations. On the other hand, MAGIC reported VHE emission from PKS 1749+096 during the night of July 24th (Mirzoyan [Mir16]).

4.2.1 Swift data analysis

Regarding the analysis of the available Swift (Burrows et al. [Bur+05]) data for the July 2016 flare, we considered data from the 11th of July (before the flare and prior to the start of HESS observations) to the 27th of July, to better examine the behaviour of the source both before and during the enhanced emission epoch. Thus, 9 different pointings were available, the details of whom are shown in Table 4.1.

Date (UTC)	MJD	Our ID	Swift ID	XRT exp.	UVOT exp.
2016-07-11	57580.02	OBS1	00036392027	2960.243	2855.143
2016-07-13	57582.40	OBS2	00036392028	2066.807	2010.76
2016-07-17	57586.92	OBS3	00036392029	2351.248	2509.68
2016-07-20	57589.65	OBS4	00036392030	2555.731	2481.073
2016-07-23	57592.5	OBS5	00036392031	2573.434	2522.136
2016-07-24	57593.8	OBS6	00036392032	2988.786	2937.822
2016-07-25	57594.8	OBS7	00036392033	2989.224	2937.383
2016-07-26	57595.8	OBS8	00036392035	2981.172	2915.072
2016-07-27	57596.7	OBS9	00036392034	2768.161	2715.742

Table 4.1 Available Swift observations for PKS 1749+096, corresponding dates (UTC and MJD, IDs and exposure times in kiloseconds.

UVOT data analysis

The Swift Ultra Violet and Optical Telescope (UVOT) telescope (Roming et al. [Rom+05]) cycled through each of its six optical and ultraviolet filters (v, b and u in the optical band, $uw1$, $uvm2$ and $uvw2$ in the ultraviolet) for the different Swift observations. UVOT also features 2 GRISM filters. For an in-depth description of the UVOT photometric system see Poole et al. [Poo+08]. The image mode level II data of all the filters were used in the present analysis with latest calibration files of UVOT. The data were processed following the standard procedure[1] using the `uvotsource` tool within the `heasoft` package.

Source counts were extracted from a circular region of radius 5 arcsec centered on the source, while background counts were derived from an nearby, source-free circular region of around 50 pixels[2]. All available filters in each UVOT observation were searched for variability with the `UVOTMAGHIST` tool. Since no variability was observed in each filter, the multiple images within were summed. Count-rates were then converted to fluxes using the standard photometric zero-points (Poole et al. [Poo+08]). Results are summarized in Table 4.2, while the top panel in Figure 4.1 shows the corresponding light curve. The highest flux observed by UVOT during this period of time corresponds to OBS6 ($F_{uvv} = (2.79 \pm 0.12)\,\mathrm{mJy}$).

[1] `http://www.swift.ac.uk/analysis/uvot/`
[2] The pixel scale of the UVOT instrument is 0.502 arcsec.

Our ID	uvv filter ($\lambda_0 = 5402$Å)		uvb filter ($\lambda_0 = 4329$Å)		uvu filter ($\lambda_0 = 3501$Å)	
	Exp	Flux	Exp	Flux	Exp	Flux
OBS1	78.52	1.58 ± 0.14	392.41	1.04 ± 0.03	314.02	$(5.14 \pm 0.17) \times 10^{-1}$
OBS2	41.07	1.58 ± 0.19	212.72	1.07 ± 0.04	132.41	$(6.79 \pm 0.28) \times 10^{-1}$
OBS3	78.52	2.53 ± 0.15	235.54	1.69 ± 0.05	157.02	$(9.73 \pm 0.29) \times 10^{-1}$
OBS4	145.22	2.42 ± 0.11	206.03	1.51 ± 0.05	145.23	$(8.97 \pm 0.29) \times 10^{-1}$
OBS5	77.52	1.94 ± 0.14	206.25	1.11 ± 0.04	77.53	$(7.35 \pm 0.36) \times 10^{-1}$
OBS6	141.51	2.79 ± 0.12	277.12	1.84 ± 0.05	141.51	1.11 ± 0.03
OBS7	127.72	2.28 ± 0.12	270.22	1.52 ± 0.04	127.71	$(7.53 \pm 0.29) \times 10^{-1}$
OBS8	78.52	2.04 ± 0.14	235.65	1.51 ± 0.04	157.13	$(7.89 \pm 0.26) \times 10^{-1}$
OBS9	136.58	2.34 ± 0.11	228.88	1.62 ± 0.05	136.59	$(8.77 \pm 0.29) \times 10^{-1}$

Our ID	$uvw1$ filter ($\lambda_0 = 2634$Å)		$uvm2$ filter ($\lambda_0 = 2231$Å)		$uvw2$ filter ($\lambda_0 = 2030$Å)	
	Exp	Flux	Exp	Flux	Exp	Flux
OBS1	715.59	$(2.09 \pm 0.09) \times 10^{-1}$	130.26	$(7.19 \pm 1.61) \times 10^{-2}$	729.77	$(8.84 \pm 0.58) \times 10^{-2}$
OBS2	265.29	$(2.85 \pm 0.15) \times 10^{-1}$	79.60	$(1.32 \pm 0.22) \times 10^{-1}$	165.13	$(1.2 \pm 1.3) \times 10^{-1}$
OBS3	314.51	$(3.91 \pm 0.16) \times 10^{-1}$	228.54	$(2.31 \pm 0.16) \times 10^{-1}$	353.14	$(2.00 \pm 0.10) \times 10^{-1}$
OBS4	292.82	$(3.70 \pm 0.16) \times 10^{-1}$	381.91	$(1.83 \pm 0.11) \times 10^{-1}$	586.15	$(1.93 \pm 0.08) \times 10^{-1}$
OBS5	156.26	$(3.18 \pm 0.20) \times 10^{-1}$	204.74	$(1.49 \pm 0.15) \times 10^{-1}$	312.76	$(1.50 \pm 0.10) \times 10^{-1}$
OBS6	283.23	$(4.69 \pm 0.17) \times 10^{-1}$	21.47	$(1.72 \pm 0.46) \times 10^{-1}$	565.72	$(2.21 \pm 0.08) \times 10^{-1}$
OBS7	255.67	$(3.03 \pm 0.16) \times 10^{-1}$	68.62	$(1.78 \pm 0.26) \times 10^{-1}$	512.56	$(1.60 \pm 0.08) \times 10^{-1}$
OBS8	314.51	$(3.46 \pm 0.15) \times 10^{-1}$	803.98	$(1.76 \pm 0.08) \times 10^{-1}$	383.08	$(1.64 \pm 0.09) \times 10^{-1}$
OBS9	272.41	$(3.57 \pm 0.16) \times 10^{-1}$	362.54	$(1.87 \pm 0.12) \times 10^{-1}$	546.03	$(1.97 \pm 0.08) \times 10^{-1}$

Table 4.2 Available UVOT photometric observations for PKS 1749+096. The first column presents our observation ID. Fluxes are in mJy, while exposure times are in seconds.

XRT data analysis

XRT observed the source in photon counting mode in the 0.3 keV-10 keV energy range. Data were analyzed following the standard `XRTPIPELINE` procedure[3] within the `HEASOFT` tools and were calibrated using the last update of `CALDB`. Source counts were extracted with the `xselect` tool from a circular region of 30 pixel ($\sim$ 71 arcsec) radius centered on the source, while background counts were extracted from a source-free region of 50 pixel radius. Pile-up corrections were not necessary given the low count rates of the observations ($< 0.5\,\mathrm{counts}\cdot\mathrm{s}^{-1}$). The ancillary and response files required for spectral fitting were obtained via the `xrtexpomap` and `xrtmkarf` tools. The spectral analysis was performed via `XSPEC`, and data were binned to ensure a minimum of 20 counts per bin.

A power law model was applied for the spectral analysis of each observation. Due to the fact that the source is located in the line of sight of a rather clumpy region, the Galactic molecular hydrogen density is not negligible for this source (Galactic atomic hydrogen column density $N_{HI} = 9.33 \times 10^{20}\,\mathrm{atom\,cm}^{-2}$, molecular hydrogen column density $N_{HII} = 5.58 \times 10^{20}\,\mathrm{atom\,cm}^{-2}$) and thus we fixed the column density to $N_{H,tot} = 1.49 \times 10^{21}\,\mathrm{atom\,cm}^{-2}$ (Willingale et al. [Wil+13]). Moreover, due to relatively high redshift of the source, $z = 0.33$, we also apply the photo-electric absorption model `zwabs` Morrison and McCammon [MM83] that allows to specify a (fixed) redshift parameter.

The energy range was limited for each observation to ensure an acceptable number of event statistics. The main issue for the XRT analysis of this source was that there are no data below 0.5 keV (even below 0.7 keV for some observation), while the energy range of XRT is 0.3 keV-10 keV. This is probably due to strong absorption, which backs up the decision of performing the analysis considering the total hydrogen column density. What is more, there are no data above 5 keV for the majority of the observations either, which left us with a narrow energy domain for model fitting, leading to a broader than usual variability in the free parameters of the model (especially in the photon index). Best fit parameters for each observation are presented in Table 4.3. The data present a 'harder when brighter' tendency, with the brightest XRT observations OBS3 and OBS4 having the hardest spectral indexes among all the observations ($\Gamma = 1.29 \pm 0.12$ and $\Gamma = 1.25 \pm 0.11$ respectively).

[3] `http://www.swift.ac.uk/analysis/xrt/`

Our ID	Energy Range	Photon Index	Normalization	χ^2/d.o.f.
OBS1	0.5 - 5	1.33 ± 0.11	$(1.16 \pm 0.11) \times 10^{-3}$	0.8235 (23)
OBS2	0.7 - 7	1.47 ± 0.15	$(1.24 \pm 0.16) \times 10^{-3}$	0.7981 (14)
OBS3	0.5 - 6	1.29 ± 0.12	$(1.51 \pm 0.15) \times 10^{-3}$	0.6966 (25)
OBS4	0.5 - 6	1.25 ± 0.11	$(1.57 \pm 0.15) \times 10^{-3}$	1.012 (29)
OBS5	0.6 - 4	1.41 ± 0.20	$\left(9.67^{+1.46}_{-1.44}\right) \times 10^{-4}$	0.549 (10)
OBS6	0.5 - 5	1.53 ± 0.16	$\left(8.15^{+0.99}_{-0.94}\right) \times 10^{-4}$	1.401 (15)
OBS7	0.5 - 4	1.51 ± 0.15	$(1.01 \pm 0.11) \times 10^{-3}$	1.332 (18)
OBS8	0.6 - 5	1.55 ± 0.15	$(9.82 \pm 0.13) \times 10^{-4}$	1.10 (17)
OBS9	0.6 - 5	1.39 ± 0.20	$(7.10 \pm 1.10) \times 10^{-4}$	1.024 (11)

Table 4.3 Fit parameters obtained with XSPEC for the available XRT observations of PKS 1749+096 with $N_{H,tot} = 1.49 \times 10^{21}\,\mathrm{atom\,cm^{-2}}$. Energy range and normalization units are in keV and $\mathrm{keV^{-1}\,cm^{-2}\,s^{-1}}$ respectively.

UVOT and XRT light curves

To characterize the X-ray flare in the ToO period with regards to the overall behaviour of the source, we compared the data featured in the 7-year XRT point-source catalog (D'Elia et al. [D'E+13]) to the July 2016 flare data. In order to make a coherent comparison, we reanalyzed the July 2016 data according to the model parameters that were used for the point-source catalog, i.e. a column density of $N_H = 9.74 \times 10^{20}\,\mathrm{atom\,cm^{-2}}$ and an absorbed power law (`phabs` × `powerlaw`). We performed the analysis for two of the three energy ranges/filters from the catalog, i.e. the 0.5 keV-2 keV and 0.5 keV-10 keV ranges, corresponding to the S and F filters respectively. The light curve plots in Figure 4.1 represent the S filter July 2016 flare data (middle), and the overall archival data and flare data in the S filter[4] (bottom). We can see that the source was at quite a high state during the 2016 July flare, although it was not at its historical maximum, which was reached in 2007.

[4]The two filters are shown in the MWL light curve in Figure 4.2.

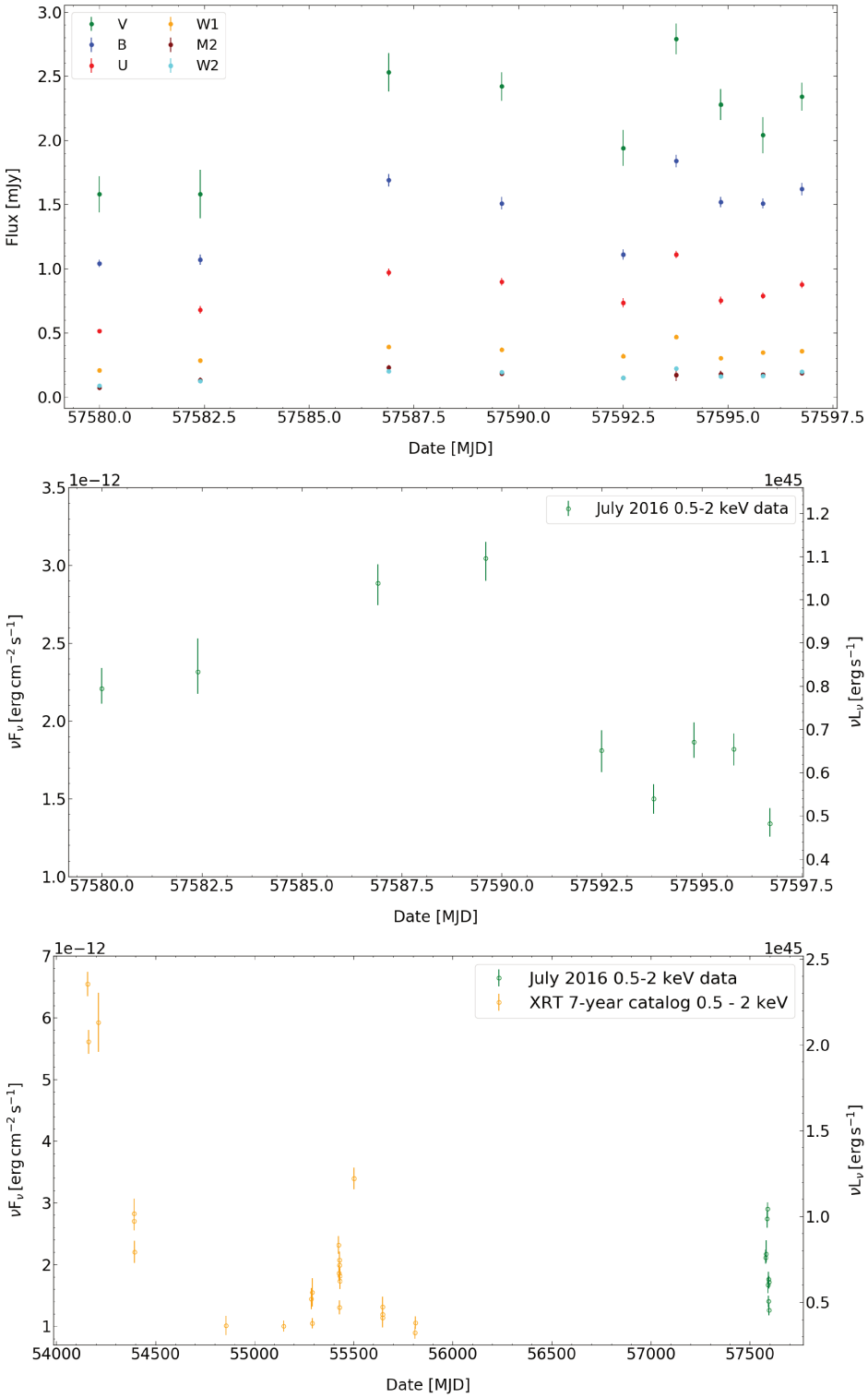

Figure 4.1 UVOT and XRT light curves of PKS 1749+096. **Top:** UVOT light curve for the July 2016 flare of PKS 1749+096. The source entered a high state on 2016-07-17, and underwent a flare on 2016-07-24, with a source doubling time-scale of around ten days. **Middle:** July 2016 flare for the S (0.5 keV-2 keV) and F (0.5 keV-10 keV) filter data from our XRT analysis. **Bottom:** XRT archival and July 2016 flare data for the S filter. From the bottom figure, we can see that the source underwent an enhanced activity period in July 2016, although it is not its historical maximum, which was reached in 2007.

4.2.2 MWL light curves and variability

Figure 4.2 shows the MWL light curve of the July 2016 flare. A closer look of both Figure 4.2 and Figure 4.1 reveals that UVOT, XRT and Fermi-LAT saw the same trend of the source that went from a low optical, X-ray and and gamma-ray state (MJD 57580 - 57582) to an enhanced activity state (MJD 57587 - 57590). However, while the source reached even higher flux levels in the UV and optical around MJD 57594, it had already gone down onto a low state in X-rays and gamma-rays, displaying X-ray fluxes lower even that at the beginning of the July observations. This higher UVOT flux was correlated with enhanced emission seen by ATOM and HESS between MJD 57592 and 57594, though.

Regarding the variability time-scale of the source, XRT presented an approximate flux doubling time between 2 or 3 days, while the Fermi-LAT flux doubled its flux on time-scales between 1.5 and 2 days. These short variability time-scales observed during the July 2016 period observations will need to be taken into account for future modeling purposes, since they set tight constraints on the size of the emitting region of the source by the usual light-travel arguments (Equation 3.8). As a preliminary estimate, a variability time-scale of 1.5 days would yield a source size of $R \leq 5.88 \times 10^{16}\,\mathrm{cm}$ under the assumption of a Doppler factor value of $\delta = 10$, value that falls within the usual values for a LBL source.

4.2.3 Prospect

These preliminary results were presented at the 2017 International Cosmic Ray Conference by the members of the ToO task force of the HESS collaboration (see Schüssler et al. [Sch+17]). The comprehensiveness of the simultaneous dataset presented is suitable for the modeling of the July 2016 high state of the source. The modeling of this high state, possibly with a simple one-zone leptonic SSC model as the one presented in the previous Chapter, will help constraining the parameters of the emission region of the source and to cast light on the emission mechanisms of this source. Indeed, the task force is currently working on a joint MAGIC, Fermi and HESS paper draft of the discovery of the source in VHE and its MWL analysis and modeling.

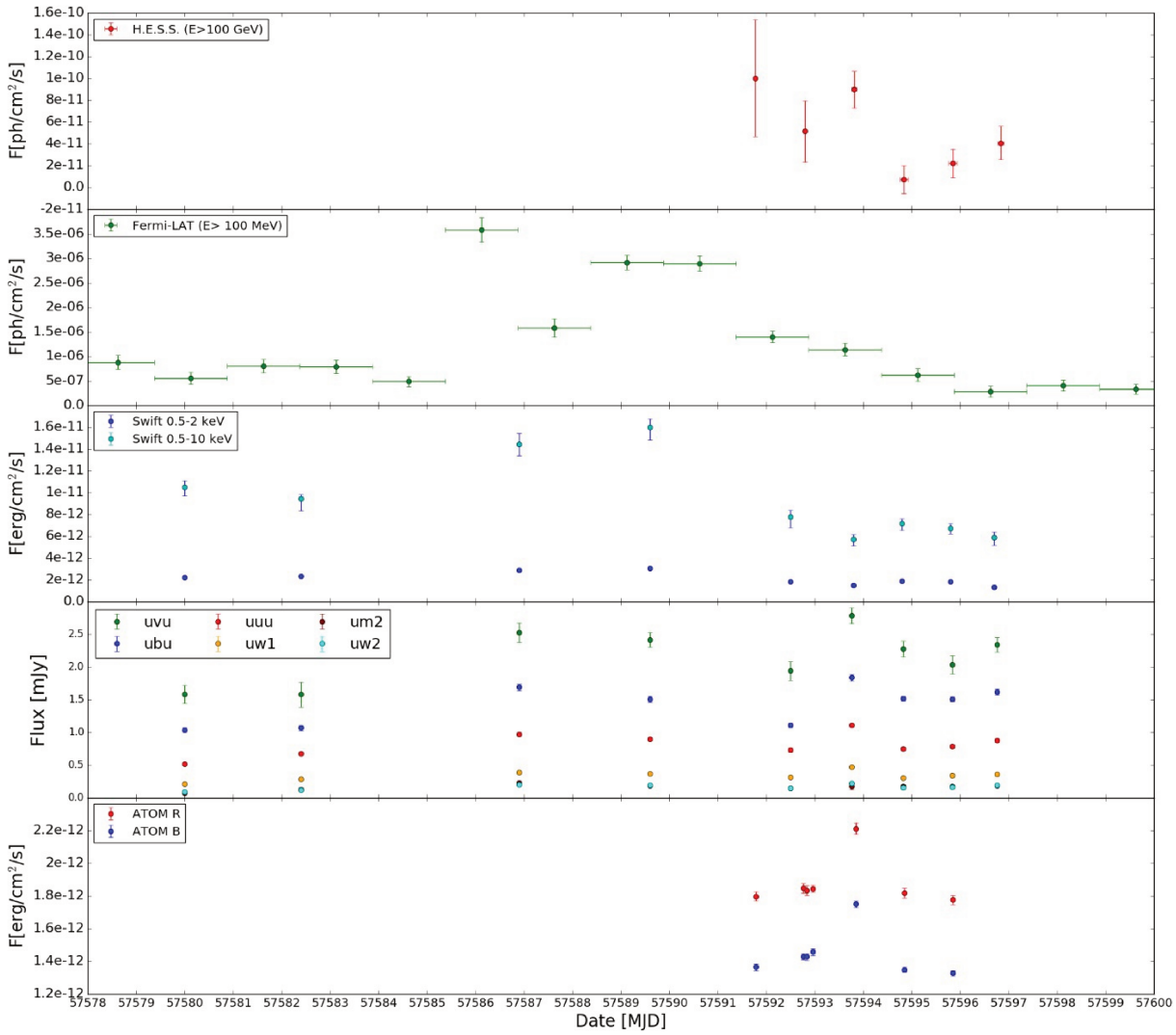

Figure 4.2 MWL light-curve of the July 2016 flare of PKS 1749+096, including data from HESS, Fermi-LAT, Swift XRT and UVOT, and ATOM observations within the ToO campaign. Image updated w.r.t. the preliminary image shown in Schüssler et al. [Sch+17].

The good MWL coverage that was achieved during this short campaign is an indicator of the important role that HESS ToO protocols can play in the bigger picture of MWL observation campaigns. This type of joint effort of facilities that observe gamma-ray emitting sources at different energies will improve our understanding of these fascinating objects.

5 Modeling the HESS-detected HBL 1ES 2322-409

In this Chapter, we present the Multi-WaveLength (MWL) analysis and modeling of the broad-band Spectral Energy Distribution (SED) of the High-frequency-peaked BL Lac (HBL) 1ES 2322−409, whose Very High Energy (VHE) emission was discovered serendipitously by HESS while looking at the nearby source PKS 2316-423. As with many BL Lac type blazars, the redshift of the source is unclear, due to the lack of bright features in its optical spectra. This issue will be discussed also.

We start with a brief description of the source and its main characteristics [Section 5.1], to continue with the analysis that was carried out for the existing HESS data through the Model++ analysis chain [Section 5.2]. Then, results of the analysis of MWL data from a variety of instruments that we performed are presented [Section 5.3]. A quasi-simultaneous dataset is obtained, which is afterwards modeled by the simple-one zone leptonic Synchrotron Self-Compton (SSC) model introduced in Section 3.2 [Section 5.4]. Considering the constraints that are set on the model by the quasi-simultaneity of the dataset chosen for modeling the source, we explore the parameter space of the SSC model parameters in order to evaluate the degeneracy of the solutions. We then provide a SSC model that describes the emission of the source for two different redshifts, $z = 0.17$ and $z = 0.06$ in an effort to cast some light on the preference for one of the values over the other [Section 5.4.1]. A discussion of the model parameters and their implications closes the Chapter.

5.1 The source

1ES 2322−409 (RA = $23:24:44.676$, Dec = $-40:40:49.38$, J2000) is a HBL type BL Lac object that was detected at VHE gamma-rays by the HESS telescopes as a serendipitous source in the field of view of PKS 2316-423 (HESS Collaboration

et al. [HES+08]). Such chance discoveries occur only rarely. In fact, the discovery of this source is the third fortuitous discovery of VHE sources by imaging atmospheric Cherenkov telescopes, following the radio galaxy IC 310 by the MAGIC telescopes (MAGIC Collaboration et al. [MAG+10]) and the blazar 1ES 1312-423, also by HESS (HESS Collaboration et al. [HES+13]).

Due to the weakness or the lack of emission lines in their optical spectra and the oft-dilution of absorption lines from the host galaxy by the non-thermally emitting AGN, the redshift of the majority of BL Lac blazars is hard to infer [Section 1.4.2]. In the case of 1ES 2322−409, the $z \sim 0.17$ value given by the 6dF Galaxy Survey (6dfgs, Jones et al. [Jon+09]) should be considered with caution, since no lines were firmly detected in the spectrum. More recently, Very Large Telescope optical spectroscopy (Landoni et al. [Lan+13]) reported a R magnitude of 15.90 from their spectrum, with whom they should have detected some line with a minimum equivalent width of $EW_{min} = 0.32$ Å. However, they were unable to identify any line to it. On the other hand, several galaxies found around 1ES 2322−409 in shallow redshift surveys (the aforementioned Jones et al. [Jon+09]; Vettolani et al. [Vet+98]; Shectman et al. [She+96]; Ratcliffe et al. [Rat+96]) present a redshift of $z = 0.06$. Both redshifts will be considered for modeling purposes in this work, to see whether one of them is favored by the application of a SSC model.

The source was first detected in X-rays by the Einstein Slew Survey Elvis et al. [Elv+92]. The Rosat All Sky Survey (RASS, Thomas et al. [Tho+98]) identified the X-ray position with an optical counterpart at an angular separation of 5 arcsec. 1ES 2322−409 is also featured in the Rosat Bright Survey by Schwope et al. [Sch+00].

At radio frequencies, the source was detected by the Sidney University Molonglo Sky Survey (SUMSS, [Mau+03]), and Anderson and Filipovic [AF09] also reported its detection at 4.8 GHz amongst a subsample of RASS sources, with a flux of $F_{4.8\,\mathrm{GHz}} = (33.6 \pm 3.2)\,\mathrm{mJy}$.

At infrared frequencies, the source is present in the Two Micron All Sky Survey (2MASS, Skrutskie et al. [Skr+06]), and also in the WISE (Wide-field Infrared Survey Explorer, Wright et al. [Wri+10]) point-source catalog. Observations for two different epochs (May and November 2010) are documented in the catalog, where no major hint of variability is observed.

Optical and UV observations from the Swift Ultra Violet and Optical Telescope (UVOT, Burrows et al. [Bur+05]) are also available for 1ES 2322−409 between 2009 and 2013, with the corresponding Swift X-Ray Telescope (XRT) observations in

the 0.3 keV-10 keV range. A total of 8 observations where taken during the 4-year period. A single observation of 1ES 2322−409 from the Gamma-Ray Optical/Near-infrared Detector (GROND, Greiner et al. [Gre+08]) was taken on October 2010 as reported by Rau et al. [Rau+12]. The simultaneity of the GROND observation (Rau et al. [Rau+12]) and the UVOT pointing of 2010-10-30 will be discussed afterwards, since it is the defining criteria of dataset for the SSC modeling that we perform.

The Rossi X-ray Timing Explorer (RXTE, Bradt et al. [Bra+93]) observed the source at hard X-ray energies (2 keV-60 keV) between the 15th and the 21st December 2011, while the source was in a higher state than the ones observed by XRT, as will be discussed later on. At gamma-rays, the source is present in the general and Fermi point source catalogs (see, for instance the 3FGL paper [Ace+15]).

5.2 HESS discovery and analysis

1ES 2322−409 was first seen at TeV energies while observations of PKS 2316-423 were being carried out, as mentioned in [Section 5.1]. Hence, during the first dataset existing for this source, i.e. 9.3 hours between 2004 and 2006, 1ES 2322−409 was not located in the center of the field of view. Instead, since the observation runs taken were indeed pointed at PKS 2316-423, 1ES 2322−409 was observed with angular distances between 1.4°-2.2°. The angular distance between both sources is around 1.78°.

A second observation campaign was dedicated to 1ES 2322−409 itself between 2011 and 2012, where a total of 16.8 hours worth of data were obtained for the source at offsets between 0.5°-0.9°. All observations were performed for zenith angles between 17°-30°.

After the data-quality selection procedure, the total exposure of the source is 20.6 hours with the Model++ HESS analysis chain. The corresponding list of runs of our source was performed using the software version `v24` and the DST tables corresponding to `model deconvoluted prod 26`. Loose cuts (see Section 2.5.7) were chosen since 1ES 2322−409 is considered to be a faint source. The significance and excess evolution as a function of the number of OFF events is shown in Figure 5.1.

The low significance in the 0- 200 OFF event range is due to the fact that the first data available were not direct pointings towards 1ES 2322−409, but to PKS 2316-423, thus the acceptance of the telescopes was lower[1].

With these cuts, and assuming a power-law spectral shape, the source was detected at a significance of 6.7σ and 6.6σ for the Multiple OFF and the Ring OFF analyses (see Section 2.5.7), respectively, as shown in Figure 5.2. The corresponding gamma-ray excesses are 212.8 and 210.8 respectively.

Maps shown in Figure 5.3 were obtained via the standard Ring Background method. The study of the morphology of the gamma-excess is compatible with a point-like source. The best fit of the gamma-ray excess position is compatible with the position of the source at a 1 σ level, as illustrated in Figure 5.4. A hot spot ($\sim 3\sigma$) corresponding to the source PKS 2316-423 (in the field-of-view of which 1ES 2322−409 was first seen) is also visible in the maps.

1ES 2322−409 being a faint source, the maximum energy cut was set to $E_{max} = 1\,\mathrm{TeV}$ in the spectral analysis in order to keep acceptable statistics for the spectral points. Through the forward-folding technique introduced in Section 2.5.7, a power-law shape of the spectrum is assumed. The log-likelihood minimization procedure yields a reduced Chi-square of $\chi^2/d.o.f = 29.1/26$. We obtain an spectral index of $\Gamma = 3.74 \pm 0.43$ and a flux at 1 TeV is $\phi_{1\,\mathrm{TeV}} = (1.1 \pm 0.7) \times 10^{-13}\,\mathrm{cm}^{-2}\,\mathrm{s}^{-1}\,\mathrm{TeV}^{-1}$, for a decorrelation energy of 0.249 TeV. The corresponding spectrum is shown in Figure 5.6. We want to remark that standard cuts were also tested for the analysis procedure, providing similar results that are compatible within statistics. The run-by-run light curve of 1ES 2322−409 is shown in Figure 5.5.

[1]The acceptance of the camera varies as a function of the radial distance between the center of the camera and a given point.

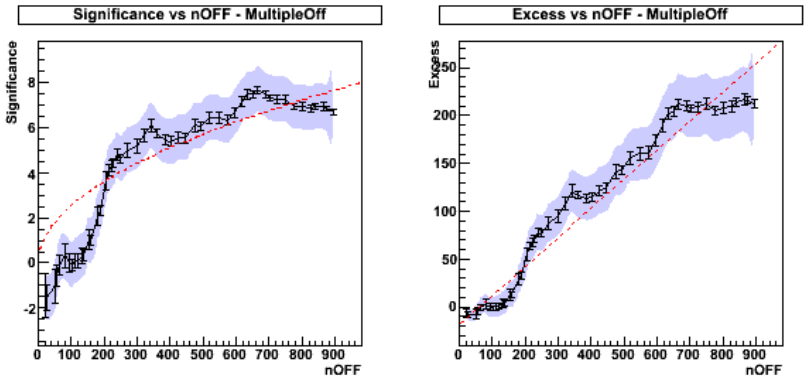

Figure 5.1 The significance and excess evolution of 1ES 2322−409 as a function of the number of OFF events. The red dashed lines represent the expected behaviour of the data, which in the case of the excess is a linear behaviour w.r.t. the OFF events, and in the case of the significance is given by the Li and Ma [LM83] statistics.

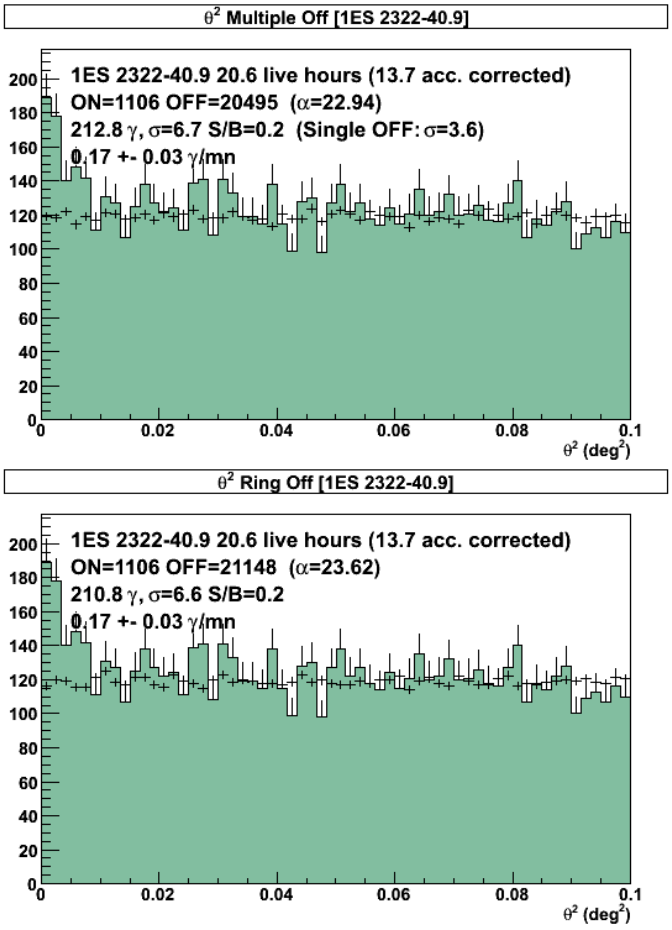

Figure 5.2 Angular distribution of gamma-ray events centered at the nominal position of the source (ON zone, filled histogram). The black crosses represent the distribution of the normalized background within the OFF region of the source.

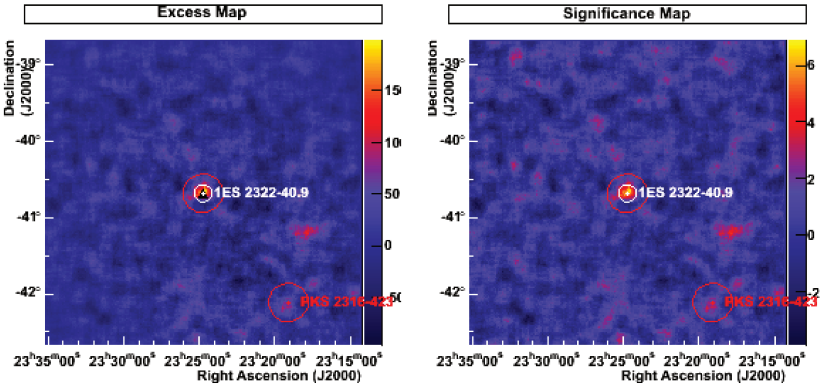

Figure 5.3 Gamma-ray excess and Li and Ma [LM83] significance map of a VHE emitting zone centered on 1ES 2322−409, and corresponding distribution. The hot spot corresponding to PKS 2316-423 is also visible in the maps. The red circles represent exclusion regions.

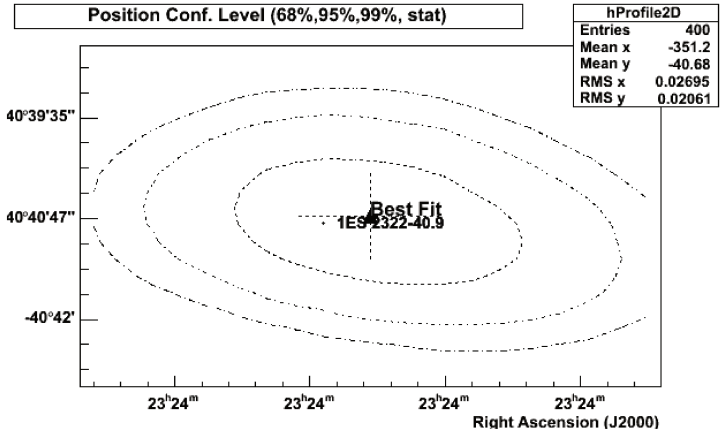

Figure 5.4 Position of the gamma-excess from the HESS analysis of 1ES 2322−409. The best fit is compatible with the position of 1ES 2322−409 at less than 1 σ.

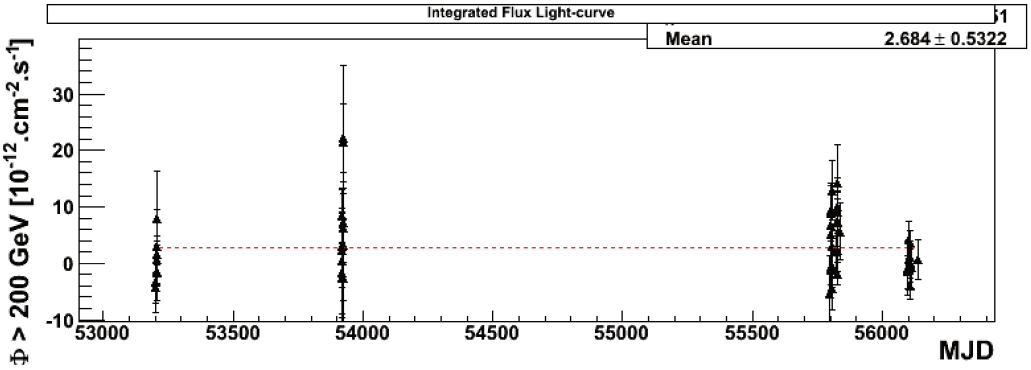

Figure 5.5 HESS run-by-run light curve for all available observations of the source. 4 different periods are evident from the light curve.

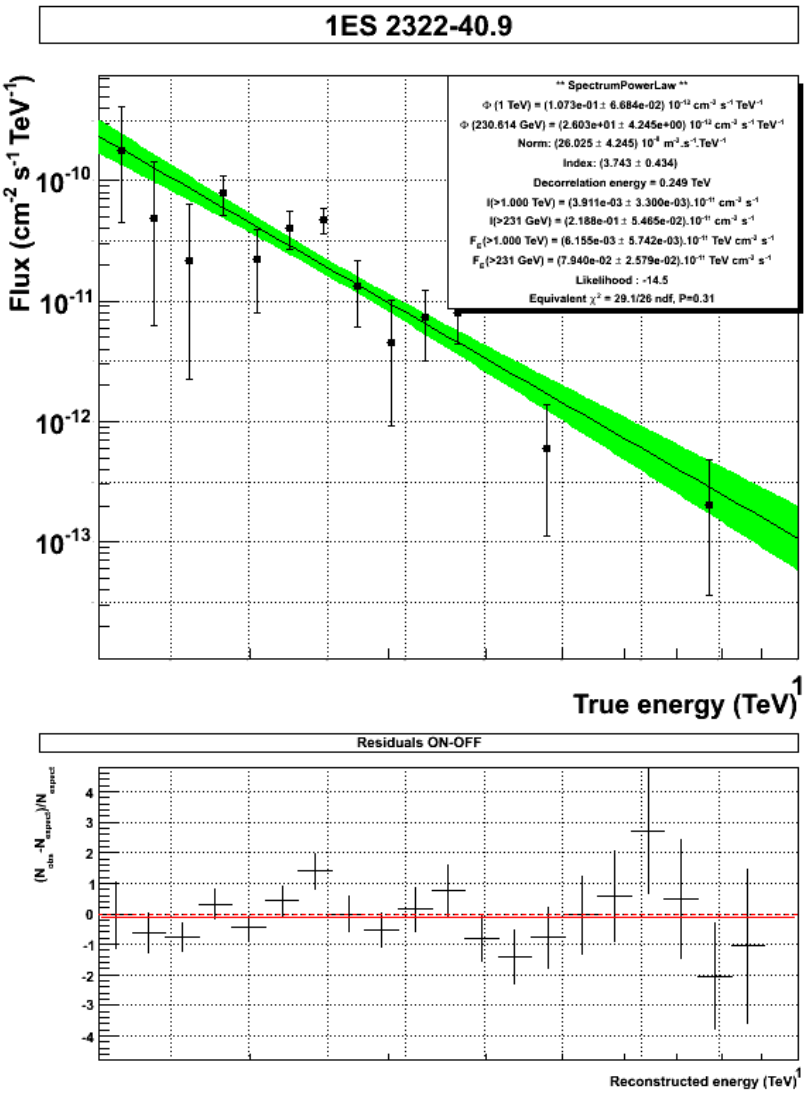

Figure 5.6 **Top:** spectrum of 1ES 2322−409 obtained with Loose cuts, 2σ data points and the maximum energy set to 1TeV. The green band represents the 1 σ confidence band for the assumed spectral shape of the source. **Bottom:** fit residuals $(N_{excess} - N_{expected})/N_{expected}$, where N_{excess} is the number of detected gamma-rays and $N_{expected}$ the number of gamma-rays predicted by the model.

5.2.1 Analysis chain comparison

The analysis that we have just presented was intended as a cross-check to the main analysis chain APC-MVA [Section 2.5.6] used for the publication of the HESS discovery and MWL analysis of 1ES 2322−409. Indeed, the publication policy within the HESS collaboration requires compatibility between at least two independent analysis chains to verify the quality of the results.

Figure 5.7 shows a comparison of the 1 σ confidence bands of the principal analysis performed for the source, APC-MVA, and the X-check performed in this work. The Model++ spectrum extends to somewhat lower energies, since APC-MVA applies more conservative cuts to avoid the influence of potential systematic errors on the effective area. Nevertheless, the results from both analysis chains are clearly compatible.

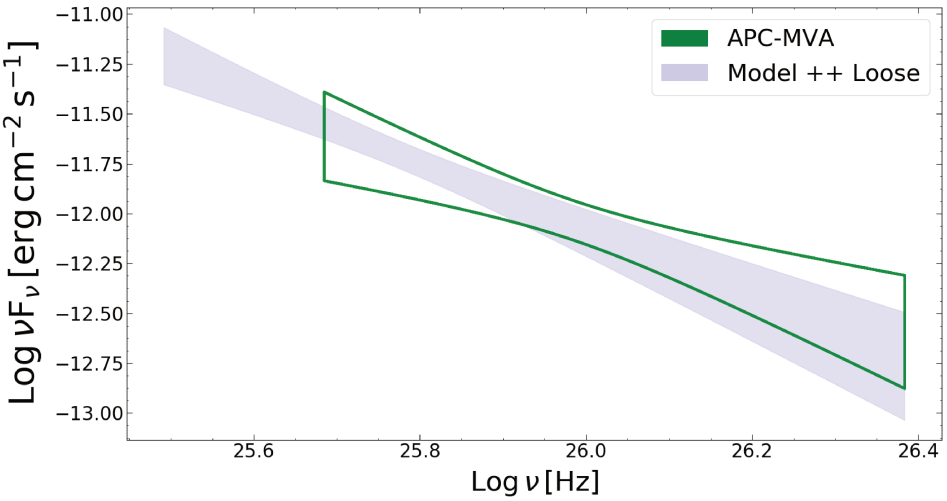

Figure 5.7 Comparison of the results obtained with the Model++ and APC-MVA HESS analysis chains for 1ES 2322−409. Both analyses are compatible, although the Model++ results extend to lower energies.

5.2.2 A closer look at M++ light curves

Linked to the variability that is observed at other wavelengths, we closely inspected the HESS light curves to search for variability at TeV energies.

When looking at the run-by-run light curves obtained with the Model ++ analysis chain, 4 main observation periods can be distinguished (Figure 5.5). A closer look reveals that the first and last periods appear to have an averaged flux close to zero, and actually are upper-limits (Figure 5.8). The first and last periods correspond to upper-limits on the detection of the source.

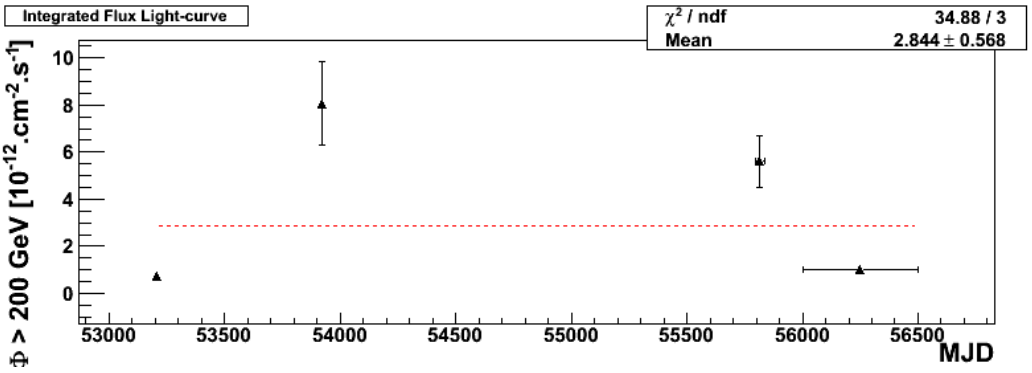

Figure 5.8 Light curve obtained with the Model++ analysis chain for a bin size of 500 MJD in order to separate the data in four distinct periods. Note that the first and last periods are upper-limit detections.

A zero-order polynomial was fitted to the data for each period, as well as to the whole data available in order to verify their contribution level to the overall flux and quantify the variability (if existing) of the source. Results of the fit are shown in Table 5.1.

Data	$\Phi_0 \pm \Delta\Phi$	Prob	χ^2/d.o.f.
Whole	1.18 ± 0.53	0.03	71.05/51
1^{st} period	0.99 ± 1.12 (U.L.)	0.74	4.324/7
2^{nd} period	6.59 ± 1.89	0.40	12.56/12
3^{rd}period	2.56 ± 0.87	0.03	32.5/19
4^{th} period	-0.11 ± 0.94 (U.L.)	0.8936	4.964/10

Table 5.1 Fit values for the zero order polynomial fit of the whole HESS data and the different periods.

From the global fits it appears that there is a 3% chance probability to have the obtained reduced χ^2 or worse if the data follow a constant, which would hint at some degree of variability in the overall light curve.

Regarding individual period fits, the third period presents similar characteristics to the whole dataset, with a chance probability of 3% too. In fact, this 3rd period is the one that contributes the most to the overall flux, and hence the fact that it shows the same tendency as the whole dataset is not striking. The first and fourth periods are upper limits. Last, chance probability of the second period goes up to 40%. One could then conclude that the source went through low states during the whole available HESS dataset.

However, this variability is not seen by the APC-MVA analysis chain, which points to the apparent variable behaviour of the source to originate from differences between the energy threshold of the chains (with the more conservative cuts of APC-MVA). Therefore, a lack of variability is assumed for the 1ES 2322−409, and the whole dataset is considered for modeling the broad-band SED of 1ES 2322−409.

5.3 MWL observations

In order to build the dataset for broad-band modeling purposes, data from a number of facilities that cover the same time-span as HESS observations (2004-2006 and 2011-2012) were gathered. Apart from VHE observations, our MWL study comprises Fermi-LAT (100 MeV–500 GeV), RXTE (2–60 keV), Swift XRT (0.2–10 keV) and Swift UVOT (uvv, uvb, uvu, $uvw1$, $uvm2$ and $uvw2$ filters), GROND (Sloan optical g, r, i and z, along with infrared J, H and K filters), WISE (3.6, 4.6, 12 and 22 μm), Catalina (V band) and ATOM (optical B and R filters) data.

All these data were closely inspected to investigate the behaviour of the source. However, most of them are not simultaneous, except for a small time-window when Fermi, Swift, Catalina, and GROND performed simultaneous observations (see Figure 5.12). These contemporaneous observations determine the epoch that is considered for the modeling. We need to underline that Fermi-LAT data were

analyzed by Jean-Philippe Lenain (LPNHE), so the analysis procedure will not be described here. We refer to the paper for more details.

5.3.1 RXTE

X-ray observations of 1ES 2322−409 were performed with the Proportional Counter Array (PCA, Jahoda et al. [Jah+96]) onboard the RXTE spacecraft. The PCA is an array of five identical xenon-filled proportional counter units that cover the energy range 2 - $60\,\mathrm{keV}$ with a total collecting area of 6500 cm^2. Seven pointings were nightly taken from the 15th to the 21st December 2011 for 1ES 2322−409. The exposures of the PCA units for the nightly pointings are listed in Table 5.2.

Date	MJD	Our ID	RXTE ID	Exp (ks)
2011-12-15 02:11:44	55910.09	OBS A	96141-01-01-00	6.3
2011-12-16 01:38:56	55911.06	OBS B	96141-01-02-00	5.94
2011-12-16 23:32:48	55911.98	OBS C	96141-01-03-00	5.41
2011-12-18 00:33:52	55913.02	OBS D	96141-01-04-00	2.34
2011-12-19 01:34:40	55914.06	OBS E	96141-01-05-00	6.54
2011-12-19 21:54:40	55914.91	OBS F	96141-01-06-00	5.68
2011-12-21 00:29:36	55916.02	OBS G	96141-01-07-00	5.68

Table 5.2 Available RXTE observations, corresponding dates and exposure times.

The analysis was performed using the standard `HEASOFT` (v6.16) and `XSPEC` (v12.9) tools. The `STANDARD2` data with a time resolution of 16 seconds and with energy information in 128 channels were extracted and filtered following the RXTE guest observer facility recommended criteria. Data were binned to ensure a minimum of 20 counts per bin. Despite the broader energy range of the instrument, the source only presented sufficient statistics for the 3 - $7\,\mathrm{keV}$ energy range. Thus, the average spectrum from of all the 7 PCA observations was calculated in this energy range for a power law function. An F-test between a power law fit and a broken power law fit showed no preference for the latter model.

Usually just the atomic hydrogen column density N_{HI} is considered in order to account for the galactic absorption of the X-ray emission from the source. But,

similar to PKS 1749+096 in Chapter 4, the molecular hydrogen column density of 1ES 2322−409 is not negligible. Therefore, the Galactic column density was fixed to the total value $N_{H,tot} = 1.67 \times 10^{20}$ atom cm^{-2}, which yielded a photon index of $\Gamma = 2.80 \pm 0.15$ and a normalization at 1 keV of $\Phi_0 = (7.26^{+1.80}_{-1.43}) \times 10^{-3}$ keV^{-1} cm^{-2} s^{-1} (see Table 5.3 for fit parameters).

In order to obtain the integrated flux light curve, we performed observation-by-observation analyses. To do so, due to low net count rates, we fixed the photon index of all individual observations to that of the average state. Corresponding fluxes in the 3 keV-7 keV range along with fit results are presented in Table 5.3.

A small flare can be inferred from the light curve between the 18th and the 19th December (Figure 5.9). The fit of a constant to the light curve indicates evidence for variability with a chance probability of $\sim 0.1\%$. To study possible spectral variations between the flare and the quiescent state, we performed an analysis of the observations corresponding to the flaring days subset (i.e. obs D and E) and another for the quiescent state observations (the rest of them). Corresponding spectral energy distributions are shown in Figure 5.10. However, due to small contribution of the high state to overall statistics, and given that RXTE data are not simultaneous to the high Swift state that we considered for the modeling, the average spectrum was considered for the MWL SED of the source, whose fit parameters are also shown in Table 5.3.

The fastest variability time-scale of around 1.5 days observed during the RXTE flare is considered for setting constraints on the variability time-scale of the source, which, as mentioned in Equation 3.8 in [Section 3.2], sets an upper limit on the size of the source within the SSC model framework. For instance, assuming a 'standard' Doppler bulk factor value for HBL objects of $\delta = 20$, the upper limit of the size of 1ES 2322−409 would be $R \leq 6.64 \times 10^{16}\,\mathrm{cm}$ and $R \leq 7.73 \times 10^{16}\,\mathrm{cm}$ for the $z = 0.17$ and $z = 0.06$ assumptions considered in this work.

Our ID	Photon Index	Normalization	χ^2_{red} (d.o.f.)	F
TOTAL	$2.80\ ^{+0.15}_{-0.15}$	$(7.26\ ^{+1.80}_{-1.43})\times10^{-3}$	1.13 (7)	$2.93^{+0.82}_{-0.86}$
OBS A	2.8	$(6.56^{+0.49}_{-0.49})\times10^{-03}$	0.970 (8)	$2.69^{+0.20}_{-0.19}$
OBS B	2.8	$(5.94^{+0.50}_{-0.50})\times10^{-03}$	0.334 (8)	$2.43^{+0.20}_{-0.20}$
OBS C	2.8	$(7.50\ ^{+0.68}_{-0.68})\times10^{-03}$	0.286 (8)	$3.06^{+0.28}_{-0.28}$
OBS D	2.8	$(1.23\ ^{+0.17}_{-0.17})\times10^{-02}$	0.733 (8)	$5.05^{+0.70}_{-0.70}$
OBS E	2.8	$(9.55\ ^{+1.01}_{-1.01})\times10^{-03}$	0.561 (8)	$3.92^{+0.41}_{-0.41}$
OBS F	2.8	$(7.26\ ^{+1.07}_{-1.07})\times10^{-03}$	0.192 (8)	$2.98^{+0.43}_{-0.44}$
OBS G	2.8	$(6.96\ ^{+1.06}_{-1.06})\times10^{-03}$	0.831 (8)	$2.85^{+0.44}_{-0.43}$

Table 5.3 Fit parameters obtained with XSPEC for RXTE observations (columns 2, 3 and 4), along with the 3 - 7 keV integrated flux in units of 10^{-12} erg cm^{-2} s^{-1} (column 5). Normalization units are keV^{-1} s^{-1} cm^{-2}. The photon index of individual observations was fixed to that of the average state due to low count-rates. See the text for more details.

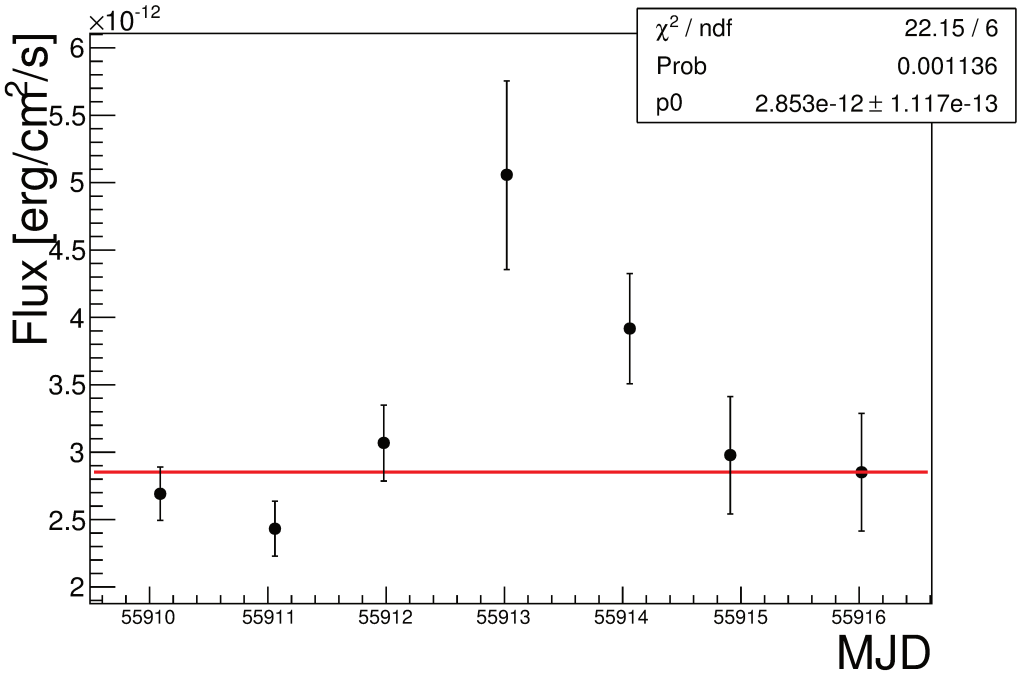

Figure 5.9 RXTE light curve for all the observations available. The fit of a constant (red line) to the light curve indicates evidence for variability with a chance probability of $\sim 0.1\%$, a strong indication of the variable behaviour of 1ES 2322−409 in this period of time. Dates are in MJD. See text for more details .

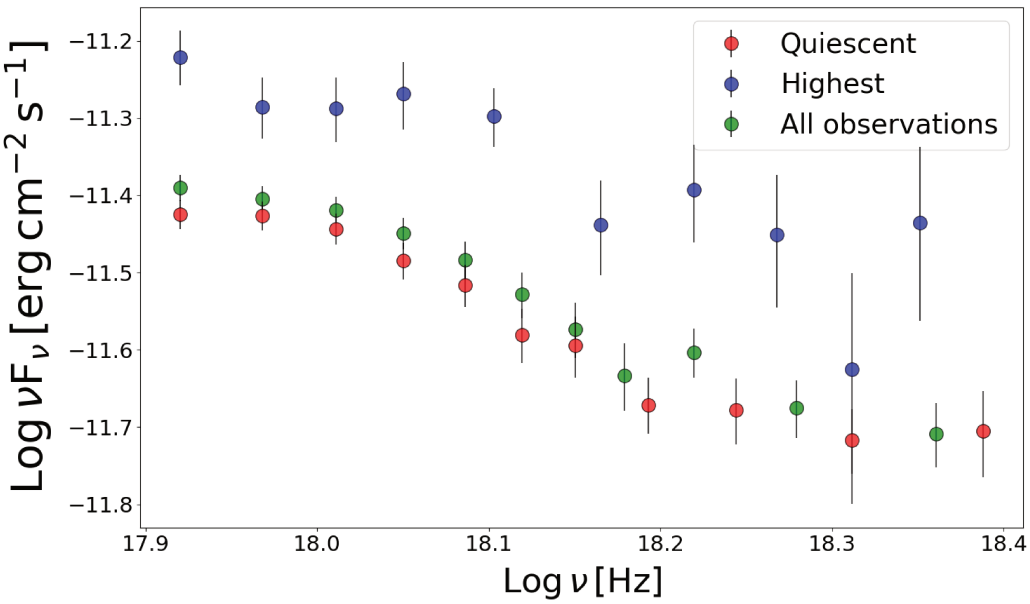

Figure 5.10 SED of the flaring and quiescent subsets of RXTE observations, along with the averaged value. Due to poor statistics, the averaged points are considered for further analysis.

5.3.2 Swift

There are eight different Swift (Burrows et al. [Bur+05]) observations available from November 2009 to October 2013 (OBS 1 to 8, see Table 5.4 for exact dates and exposure times). UVOT and XRT analyses have been performed both separately for each observation and considering all the eight observations together.

Date	MJD	Our ID	Swift ID	Exposure (ks)
2009-11-17 13:37:00	55152.56	OBS1	00031537001	4.43
2010-03-30 06:53:00	55285.28	OBS2	00040685001	1.18
2010-03-30 08:33:00	55285.35	OBS3	00040685002	4.50
2010-10-30 05:33:00	55499.23	OBS4	00041657001	1.13
2010-10-30 10:24:01	55499.43	OBS5	00041656001	1.23
2012-11-04 02:51:00	56235.11	OBS6	00040854001	1.24
2013-10-09 18:41:29	56574.77	OBS7	00031537002	3.97
2013-10-12 00:54:00	56577.03	OBS8	00031537005	3.12

Table 5.4 Available 8 Swift observations, corresponding dates, IDs and exposure times in kiloseconds.

XRT

The procedure presented for the XRT analysis of PKS 1749+096 in Chapter 4 was also followed for 1ES 2322−409. In the case of 1ES 2322−409, though, OBS5 is not considered for further analysis since the source is barely in the field of view and in a region with badly corrected exposure maps.

In the case of the observation with the best statistics, energies ranged from 0.4 - 6.0 keV, while for the integrated fluxes featured in the light curve (Figure 5.12), a common range from 0.4 - 4.0 keV was selected. Similar to the RXTE data analysis, an absorbed powerlaw with the total Galactic hydrogen column density was fit to the different datasets. Table 5.5 gathers the best-fit parameters derived for each individual observation, along with the integrated fluxes. The XRT light curve (Figure 5.12) shows variable behaviour of the source on time-scales of a couple of months, with OBS1 and OBS4 having the largest fluxes.

A closer look to the fit parameters from Table 5.5 reveals a "harder when brighter" trend, with the brightest observation, OBS4, presenting the hardest spectral index, $\Gamma = 2.14 \pm 0.09$, closely followed by the second brightest observation, OBS1 with an index of $\Gamma = 2.35^{+0.05}_{-0.06}$. The faintest observation, OBS6, has the largest spectral index, $\Gamma = 2.67 \pm 0.17$, which overlaps with the index of the total spectrum considered for RXTE, $\Gamma = 2.80 \pm 0.15$. This is also visible in Figure 5.11. The modeling presented in Section 5.4 will focus on the high state of the source as seen by Swift in OBS4.

Our ID	Energy Range	Photon Index	Normalization	χ^2_{red}(d.o.f.)	F
OBS1	0.4 - 6	$2.35\ ^{+0.05}_{-0.06}$	$(2.32 \pm 0.07) \times 10^{-3}$	1.08(52)	$8.09^{+0.46}_{-0.46}$
OBS2	0.4 - 4	$2.30\ ^{+0.15}_{-0.15}$	$(1.13 \pm 0.09) \times 10^{-3}$	0.76(8)	$3.95^{+0.24}_{-0.34}$
OBS4	0.4 - 4	$2.14\ ^{+0.09}_{-0.09}$	$(2.59 \pm 0.13) \times 10^{-3}$	1.10(21)	$9.27^{+0.31}_{-0.31}$
OBS6	0.4 - 4	$2.67\ ^{+0.17}_{-0.17}$	$(1.01 \pm 0.09) \times 10^{-3}$	1.01(7)	$3.47^{+0.52}_{-0.52}$
OBS8	0.4 - 5	$2.43\ ^{+0.19}_{-0.18}$	$(1.17 \pm 0.06) \times 10^{-3}$	1.10(15)	$4.06^{+0.81}_{-0.80}$

Table 5.5 Fit parameters obtained with XSPEC for the available XRT observations, along with the 0.4 - 4.0 keV integrated flux in units of 10^{-12} erg cm^{-2} s^{-1} featured in the light curve shown in Figure 5.12. Energy range and normalization units are in keV and keV^{-1} cm^{-2} s^{-1} respectively. As will be explained in the next subsection, neither OBS3 nor OBS7 are considered for the analysis of the source due to UVOT constraints.

UVOT

The same procedure presented for PKS 1749+096 in Chapter 4 was followed for the UVOT analysis of 1ES 2322−409. However, in the case of 1ES 2322−409, for OBS3 only the $uvw2$ filter was available, which reduces the information about the spectra that this observation provides. Thus, OBS3 was not further considered for the analysis. On the other hand, OBS7 was of GRISM type, and hence it was not possible to obtain a photometric analysis from it, so we did not consider it for analysis purposes either.

Note that each UVOT observation was searched for variability over the different extensions with the `uvotmaghist` tool, and it was verified that the source did not vary over the exposure time of each observation. The source did, however, exhibit variability between different observations, reaching a maximum flux around MJD 55500 (see Table 5.6 and Table 5.7 for UVOT exposure times and magnitudes for each passband). The reported fluxes are de-reddened for Galactic absorption following the procedure in Roming et al. [Rom+09], with $E(B-V) = 0.0200 \pm 0.0004$. Figure 5.11 presents the joint UVOT and XRT SED obtained in our analysis.

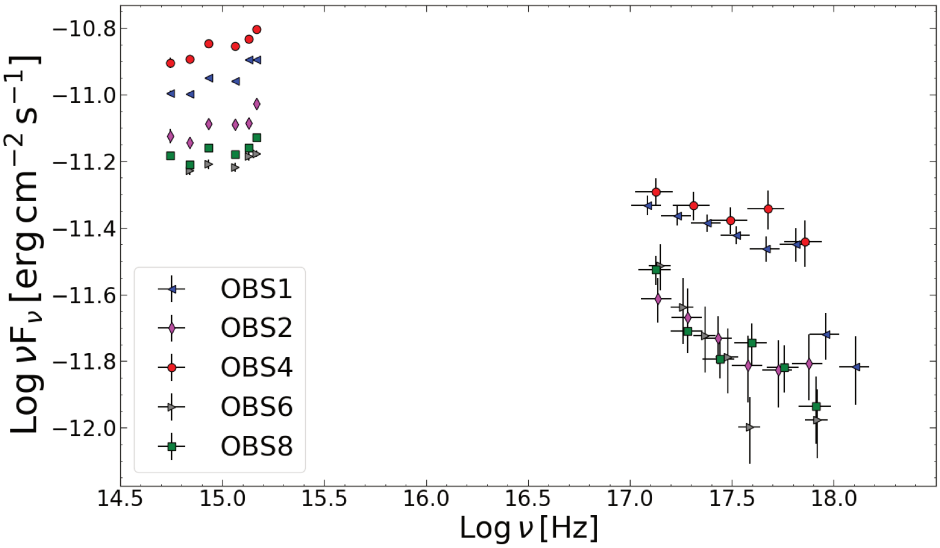

Figure 5.11 SED of different Swift UVOT (absorption corrected) and XRT observations. Red points correspond to the highest state (OBS4) that will be afterwards used for the modelling of the source's energy distribution. Blue, magenta, red, gray and green points correspond to OBS 1, 2, 4, 6 and 8 respectively.

Our ID	Ext.	uvv filter ($\lambda_0 = 5402$Å)			uvb filter ($\lambda_0 = 4329$Å)			uvu filter ($\lambda_0 = 3501$Å)		
		Exp	Mag	Flux	Exp	Mag	Flux	Exp	Mag	Flux
OBS1	7	266.4	15.79±0.04	1.76±0.06	266.4	16.16±0.03	1.39±0.04	266.4	15.17±0.03	1.23±0.03
OBS2	1	95.2	16.09±0.07	1.33±0.08	95.2	16.50±0.05	1.02±0.04	95.2	15.51±0.04	0.90±0.03
OBS4	1	100.1	15.57±0.05	2.15±0.10	100.1	15.91±0.03	1.75±0.06	100.2	14.94±0.03	1.52±0.05
OBS6	2	-	-	-	40.2	16.62±0.07	0.91±0.06	40.1	15.83±0.04	0.67±0.04
OBS8	6	187.1	16.23±0.05	1.17±0.05	243.9	16.68±0.03	0.86±0.03	244.0	15.72±0.03	0.75±0.02

Table 5.6 Available UVOT photometric observations. The first column presents our observation ID, while the second states the number of individual images (extensions) within each observation. Magnitudes and fluxes (non corrected for absorption) are in the Vega system and in mJy Hz^{-1} respectively, while exposure times are in seconds.

Our ID	Ext.	$uvw1$ filter ($\lambda_0 = 2634$Å)			$uvm2$ filter ($\lambda_0 = 2231$Å)			$uvw2$ filter ($\lambda_0 = 2030$Å)		
		Exp	Mag	Flux	Exp	Mag	Flux	Exp	Mag	Flux
OBS1	7	534.2	15.04±0.03	0.86±0.02	555.6	14.96±0.03	0.80±0.02	1069.6	15.01±0.02	0.73±0.02
OBS2	1	190.7	15.37±0.04	0.64±0.02	289.8	15.29±0.04	0.59±0.02	381.7	15.34±0.03	0.54±0.01
OBS4	1	200.6	14.83±0.03	1.04±0.03	300.1	14.71±0.03	1.00±0.03	401.3	14.82±0.03	0.87±0.02
OBS6	2	85.6	15.75±0.06	0.45±0.02	120.8	15.50±0.06	0.48±0.03	161.2	15.80±0.05	0.35±0.02
OBS8	6	491.9	15.66±0.03	0.49±0.01	368.6	15.53±0.04	0.47±0.02	918.2	15.68±0.03	0.40±0.01

Table 5.7 Continuation of Table 5.6.

5.3.3 Additional archival data

As mentioned in Section 5.1, the source has historically been observed by a number of facilities.

The ATOM telescope (see Section 2.5.4) observed 1ES 2322−409 in the R and B bands between MJD 55850 and 56300, which makes them simultaneous to HESS data only for a short period of time. As can be seen from Figure 5.12, the source went into a state of increasing flux with a hint of a flare peaking between MJD 55850 and MJD 56000. Another smaller flare was observed around MJD 56100-56150.

WISE observations were taken in two different time windows: the four filters (3.4 μm, 4.6 μm, 12 μm and 22 μm) were active during the first one ($\sim$ MJD 55340), but only two (W1 and W2) remained for the second one ($\sim$ MJD 55530). WISE is an infrared-wavelength astronomical space telescope launched in December 2009. With a 40-centimeter-diameter (16-inch) aperture, it was designed to continuously image broad stripes of sky at four infrared wavelengths as the satellite orbits the Earth. Given that the second time window for which observations exists is contemporary to the highest Swift observation, light curves were closely inspected in search of variability during this contemporaneous period. The lack of it allows us to consider the averaged spectral points for the SED.

Data are also available from the Catalina Sky Survey (CSS, Drake et al. [Dra+09]) over the same period of time as the Fermi-LAT data sampled here. The CSS consists of seven years of photometry taken with the Catalina Schmidt Telescope located in Arizona (USA). Figure 6 presents V mag light curve for 1ES 2322−409, which is found to be highly variable in the optical, confirming the tendency also observed with ATOM. The CSS dataset was used mainly for exploring the longterm variability of the source, but it is not considered for modeling purposes because the telescope does not have a filter, so it is not possible to convert the data into a spectrum. CSS data confirm the variable nature of the source at optical frequencies, as seen by ATOM.

Last, a single GROND observation was taken on 2010-10-30 at 05:42 (Rau et al. [Rau+12]), which makes this observation simultaneous to the Swift high state (see Figure 5.11 and the light curve in Figure 5.12). GROND is a 7-channel imager mounted at the MPG/ESO 2.2 m telescope in La Silla, Chile. Three infrared bands (J = 1.24 μm, H = 1.63 μm, K_s = 2.19 μm) and the Sloan optical bands (g = 475 nm, r = 622 nm, i = 763 nm, and z = 905 nm) are observed simultaneously, which is particularly interesting to analyze rapidly-variable sources such as blazars. According

to (Kruhler et al. [Kru+11]), the spectral overlap of UVOT and GROND can be used to correct the data between both instruments and make further comparison. Hence, we applied the variability-correction factor $\Delta M_{GR \to UV} = 0.3$ from Rau et al. [Rau+12] based on the mentioned spectral overlap to directly compare GROND data to the corresponding simultaneous UVOT data of OBS4.

5.3.4 MWL light curves

The MWL light curves for the data from the aforementioned instruments are shown in Figure 5.12. There is no evidence of strong variability observed in gamma-rays in the Fermi-LAT and HESS data (see Section 5.2.2), but variable behaviour is seen both in optical, with time-scales of around a month for Catalina and ATOM, and in X-rays, with around 1.5 day variability time-scale in RXTE and a few months in XRT.

Swift UVOT and XRT observations show correlated behaviour: higher fluxes in UVOT have high flux counterparts in XRT. Moreover, the highest flux observed with ATOM was contemporary to the flare observed in RXTE around MJD 55900, which closely followed the highest state observed with HESS (around MJD 55800). This is a hint towards the emission originating from the same region of the AGN.

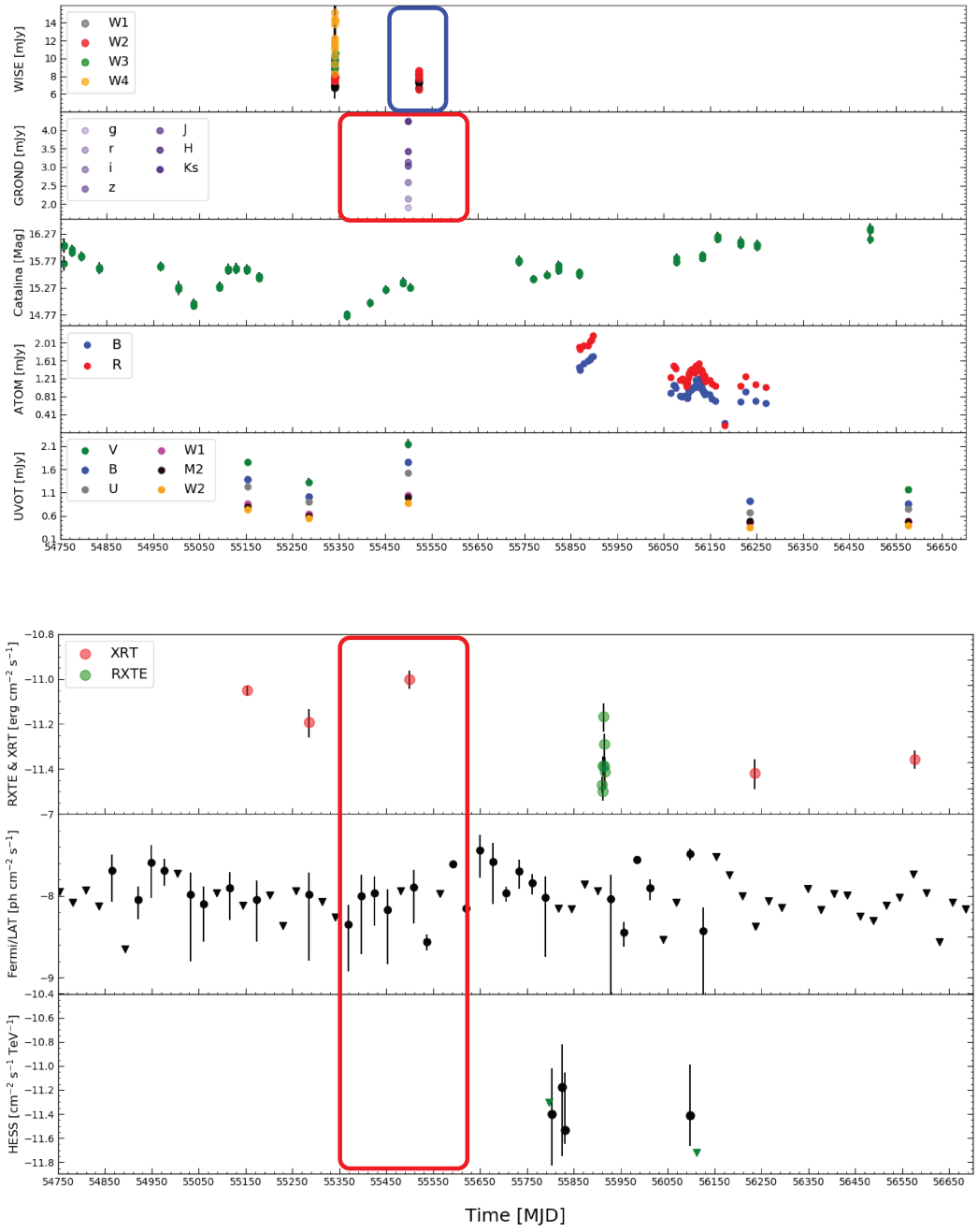

Figure 5.12 Multi-wavelength light curves of 1ES 2322−409, from MJD 54750 to MJD 56700, in order of increasing energy, i.e. from top to bottom WISE, GROND, Catalina, ATOM, UVOT (non corrected for absorption), XRT, RXTE, Fermi-LAT (upperlimits as black triangles) and HESS (upperlimits as green triangles). The red rectangle encompasses the available simultaneous data, i.e. GROND, Swift UVOT and XRT, and Fermi-LAT data, which are used for the modeling of the Swift high state of the source, while the blue rectangle shows the contemporaneous WISE data, also considered for the modeling. Note that a zoom into the epoch for which most MWL observations were taken has been applied, so the totality of existing HESS data are not shown in this picture (see Figure 5.5 for the whole HESS light curve). All the available HESS data is considered for the modeling.

5.4 Modeling the SED

The general lack of simultaneous data over all wavelengths represents a difficulty for the interpretation of the SED of this source. Like we have previously mentioned, we construct a high state dataset for further analysis centered in the Swift observations that present the highest flux. Figure 5.11 presents the SED of the Swift observations that were analyzed, and OBS4 stands out as the brightest in UVOT and XRT data (MJD 55499).

The dataset we will use for modeling then comprises XRT and UVOT data from MJD 55499, the simultaneous GROND observations, Fermi-LAT data between MJD 55350 and 55650 and the whole HESS data set. The contemporaneous WISE observations ($\sim$ MJD 55530) are also considered for the modeling, due the aforementioned lack of variability. The simultaneous data are shown with a red rectangle in the MWL LCs shown in Figure 5.12, while the contemporaneous WISE data are surrounded by a blue rectangle.

The SED corresponding to the selected broad-band dataset is shown in Figure 5.15. We interpreted the data by applying the one-zone stationary homogeneous SSC model based on Katarzyński et al. [Kat+01] that has been presented in Section 3.2. For the sake of the discussion, we will recall that the model can be completely described with three parameters related to the global features of the emitting region, i.e. the magnetic field B, the radius of the emission region R and its bulk Doppler factor δ, and with six parameters linked to the electron energy distribution, i.e. the indexes of the broken power law particle energy distribution before and after the energy break n_1 and n_2, the minimal and maximal electron energies γ_{min} and γ_{max}, the break energy γ_b and the normalization of the electron distribution at $\gamma = 1$.

5.4.1 Results

As Figure 5.13 shows, the simultaneity of the UVOT, GROND and XRT, along with the quasi-simultaneous WISE data help to greatly constrain the position and shape of the synchrotron peak of the SED. The position of the Compton hump of the energy distribution can in turn be well constrained by the Fermi-LAT data and HESS data at HE and VHE respectively.

The estimation of the position of the synchrotron peak and Compton peak energies serves as a starting point to define the value of the electron distribution break energy γ_b. The break energy in the electron distribution γ_b is proportional to the square root of the ratio of the peak emission energies, and should be around $(3\nu_c\,/4\nu_s\,)^{1/2}$ (Equation 3.9).

In order to have a more accurate estimation of the synchrotron peak (other than estimating its position by eye), a log-parabolic function was fitted to the Swift high state, the GROND and WISE data (see Figure 5.13). The fit yielded a pivot energy of $E_0 = (0.002\,98 \pm 0.000\,28)\,\mathrm{keV}$, an index of $\alpha = 0.609 \pm 0.040$, and a curvature of $\beta = 0.174 \pm 0.011$. Based on the approach by Massaro et al. [Mas+04], were the energy of the peak of the log-parabola is given by

$$E_p = E_0 10^{(2-a)/2b} \tag{5.1}$$

we calculated the approximate synchrotron peak frequency, which is estimated to be $\nu_S \sim 7 \times 10^{15}$ Hz. On the other hand, from the high energy data of the source (Fermi-LAT and HESS bow-ties in Figure 5.15) it can be seen that the curvature of the IC component takes place at 10^{25} Hz, which in the Thomson regime yields $\gamma_b \sim 3 \times 10^4$ (Equation 3.9).

From Equation 3.11 and Equation 3.16 we know that the $B - \delta$ product, and hence their parameter space, is also constrained by the synchrotron and Compton peak positions and by the ratio of the corresponding luminosities. Given this constraint, the combined magnetic field and Doppler factor parameter space was explored in order to find the most suitable parameter range for our simultaneous and contemporary data set. Figure 5.14 shows the parameter space for the two different redshifts considered for the source. The yellow and green bands correspond to the luminosity and peak constraints from Tavecchio et al. [Tav+98], whereas the vertical blue line represents the pair-production constraint from the same publication. The diagrams show that for the lower redshift $z = 0.06$ consistency is attained (i.e. valid solutions exist) roughly in the $\delta \sim$ [5, 100] and $B \sim$ [10^{-4}, 1] G ranges, and within $\delta \sim$ [10, 100] and $B \sim$ [3×10^{-4}, 0.6] G ranges for the higher one.

As indicated in Equation 3.8, the variability time-scale constrains the radius of the blob for a given Doppler factor δ via the usual light travel arguments. For a given redshift and Doppler factor of the source, Equation 3.8 yields the maximal size of the spherical emission region one can expect for the observed fastest variability of the source, and serves as a limit to the input parameter of the radius of the source

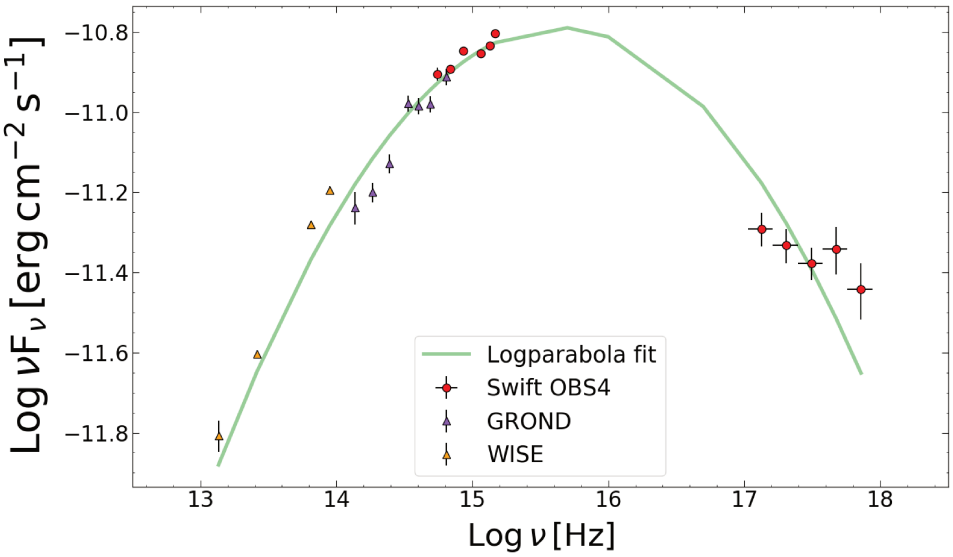

Figure 5.13 Spectral energy distribution of the source zoomed over the synchrotron peak energy range. In green, log-parabolic fit of the simultaneous GROND, UVOT and XRT data along with contemporaneous WISE data, which helps to determine the location of the synchrotron peak of the source. Orange and violet triangles correspond to WISE and GROND data respectively, while red circles represent Swift UVOT and XRT data for the high state (OBS4).

applied in the SSC model. Here, we used the ~ 1.5 day variability time-scale of the jet as seen in the X-ray band by RXTE, as introduced in Section 3.2. More simultaneous MWL data would be necessary for a better time sampling of the source that allows better constraints on its variability.

To further constrain the SSC model and reduce its degeneracy, the parameter space was systematically explored via the algorithm developed by Cerruti et al. [Cer+13a] (see Section 3.2). Based on a number of observables as input (i.e. the approximate synchrotron and Compton peak frequencies and luminosities, the GeV slope, the TeV slope, the variability time-scale of the source), Cerruti et al. [Cer+13a] scan the multi-dimensional parameter space through simulations of a vast number of SEDs, to compare them to the actual observed broad-band SED. The algorithm selects solutions that are compatible with observations, but no χ^2 minimization is performed.

To reduce the number of free parameters of the algorithm, some input parameters can be fixed if the data are constraining enough. For 1ES 2322−409, both XRT and Fermi-LAT spectra set strong constraints on the first and second slopes of the electron distribution, and hence were fixed to values within the uncertainties of the spectral indexes obtained from our analysis, i.e. $n_1 = 1.7$ ($z = 0.06$), $n_1 = 1.8$ ($z = 0.17$) and

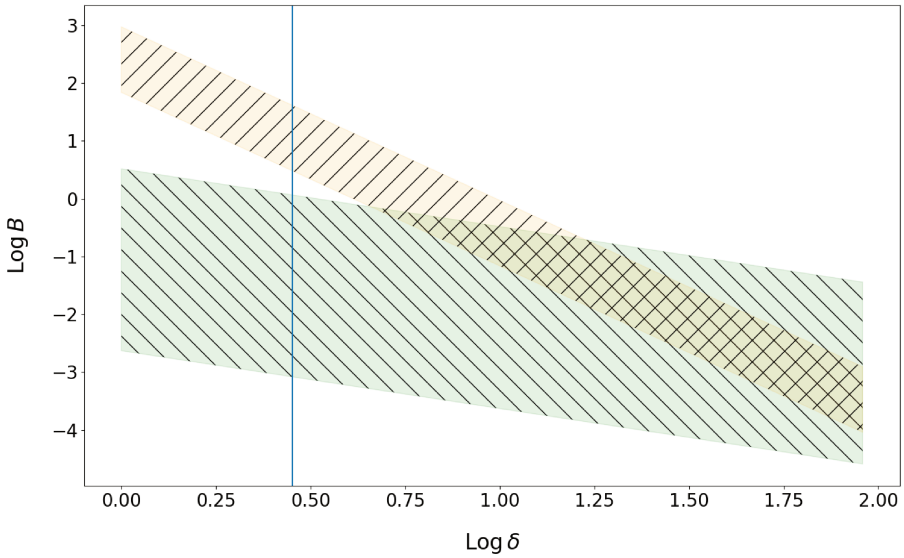

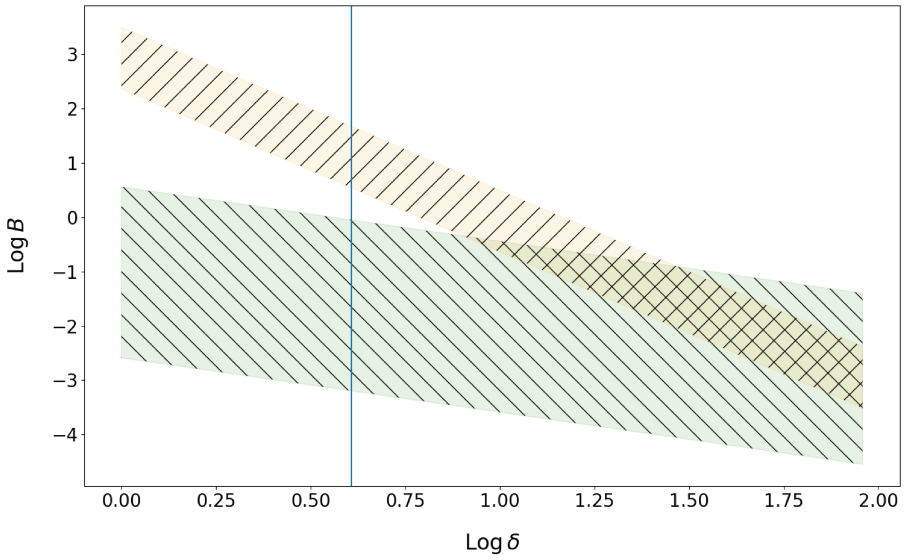

Figure 5.14 $B - \delta$ parameter space for lower redshift (top) and higher redshift (bottom) of the source. The yellow and green band correspond to the luminosity and peak constraints from Tavecchio et al. [Tav+98], whereas the vertical blue line represents the pair-production constraint from the same publication. See text for more details.

$n_2 = 3.5$ (both redshift hypothesis). In addition, the minimal and maximal energies of the electrons can arbitrarily be fixed too ($\gamma_{min} = 100$ and $\gamma_{max} = 5 \times 10^6$), since their impact on the SSC model of 1ES 2322−409 is minimum.

Although the parameter scan reduces the degeneracy of the solutions, an 'optimal fit solution' cannot be provided. Instead, Table 5.8 presents an exemplary solution for each of the redshift hypothesis that are considered, along with the corresponding 1 σ confidence bands of the parameters. Representative solutions featuring low Doppler factors and parameters similar to those found for other HBL sources have been chosen. Note that the δ and B parameter ranges are compatible with but narrower than those inferred from the B-δ diagrams, showing the reduction of the degeneracy obtained with the Cerruti et al. [Cer+13a] algorithm.

For the source redshift z = 0.17 proposed by Jones et al. [Jon+09], the allowed Doppler factor values are higher than the typical $\delta \sim$ 10-20 ones expected for HBL-type objects. A solution close to standard parameters is obtained when we fix the Doppler factor to $\delta = 30$, with a magnetic field of $B = 0.01$ Gauss and a radius of R $\sim 1.6 \times 10^{17}$ cm which is near the limit set by the variability time-scale for $\delta = 30$. The particle energy distribution is described with $\gamma_b = 4 \times 10^4$, a value larger than expected from the peak ratio in order to reach the VHE data without unphysical values of the radius of the blob. The index variation between the first and second slopes of the broken power-law does not account for a simple synchrotron cooling break, due to the need of a relatively steep slope to pass through the Swift XRT data points. This points to the known limitation of the simple one-zone model, where potential energy loss and particle escape mechanisms are not explicitly modeled (Katarzyński et al. [Kat+01]). In this scenario, the emitting region is somewhat far from equipartition with a value of the electron energy density to magnetic energy density ratio, $u_e/u_B \sim 36$. Such large deviations are not unexpected for a HBL type of source like 1ES 2322−409 (see e.g. Cerruti et al. [Cer+13a]).

Considering the second redshift value of $z = 0.06$, the electron distribution is constrained by the peaks and thus must remain the same regardless of the redshift. The only changes applied to the lower redshift model were a smaller break energy $\gamma_b = 3 \times 10^4$, which is precisely the value deduced from the peak ratio, and a slightly lower n_1 index (that nevertheless falls within the uncertainties of the Fermi spectral index) to compensate the changes caused by the smaller redshift.The second redshift allows for exemplary solutions with lower bulk Lorentz factors, so we chose a typical value of $\delta = 20$, which yields to a slightly larger magnetic field value, as expected from the $B - \delta$ relation. However, the inferred radius of R $\sim 6.7 \times 10^{16}$ cm is still large w.r.t. the limit set by the variability time-scale estimate. The chosen set of

parameters yields an electron and magnetic energy density ratio of $u_e/u_B \sim 19$, closer to equipartition than the former redshift.

The model results are shown in Figure 5.15. The Extragalactic Background Light (EBL) absorption has been considered by absorbing the VHE emission according to the Franceschini et al. [Fra+08] EBL model. We note that neither model does account for the low-energy non-simultaneous SUMSS data point, which can in turn be ascribed to different larger regions of the jet. The parameter sets for both redshift estimates are so similar from one another that it is difficult to discard one of the redshifts in favor of the other.

	z = 0.06		z = 0.17	
	Value	Range	Value	Range
δ	20	[14, 46]	30	[26, 100]
K [1/cm^3]	5	[2.55, 111]	5	[0.43, 269.52]
R [cm]	6.7×10^{16}	$[1.3\times10^{16}, 7.3\times10^{16}]$	1.6×10^{17}	$[1.3\times10^{16}, 1.6\times10^{17}]$
B [G]	0.02	[0.014, 0.039]	0.01	[0.003, 0.026]
$n1$	1.7	N/A	1.8	N/A
$n2$	3.5	N/A	3.5	N/A
γ_{min}	100	N/A	100	N/A
γ_b	3×10^4	$[2\times10^4, 3.16\times10^4]$	4×10^4	$[2\times10^4, 4.5\times10^4]$
γ_{max}	5×10^6	N/A	5×10^6	N/A
u_e/u_b	19.2		35.6	
n_e [1/cm^3]	0.28		0.15	

Table 5.8 SSC model parameters for $z = 0.06$ and $z = 0.17$. See main text for parameter description. The values with N/A "Range" column correspond to those fixed in the algorithm for constraining the parameter space. Note that the δ and B parameter spaces are much narrower than those inferred from the B-δ diagrams in Figure 5.14, showing the effect of the algorithm in reducing the degeneracy of the model.

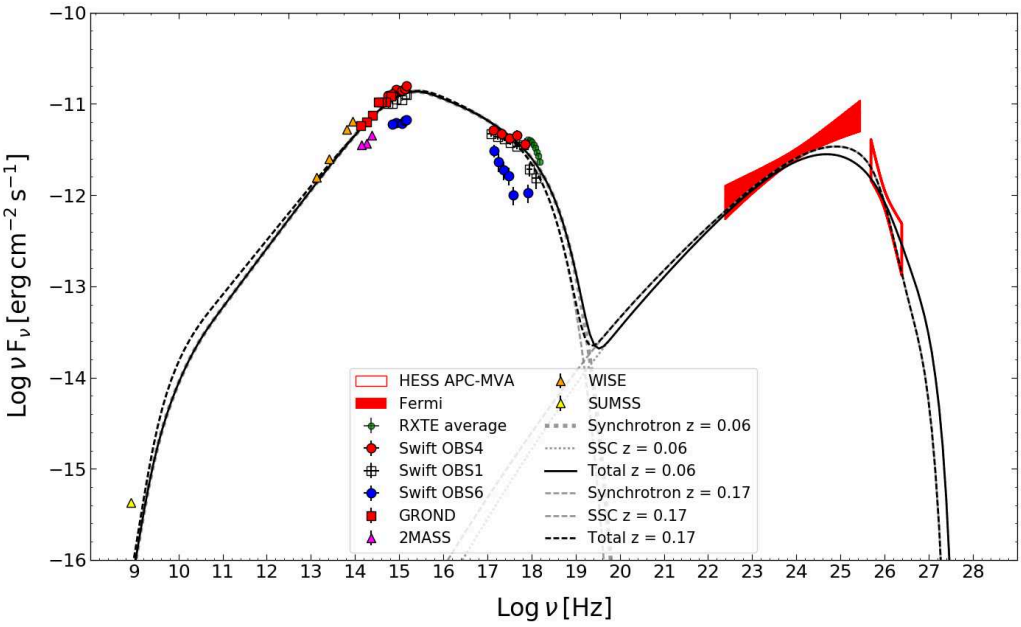

Figure 5.15 SSC modeling of the SED of 1ES 2322−409 for high state and both redshift estimates. Yellow triangles correspond to SUMSS data, pink triangles to 2MASS data, orange triangles to WISE data, red squares to GROND data, red circles to high-state Swift data, blue circles to lowest Swift data points (OBS6), green circles to RXTE data, while the filled red and hollow red bow-ties represent Fermi-LAT (for the Swift high-state period) and APC-MVA data for the whole HESS observations. As explained in the text, only data corresponding to the high state are considered for the SED modeling of the source. The dashed black line correspond to the total high redshift SSC model, whereas the solid black line correspond to the total low redshift SSC model. See Table 5.8 for input parameters for the model.

5.5 Discussion

In this Chapter, we have presented the Model++ analysis of the available HESS data of 1ES 2322−409 that was used as a cross check for the principal analysis chain used within the framework of the HESS analysis of this source, APC-MVA. The results that we obtain are fully compatible with those obtained by APC-MVA.

However, due to the systematics of each different method, a hint of variability that is not seen with APC-MVA was observed with Model++. A more detailed study of the different observational period at VHE was performed, but the inability to contrast the hint of variability with the APC-MVA method meant that we neglect this hint of variable behaviour and instead consider the whole dataset as an indicator of the overall behaviour of the source for modeling purposes.

Existing MWL data contemporaneous to HESS observations were analyzed, and a high state for which a wealth of simultaneous and quasi-simultaneous data exist was generated for modeling the SED of the source.

The broad-band dataset was modeled with a simple one-zone leptonic SSC model that, similar to the majority of HBL type sources, gives a good description of the high state of the source for the two potential redshifts considered for the source. None of the redshifts is clearly favored from the constraints and parameters obtained from the model. However, the parameters for the lower redshift are closer to the expected values, which could be considered as a minor preference for the lower value $z = 0.06$.

6 Modeling a sample of selected gamma-loud NLS1 galaxies

This Chapter is devoted to the application of the multi-component model we have developed [Chapter 3] to three gamma-loud Narrow Line Seyfert 1 (NLS1) galaxies - 1H 0323+342 [Section 6.1], B2 0954+25A [Section 6.2] and PMN J0948+0022 [Section 6.3].

Starting from 1H 0323+342, and after a general overview of the characteristics of the source, we present the datasets used for modeling its Spectral Energy Distribution (SED). Since we are especially interested in the variable gamma-ray behaviour of the sources that, similar to blazars, is a hint of the presence of a relativistic jet, we select a quiescent or low state and a flaring state w.r.t. gamma-ray energies. We then display the models that we obtain for each of the states, discussing the parameter variation that is required to transition from a quiescent or low to a high state for two different scenarios.

Firstly, we present solutions whose Inverse Compton (IC) emission is dominated by the disc and Broad Line Region (BLR) components (henceforth disc-IC and BLR-IC scenario). Then, we present a second possible scenario where the most predominant IC component corresponds to reprocessed torus photons (henceforth torus-IC scenario). For the two scenarios, we explain the variability of the source mostly by changes in the jet characteristics (principally the Doppler factor and the density of the blob), keeping the parameters linked to the external photon fields constant.

The same structure and approach are subsequently followed for B2 0954+25A and PMN J0948+0022. For the latter, in addition to the intermediate and a flaring state, we present a third epoch corresponding to an orphan X-ray flare that has been modeled following the previous approach, also for the two different scenarios [Section 6.3.3].

Then, we explore the effect that changing the mass accretion rate of the disc has on the model components, to investigate whether a variable disc would be fit for describing the variable behaviour of gamma-emitting NLS1 sources [Section 6.4]. The flaring epoch of PMN J0948+0022 is modeled following this alternative approach were the external photon fields no longer remain constant between different epochs.

The Chapter is concluded with a discussion of our findings for the different sources and different scenarios, and a comparison with previous models by other authors [Section 6.5].

6.1 1H 0323+342

1H 0323+342 was first discovered in X-rays in the HEAO-1 X-ray survey (Wood et al. [Woo+84]), and was later spectroscopically classified as a Seyfert 1 with strong FeII lines and weak forbidden lines by Remillard et al. [Rem+93].

With a redshift of $z = 0.0629$ (Zhou et al. [Zho+07]), 1H 0323+342 is the closest source amongst the small sample of gamma-ray detected NLS1s. This means not only that its host galaxy can be resolved by ground-based imaging (e.g. Antón et al. [Ant+08] or Tavares et al. [Tav+14]), but also that the mass of the central Black Hole (BH) can be determined from single-epoch spectra using several broad emission lines (e.g. Landt et al. [Lan+17]).

For example, Antón et al. [Ant+08] estimated the mass of the central BH to be close to $1 \times 10^7\ M_\odot$ following the approach by Greene and Ho [GH05]. Such low mass value is similar to the one published by Zhou et al. [Zho+07] a year or so earlier. The observations and analysis conducted by Landt et al. [Lan+17], which involve multi-wavelength observations of simultaneous Gemini near-infrared and Keck optical data complemented by 2-year prior NuSTAR X-ray observations, also suggest a mass estimate of $\mathrm{M}_{BH} \sim 2 \times 10^7\ \mathrm{M}_\odot$.

These values fall into the overlapping range of BH masses between blazars (larger BH masses) and NLS1 (smaller BH masses). However, there is increasing evidence that

NLS1 BH masses are underestimated by single epoch virial methods. Using different techniques (accretion disc fitting, spectropolarimetry or BH mass-bulge luminosity relation), Calderone et al. [Cal+13], Baldi et al. [Bal+16a] and D'Ammando et al. [D'A+17] estimated masses that are similar to those of FSRQs and BL Lacs, of the order of $M_{BH} \sim 10^8$ $M_\odot$. In the case of 1H 0323+342, though, there is not strong enough evidence yet to support larger masses than the $M_{BH} \sim 2 \times 10^7$ $M_\odot$ value found by Landt et al. [Lan+17], which is the value that we will use in our models. What is more, Wang et al. [Wan+16] also obtained mass estimates of $M_{BH} \sim 3 \times 10^7$ $M_\odot$.

In their work, Landt et al. [Lan+17] also tried to constrain the spin of the central BH, which enables the determination of the Eddington ratio and hence the bolometric luminosity of the AGN. Unfortunately, the coverage of the Swift spectrum they used is not large enough to narrow down the parameter space more than to limit the Eddington ratio value range to $L/L_{Edd} \sim$ 0.5-1, a range that indicates a very efficient accretion regime, typical for NLS1 sources.

The fact that 1H 0323+342 presents a rather high accretion rate with a relatively small BH mass along with an also rather high radio-loudness ($R_{1.4\,\mathrm{GHz}} = 318$ Foschini [Fos11]; $R_{5\,\mathrm{GHz}} = 246$ Doi et al. [Doi+12]) seems to be contradictory to previous studies that showed correlated behaviour between the BH mass and the radio-loudness (e.g. McLure and Jarvis [MJ04]) and an anti-correlation between accretion-rate and radio-loudness (e.g. Greene et al. [Gre+06]). One possibility is that 1H 0323+342 is not that radio loud and the observed high radio-loudnesses are simply due to Doppler boosting effects, as shown by Wajima et al. [Waj+14], who derived intrinsic radio loudnesses of $R_{1.4\,\mathrm{GHz}} = 17$ and $R_{5\,\mathrm{GHz}} = 13$ after corrections. Despite those values falling within the radio-loud regime, they are much lower than initially expected.

Regarding the morphology of its host galaxy, 1H 0323+342 its quite a curious case, since its clearly non-elliptical morphology is difficult to reconcile with the fact that jets are thought to be generally harboured by elliptical galaxies. What is more, there is not a total agreement within the non-elliptical morphology scenario, since space-based telescopes such as the Hubble Space Telescope (HST) point towards the AGN being hosted by a one-arm spiral galaxy (Zhou et al. [Zho+07]), while ground-based observations in the B and R bands with the Nordic Optical Telescope suggest a ring-like host that might be a remnant of a galaxy merger (Antón et al. [Ant+08]), due to its likeness to the inner parts of Arp 10 (Charmandaris and Appleton [CA96]). More recently, in a detailed multi-filter host-galaxy study that agrees with Antón et al. [Ant+08] findings, Tavares et al. [Tav+14] found hints

of a ring structure that might have been caused by a recent merger episode. Their results were not conclusive w.r.t. whether the host is a spiral galaxy or not. Despite 1H 0323+342 being so-far the only gamma-loud NLS1 for which the host has been resolved, these discoveries question the conjecture that only giant elliptical galaxies can form powerful relativistic jets (see e.g. Böttcher and Dermer [BD02]; Sikora et al. [Sik+07]).

Radio-emission studies of the parsec-scale jet and kinematics of the source conducted by Karamanavis et al. [Kar+17] show that the source features a prominent core feature dominating its core-jet morphology, a jet, and no emission from the receding side of the jet, meaning that no counter-jet is detected. Karamanavis et al. [Kar+17] also observed up to 5 superluminal jet components, with velocities ranging from 1 c to 7 c (see also Karamanavis [Kar15]; Fuhrmann et al. [Fuh+16]). Remarkably enough, the radio variability registered by both Very Long Baseline Interferometry (VLBI) and single-dish monitoring is faster than the variability expected in long-term behaviour of blazars. The research by Fuhrmann et al. [Fuh+16] determined a viewing angle of $\theta \leq 4°$-$13°$ which we will consider for modeling purposes.

Zhou et al. [Zho+07] showed that the Infrared (IR)-optical emission of 1H 0323+342 is dominated by the thermal radiation from a Seyfert-like nucleus, while both its radio and X-ray emission can be described by jet synchrotron and Synchrotron Self-Compton (SSC) radiation. Indeed, 1H 0323+342 is highly variable in X-rays as documented in e.g. Zhou et al. [Zho+07], Paliya et al. [Pal+14]. What is more, Foschini et al. [Fos+09] found remarkable variations in the X-ray emission above 20 keV: the source went from a low flux, soft spectrum state in 2004 to a high flux, hard spectrum in 2006-2008, which can be interpreted as disc/corona emission dominating in 2004 and a more important jet contribution in 2006-2008.

Regarding broad-band SED modeling, Abdo et al. [Abd+09c] presented a thorough study including SED fits. The presence of a jet was already apparent in these studies; but in an episodic manner and not as a fully developed constantly broadband-emitting jet. The computed jet power placed the source in the BL Lac range. It is worth noting that they computed accretion rates that reach extreme values of up to 90% of the Eddington luminosity, yet another peculiar property of the radio-loud, gamma-loud NLS1s.

More recently, Paliya et al. [Pal+14] carried out a comprehensive study of a Multi-WaveLength (MWL) dataset and reported the presence of a number of orphan flares in the optical and X-ray bands that had no counterpart at gamma-ray energies. They also reported a hint of correlation in the flares after MJD 56000 (see Figure 6.1), but no major statistic claims could be made due to the scarce data sampling. They

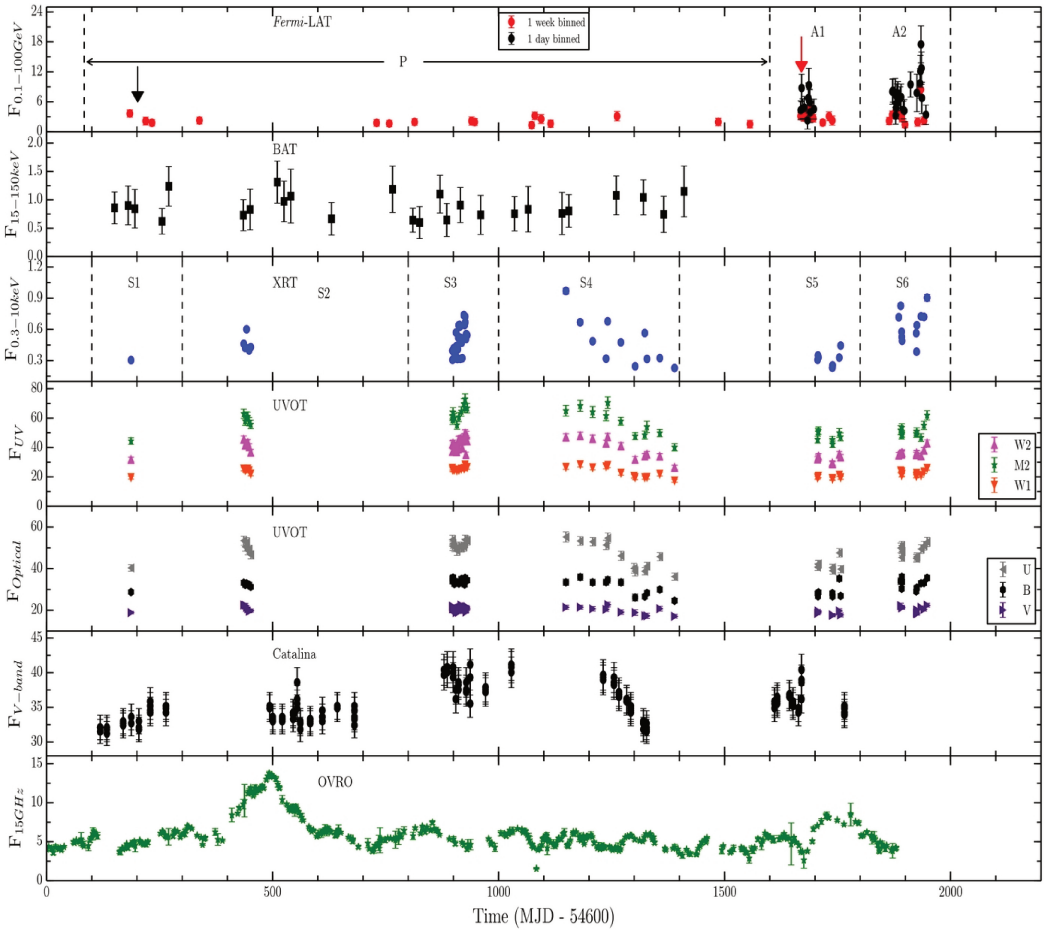

Figure 6.1 MWL LC of 1H 0323+342 from Paliya et al. [Pal+14], OVRO units are 10^{-14} erg cm^{-2} s^{-1}. Catalina and UVOT units are 10^{-12} erg cm^{-2} s^{-1}. Soft and hard X-rays from XRT and BAT are in counts s^{-1} and counts s^{-1} pixel^{-1} respectively. Gamma-ray data from Fermi-LAT are in 10^{-7} ph cm^{-2} s^{-1}.

found a gamma-ray flux doubling time-scale as short as $\sim$ 3 hours. Their X-ray data analysis found that 1H 0323+342 shows similar behaviour to other NLS1 galaxies in the 0.4 keV-50 keV range, featuring a soft excess and a relativistically blurred Fe line. They also modeled the broad-band emission from the source during 4 different states, two of which will be discussed in the following.

In 2015, Yao et al. [Yao+15] presented results of simultaneous X-ray and optical monitoring of Swift Ultra-Violet and Optical Telescope (UVOT) and X-ray Telescope (XRT) data, where 1H 0323+342 showed statistically correlated variability in Ultra-Violet (UV) and X-ray bands, both on daily and yearly timescales. They also analysed Suzaku data, finding much shorter X-ray variabilities of few tens of thousand seconds and a typical Seyfert 1 galaxy spectrum. They modeled the SED of the source for a simultaneous dataset comprising Suzaku data taken on 2009 July 26-27 and Swift UV/optical data from 2009 July 27 with a model that takes into account SSC from

the jet and external photon fields from the accretion disc and the corona. The details of their modeling will be later discussed. They found that the correlated UV/X-ray variability timescale of days is consistent with X-ray emission from reprocessed accretion disc photons. Moreover, the shortest Suzaku variability timescale suggests a relatively small mass of the BH, of $\sim 10^7$ $M_\odot$, compatible with the value we consider for our models.

Recently, we (Kynoch et al. 2017, submitted to MNRAS) observationally constrained the external photon fields of 1H 0323+342 through a quasi-simultaneous near-IR, optical and X-ray dataset comprising GNIRS data from September 2015, Keck data from February 2016 and XMM-Newton data from August 2015, along part of the existing wealth of archival data. A one-zone leptonic SSC model coupled with external components was applied to the dataset in order to simulate the jet parameters.

We found that a low BH spin scenario is preferred over a rapidly rotating BH. Indeed, in the multi-component model developed in the present work, the non-rotating Schwarzschild BH framework introduced in Section 3.3.3 is considered. Also, we concluded that apart from the relativistic jet used for modeling the SED, nothing sets 1H 0323+342 apart from other NLS1 sources, although the mass and Eddington ratio we used are slightly larger than those found by Rakshit et al. [Rak+17a] in their sample.

The main difference between our work in Kynoch et al. 2017 and the present work is the fact that here we focus on the variable gamma-ray behaviour of the source, and we try to model such variability by means of changes within the relativistic jet for the two different datasets that are presented next.

6.1.1 The dataset

Two different epochs with regards to gamma-ray variability are considered for the modeling of this source: an average or quiescent state, and a flaring state.

For the quiescent epoch, averaged Swift XRT and UVOT data from observations taken in September 2013 and December 2014, along with with NuSTAR data from March 2014 (see Landt et al. [Lan+17] for further details) and Fermi data from the quiescent state in Paliya et al. [Pal+14] (MJD 54775 - 54805) are considered, and are depicted in light green in Figure 6.3. Strictly speaking, this generates a non-simultaneous data set for the low-energy part of the spectrum. The main motivation behind our choice was the comprehensiveness of the NuSTAR dataset, which enables constraining the hard X-ray range of the SED of 1H 0323+342.

For the flaring state, we consider the third flaring state from Paliya et al. [Pal+14] that comprises simultaneous Fermi-Large Area Telescope (LAT) and Swift UVOT and XRT data from August 2013 (MJD 56531 - 56535). Corresponding data are plotted in orange in Figure 6.3.

Wide-field Infrared Survey Explorer (WISE) Light Curves (LCs) were extracted to inspect the behaviour of the source. The source does not present major variability, as illustrate the panels in Figure 6.2, where the zoomed-in LC for the two time-windows $\sim$ MJD 55240 and $\sim$ MJD 55430 are shown in the middle and bottom panels respectively. Although there are no simultaneous or contemporary data at IR/optical frequencies for neither of our two datasets, considering the lack of major variability from WISE (see Figure 6.2) we try to obtain models that do not deviate much from the archival data available at those frequencies.

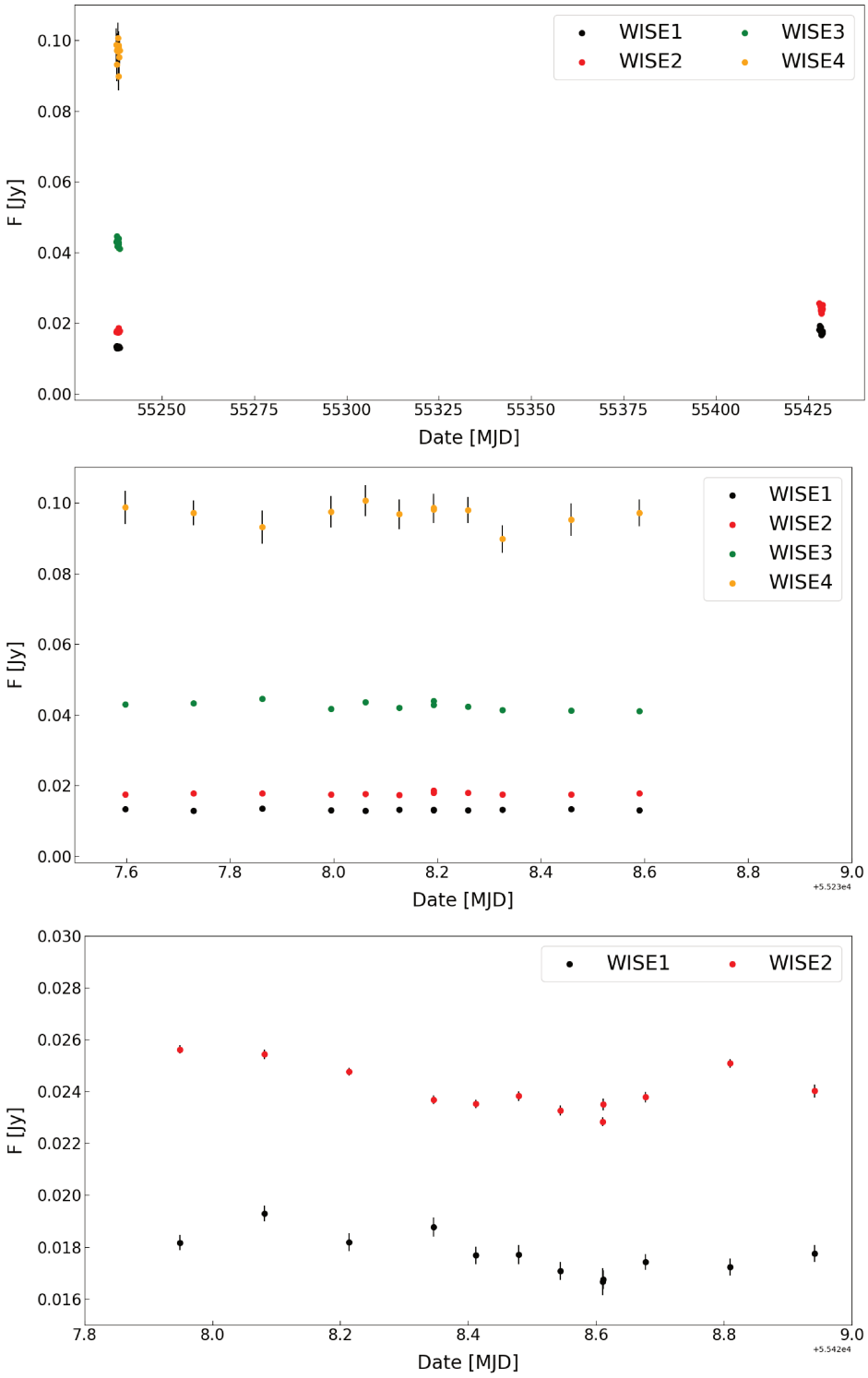

Figure 6.2 Overall (**top**) and zoomed (**middle** and **bottom**) WISE LCs. Dates are in MJD and fluxes in Jy. No major variability is observed in neither of the available observation windows ($\sim$ MJD 55240 and $\sim$ MJD 55430 respectively).

6.1.2 The models

One of the initial motivations to apply our model to this source was whether we could improve the heavily self-absorbed models in the bibliography (see e.g. Paliya et al. [Pal+14]) and still be able to describe the observed gamma-ray emission from the source.

The approach we followed was to first adjust the parameters that affect the jet radiation (i.e. synchrotron and SSC) to describe the observed radio to IR radiation from the synchrotron peak (which is not necessarily a very visible peak for all gamma-loud NLS1s, given that the direct emission from the torus and disc can be more predominant) and eventually change the remaining parameters to model the X-ray to gamma-ray emission with External Inverse Compton (EIC) components.

We assume that the external radiation fields do not vary between a quiescent flaring states. Thus, all the model parameters that represent the external photon fields remain unchanged for each of the scenarios we consider. This is a strong assumption that is backed up by the lack of variability of the accretion disc for the chosen datasets of the source. Thus, one can also assume that the external components that are directly proportional to the disc emission remain unchanged also.

Disc and BLR dominated scenario

For the disc- and BLR-IC dominated solution of 1H 0323+342, the Eddington ratio of the source was fixed to $l_{Edd} \simeq 0.76$, and the source is considered to be seen under an angle of $\theta = 5°$, value that is in agreement with the range provided by Fuhrmann et al. [Fuh+16].

The direct torus emission peaks at $T_{IR} = 1200$ K, with an efficiency of $\tau_{IR} = 0.1$. The corona features an index $\alpha_X = 0.9$ and a normalization $\tau_X = 0.18$. The inner and outer radii of the BLR are constrained by the disc luminosity and set to 4.77×10^4 R_G and 1.5×10^5 R_G respectively, with an opacity of $\tau_{BLR} = 0.1$.

The transition from a quiescent state to a flaring state is described simply by a more energetic, denser blob within the jet, and hence the larger Doppler factor and particle distribution normalization factor K in the high state (first and second columns in Table 6.1). All the parameters linked to the external photon fields remain the same for both states.

The main difference between both epochs is the slope of the Fermi data, which is much steeper during the low state, and harder for the flaring state, as can be seen in Figure 6.3. The variation of the spectral index requires a larger n_2 value for the flare, which in turn affects all the components from the model by flattening their slopes after the peak. Hard X-ray data are ascribed to a combination of the direct corona and SSC radiation. On the contrary, the contribution from SSC radiation is minimal in the quiescent state of the source, where the radiation from the corona is enough to explain the emission.

Our model underestimates the IR and optical radiation for the quiescent state which could be ascribed to our simplified description of the accretion disc as a BBB. Moreover, the steep second slope of the particle distribution required to model the gamma-ray data yields a steep synchrotron spectrum after the break that does not account for the fluxes observed between the 10^{14} Hz-10^{15} Hz range. The flatter slope after the break necessary to describe the GeV data, along with a more important synchrotron contribution, help diminishing this underestimation in the flaring state, though. See Figure 6.3 for the models and Table 6.1 for the corresponding parameters.

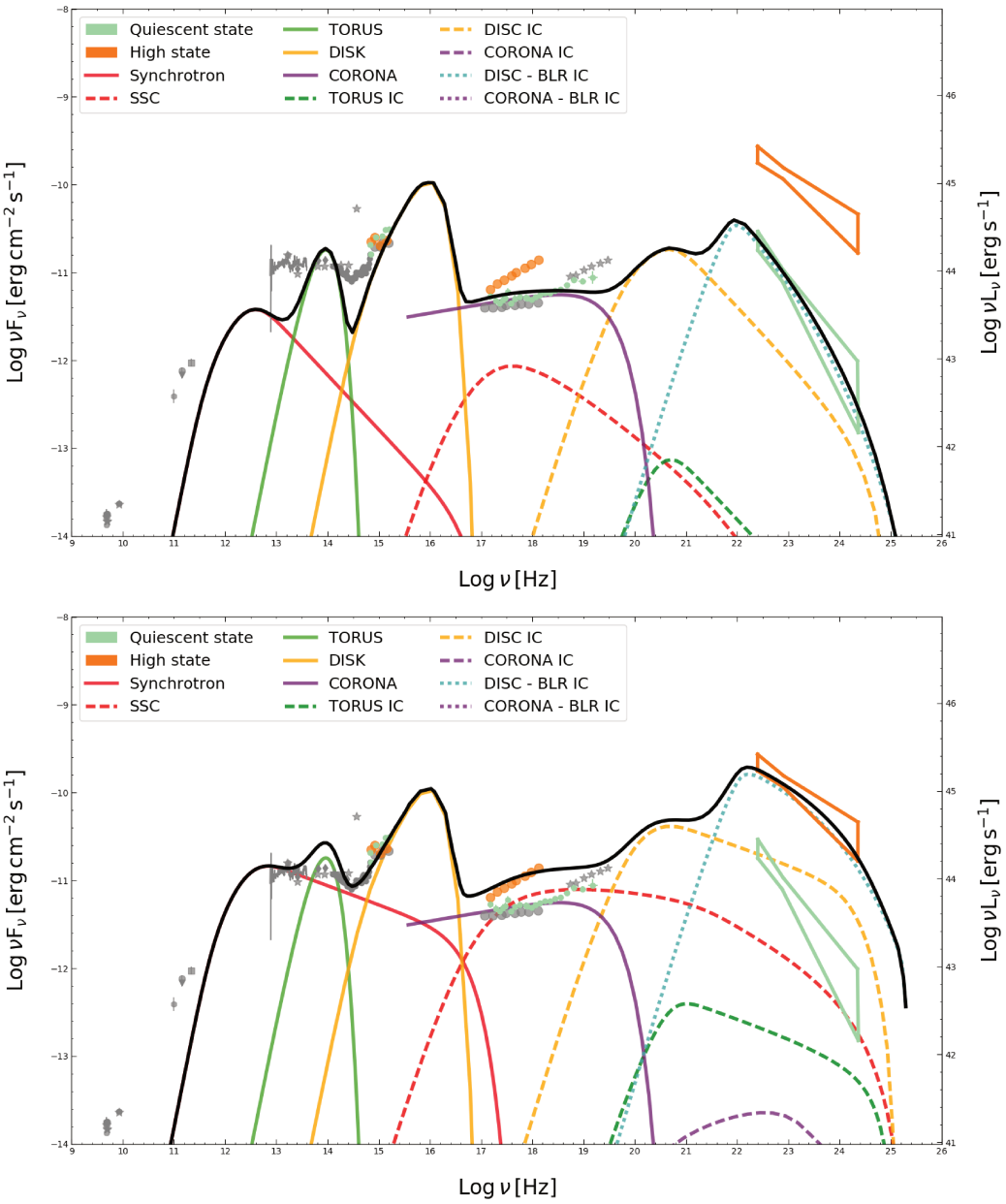

Figure 6.3 Disc- and BLR-IC dominated models for the quiescent (**top**) and flaring (**bottom**) states of 1H 0323+342. The different lines represent the model components as explained in the legend. Gamma-ray flaring state data are depicted in orange, gamma-ray quiescent data in green and archival data in grey.

Torus dominated scenario

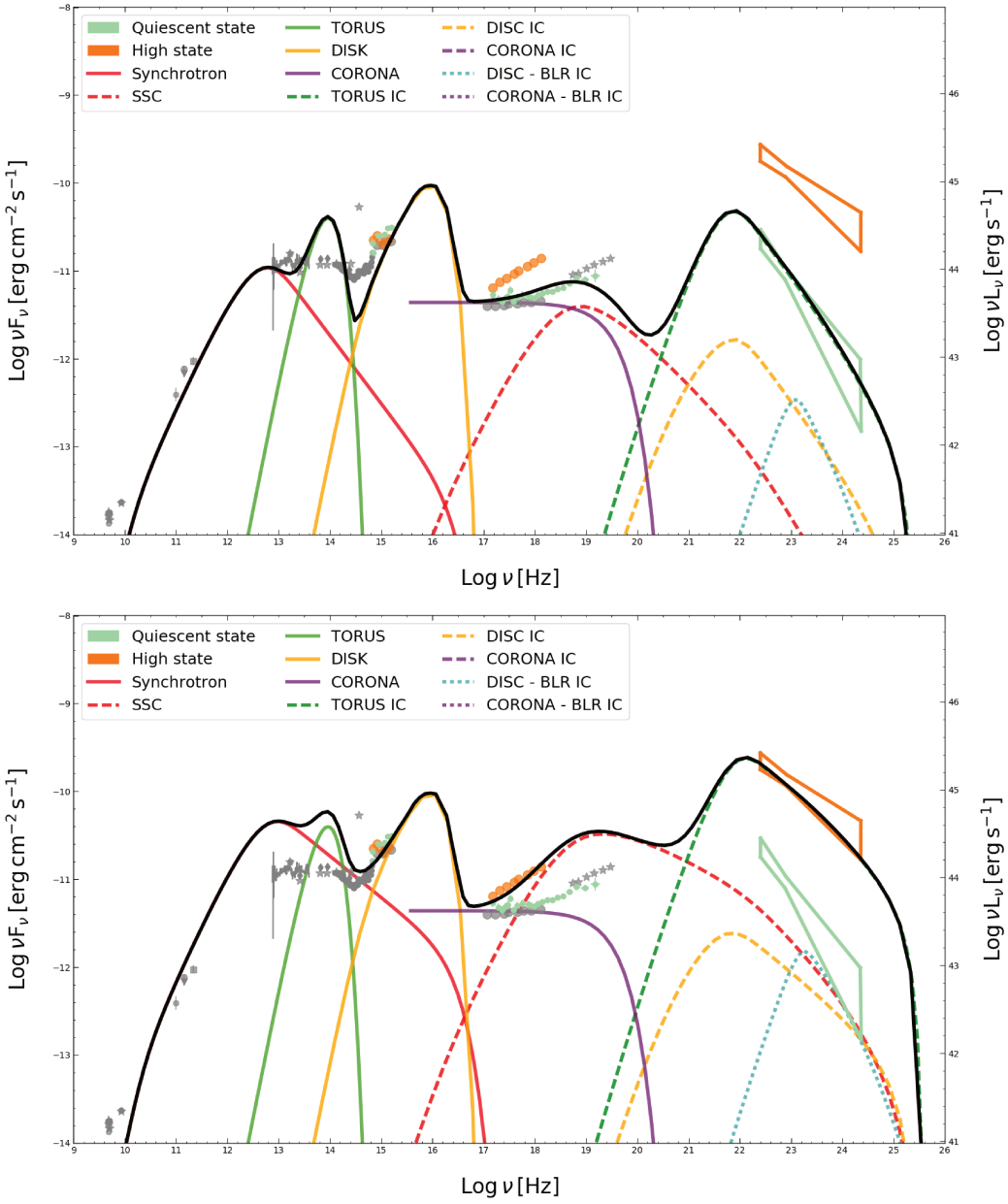

Figure 6.4 Torus-IC dominated SED models of the quiescent (**top**) and flaring (**bottom**) states of 1H 0323+342.

In this second scenario, the transition from a quiescent to a flaring state is also achieved simply by changes in the jet and in the electron population. The flare requires larger Doppler factor and a denser blob, in addition to a smaller index of the particle distribution after the break to account for the hardening of the GeV spectrum, similar to the disc- and BLR-IC dominated solutions.

On the contrary, the Eddington ratio l_{Edd} is slightly smaller in this scenario, which results in a slightly lower disc luminosity L_{Disc} and a BLR located slightly closer. Also, the energy densities are lower in the torus-dominated scenario, which implies less synchrotron self-absorption at radio frequencies.

In this framework, the low-energy electrons contribute more to the emission of the source, which is translated as a larger γ_b parameter value of $\gamma_b = 650$. Moreover, the fact that the peak of the electron distribution happens at much higher energies shifts all the IC components of the model to higher energies. This, coupled with an emission region located in the outermost edge of the BLR that minimizes the ionization degree caused by the accretion disc photons, and a covering factor of the order of $\tau_{BLR} \sim 10^{-4}$ reduces the contribution of the BLR and disc IC components of the model.

Synchrotron emission from the jet describes the far-IR and radio data in the quiescent state, but it overestimates far-IR radiation for the flaring state. The torus description of the near-IR data is overestimated (but they are non simultaneous archival data) but still required for the corresponding IC process to dominate. Synchrotron self-absorption is minimized in this scenario, but still our models underestimate the UV radiation from the BBB during the quiescent epoch. A combination of synchrotron and torus direct emission describes the UV data corresponding to the BBB during the flare.

SSC and torus IC components, along with the emission from a flat corona, are enough to account both for the X-ray and gamma-ray emission from the source in this scenario for both the quiescent and the flaring states.

The torus-IC dominated solutions lie further away from the equipartition between the electron and the magnetic energy densities than the disc- and BLR-IC dominated ones.

Figure 6.4 shows the models for the quiescent and flaring states in a torus-IC dominated scenario. Table 6.1 shows the parameters for the previously shown disc- and BLR-IC dominated scenario, along with the parameters for this second scenario (columns 3 and 4 in Table 6.1).

	Disk & BLR		Torus	
	Average	Flare	Average	Flare
δ	9	11	9	11
K [1/cm^3]	6.5×10^{6}	8×10^{6}	8.4×10^{6}	1.3×10^{7}
R_{src} [cm]	1.15×10^{15}	1.15×10^{15}	1.43×10^{16}	1.34×10^{16}
B [G]	2.6	2.6	0.28	0.3
$n1$	2.2	2.2	2.7	2.7
$n2$	4.2	3.4	4.5	3.9
γ_{min}	120	120	500	500
γ_b	170	180	650	680
γ_{max}	2×10^{4}	2×10^{4}	4×10^{4}	4×10^{4}
T_{IR} [K]	1200	1200	1200	1200
τ_{IR}	0.1	0.1	0.25	0.25
α_X	0.9	0.9	1.0	1.0
τ_X	0.18	0.18	0.18	0.18
R_γ [R_G]	3×10^{3}	3×10^{3}	1.4×10^{5}	1.4×10^{5}
τ_{BLR}	0.1	0.1	1×10^{-4}	1×10^{-4}
R_{in}^{BLR} [R_G]	4.77×10^{4}	4.77×10^{4}	4.67×10^{4}	4.67×10^{4}
R_{out}^{BLR} [R_G]	1.5×10^{5}	1.5×10^{5}	1.4×10^{5}	1.4×10^{5}
u_e/u_b	5.64	9.63	15.85	26.3
n_e [1/cm^3]	1.85×10^{6}	3.16×10^{6}	6.04×10^{4}	1.15×10^{5}
l_{Edd}	0.76		0.73	
L_{Disc} [erg/cm]]	2×10^{45}		1.92×10^{45}	

Table 6.1 Model parameters for disc-BLR and torus dominated IC for quiescent and flaring epochs of 1H 0323+342.

6.2 B2 0954+25A

The second gamma-emitting NLS1 considered in this work is B2 0954+25A ($z = 0.712$ in Adelman-McCarthy [Ade09]). B2 0954+25A is slightly polarized (1.29% according to Wills et al. [Wil+92]), variable (Pica et al. [Pic+88]) and unresolved in the optical range. Woo and Urry [WU02] estimated the bolometric luminosity to be $\log(L_{bol}/\mathrm{erg\,s^{-1}}) = 46.59$ from SED fitting.

Jackson and Browne [JB91b] and Jackson and Browne [JB91a] found the Full Width Half Maximum (FWHM) of the Hβ line in the rest frame to be FWHM(Hβ) = 64 Å, which is equivalent to a velocity of $v \sim 4000\,\mathrm{km\,s^{-1}}$. In contrast, the source has FWHM(Hβ) = $1870\,\mathrm{km\,s^{-1}}$ in the Shen et al. [She+11] catalog that contains several measurements extracted from automatically analyzing the SDSS FR7 spectrum. Calderone et al. [Cal+12] suggest that such strinkingly different values are due to an overestimation by Jackson and Browne [JB91b] and a poor fit of the red-wing asymmetry of the broad Hβ line by Shen et al. [She+11]. To correct for this asymmetry, Calderone et al. [Cal+12] fitted a second Gaussian component to the line, and obtained a FWHM(Hβ) = 46 Å that yields $v \sim 2800\,\mathrm{km\,s^{-1}}$, and a BH mass in the M_{BH} = 1-3 $\times$ 10^8 $M_\odot$ range, which is the value we considered for modeling the source.

The red-wing asymmetry seen in the Hβ broad emission line of B2 0954+25A is indeed probably at the origin of the wide range of BH mass estimates from the literature, which furthermore are quite large for the values expected for NLS1s. This type of asymmetry is often observed in many AGN, and depending on the decomposition chosen to analyze the optical spectrum, might result in the FWHM of the Hβ broad line being lower than the $2000\,\mathrm{km\,s^{-1}}$ threshold used to classify sources as NLS1s, and hence yield a different BH mass estimate.

Concerning radio wavelengths, the source is a compact, radio-loud, flat spectrum radio quasar. Due to its relatively high radio flux density ($\leq$ 1 Jy, Kuehr et al. [Kue+81]) and its emission extending down to very low radio frequencies (74 MHz as documented by Cohen et al. [Coh+07]), B2 0954+25A has been repeatedly used for statistical studies of radio properties of quasars. The wealth of radio data is well illustrated by the VizieR photometry shown in Figure 6.5.

While usually flat, the radio spectrum of the source becomes inverted during burst activity (Torniainen et al. [Tor+05]). Moreover, the jet of this source is clearly visible in radio maps such as the 1.64 Hz of the Very Large Array, and Kovalev et al.

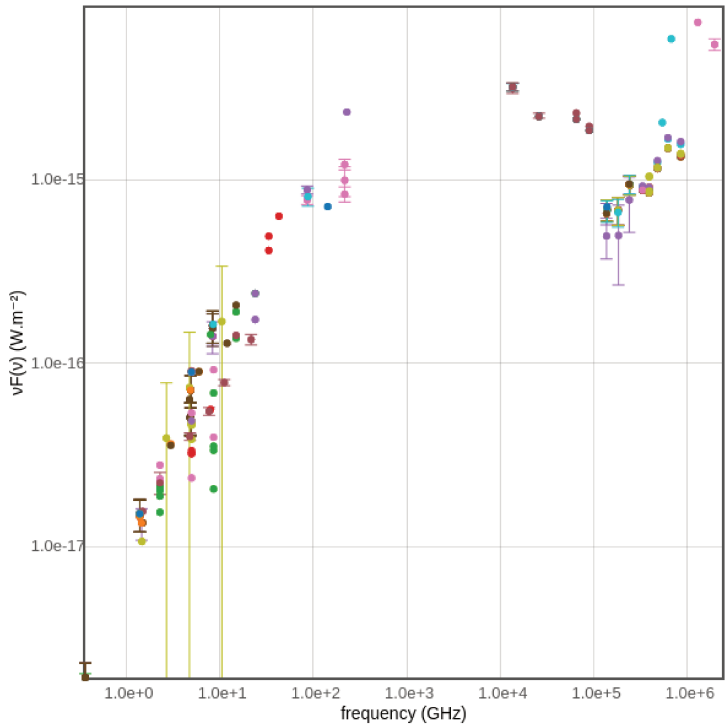

Figure 6.5 Vizier photometric data for B2 0954+25A.

[Kov+05] estimated the FWHM major axis of the VLBA[1] core component to have an angular size of $\theta_{maj} \sim 0.23$ mas $\times$ 0.07 mas at 15 GHz, which in linear size translates as 1.6 pc $\times$ 0.49 pc. Superluminal motion has been observed in several components of the jet (Kellermann et al. [Kel+04]), and a one-sided jet expands from the core towards the south-west direction (Liu and Zhang [LZ02]).

In the X-ray energy range, B2 0954+25A has been observed by several facilities such as Einstein, Chandra, ROSAT or Swift-XRT. WISE data are also available for the source, from 2010-05-07 to 2010-05-08. 2MASS data date back to 1998-11-30. CSS data are also available. Regarding HE, the source is present in the so far published three Fermi-LAT point source catalogs (i.e. 1FGL, 2FGL and 3FGL, Abdo et al. [Abd+10a], Nolan et al. [Nol+12] and Acero et al. [Ace+15] respectively).

Interestingly, B2 0954+25A has been observed in (at least) three different emission states: partially jet dominated (Jackson and Browne [JB91c]), disc dominated (SDSS, Abazajian et al. [Aba+09]), and totally jet dominated (SDSS, Adelman-McCarthy et al. [Ade+06]). For an illustration of the variation from the partially jet dominated to the totally jet dominated state, see Figure 6.6.

[1]Very Long Baseline Array.

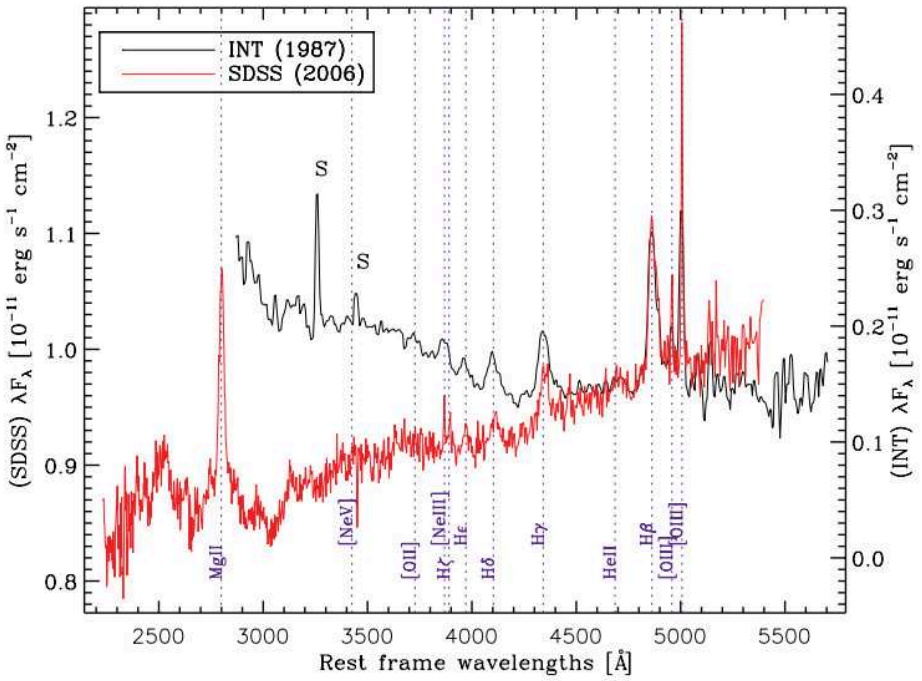

Figure 6.6 Optical spectrum of B2 0954+25A from Calderone et al. [Cal+12]. The black line represents the INT observations from 1987, while the red line corresponds to SDSS data from 2006. Respective flux scales are on the right and left axes. The letter 'S' denotes indicates teluric lines. The comparison of both spectra reveals that both the intensity and the slope changed between both states. Note that the intensity of the Balmer lines seems to be equal in both spectra.

Calderone et al. [Cal+12] also documented one of the most interesting characteristics of this source: the uncorrelated variability observed in X-rays and gamma-rays. While the source is quite variable in X-rays, only a single flare is observed in gamma-ray frequencies during the first half of 2010. As for X-ray behaviour during gamma-ray flares, there are Swift XRT data taken in June 2010, but probably due to its short exposure time, the statistics are scarce and not much information can be extracted from its spectrum. This aspect will be developed in the following section.

Another interesting fact is that Calderone et al. [Cal+12] propose this source to be a transition object between FSRQs and gamma-loud NLS1s, due to its characteristics of both classes: the blazar appearance from the SED model parameters they derive, and the similarity of its SED and that of PMN J0948+0022, the third gamma-loud NLS1 considered in this work.

6.2.1 The dataset

To construct the average state, we consider archival Chandra data from 2009 from Calderone et al. [Cal+12] along with long-term averaged (3FGL) Fermi-LAT data (Acero et al. [Ace+15]).

In order to build the corresponding MWL SED, existing Swift observations were analized. 8 different pointings from May 2007 to November 2016 are available. Details of dates, IDs and exposure times for both XRT and UVOT observations are presented in Table 6.2.

Date	MJD	Our ID	Swift ID	XRT Exp.	UVOT Exp.
2007-05-31	54251.69	OBS1	00036325001	2000.15	1995.15
2007-06-01	54252.03	OBS2	00036325002	7626.18	7616.69
2007-06-05	54256.05	OBS3	00036325003	2039.59	2036.52
2010-06-15	55362.21	OBS4	00036325004	2567.46	2563.66
2011-03-30	55650.26	OBS5	00036325005	4785.06	4772.63
2016-11-18	57710.88	OBS6	00036325006	1995.82	1967.11
2016-11-22	57714.47	OBS7	00036325007	1985.63	1952.71
2016-11-24	57716.20	OBS8	00036325008	1973.24	1919.73

Table 6.2 Available 8 Swift observations, corresponding dates, IDs and exposure times in kss.

The same procedure as the one followed for PKS 1749+096 and 1ES 2322−409 was followed for the XRT and UVOT analyses. An absorbed powerlaw was fit to the different datasets for the common range from 0.3 keV-6.0 keV. Table 6.3 presents the results of the Swift-XRT analysis considering a power-law model, with a total Galactic hydrogen density of $N_H = 3.57 \times 10^{22}\,\mathrm{cm}^{-2}$ and a minimum grouping of 20 counts.

The only relevant detection of the source corresponds to the observation taken on June 1st 2007 (OBS2 in Table 6.3). This is probably due to the fact that the source was going through a flaring state in the X-rays. Moreover, OBS2 presents the longest exposure time ($\sim$ 7 ks), a much longer exposure time than the rest of the observations, which also contributes to the better statistics of this observation. However, the statistics for the observation with the second longest exposure time (OBS5, $\sim$ 4.5 ks) are not significant, which points towards the possibility of the source being quite faint and hence a flaring state would be necessary for it to be

Our ID	Photon Index	Normalization	χ^2/d.o.f.
OBS1	0.92 ± 0.80	$(2.56 \pm 1.00) \times 10^{-4}$	0.33/1
OBS2	1.58 ± 0.19	$(3.14 \pm 0.40) \times 10^{-4}$	1.08/13
OBS4	1.36 ± 0.58	$(2.04 \pm 0.65) \times 10^{-4}$	0.47/1
OBS7	1.69 ± 0.65	$(3.27 \pm 1.00) \times 10^{-4}$	0.08/1
OBS8	$1.41^{+0.41}_{-0.38}$	$(3.15 \pm 0.90) \times 10^{-4}$	1.32/2

Table 6.3 Fit parameters obtained with XSPEC for the available XRT observations of B2 0954+25A. Normalization units are $\mathrm{keV}^{-1}\,\mathrm{cm}^{-2}\,\mathrm{s}^{-1}$. Due to poor statistics, data could not be fitted for OBS3, OBS5 and OBS6, and hence are not shown in the table.

detected. Due to the bad statistics, it was not possible to extract an overall XRT LC for the source.

We also analyzed the UVOT data of the corresponding Swift observations. Results are presented in Table 6.4 and Table 6.5. OBS6 and OBS8 are the only observations for which data from all 6 filters exist. The majority of the observations feature only a single filter ($uvw1$ for OBS1, uvu for OBS2 and OBS3, and $uvm2$ for OBS4 and OBS5), while for OBS7 4 filters are available (except uvv and $uvm2$). Again, the available filters in each UVOT observation were searched for variability with the UVOTMAGHIST tool. No variability was observed so the multiple images within each band were summed. The same count extraction and flux conversion criteria as for the previous sources were used. The fluxes were de-redenned with a $E(B-V) = 0.0378 \pm 0.0014$ (Willingale et al. [Wil+13]).

Fermi did not start its operation until 2008, so no contemporary GeV data are available for the high X-ray state of 2007. Therefore, for the SED of the gamma-ray flaring state, we analyzed Fermi-LAT data from the single flaring epoch so far observed for B2 0954+25A, i.e. Jan 2010 (LAT 55200) - Jul 2010 (LAT 55400). Assuming a power-law spectral shape, a binned likelihood analysis yields a detection with a Test Statistic TS = 216.85 which is equivalent to 14.7 σ, with a flux in the 0.1-500 GeV of $F_{0.1-500\,\mathrm{GeV}} = (5.99 \pm 0.70) \times 10^{-8}\,\mathrm{ph\,cm^{-2}\,s^{-1}}$ and a photon index $\Gamma = 2.475 \pm 0.087$.

Given the fact that no major variability is observed in the Fermi-LAT light curve other than the flare from 2010, we consider the OBS2 Swift observation from the X-ray flaring period in June 2007 along with the Fermi spectrum for the gamma-ray flaring period to model the source at a high state.

Our ID	Ext.	uvv filter $\lambda_0 = 5402$Å		uvb filter $\lambda_0 = 4329$Å		uvu filter $\lambda_0 = 3501$Å	
		Mag	Exp	Mag	Exp	Mag	Exp
OBS1	5	-	-	-	-	-	-
OBS2	10	-	-	-	-	17.06 ± 0.02	7496.56
OBS3	3	-	-	-	-	16.94 ± 0.03	2004.40
OBS4	1	-	-	-	-	-	-
OBS5	1	-	-	-	-	-	-
OBS6	1	17.78 ± 0.18	314.73	17.84 ± 0.10	157.26	17.06 ± 0.08	157.26
OBS7	1	-	-	18.20 ± 0.10	314.52	17.73 ± 0.13	157.22
OBS8	2	> 17.74	65.66	18.16 ± 0.13	159.98	17.68 ± 0.19	65.72

Table 6.4 Available UVOT photometric observations for B2 0954+25A. The first column presents our observation ID, while the second states the number of individual images within each observation. Magnitudes and fluxes (non corrected for absorption) are in the Vega system and in $mJy\,Hz^{-1}$ respectively, while exposure times are in seconds.

Our ID	Ext.	$uvw1$ filter $\lambda_0 = 2634$Å		$uvm2$ filter $\lambda_0 = 2231$Å		$uvw2$ filter $\lambda_0 = 2030$Å	
		Mag	Exp	Mag	Exp	Mag	Exp
OBS1	5	16.54 ± 0.03	1963.68	-	-	-	-
OBS2	10	-	-	-	-	-	-
OBS3	3	-	-	-	-	-	-
OBS4	1	-	-	16.72 ± 0.03	2523.23	-	-
OBS5	1	-	-	16.96 ± 0.03	4697.36	-	-
OBS6	1	16.68 ± 0.06	314.70	16.46 ± 0.06	362.45	16.70 ± 0.04	629.69
OBS7	1	16.90 ± 0.07	314.71	-	-	16.90 ± 0.05	479.16
OBS8	2	16.78 ± 0.09	130.67	16.64 ± 0.09	182.91	16.76 ± 0.07	262.57

Table 6.5 Continuation of Table 6.4.

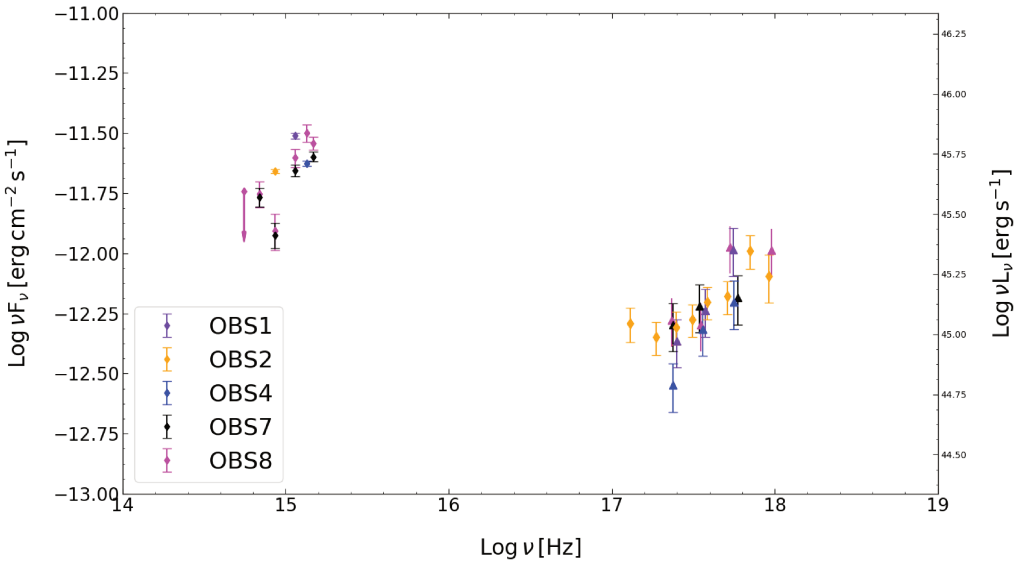

Figure 6.7 Swift UVOT and XRT SED for all available observations of B2 0954+25A. Due to poor statistics, data could not be fitted for OBS3, OBS5 and OBS6, and hence are not shown in the table.

Last, WISE data LCs are presented in Figure 6.8. Although data are not extended enough in time, we take the lack of variability in the two time windows as an indicative of a lack of major variability of the source, and consider them for modeling purposes. The same applies to 2MASS data.

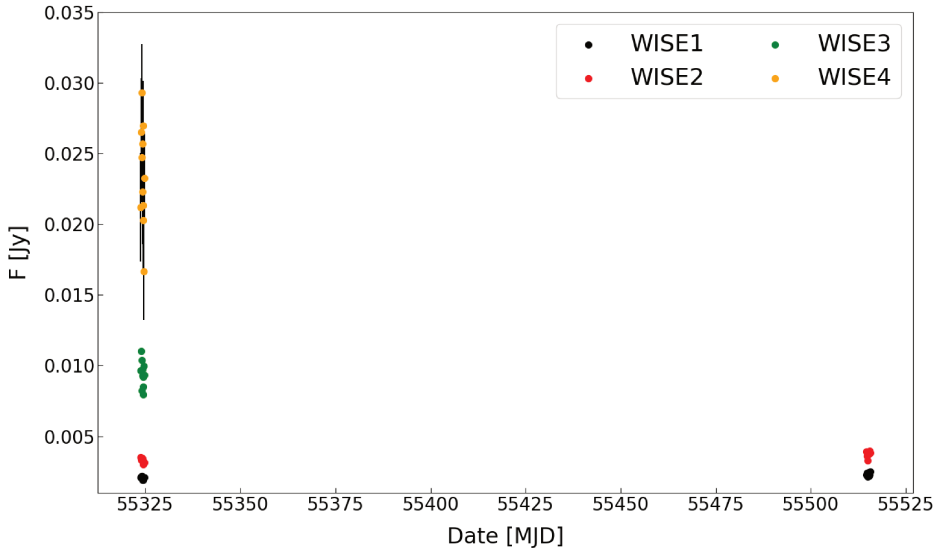

Figure 6.8 Overall WISE LC of B2 0954+25A.

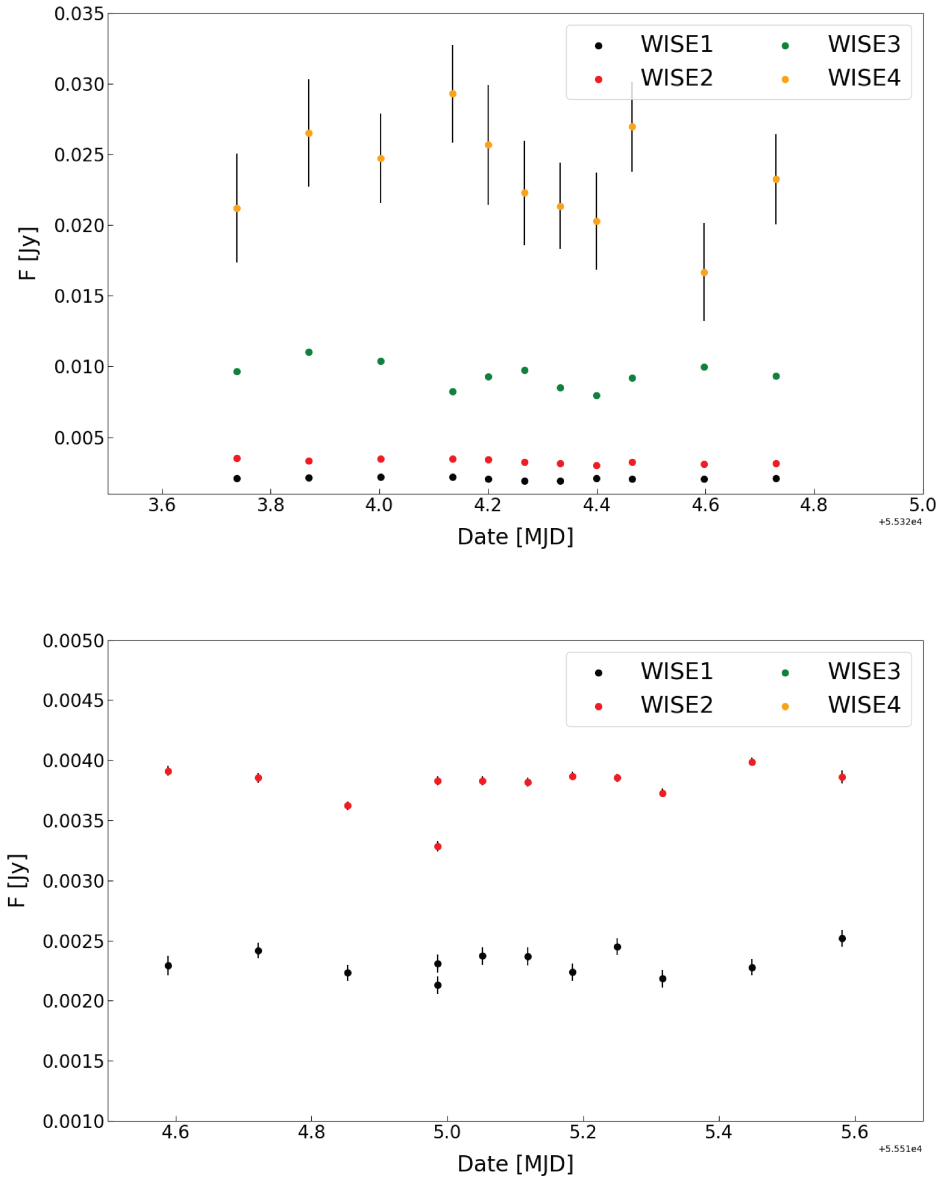

Figure 6.9 Zoom on the two epochs for which WISE data are available for B2 0954+25A. No variability is observed in neither of the available observation windows (∼ MJD 55320 and ∼ MJD 55515 respectively). Fluxes are in Jy.

6.2.2 The models

As for 1H 0323+342, the average state is depicted in light green, whereas the flare is plotted in orange. The viewing angle was set to $\theta = 3°$ (Calderone et al. [Cal+12]), and a mass of $M_{BH} = 1.5 \times 10^8\ M_\odot$. Following the same procedure as for the previous source, the external photon fields remain invariant in both states.

Disc and BLR dominated scenario

In this case, the Eddington rate of the accretion disc was set to $l_{Edd} = 0.66$. The peak torus temperature is $T_{IR} = 1200$ K, and this thermal component has an efficacy of $\tau_{IR} = 0.2$. The inner and outer radii of the BLR fixed at 2.5×10^4 and $7.5 \times 10^4\ R_G$, with an opacity of the region of $\tau_{BLR} = 0.1$.

Likewise to 1H 0323+342, and probably due to the description of the accretion disc we consider, the non-simultaneous infrared and sub-mm emission are underestimated by the synchrotron radiation from the relativistic jet in the average state. Similar to 1H 0323+342, in the disc and BLR-IC dominated scenario, radio data of B2 0954+25A are not well described by our model due to the synchrotron self-absorption of the electron population.

Although less prominent than for 1H 0323+342, the presence of the accretion disc is also major in this source at optical/UV frequencies. Unlike for 1H 0323+342, the hard X-ray emission is well explained simply by the combination of SSC and disc IC contributions both for the average and flaring state. The presence of a X-ray corona is not necessary in this scenario. The jet is necessary to explain gamma-ray emission in both states via inverse comptonization of external photons. In this respect, in both states the gamma emission is attributed to a combination of disc and BLR IC components. No change of gamma-ray slope is observed between the two states, so the indexes of the electron energy distribution remain unchanged in the case of B2 0954+25A.

Similar to 1H 0323+342, the Doppler factor is higher during the flaring state, while the blob remains at the same position. The flaring state features a slightly less dense emission region in this case, though. No increase of the magnetic field is

required from the quiescent to the flaring state, since the only major change is the luminosity of the IC component, which can be well described by the increase in the electron density and Doppler factor. These variations provide the larger contribution of inverse comptonized external photon fields that is necessary to model the higher fluxes during the flare. Finally, both average state and flaring state solutions are close to equipartition between the electron and the magnetic energy densities.

Figure 6.10 shows the multi-component model results for B2 0954+25A in the average and flaring state (top and bottom panels respectively).

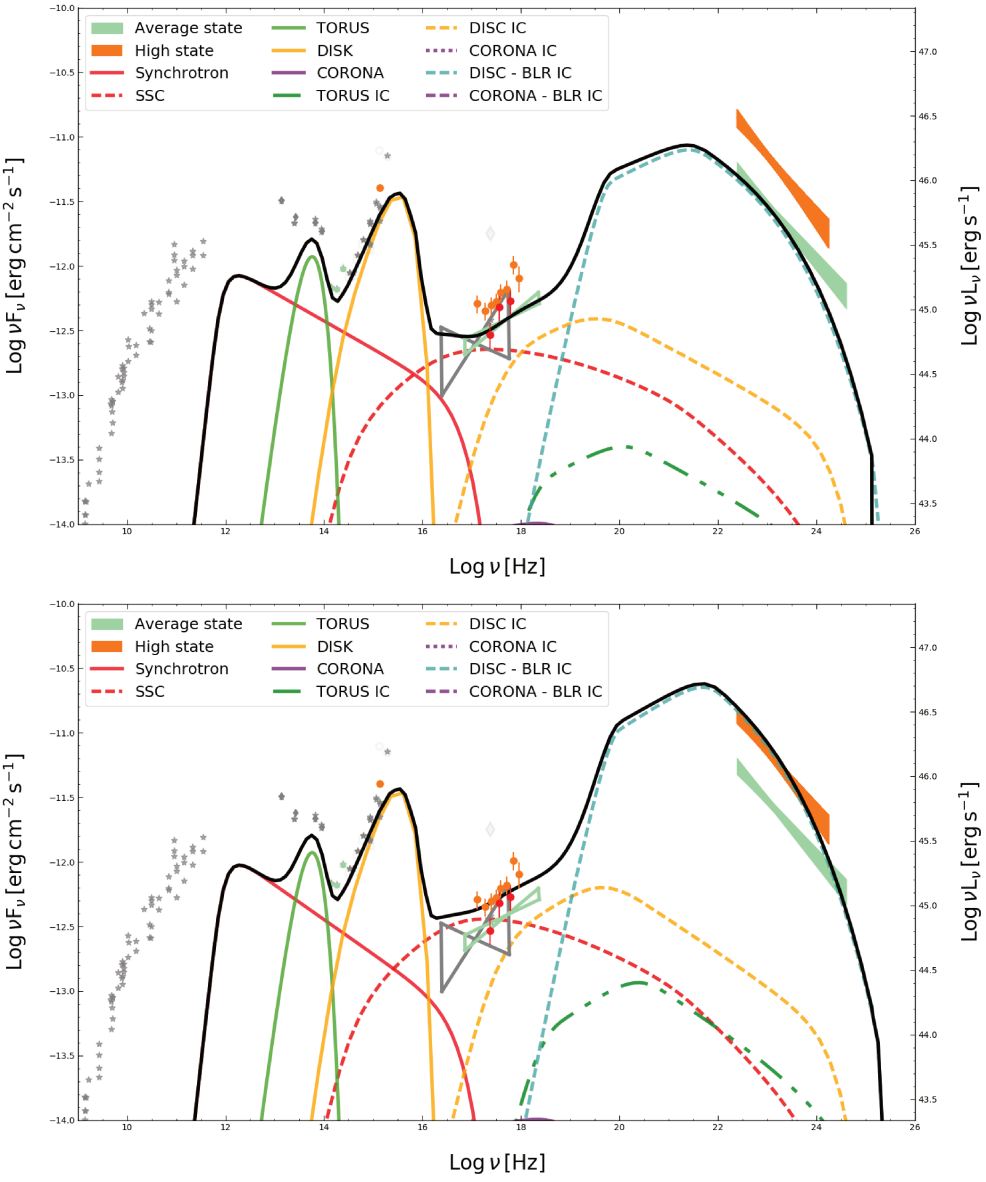

Figure 6.10 Multi-component model for the average state (**top**) and the high state (**bottom**) of B2 0954+25A.

Torus dominated scenario

For the torus-dominated solution, the Eddington ratio is set to $l_{Edd} = 0.72$, slightly larger than that of the disc-BLR dominated solution, with the previously mentioned implications that this has on the disc luminosity and BLR distance.

The torus-IC dominated scenario for B2 0954+25A is not that different from the one for 1H 0323+342. There is a quite marked evidence though regarding the synchrotron self-absorption which is more marked for B2 0954+25A, due to larger electron densities. Near-IR is again ascribed to the dusty torus, and hard X-rays are a combination of SSC and coronal emission for this source too for both states.

The flaring state presents a more Doppler-boosted, denser plasma than the quiescent state. Contrary to 1H 0323+342 though, the flaring state of B2 0954+25A presents a smaller break energy of the electron distribution, meaning that less low-energy electrons contribute to the emission.

Regarding the model parameters that describe the external photon fields, for the IC to be torus dominated, we require a somewhat higher covering factor of the torus, while the peak temperature remains the same. Also, and similar to 1H 0323+342 and any other source if we model its SED on a torus-dominated scenario, the emission region is located at the outer radius of the BLR, which automatically reduces the contribution of the disc and BLR SSC components. Again, the opacity of the BLR needs to be minimal.

Table 6.6 shows the parameters for the previously shown disc and BLR dominated scenario, along with the parameters for the torus IC dominated scenario. The model results are displayed in Figure 6.11.

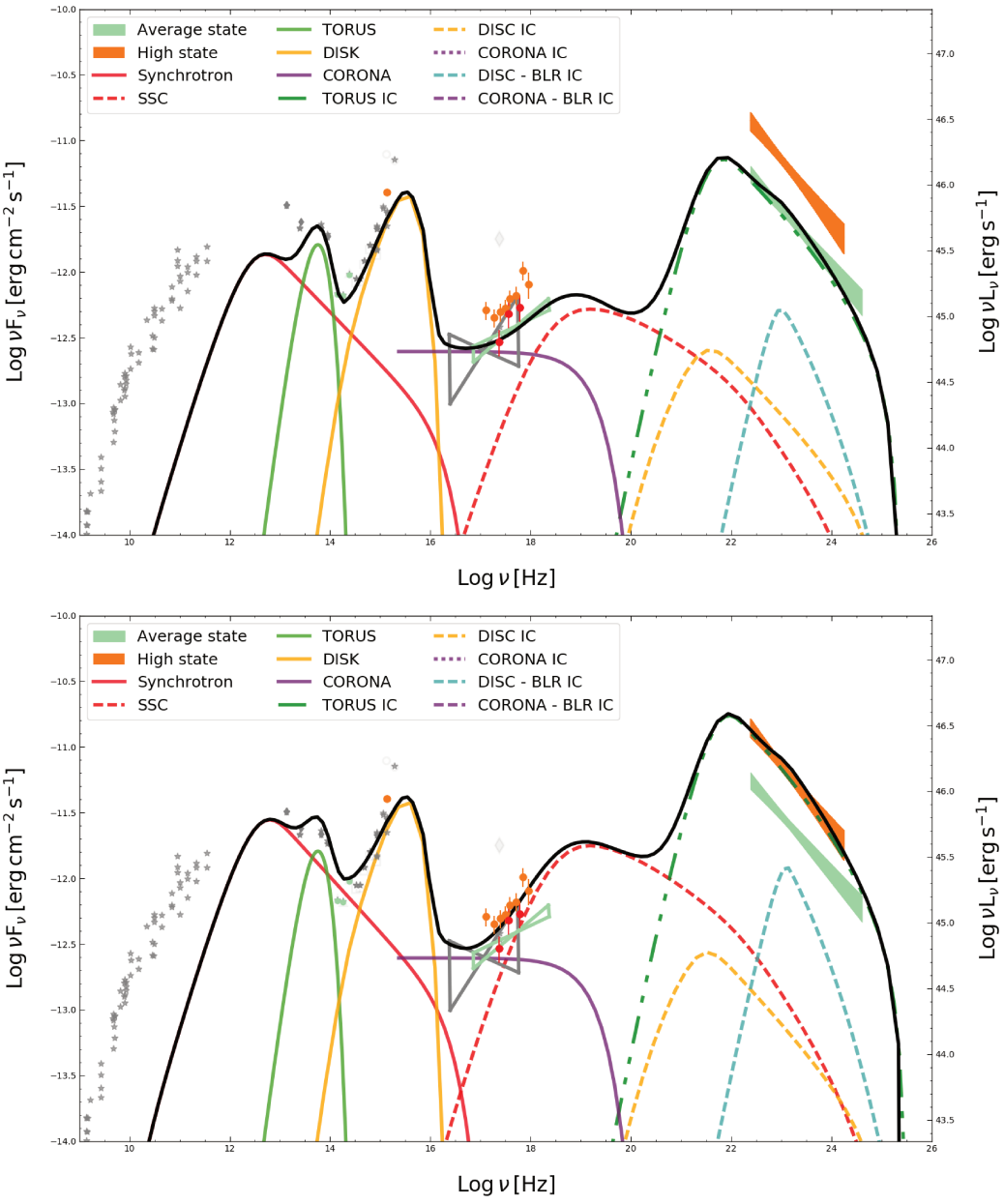

Figure 6.11 Torus IC dominated SED modeling of B2 0954+25A

	Disc & BLR		Torus	
	Average	Flare	Average	Flare
δ	13	15	10	12
K [1/cm^3]	8×10^6	9×10^6	8×10^5	2.5×10^6
R_{src} [cm]	4.97×10^{15}	4.97×10^{15}	5.49×10^{16}	3.77×10^{16}
B [G]	2.0	2.0	0.27	0.3
$n1$	2.6	2.7	2.6	2.6
$n2$	3.4	3.4	3.75	3.8
γ_{min}	10	10	500	500
γ_b	100	150	680	550
γ_{max}	3×10^4	3×10^4	5×10^4	5×10^4
T_{IR} [K]	1200	1200	1200	1200
τ_{IR}	0.2	0.2	0.25	0.25
α_X	1.0	1.0	1.0	1.0
τ_X	0.01	0.01	0.25	0.25
R_γ [R_G]	3×10^3	3×10^3	4.5×10^4	4.5×10^4
τ_{BLR}	0.1	0.1	1×10^{-3}	1×10^{-3}
R_{in}^{BLR} [R_G]	2.5×10^4	2.5×10^4	1.5×10^4	1.5×10^4
R_{out}^{BLR} [R_G]	7.5×10^4	7.5×10^4	4.5×10^4	4.5×10^4
u_e/u_b	14.81	13.11	4.02	8.26
n_e [1/cm^3]	2.87×10^6	2.54×10^6	1.42×10^4	3.61×10^4
l_{Edd}	0.66		0.72	
L_{Disc} [erg cm^{-1}]	1.13×10^{46}		1.23×10^{46}	

Table 6.6 Model parameters for the different scenarios considered here for B2 0954+25A.

6.3 PMN J0948+0022

PMN J0948+0022 ($z = (0.583\,84 \pm 0.000\,12)$ Ahn et al. [Ahn+12]) was identified as a NLS1 by Williams et al. [Wil+02], and presents the typical NLS1 optical spectrum features, with FWHM $(H\beta) = (1500 \pm 55)\,\mathrm{km\,s^{-1}}$, [OIII]/H$\beta < 3$, and strong optical FeII emission (Zhou et al. [Zho+03]).

It was also Zhou et al. [Zho+03] who discovered the flat radio spectrum of the source, which was unexpected from a source classified as NLS1. They measured a radio luminosity at 5 GHz of $L_{5\,\mathrm{GHz}} \sim 10^{43}\,\mathrm{erg\,s^{-1}}$, relatively large for a NLS1, which resulted in a radio-loudness factor $R \gtrsim 10^3$. These findings, along with the observed large brightness temperatures $T_b \gtrsim 10^{13}\,\mathrm{K}$ and the inverted radio spectrum, all characteristics found in blazar type objects, pointed towards the presence of a relativistic jet in PMN J0948+0022.

These suppositions were confirmed when PMN J0948+0022 turned out to be the first NLS1 to be detected in gamma-rays (Abdo et al. [Abd+09b]), and hence considered as the archetypal jetted gamma-loud NLS1 galaxy. Ever since its gamma-discovery, the source has undergone strong gamma-ray flares as reported by Donato [Don10], Foschini [Fos10] and D'Ammando and Ciprini [DC11] (see Foschini et al. [Fos+11] for a deeper insight of the 2011 flare, which was actually the first gamma-ray flare observed from a NLS1). Another gamma-ray flare that reached up to a $F_{0.1\,\mathrm{GeV}-100\,\mathrm{GeV}} = (155 \pm 31) \times 10^{-8}\,\mathrm{ph\,cm^{-2}\,s^{-1}}$ daily flux, was detected by the Fermi/LAT telescope between December 2012 and January 2013 (D'Ammando, F. et al. [D'A+13]). Such flux translates into apparent luminosities of $L \sim 1.5 \times 10^{48}\,\mathrm{erg\,s^{-1}}$, values at the level of those observed in the most powerful blazars.

Not only is the source highly active at gamma-ray energies, but also at radio and optical wavelengths. Extreme optical variability was reported by Maune et al. [Mau+13], while Liu et al. [Liu+10] reported strong intra-night variability. The optical polarization of the source is quite variable too (Eggen et al. [Egg+13]), even at minute-scale (Itoh et al. [Ito+13]).

As a part of a large multi-wavelength campaign carried out in 2009, PMN J0948+0022 was the object of the first global e-VLBI[2] campaign, which deployed a maximum baseline length of around 12 500 km. Several simultaneous observations at 22 GHz showed that the radio structure of the source is dominated by a bright component,

[2]Very Long Baseline Interferometry.

and that relativistic beaming is expected due to the observed high brightness temperature $T_b = 3.4 \times 10^{11}$ K. They also confirmed the inversion of the radio spectrum as pointed out by Zhou et al. [Zho+03], which in turn reinforces the validity of the presence of relativistic jets in this type of object.

In the X-ray domain, the source was observed by the XMM-Newton telescope (Turner et al. [Tur+01], Strüder et al. [Str+01]) at two epochs in April 2008 and May 2011. Bhattacharyya et al. [Bha+14] found that XMM spectra (see Figure 6.12) of these observations present a soft excess in the 0.3 keV-2.5 keV range, and a hard power-law beyond 2.5 keV. In the same paper, they also present Swift-XRT data simultaneous to the May 2011 XMM data in photon counting mode, and attribute the lack of the soft excess in the XRT to poor statistics. Although their best-fit models feature a thermalized corona with a power-law spectrum above the accretion disc, they state that simultaneous hard X-ray data would be necessary to completely validate this scenario.

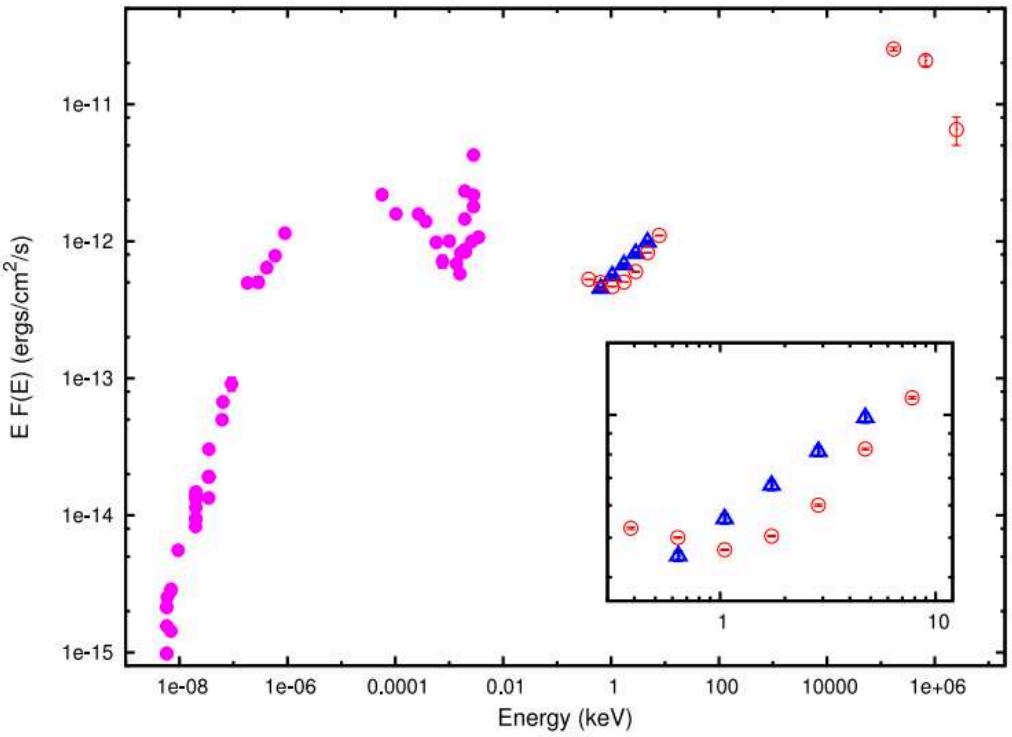

Figure 6.12 Broad band SED showing the soft X-ray excess from Bhattacharyya et al. [Bha+14]. Blue and red points correspond to Swift-XRT and XMM data respectively. Magenta points are archival data from the ASDC.

In their 2015 paper, D'Ammando et al. [D'A+15] present a comprehensive study of the extensive data available for the source between 2008 and 2011. They selected 5 different epochs to show the changing activity of the source over the years. They

found that in 2009 and 2010, the gamma-ray emission was followed by the peak radio emission after a couple of months, thus showing that the jet emission behaved as expected from the canonical relativistic jet model (e.g. Blandford and Königl [BK79]). On the other hand, a prolonged activity marked the 2011 period, with an orphan optical/X-ray flare. Orphan flares are a phenomenon also observed in blazars, see e.g. Acciari et al. [Acc+11], Marscher et al. [Mar+12], which can be considered as another hint of the resemblance between both types of objects.

6.3.1 The dataset

Following the same logic as for the other NLS1s considered, we choose two different states for PMN J0948+0022: one corresponding to a flaring episode in Fermi data, and another corresponding to an intermediate state of the source in this case.

For the intermediate state, we consider the dataset from D'Ammando et al. [D'A+15] that features Fermi-LAT data from 2011 May 22 to June 11, XMM-Newton on 2011 May 28-29 and Effelsberg radio data at 15 and 32 GHz on 2011 May 24. This state is particularly interesting since the soft-excess is clearly visible in the X-ray data.

The dataset for the flare is taken from the study by Foschini et al. [Fos+12], because they are quite comprehensive frequency-wise, and what is more important, they feature mostly simultaneous or contemporary data (see Figure 6.13). From the 5 different epochs presented in their paper, we have considered that of July the 8th 2010, which corresponds to the first documented gamma-ray outburst of the source, as a high state for modeling. Figure 6.13 shows the MWL LC for the source. For their dataset, Foschini et al. [Fos+12] considered Fermi-LAT data integrated over one day while Swift observations from July 3rd are considered. For more details on the procedures followed for the data extraction and analysis, see Foschini et al. [Fos+12].

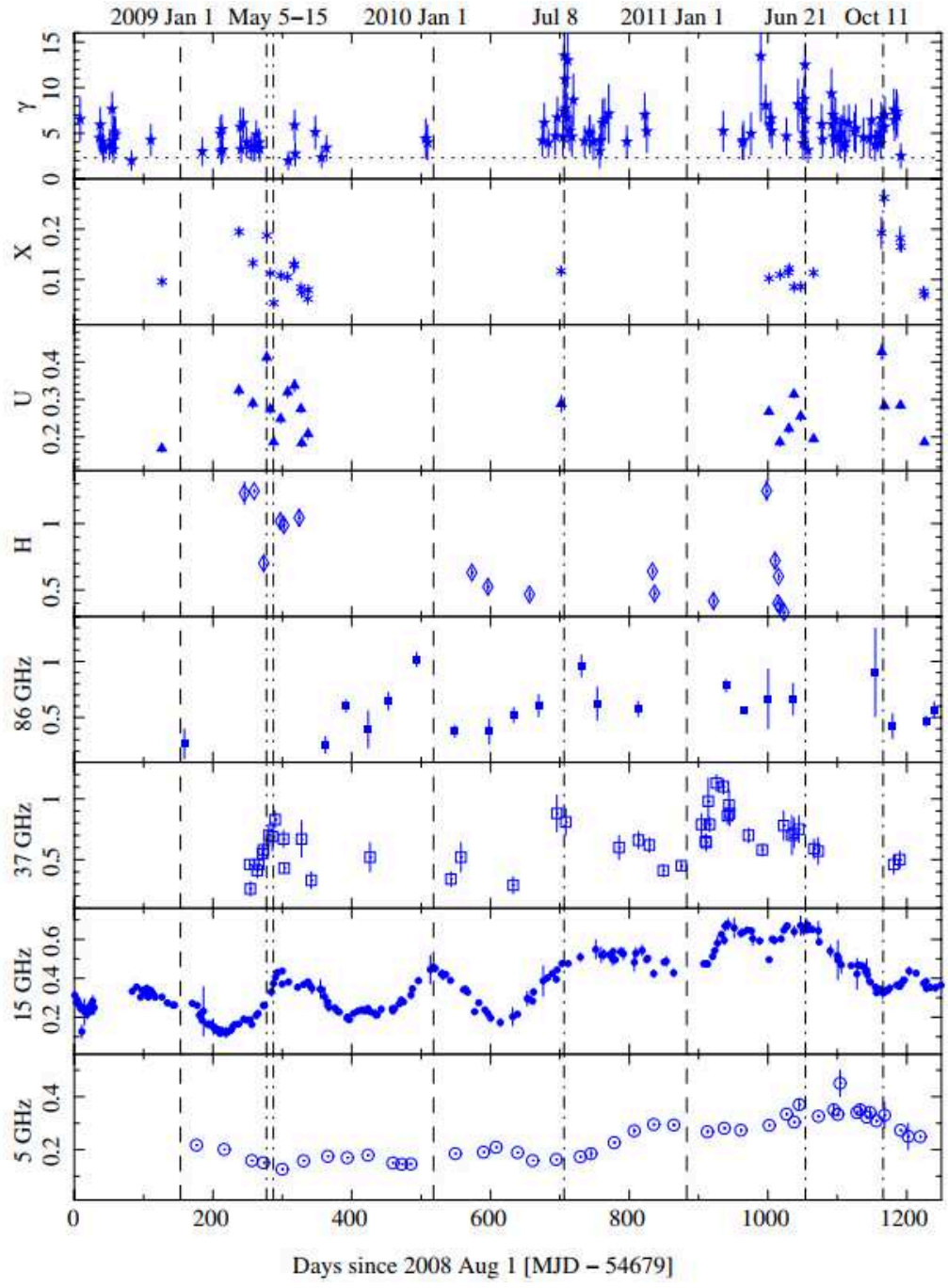

Figure 6.13 MWL light curve of PMN J0948+0022 from Foschini et al. [Fos+12]

6.3.2 The models

For this third gamma-emitting NLS1 the same approach than for 1H 0323+342 and B2 0954+25A is followed. The viewing angle was set to $\theta = 3°$, and we considered a mass of $M_{BH} = 1.5 \times 10^8\ M_\odot$.

Disc and BLR dominated scenario

Similar to 1H 0323+342 and B2 0954+25A, the transition from an intermediate state to a flaring state is explained by variations in the parameters linked to the jet itself. The parameters describing the external photon fields remain invariant in both states.

In this case, the Eddington rate of the accretion disc is set to $l_{Edd} = 0.55$. The peak torus temperature is $T_{IR} = 1200$ K, and presents an efficiency of $\tau_{IR} = 0.1$. The corona features an index $\alpha_X = 1.2$, with an efficiency of $\tau_x = 0.3$. The inner and outer radii of the BLR are fixed at 1.5×10^4 and $4.5 \times 10^4\ R_G$, with an opacity of the region of $\tau_{BLR} = 0.15$.

The flaring state of the source is again explained by a larger Doppler factor and a slightly larger electron density. A trend of 'harder when brighter' is also observed at gamma-rays, which requires the electron distribution index after the energy break to be smaller. Note that the particle energy distribution of the flare features a break at somewhat larger energies which is required to reach up to the flux levels seen by Fermi. This, in turn, requires the flare to have a smaller magnetic field value since the effect of the larger Doppler factor on the synchrotron and SSC components needs to be compensated, while keeping a high level of the BLR flux, which hampers major changes on either the normalization K or the radius of the source that greatly affect the EIC contribution from the BLR. In this scenario, the blob is located closer from the central engine.

The soft excess is slightly underestimated by the corona in the intermediate state. In both states, hard X-ray emission is explained by the disc IC component, while gamma-ray emission originates from BLR reprocessed accretion disc photons. The effect of synchrotron self-absorption is marked for both states, underestimating the

radio emission. The contribution from the SSC is minor in the case of this scenario and this source.

We would like to remark that for PMN J0948+0022 the corona is no longer flat. We tried to explain the hint of a soft-excess seen in the intermediate state via the corona, but as more complex models of the accretion flow (e.g. Done et al. 2012) found out, it is not sufficient and a second, cooler thermal component would be necessary to properly account for this soft-excess.

The corresponding models are shown in Figure 6.14, and the parameters that will be discussed in the following are summarized in Table 6.7.

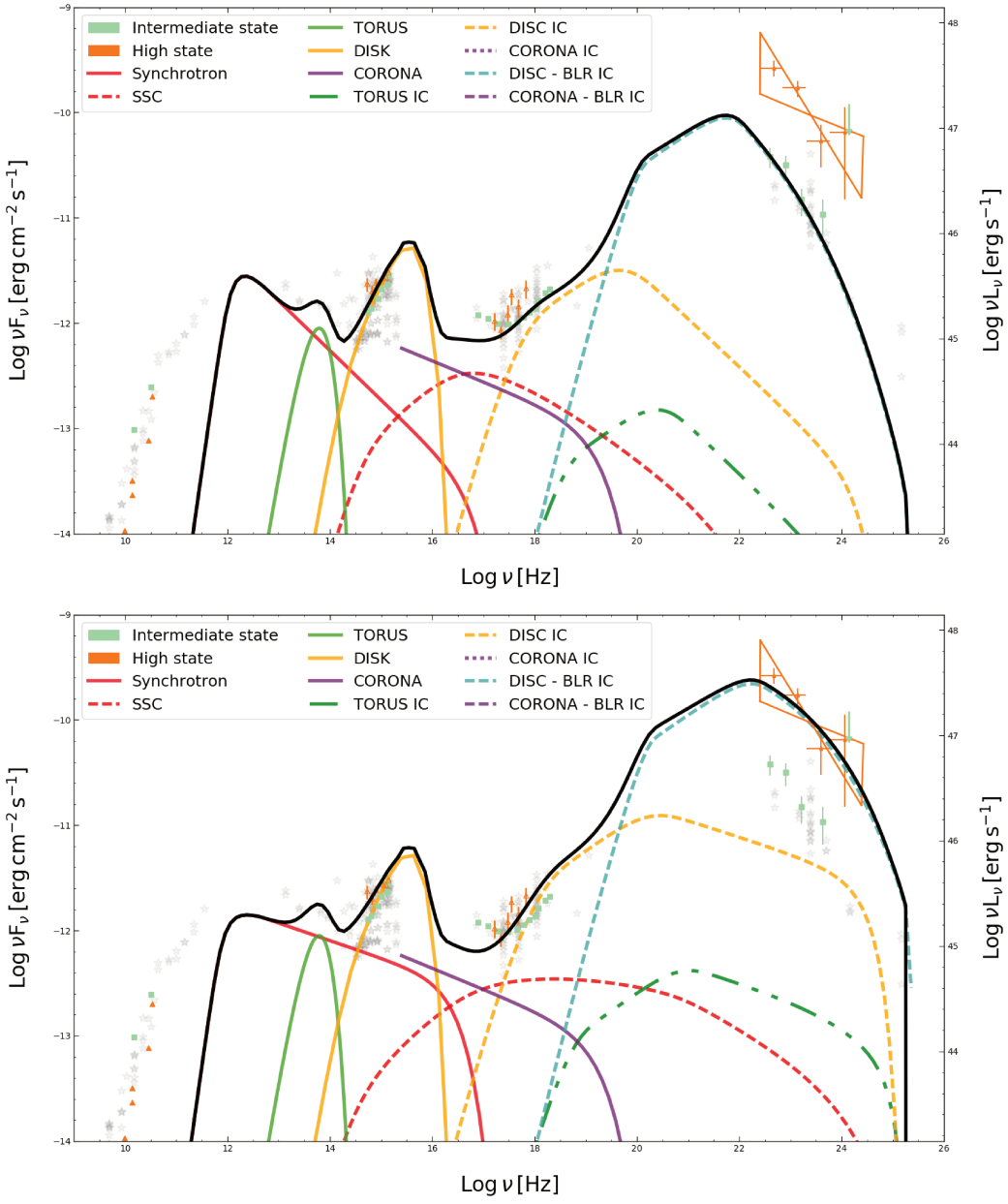

Figure 6.14 Disc and BLR-IC dominated solutions for PMN J0948+0022.

Torus dominated scenario

Likewise for 1H 0323+342 and B2 0954+25A, the transition from a lower state to a high state is explained by means of changes in the jet parameters. The Eddington ratio is slightly larger than that of the disc and BLR-IC scenario.

In the scenario where high-energy emission is dominated by the torus-IC component, the synchrotron self-absorption is much reduced, due to lower electron densities w.r.t. the disc and BLR dominated scenario. The electron densities are similar in both states, but the flare presents a smaller magnetic field density and a larger break energy Lorentz factor.

For both states, synchrotron emission accounts for radio and far-IR emission, while near IR and IR (although there are not simultaneous data in these frequencies) are ascribed to the dusty torus. The UV excess of the BBB is well described by the simplistic multi-temperature accretion disc, and a combination of the X-ray corona and SSC from the jet account for the hard X-ray radiation. Gamma-ray emission from Fermi is explained by the up-scattered dusty torus photons. Again, the emission region needs to be located at the outermost edge of the BLR for the torus-IC to dominate.

The torus-IC dominated model is shown in Figure 6.15, while Table 6.7 shows the parameters for the aforementioned disc and BLR dominated scenario, along with the parameters for the torus dominated one.

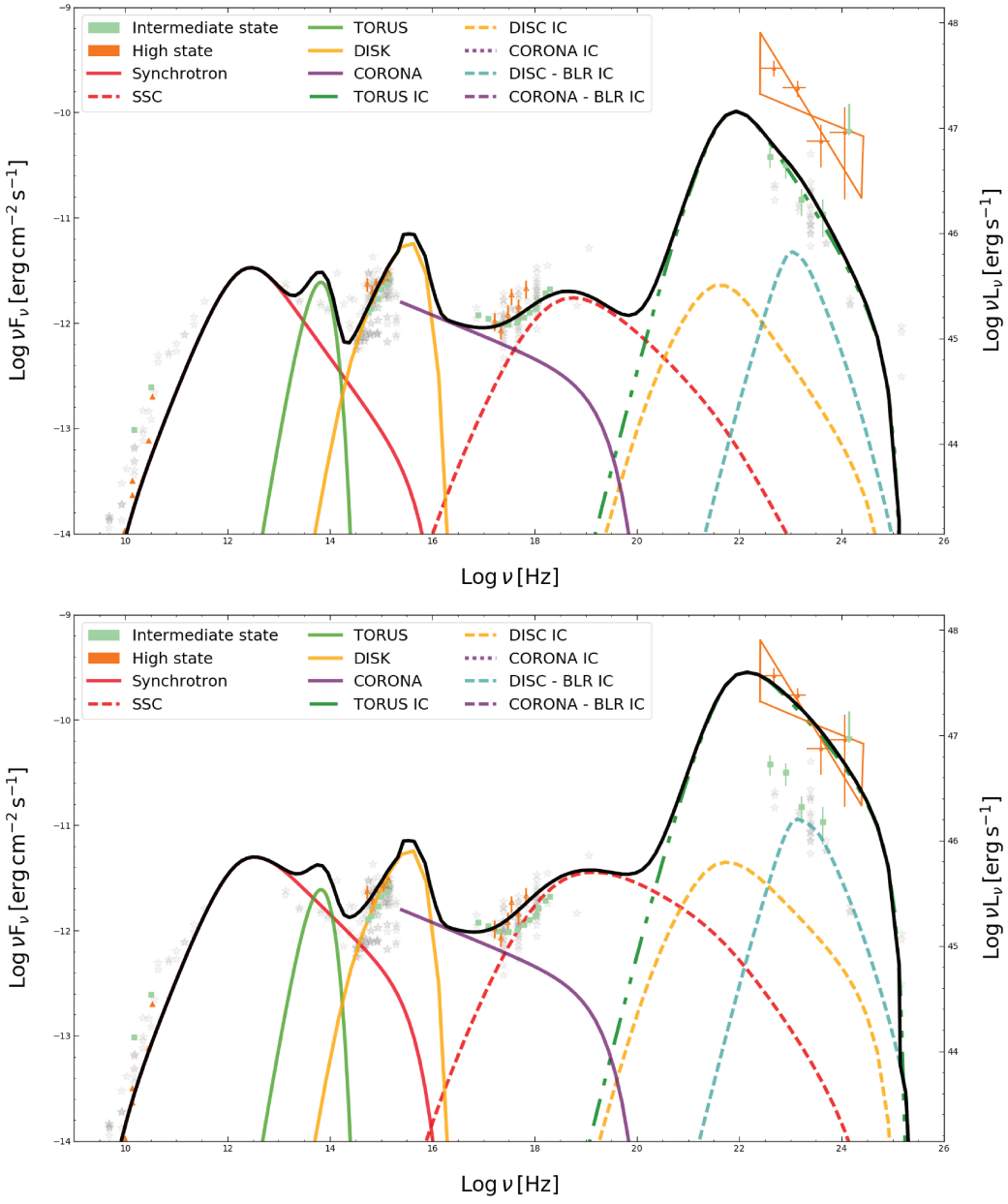

Figure 6.15 Torus IC dominated SED modeling of PMN J0948+0022

	Disc & BLR		Torus	
	Average	Flare	Average	Flare
δ	16	19	10	11
K [1/cm^3]	1.5×10^{6}	1.5×10^{6}	1×10^{6}	8×10^{5}
R_{src} [cm]	5×10^{15}	4×10^{15}	1.12×10^{17}	1.32×10^{17}
B [G]	3.0	1.4	0.14	0.11
$n1$	2.3	2.3	2.7	2.7
$n2$	4.0	3.3	4.3	3.9
γ_{min}	10	10	500	500
γ_b	100	140	900	1.2×10^{3}
γ_{max}	2×10^{4}	2×10^{4}	3×10^{4}	3×10^{4}
T_{IR} [K]	1200	1200	1300	1300
τ_{IR}	0.1	0.1	0.25	0.25
α_X	1.2	1.2	1.2	1.2
τ_X	0.3	0.3	0.5	0.5
R_γ [R_G]	2.3×10^{3}	2×10^{3}	4.5×10^{4}	4.5×10^{4}
τ_{BLR}	0.15	0.15	1×10^{-3}	1×10^{-3}
R_{in}^{BLR} [R_G]	1.5×10^{4}	1.5×10^{4}	1.5×10^{4}	1.5×10^{4}
R_{out}^{BLR} [R_G]	4.5×10^{4}	4.5×10^{4}	4.5×10^{4}	4.5×10^{4}
u_e/u_b	7.92	17.18	10.25	16.23
n_e [1/cm^3]	1.4×10^{6}	1.63×10^{6}	9.76×10^{3}	9.66×10^{3}
l_{Edd}	0.66		0.72	
L_{dis} [erg cm^{-1}]	1.13×10^{46}		1.23×10^{46}	

Table 6.7 Model parameters for different scenarios of PMN J0948+0022.

6.3.3 Modeling an additional state of PMN J0948+0022

Apart from the intermediate and flaring states of PMN J0948+0022 that have been presented in Section 6.3.1, there are other periods of PMN J0948+0022 for which simultaneous or quasi-simultaneous data exist. In the following, we present models for one of these additional states, again for the disc and BLR-IC dominated and torus-IC dominated scenarios.

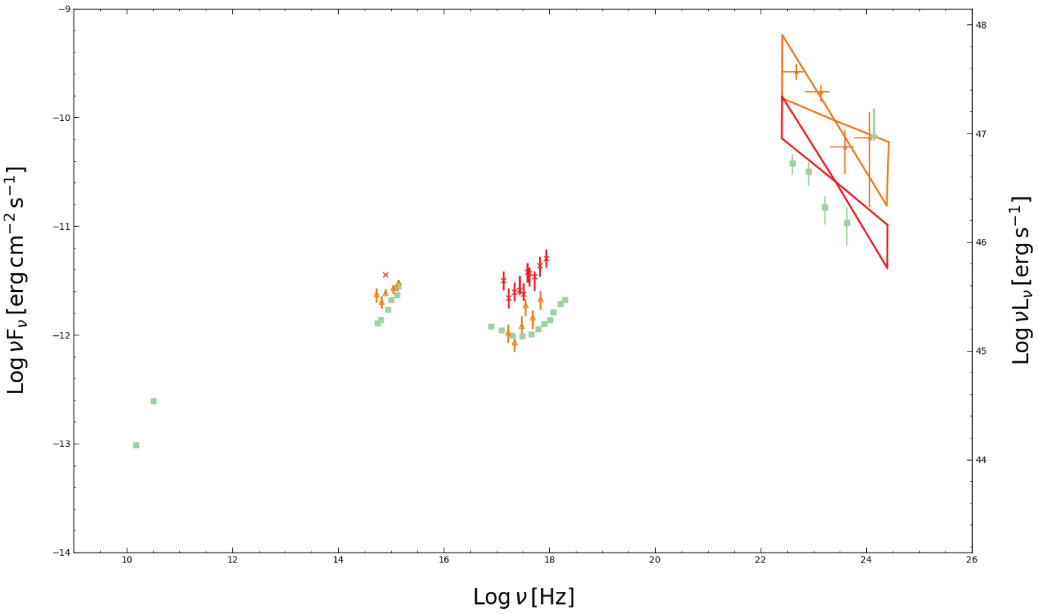

Figure 6.16 Available different states for PMN J0948+0022. The orange corresponds to the first gamma-ray burst, i.e. the flare we consider, the red to the orphan X-ray, and the light green to the intermediate state.

In addition to the state that we have previously considered as the flaring state of the source, Foschini et al. [Fos+12] also present other 4 activity states of the source. The additional state that we consider is that of October 9-12th 2011 (maximum optical-to-X-ray flux, an orphan flare in X-rays, depicted in red in Figure 6.16). Figure 6.16 illustrates the different states that have been considered throughout this work.

The orphan X-ray flare seen by Swift on October 9-12 2011 featured the highest optical/X-ray fluxes observed, with a flux in the 0.3 keV-10 keV of $F_{0.3\,\mathrm{keV}-10\,\mathrm{keV}} \sim 10^{-11}$ erg cm^{-2} s and a flux in the uvu band of $F_U \sim 0.43$ mJy. No high activity was detected in gamma-rays during that epoch though. The dataset featured in Foschini et al. [Fos+12] and that we consider for the modeling is obtained by integrating Fermi/LAT data over 5 days centered on October 11th, along with the average of Swift observations taken on the 9th an 12th of October.

Following the same approach as before, we try to keep the parameters of the external photon fields constant, and vary the ones linked to the jet and its blob to account for the enhanced flaring radiation. The same external field parameters than the ones featured for the intermediate and flaring states are used here.

Disc and BLR dominated scenario

The orphan X-ray flare is explained by an emission region located closer to the central engine whose electron density is larger than that of the flaring state. Also, the magnetic field is larger than both for the intermediate and the flaring states. However, the Doppler factor remains the same as for the intermediate state.

A slightly smaller (steeper) first index of the particle distribution is necessary to describe the shape of the high-energy emission, which is ascribed to a combination of SSC and disc-IC components. The second index is in-between that of the intermediate and the flaring states. The break of the particle energy distribution happens at the same energy as for the flaring state, while the minimum and maximum energy remain the same.

In fact, the major difference between the previously modeled states of PMN J0948+0022 and this orphan X-ray flare is the position of the emission region: the enhanced X-ray emission is ascribed to a denser blob located much closer to the BH, which increases the disc and BLR-IC contributions to the overall model.

Like the previously presented models in this scenario, the synchrotron self-absorption is strong for the orphan flare too, due to large electron densities.

Table 6.8 presents the model parameters for a disc and BLR scenario for the additional state that we model.

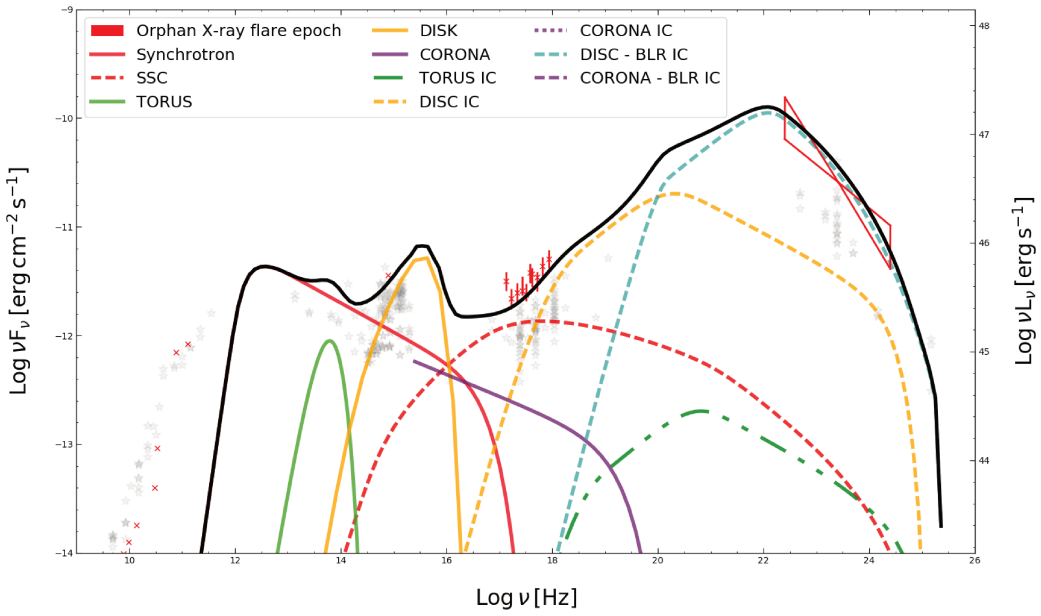

Figure 6.17 Disc and BLR-IC dominated model for the orphan flare of PMN J0948+0022.

	Intermediate	X-ray flare	Flare
δ	16	16	19
K [1/cm^3]	1.5×10^{6}	1.7×10^{6}	1.5×10^{6}
R_{src} [cm]	5×10^{15}	3.67×10^{15}	4×10^{15}
B [G]	2.5	3.0	1.4
$n1$	2.3	2.2	2.3
$n2$	4.0	3.5	3.3
γ_{min}	10	10	10
γ_b	100	140	140
γ_{max}	2×10^{4}	2×10^{4}	2×10^{4}
R_γ [R_G]	2.5e3	1.4e3	2×10^{3}
u_e/u_b	7.19	6.00	17.18
n_e [1/cm^3]	1.4×10^{6}	2.628×10^{6}	1.63×10^{6}

Table 6.8 Model parameters for disc and BLR-IC dominated scenario for the orphan X-ray flare of PMN J0948+0022, including the previously shown intermediate and flaring states.

Torus dominated scenario

Since the emission region needs to be at the farthest edge of the BLR for the torus-IC to dominate, the orphan X-ray flare is explained by means of a much denser emission region with a Doppler factor that is larger than for the gamma-ray flare.

Also, the magnetic field intensity is much larger so as to increase the contribution of the SSC component to which the enhanced X-ray emission is ascribed. This, in turn, implies a smaller break energy so that the synchrotron peak is not shifted towards higher energies.

Summing up, in the disc and BLR-IC dominated scenario, the flare originates from an emission region located closer to the BH, while in the torus-IC dominated scenario a more energetic blob that translates in a more predominant SSC radiative component explains the observed radiation.

Similar to the majority of the previously presented torus-IC dominated models that we present, the synchrotron self-absorption is reduced in this scenario when applying it to the orphan X-flare of PMN J0948+0022 due to the smaller electron densities w.r.t. the disc and BLR-IC scenario.

The models and corresponding parameters are shown in Figure 6.18 and Table 6.9 respectively.

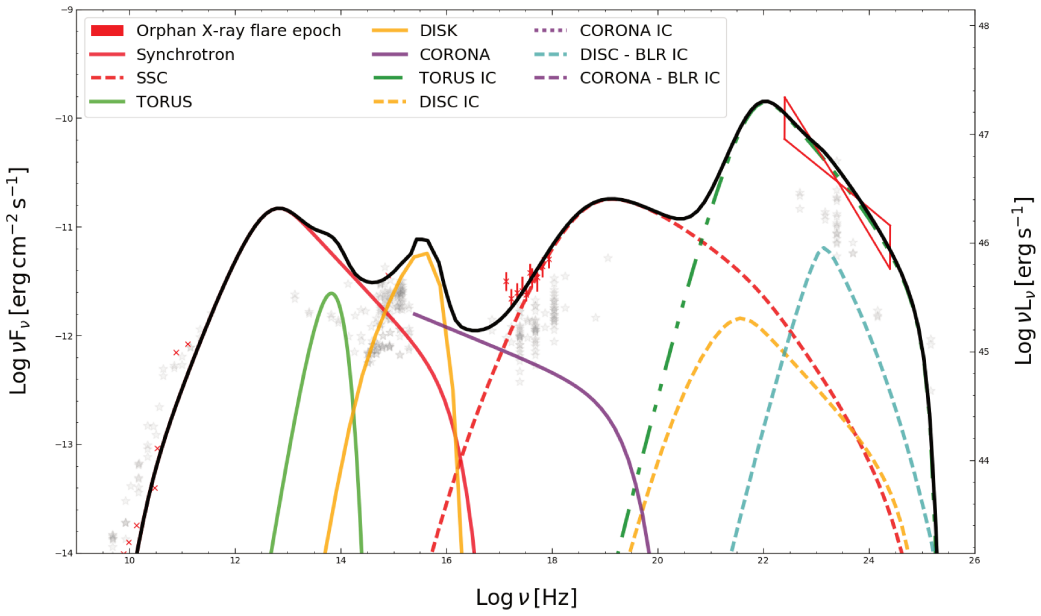

Figure 6.18 Torus IC-dominated model for the orphan flare of PMN J0948+0022

	Intermediate	X-ray flare	Flare
δ	10	12	11
K [1/cm^3]	1×10^{6}	6×10^{6}	8×10^{5}
R_{src} [cm]	1.12×10^{17}	5×10^{16}	1.32×10^{17}
B [G]	0.14	0.3	0.11
$n1$	2.7	2.7	2.7
$n2$	4.3	4.0	3.9
γ_{min}	500	500	500
γ_b	900	700	1.2×10^{3}
γ_{max}	3×10^{4}	3×10^{4}	3×10^{4}
R_γ [R_G]	4.5×10^{4}	4.5×10^{4}	4.5×10^{4}
u_e/u_b	10.25	12.03	16.23
n_e [1/cm^3]	9.76×10^{3}	5.264×10^{4}	9.66×10^{3}

Table 6.9 Model parameters for torus dominated scenario for the orphan flare of PMN J0948+0022, including the previously shown intermediate and flaring states.

6.4 An alternative scenario to explain flaring states

So far, one of the main assumptions of our multi-component model has been the invariability of the external photon fields of each source. As we have seen, these external fields are highly dependent on the characteristics of the accretion disc.

As introduced in Section 3.3.3, we have until now considered a standard accretion disc for a non-rotating Schwarzschild BH where the fraction of angular momentum captured by the latter is fixed to $\beta_i = 1$, and the efficiency of the gravitational energy release is $\eta_{Edd} = 1/12$. The mass accretion rate $\dot{m}$ is hence considered to be constant between different epochs.

In this section, we present an alternative scenario where the mass accretion rate of the BH changes between the quiescent to the flaring state, to account for the enhanced emission. In our code, for a constant η_{Edd}, an increase in the mass accretion rate leads to a larger luminosity and thus translates as a larger l_{Edd}.

Taking the disc-BLR dominated intermediate state solution from Table 6.7 as a starting point (where $l_{Edd} = 0.66$), we increase the Eddington ratio up to $l_{Edd} \simeq 1.0$ and $l_{Edd} \simeq 1.3$ to explore whether a BH accreting at the Eddington limit or at a super-Eddington rate respectively can account for the enhanced high energy emission seen during flaring states. In Figure 6.19 it can be seen that, although there is an increase in the disc and BLR-IC luminosities, this increased flux is not enough to model the observed GeV data.

Both for the Eddington limit and the super-Eddington solution, the changes that need to be applied to the model parameters correspond only to the magnetic field of the blob-in-jet and the second slope of the particle energy distribution. Indeed, just by lowering down the intensity to $B = 1.5$ and $B = 1.0$ for the $l_{Edd} \simeq 1.0$ and $l_{Edd} \simeq 1.3$ cases, and by softening the slope after the break to $n_2 = 3.3$, our model can describe the X-ray and gamma-ray emission from the flaring epoch of PMN J0948+0022 (Figure 6.20). However, the UV emission from the sources is overestimated by our models.

In the torus-IC dominated scenario where the contributions from the disc-IC and the BLR-IC are minimal, it is not that obvious to account for the flaring state by a differently accreting disc, since the emission region is located far away from the central engine and the torus-IC does not vary with the disc luminosity Section 3.3.5. This is the reason why only the disc and BLR-IC model is presented here.

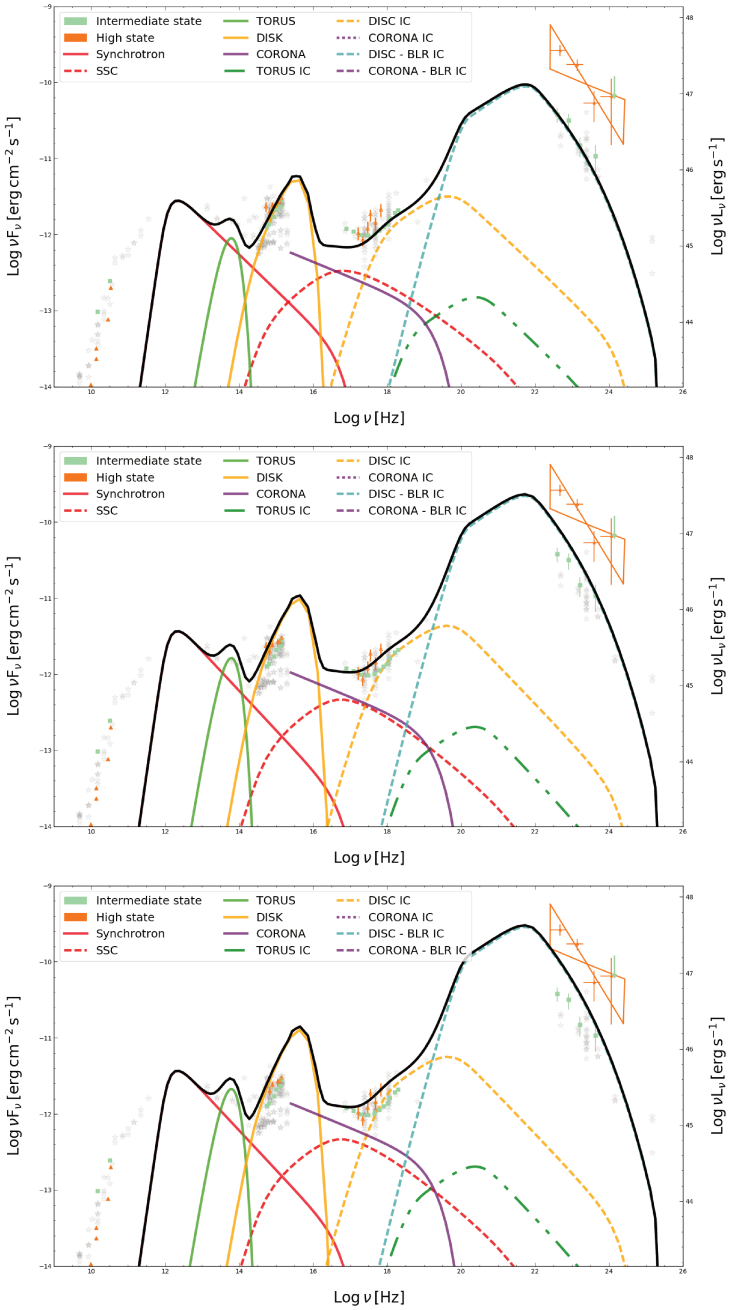

Figure 6.19 Effect of changing the l_{Edd} value on the disc-BLR dominated intermediate solution of PMN J0948+0022. We vary l_{Edd} from 0.66 (**top**) to 1.0 (**middle**) 1.3 (**bottom**), showing that a change in the Eddington ratio is not sufficient to describe the gamma-ray regime.

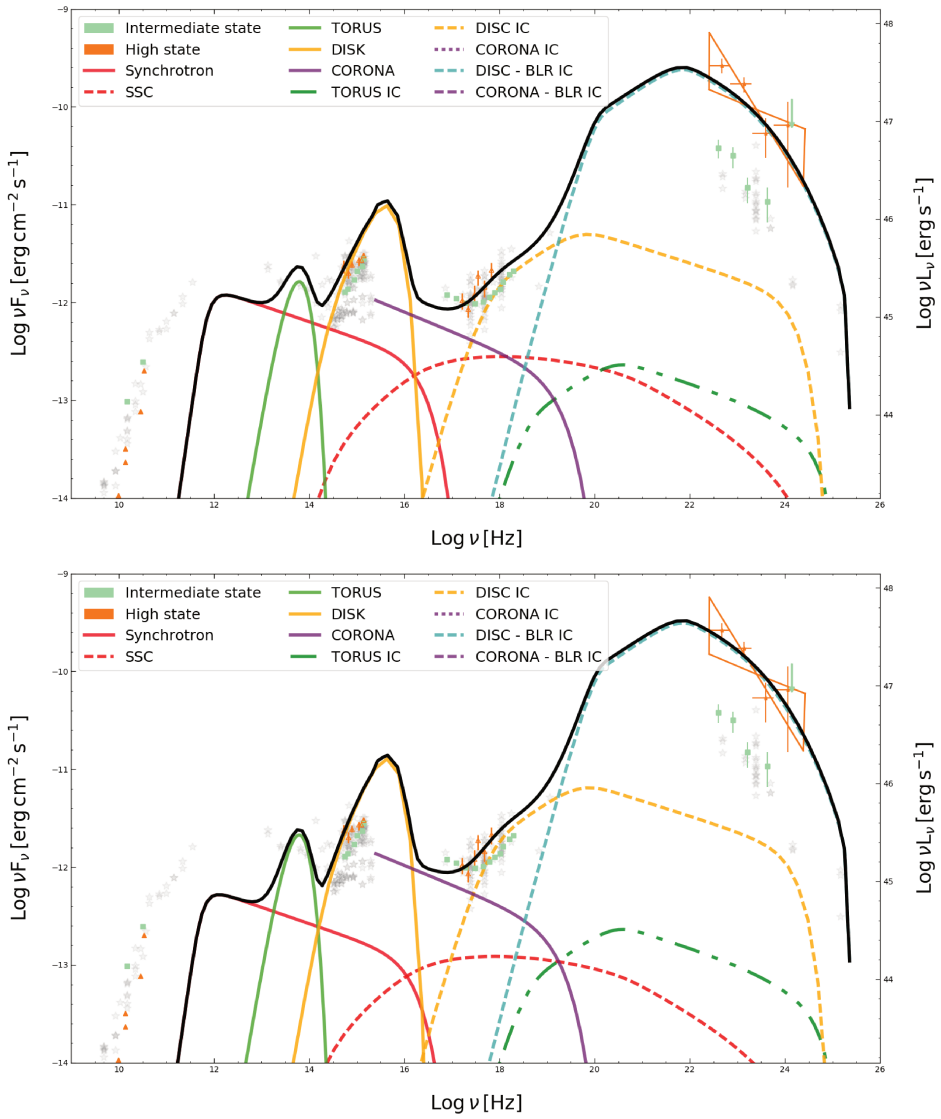

Figure 6.20 Model examples for the flaring state of PMN J0948+0022 for BHs with larger mass accretion rate ($l_{Edd} = 1.0$ in the **top** panel and $l_{Edd} = 1.3$ in the **bottom** one). Minimal changes are necessary to account for the enhanced radiation during the flaring epochs. See text for more details.

6.5 General discussion

Our multi-component radiative model describes the SED of the three gamma-emitting NLS1s presented here, both in the flaring and quiescent/average states. In this section, we will discuss our findings and their implications first focusing on the three sources, then on the two scenarios, and afterwards on the previously existing models from the literature. Finally, we say a word about the link between the potential higher mass counterparts of gamma-loud NLS1s, FSRQs.

6.5.1 The three sources

One of the most marked differences amongst 1H 0323+342, B2 0954+25A and PMN J0948+0022 is probably the BH mass, which in turn affects all the external components of the model. For 1H 0323+342, we consider the mass determined by Landt et al. [Lan+17], i.e. 2×10^7 $M_\odot$, which is one order of magnitude smaller than that of B2 0954+25A and PMN J0948+0022. Such difference might arise from the technique that was implemented for the determination of the mass, though, as mentioned in Section 1.4.3.

Although all three sources are located in the local Universe, B2 0954+25A and PMN J0948+0022 ($z \sim 0.7$ and $z \sim 0.58$ respectively) are further away than 1H 0323+342. The redshift difference can greatly affect the required jet parameters, and since those parameters are the ones we vary to go from one state to the other, they might be at the origin of some of the differences amongst the sources. However, it is striking to see the sources that are further away are the most luminous gamma-ray emitters of our small sample.

The soft excess, presented in Section 1.2.2 is a feature that has been detected in sources with a visible accretion flow component. Amongst the three sources and the datasets we consider only PMN J0948+0022 shows evidence of such excess during the intermediate epoch dataset we consider. The accretion disc model that we implement in our multi-component code does not take into account the soft-excess component, so it is not enough to describe such radiation when observed. The lack of this feature in the SEDs of 1H 0323+342 and B2 0954+25A is probably due to the lack of sampling at soft X-rays for these sources.

For the three sources that we have considered in the present work, the presence of the jet accounts for the high energy part of the spectrum, through IC scattering of photons from the disc and BLR, or the torus. Hence, the different inverse Compton interactions between the external photon fields and the relativistic jet are paramount to describe the high energy emission from this type of source.

The transition from quiescent/average to flaring states in the three sources is accounted for by denser relativistic knots featuring larger Doppler factors that provide the observed enhanced gamma-ray emission. The indexes of the particle energy distribution might also vary to account for a hardening/flattening of the gamma-ray spectrum. An alternative scenario where increased accretion rates would explain the observed enhanced activity has also been explored [Section 6.4].

Infrared and sub-mm data are much underestimated in the case of disc and BLR-IC scenarios for all three sources due to large electron densities and the accompanying synchrotron self-absorption [Section 3.1.1], while this effect is reduced for the torus-dominated scenarios of 1H 0323+342 and PMN J0948+0022, but not as much for that of B2 0954+25A.

Regarding how prominent each IC component is in the source's SED, we find that while for 1H 0323+342 the disc and BLR-IC components are similar in luminosity, for B2 0954+25A and PMN J0948+0022 the BLR-IC component is much more predominant than the disc-IC. This is probably due to the fact that B2 0954+25A and PMN J0948+0022 have larger accretion disc luminosities that translate into a BLR that is closer to the central engine according to the $r - L$ relationships obtained from reverberation mapping techniques [Section 1.2.3] from which we calculate the BLR distances (Equation 1.13), hence increasing the dominance of the BLR component over the disc-IC component.

6.5.2 The two scenarios

From applying the two different scenarios (i.e. disc-IC and BLR-IC dominated emission or torus-IC dominated emission) to the three gamma-emitting NLS1s considered in this work, we can infer some differences regarding the model parameters of each scenario. We need to keep in mind that the statistical significance of these

conclusions are quite biased by the reduced size of the sample to which the models have been applied.

First and foremost, we want to emphasize that transitions between the quiescent and the flaring states can be described by blobs with larger Doppler factors and larger electron densities regardless of the scenario. Since the emission regions in the torus-dominated scenario are less dense than in the disc/BLR-dominated one, synchrotron self-absorption is reduced in the former scenarios for 1H 0323+342 and PMN J0948+0022. However, the difference is not so obvious for B2 0954+25A.

For B2 0954+25A and PMN J0948+0022, disc/BLR-IC dominated scenarios feature larger Doppler factors and magnetic field intensities than the torus-IC dominated ones. Both scenarios have the same Doppler factors in the case of 1H 0323+342 though.

All quiescent to flaring state transitions require larger break energy values except for the torus IC dominated solution of B2 0954+25A (were the quiescent solution requires a larger γ_b value). Also, for the torus to dominate, we need the minimum and break energies of the electron distribution to be shifted to much higher energies than those of the disc/BLR-IC dominated scenario. Larger γ_b values require smaller magnetic field intensities in the torus-IC dominated scenario (around one order of magnitude smaller than for the disc/BLR IC dominated scenario) to reduce the shift towards higher energies of the peak of the synchrotron component.

For the orphan X-flare of PMN J0948+0022, the disc/BLR-IC dominated scenario presents the same γ_b as the flaring state, while the torus–IC dominated solution features a break energy lower than that of the intermediate state, which coupled to a slightly larger magnetic field intensity is necessary to explain the observed enhanced X-ray emission.

Regarding the shape of the electron distribution, the hardening of the Fermi spectra during flares requires smaller values of the second slope of the distribution n_2 in both scenarios. However, the index of the disc/BLR-IC dominated scenario is somewhat harder than that of the torus-IC dominated scenario. On the contrary, the torus-dominated scenario presents larger values of the initial slope.

In the torus-dominated scenario, including the orphan flare of PMN J0948+0022, the SSC emission from the jet along with the emission from the corona account for the X-ray emission from the source, while gamma-ray emission is ascribed to the torus-IC component. Regarding this last component, the peak temperature of the

torus is the same in both scenarios but for the IC to be torus dominated, larger τ_{IR} scaling factors are necessary.

In disc/BLR dominated scenarios, identifying a trend is not that simple though. For 1H 0323+342, a combination of coronal and disc-IC with a minor contribution from the SSC component accounts for hard X-rays in the quiescent epoch, while the enhanced X-ray emission during the high state requires a larger SSC component. For B2 0954+25A, SSC and disc-IC emission with a negligible coronal contribution give a good description of both states. For PMN J0948+0022, coronal and disc-IC with minimal contribution from SSC radiation describe X-ray data in both states. Note that the SSC contribution is more marked for the orphan flare of PMN J0948+0022 in this disc/BLR dominated scenario.

The most marked differences between both scenarios are the position of the emission region and the opacity of the BLR. In disc/BLR dominated models, the source needs to be located below the BLR at a distance of around 3×10^3 R_G and hence much closer from the central engine. On the contrary, the emission region is located at the outermost radius of the BLR where ionization is less important in torus-dominated models. For the torus to dominate at GeV energies, we need to have a very low covering factor of the BLR τ_{BLR} which reduces the contribution of the ionized lines to the IC spectrum.

Discs in disc and BLR-dominated solutions accrete at slightly lower Eddington ratios, which results in a slightly lower disc luminosities. Note that different Eddington rates yield different luminosities, which according to the $r - L$ relation obtained from reverberation mapping [Section 1.2.3] in turn locate the BLR slightly closer (for lower luminosities) or farther (for higher luminosities) from the BH. In our models, though, due to the small luminosity differences between both scenarios, the size and position of the BLR are approximately equal in both scenarios.

The disc and BLR-IC dominated scenario is favored w.r.t. the equipartition relation between the electron energy density and the magnetic energy density. Anyhow, the values remain within the expected range for gamma-ray emitting AGN for both scenarios.

Let us remind the reader that an additional framework where the mass accretion rate of the object varies has also been explored in order to explain the enhanced high energy emission from the during the flaring state of PMN J0948+0022 for the disc/BLR-IC dominated scenario [Section 6.4]. Due to the lack of dependence of the torus-IC scenario on the disc luminosity (see Section 3.3.5), we did not consider this second scenario for the varying accretion disc framework.

As introduced in Section 3.3.5, the location of the emission region in gamma-loud AGN is an open question. Due to size-constraints set by rapid variability time-scales, the source should not be located far away from the central engine if one considers that the blob expands over the whole cross-section of the conical jet, which would favor the disc and BLR-IC dominated scenario. On the other hand, gamma-ray emission from a region located close to the BH (and hence to the accretion disc) should suffer from absorption due to the interaction between soft-photons from the disc and TeV photons from the blob. The lack of such absorption features in the so far detected TeV-blazars could mean the emission actually takes place in a torus-dominated, more distant location. From the results obtained in the present work, we do not have strong preferences of one of the scenarios over the other.

Indeed, in the case of gamma-loud NLS1s the lack of detection at VHE might also be due to the sensitivity of the current generation of IACTs, which will definitely be improved by the upcoming Cherenkov Telescope Array (CTA) that will lower down the threshold in energy and thus will be really suitable to observe this type of source, perhaps not only during flaring episodes as is currently the case.

Other authors have also modeled these sources in disc/BLR and torus dominated scenarios. Although the applied models differ at different degrees from ours, and the epochs they choose might not necessarily correspond to the ones we have presented here, we can still compare our results to theirs to some extent, and see whether they find the same trends as we do.

6.5.3 Previous models

In this section, we present an overview of previous models by other authors of the gamma-loud NLS1s considered in this work. If an author provided different states in their work, regardless of us not considering them for modeling purposes, we compare how the approach they followed to transition between low and high gamma-ray states differs from ours.

1H 0323+342

In Kynoch et al. 2017 (submitted to MNRAS) where the main modeling was done by collaborators, we modeled a low state of 1H 0323+342 for different locations of the emission region. The dataset was non-simultaneous as a whole, although it comprehended a subset of quasi-simultaneous data, namely GNIRS (September 2015), Keck (February 2016) and XMM-Newton (23-24 August 2015) data. The present work, apart from considering a different dataset, focuses on modeling the variability of the source in two different scenarios, which will be published in a future paper.

Indeed, in Kynoch et al. 2017 we did not perform a variability study, but instead the dataset was modeled for three different locations of the emission region: below the BLR, inside the BLR and outside of it. We found the first scenario, where the high-energy emission is dominated by disc IC photons with a minor BLR contribution, to provide the best model. The present work was focused in studying the gamma-ray variability of the source at gamma rays for two different datasets, thus we considered both the disc and BLR-IC dominated scenario and the torus-IC dominated scenario, and we do not find strong preferences for neither of them.

In Kynoch et al. 2017 we found that a non-rotating BH scenario was preferred over a Kerr BH. A non-rotating Schwarzschild BH paradigm has been considered throughout the present work.

Similar to Kynoch et al. 2017, the present work also constrains the luminosity of the BBB from optical data. The obtained models implied Eddington luminosity ratios of $l_{Edd} \sim 0.6 - 0.8$, yielding accretion disc luminosities of $\mathrm{L}_{Disc} \sim 2 \times 10^{45}\,\mathrm{erg\,s^{-1}}$, values that are compatible with what we find for the dataset considered in the present work.

The emission region is located closer to the BH in Kynoch et al. 2017, at approximately half the distance considered in this work. Moreover, the Doppler factor for their disc-IC dominated low state model is larger than our quiescent state Doppler factor, as is the magnetic field intensity.

Both Kynoch et al. 2017 and the present work ascribe mid-IR radiation to the torus, which limits the synchrotron peak luminosity, and in turn increases the Compton-dominance in the SED. This positions 1H 0323+342 close to FSRQs in shape but with luminosities more like the ones observed in BL Lacs.

In Kynoch et al. 2017, we ascribed hard X-rays to the low-energy side of the Compton hump. The case were the corona reproduces all the 2-10 keV X-ray emission could not be strongly rejected, but a model that includes jet contribution yielded a better fit and model parameters closer to the ones expected for NLS1s. However, for the quiescent state we consider in the present work, the jet SSC contribution is minimal, and X-rays can indeed be ascribed to the hot corona.

Regarding the BLR parameters, they estimate the BLR luminosity from Celotti et al. [Cel+97], and they obtain $\log(L_{BLR}/\mathrm{erg\,s^{-1}}) \sim 43.33$. They estimate the radius of the BLR to be $\mathrm{R}_{BLR} \sim 31$ light-days $\sim 8.02 \times 10^{16}\,\mathrm{cm}$, which is compatible to the value from our model $\mathrm{R}_{in}^{BLR} = 2 \times 10^4\ \mathrm{R}_G \simeq 7.4 \times 10^{16}\,\mathrm{cm}$.

Paliya et al. [Pal+14] (from which we extract the Fermi data of our quiescent state and the flaring state dataset) presented BLR-IC dominated models for all the 4 states in their paper. Unlike us, that explain the variability between different states simply by variations in the jet parameters, Paliya et al. [Pal+14] describe the differences amongst their 4 states by changing the parameters of the external components of the model, mainly through emission regions located closer or further away from the central engine, as well as with changes in the jet and the electron distribution.

Abdo et al. [Abd+09c] modeled a dataset comprising Swift data between 2006 and 2008. They found a low synchrotron peak frequency (around 10^{13} Hz, similar to those found in FSRQs) and a strong disc/corona component, which is in agreement with our models. In general, the so far detected gamma-emitting NLS1s seem to be low-frequency peaked blazar objects (e.g. Abdo et al. [Abd+09c], D'Ammando et al. [D'A+12]), and Yao et al. [Yao+15] findings corroborate this statement.

On the other hand, Yao et al. [Yao+15] considered a simultaneous dataset comprising Suzaku data taken on 2009 July 26-27 and Swift UV/optical data from 2009 July 27. They applied a χ^2 minimization procedure to the jet parameters, and considered two different scenarios: a BLR-IC dominated one and a torus-IC dominated one. Although they provide the fit parameters for both, the graphical representation of the former scenario is only shown, so we cannot compare our torus-IC scenario results but to a superficial level, due to the different modeling procedure that is followed. Similar to us, they found no preference over neither of the scenarios. The fact that different scenarios implementing different emission region locations can model the observed emission well indicates that, at the moment and with the existing data, no scenario seems to be preferable to describe the emission of 1H 0323+342. However, we can mention the differences in the assumptions they make for the model components.

For instance, they consider a disc that extends from 3 R_S to 700 R_S, while ours extends to 500 R_S. This implies that their disc will contribute more at lower frequencies, as shown in Figure 3.15. Also, they consider a jet that is aligned with the line of sight at a very small angle $\theta = 1°$, which in principle is not compatible with the 4-13 degree range found by Fuhrmann et al. [Fuh+16]. They ignore thermal emission from the torus arguing that WISE emission in some similar NLS1s is highly variable at timescales of hours which hints at a jet-dominance at IR frequencies (Jiang et al. [Jia+12]), and also justifying the fact that Abdo et al. [Abd+09c] found the IR contribution of a torus to be negligible when compared to synchrotron emission from the jet for several gamma-emitting NLS1s. However, since there are no contemporary WISE data for our datasets, we choose to model the torus anyways.

Yao et al. [Yao+15] find a $l_{Edd} = 0.8$ from a bolometric luminosity of $L_{bol} = 1.9 \times 10^{45}$ erg s. In their models, regarding of the scenario, X-rays are dominated by coronal emission, and the jet contribution is minimal for their dataset, although they reckon it might increase at hard X-rays during flaring episodes. One of the most remarkable discoveries of Yao et al. [Yao+15] probably is the fact that they find statistically significant correlated UV to X-ray variability on daily timescales for the first time in a gamma-emitting NLS1 galaxy.

Yao et al. [Yao+15] modeled the SED of 1H 0323+342 for a torus-dominated scenario too. They found the torus-IC dominated scenario to feature a smaller magnetic field intensity, like we do. They also present solutions were the torus-dominated scenario requires larger maximum electron energies, but their disc/BLR dominated scenario needs larger minimum and break energies, just the opposite that we find. The Doppler factor changes between the two scenarios, while it remains the same in ours.

B2 0954+25A

Calderone et al. [Cal+12] modeled B2 0954+25A via the Ghisellini and Tavecchio [GT09] model for two different datasets: one where the disc dominated at low frequencies, and another where low energy emission was dominated by jet synchrotron emission (see Figure 6.21).

Contrary to Calderone et al. [Cal+12], the present work focused on the gamma-ray variability of the sources, so our datasets are dominated by the Seyfert-like nucleus at low frequencies. Further comparison can thus be made between their disc-dominated state and our quiescent state. However, we need to stress that their dataset is not the same as ours, since our quiescent-state Fermi dataset is time-wise more comprehensive (we considered the 3FGL data while at the time of their publication data up to 2011 were only available).

From their calculations, they obtain a BLR luminosity of $L_{BLR} \sim 6.3 \times 10^{44}\,\mathrm{erg\,s^{-1}}$, which results in a bolometric luminosity of $L_{bol} \sim 10^{46}\,\mathrm{erg\,s^{-1}}$. Due to the caveats in their method, they report an uncertainty of at least a factor of 2 in their results. On the other hand, our model yields a disc luminosity of $L_{Disc} = 1.13 \times 10^{46}\,\mathrm{erg\,s^{-1}}$, which is compatible with their findings. Given that the covering factor of the BLR that we use is the sames as theirs, our BLR luminosity is also in agreement.

To determine the radius of the BLR, they apply the $r - L$ correlation, which is the same procedure we follow. Thus, the fact that their luminosity is compatible with ours means both models feature a BLR that is at the same distance from the BH, $R_{BLR} \sim 1.5 \times 10^4 R_G$.

Regarding the position of the emitting region, they fix their blob at a distance $R_\gamma = 2663 R_G$ from the BH, closer than in our case where the blob is at $R_\gamma = 3000 R_G$. Anyways, both models feature emission regions well below the BLR. On the other hand, their magnetic field is approximately 2.5 times larger than ours ($B = 5.2\,\mathrm{G}$ vs $B = 2.0\,\mathrm{G}$). However, we need to recall that their disc dominated state dataset is not exactly the same as our quiescent state dataset, so comparisons need to be done with care.

As mentioned at the beginning of this section, Calderone et al. [Cal+12] also modeled the source for a state where the low-energy emission is jet-dominated (see Figure 6.21). The fact that states were the contribution from the Seyfert-like nucleus of B2 0954+25A is completely overpowered by synchrotron emission from the jet shows a marked FSRQ-like behaviour of this source. Indeed, the Seyfert

like nucleus is seldom observed in FSRQs, which increases the interest of studying gamma-emitting NLS1s to cast light upon sources that alternate between Seyfert-like and blazar-like behaviour through different epochs.

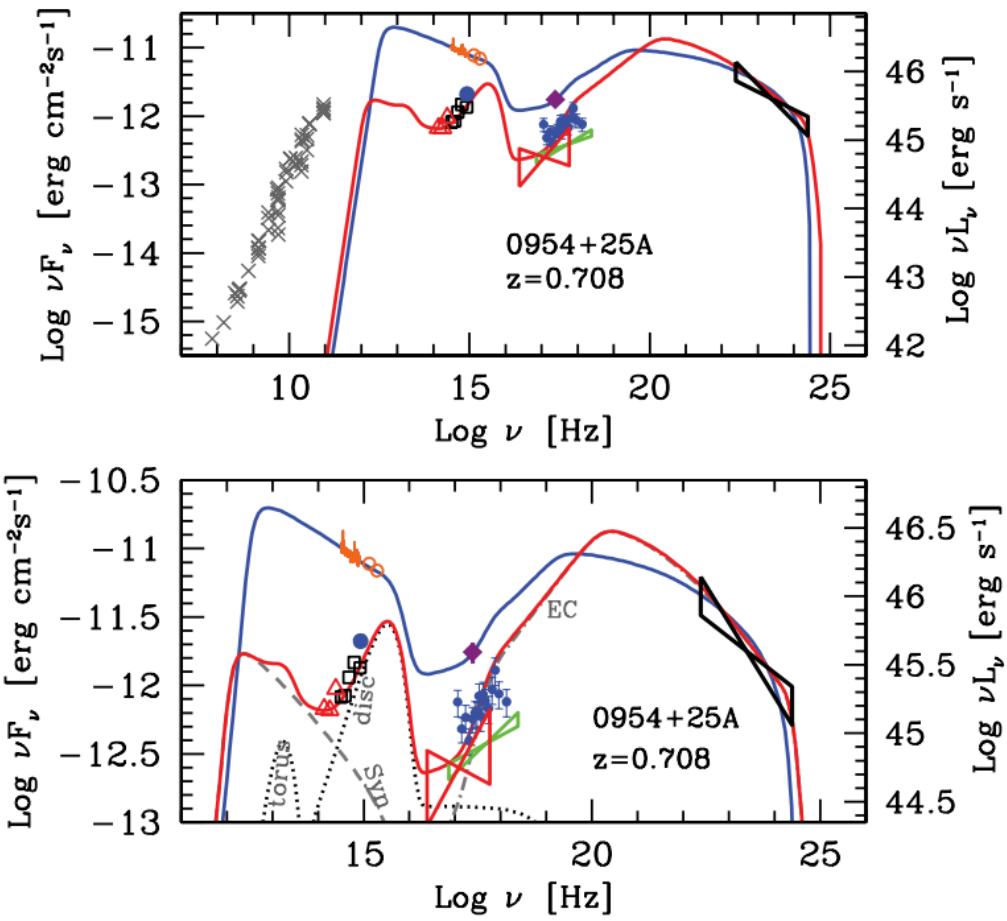

Figure 6.21 SED modeling of B2 0954+25A from Calderone et al. [Cal+12]. They model the source for two different states: one dominated by the disc (red) and another dominated by the jet (blue). Our quiescent state takes into account the Chandra bowtie in light green.

PMN J0948+0022

For modeling PMN J0948+0022, we considered the intermediate state from D'Ammando et al. [D'A+15] (red datapoints in the upper panel of Figure 6.22) and the first gamma-flare from Foschini et al. [Fos+12] (blue datapoints in the lower panel of Figure 6.22). Both D'Ammando et al. [D'A+15] and Foschini et al. [Fos+12] modeled the datasets we consider in this work in BLR-dominated scenarios, so we can compare our results to theirs to some extent.

For the modeling of the intermediate state, D'Ammando et al. [D'A+15] have much larger Doppler and Lorentz factors than us ($\delta = 30$ vs $\delta = 19$). They describe the X-rays as a combination of coronal emission and IC emission, with a weak SSC contribution, while in our model it is mostly the disc-IC emission that accounts for the X-ray data, with a minor contribution of both the corona and SSC components.

D'Ammando et al. [D'A+15] also modeled the source during a jet-dominated state in 2013 similar to the previously presented jet-dominated state of B2 0954+25A modeled by Calderone et al. [Cal+12]. D'Ammando et al. [D'A+15] modeled the 2013 flare both for a BLR-dominated and a torus-dominated scenario. Although we do not consider the jet-dominated state of PMN J0948+0022 for modeling, we can still compare the approach D'Ammando et al. [D'A+15] followed to transition from the intermediate state to a enhanced high-energy emission state.

Similar to us, and always in the BLR-dominated scenario, D'Ammando et al. [D'A+15] explain the flare with a denser blob that however features much smaller Doppler factors during the flare ($\delta = 30$ for their intermediate state while $\delta = 12$ for their flaring state). In our models, flaring epochs always present denser blobs with larger Doppler factors than quiescent or lower activity epochs. Contrary to us, D'Ammando et al. [D'A+15] explain the flare with lower magnetic field intensities.

In the torus-IC scenario, they require much larger Doppler factors for modeling the torus-dominated scenarios, which is the opposite than what we observe in our models, which is probably due to the fact that the 2013 flare was jet-dominated at low energies, and they required a more predominant synchrotron component to model the emission. Unfortunately, the graphic representation of their models does not show each of the components of their model, so it is not evident to draw further conclusions. The magnetic field intensity does not vary in their models, although the torus-dominated scenario features a smaller break electron Lorentz factor. Also,

their torus-dominated scenario suffers from stronger synchrotron self-absorption than ours, due to larger electron densities.

They concluded that none of the scenarios was strongly preferred over the other, although their BLR-dominated solution was farther from equipartition, while both scenarios are at similar electron and magnetic energy density ratios for our flaring episode solutions (see Table 6.7).

Regarding the flaring state from Foschini et al. [Fos+12] that we model, let us begin by stating that they apply the model by Ghisellini and Tavecchio [GT09]. The Lorentz factors of their jet are very similar to ours ($\Gamma = 16$ in their model versus $\Gamma = 17$ in ours). On the other hand, their magnetic field is also around the double of ours ($B = 2.5$ in contrast to our $B = 1.4$). For the same value of the mass of the BH, they obtain an accretion disc luminosity of $L_{disc} = 9 \times 10^{45}\,\mathrm{erg\,s^{-1}}$ that corresponds to an Eddington ratio of $\mathrm{l}_{Edd} = 0.4$. With our parameters, we obtain a luminosity of $L_{disc} = 1.13 \times 10^{46}\,\mathrm{erg\,s^{-1}}$ for a disc that accretes at a slightly higher rate of $\mathrm{l}_{Edd} = 0.66$. Their torus component peaks at a temperature of 1700 K much higher than ours, where peak temperature is 1200 K. The lack of simultaneous data at IR frequencies causes the torus peak not to be tightly constrained. Nonetheless, the torus luminosities are compatible ($\sim 10^{45}\,\mathrm{erg\,s^{-1}}$).

Given that the accretion disc luminosities are similar, so is the distance of the BLR, $R_{BLR} = 1.3 \times 10^4 R_G$ in their case and $R_{BLR} = 1.5 \times 10^4 R_G$ in ours. Their blob is located closer to the central engine at a distance of 1150 R_G from the BH, while ours is almost at the double distance, $R_\gamma = 2000 R_G$.

Their flaring state presents a higher bulk Lorentz factor, along with a smaller magnetic field than the other, lower states of the source they feature in their paper. This is similar to the approach we take to transition from our intermediate state to the flaring state. A X-ray corona is also present in their model.

As far as the interpretation of the SED of the source is concerned, Foschini et al. [Fos+12] ascribe X-ray emission to SSC emission, while in our case it is the IC emission from the disc that mostly accounts for such emission, with minor contributions from the SSC and corona components. However, the representation of their model does not show each of the components individually, so further comparison with regards to the differences between their approach and ours is difficult to make.

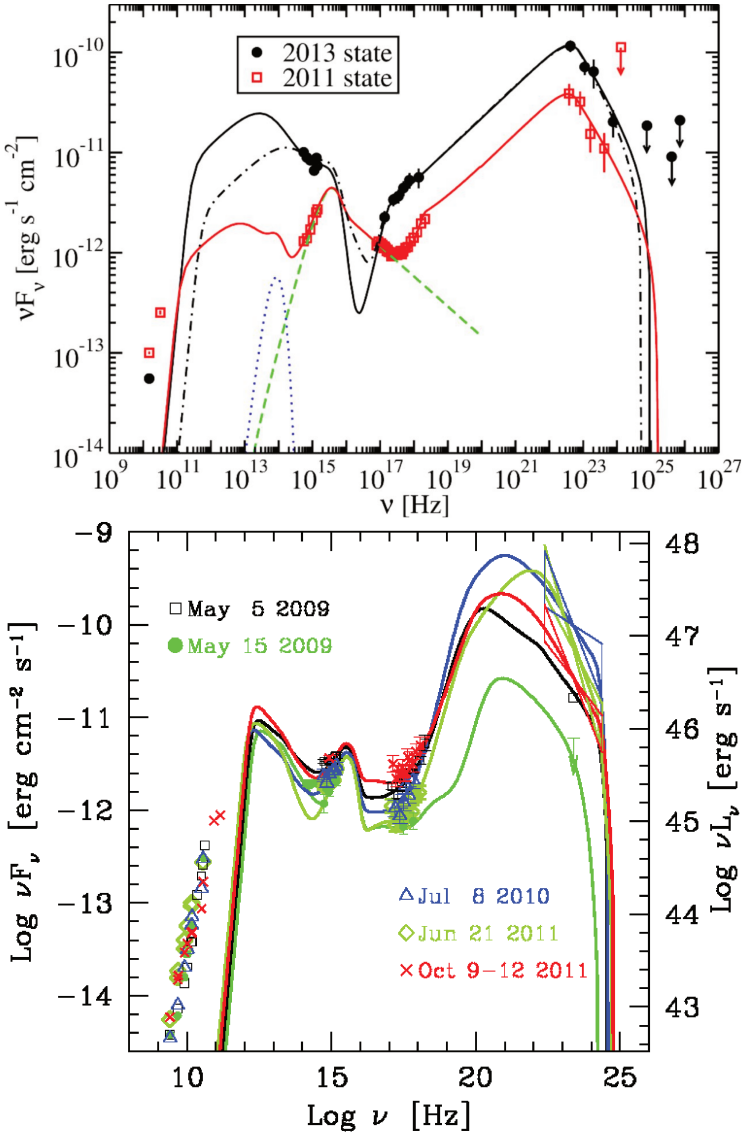

Figure 6.22 PMN J0948+0022 models by D'Ammando et al. [D'A+15] (**top**) and Foschini et al. [Fos+12] (**bottom**). Our intermediate state is the red state in the top figure, and our flaring state corresponds to the blue state in the bottom one. Further comparison is provided in the text.

6.5.4 A word on FSRQs

The detection of gamma-ray emission from some NLS1s showed that at least a subsample of this type of object can host powerful relativistic jets.

Given that gamma-loud NLS1s accrete close to the Eddington limit, one of the greatest open questions is where these AGN fall within the blazar sequence. Past evidence seemed to hint at gamma-loud NLS1s being the low-mass counterparts of FSRQs. However, there is increasing evidence that gamma-loud NLS1s actually have masses that are close to those of BL Lacs and FSRQs, so they might actually be more similar to FSRQs, given their high accretion rates, than a subclass in their own.

Regarding the results from our modeling, our solutions for both disc-BLR and torus-dominated scenarios have synchrotron components peaking at around 10^{13} Hz, the range at which the low-energy hump peaks in FSRQs. The fact that there is a tendency for Compton dominance in the SEDs of gamma-loud NLS1s is also another common detail they share with FSRQs.

FSRQs are jet-emission dominated also at low frequencies, while for the datasets that we consider for the gamma-emitting NLS1s in this work, the Seyfert 1 like nucleus is always visible. This might not always be the case, though. For instance, Calderone et al. [Cal+12] model a second scenario apart from the one presented here where the emission from the nucleus is completely drowned in emission from the jet synchrotron. Likewise, D'Ammando et al. [D'A+15] present a second epoch of PMN J0948+0022 apart from the intermediate epoch that we model, where a major contribution from the jet dominated over the emission from the nucleus of the AGN. This changing dominance points towards gamma-emitting NLS1s having a FSRQ-like behaviour for given high-flux-at-low-energies states. This might be confirmed if both jet-dominated and nucleus-dominated states are observed in more gamma-loud NLS1s by future campaigns.

7 Conclusions and outlook

The present manuscript summarizes the work done regarding the Multi-WaveLength (MWL) data analysis and the modeling of the broad-band Spectral Energy Distributions (SEDs) of sources that fall into two different categories of gamma-emitting Active Galactic Nuclei (AGN): blazars and gamma-loud Narrow Line Seyfert 1s (NLS1s).

The first part of the manuscript comprises the background necessary for understanding AGN in general and the two gamma-loud subtypes that we have studied in particular, along with the techniques of ground-based gamma-ray detection and the data acquisition and analysis procedure of the High Energy Stereoscopic System (HESS) telescopes. The description of the two different broad-band SED models that we have applied to the gamma-loud AGN in the present work is also provided.

More precisely, in Chapter 1 we have provided an overview of AGN discovery, along with an outline of the unification model and the main building blocks of AGN. Due to our focus on gamma-ray emitting AGN, a special emphasis is made on the main characteristics of the two subtypes of AGN that are further considered for modeling purposes, blazars and gamma-loud NLS1s.

Chapter 2 presented the principles of ground-based TeV astronomy and Imaging Atmospheric Cherenkov Telescopes (IACTs), with a summary of their history and a special interest on one of the third-generation IACT facilities: the HESS experiment. The key points of HESS data extraction and analysis have been given, and we also introduced the extragalactic Target of Opportunity (ToO) protocol that closely monitors the multi-wavelength behaviour of a number of well-known TeV emitters in order to rapidly trigger HESS observations if a given source enters an interesting enhanced emission state. ToO monitoring is also useful to trigger MWL observations provided that HESS observes an interesting high-emission state at TeV energies. Comprehensive multi-wavelength datasets such as the ones that can be obtained thanks to ToO campaigns are paramount to understand the broad-band behaviour and characteristics of AGN.

In Chapter 3 we introduced and described the different models that we have applied to a number of gamma-emitting AGN. First, we have presented the simple leptonic

one-zone SSC model based on Katarzyński et al. [Kat+01] that gives a good description of the 2-bumped SED of some BL Lac objects, specially High frequency-peaked BL Lacs (HBLs). The constraints that can be set upon model parameters and the consequent parameter space exploration that can be performed based on a number of observables have also been presented. Second, we have presented the development of a pre-existing lepto-hadronic one-zone SSC numerical code to include external photon fields that account for the observed emission from gamma-loud objects whose SED is more complex than that of HBLs. We have provided the details of the formalism that is applied to the radiative components originating from the different external photon fields we consider, namely the direct and Inverse Compton (IC) emission from the torus, the accretion flow and the Broad Line Region (BLR) of the AGN. The effect that different model parameters have on the overall model was also explored. At the end of the Chapter, we have provided a brief summary of some other models from the bibliography that can account for the observed SED of different types of gamma-loud AGN.

The second part of the manuscript consists of the actual multi-wavelength data analysis and the application of the aforementioned models to the SED of a couple of selected sources.

First, in Chapter 4 we have presented an example of the ToO monitoring protocol of the HESS collaboration, specifically the MWL campaign of the Low frequency peaked BL Lac (LBL) PKS 1749+096 during its flaring episode on July 2016. The enhanced flux seen by Fermi-Large Area Telescope (LAT) triggered MWL observations from a number of facilities, e.g. Swift and HESS. The results of the Swift-Ultra Violet/Optical Telescope (UVOT) and X-Ray Telescope (XRT) data analysis of the flaring-period observations that were performed as a part of the present work have been presented in the Chapter.

The MWL light curves of the flaring period showed that the source presented correlated Swift-XRT and Fermi-LAT variability during the beginning of the enhanced activity period, while correlated UVOT, Automatic Telescope for Optical Monitoring (ATOM) and HESS behaviour was seen at the end of the flare. Preliminary results for the MWL analysis of PKS 1749+036 along with a summary of the HESS ToO performance during the 2016 campaign can be found in Schüssler et al. [Sch+17]. The good MWL coverage of the observations during the flare look very promising for the extraction of a simultaneous dataset suitable for modeling. The variability constrains that can be deduced from the analysis of the MWL light curve will set preliminary constraints on the size of the emitting region, narrowing down the parameter space of the model. A joint MAGIC, Fermi and HESS paper is foreseen in

the near future were the broad-band variability and the SED of the source will be explored in more detail.

In Chapter 5, the multi-wavelength analysis and modeling of the HBL source 1ES 2322−409 that was first detected as a TeV emitter by HESS have been presented. HESS data were analyzed through the Model++ analysis chain introduced in Chapter 2. Available multi-wavelength data from a number of facilities were also analyzed, and a quasi-simultaneous dataset centered on the highest Swift-XRT observation of the source was extracted. This dataset was then modeled with the one-zone leptonic SSC model introduced in Chapter 3, which is sufficient to describe the spectral profile of the simultaneous observations available.

The modeling of 1ES 2322−409 was tackled with an special interest given the fact that the redshift of this source remains unclear due to the lack of deep-field surveys. Consequently, the model was applied to two different redshifts: the 'official' value of $z = 0.17$ from Jones et al. [Jon+09], and a second, smaller value of $z = 0.06$ that corresponds to the redshift of a number of galaxies in the field of view of 1ES 2322−409. The underlying idea was to explore whether the observational constraints of the available simultaneous MWL dataset would rule out models with one of the two redshift values. Given that the parameter sets for the solutions we present do not greatly differ from one another, no major conclusion could be drawn w.r.t. the preference of one particular redshift over the other, at least with the currently available data. More exhaustive MWL data taking when the source is in a bright state would be helpful to clarify the issue, along with the so far lacking deep-field surveys to directly study/determine the redshift of the source, of course.

Next, Chapter 6 gathers the results of the application of our multi-component model to the recently discovered gamma-ray emitting subclass of NLS1s. The motivation of applying our multi-component model to gamma-loud NLS1s was to study the suitability of modeling this type of source with our model, since, similar to the FSRQ subclass of blazars, the radiative components from the relativistic jet do not appear to be enough to describe the observed emission in this type of source.

Like for FSRQs (and blazars in general), there are many open questions regarding gamma-loud NLS1s. One of the most interesting ones for both FSRQs and gamma-emitting NLS1s is the location of the emission region, which causes high-energy emission to be dominated by IC components stemming from different photon fields of the AGN. To study the matter, we applied our multi-component model to three gamma-emitting NLS1s - 1H 0323+342, B2 0954+25A and PMN J0948+0022- for two different hypotheses of the position of the emission region. First, we modeled each source in a scenario where the emission region is located within the BLR of

the AGN such that a combination of the disc-IC and BLR-IC radiative components is at the origin of the observed gamma-ray emission. Second, we assumed a scenario where the emission region is located outside the BLR, which causes the torus-IC component to dominate at high energies.

One peculiarity of the so-far detected gamma-loud NLS1s is that they have only been detected at gamma-ray energies during flaring episodes. Therefore, we took an interest in modeling both gamma-ray quiescent (or low) states and gamma-ray flaring states of the sources for both emission region location hypotheses. The aim was to explore how the behaviour of the sources changed and how our multi-component model could explain those changes.

On a first approach, the observed gamma-ray variability is explained by changes in the jet and the electron distribution of the emission region, assuming that none of the external fields change. We show that both epochs of each source can be well described by our model under this hypothesis for the two emission region position assumptions. The torus-dominated scenarios present lower densities of the emission region, which reduces the synchrotron self-absorption in this scenario. In the torus-IC dominated scenario, X-rays are in general ascribed to a combination of SSC and corona emission for all three sources, with a more important contribution from the former component during flaring states. In the disc-IC and BLR-IC dominated scenario, it is a combination of the SSC, disc-IC and corona components that accounts for the X-ray emission in 1H 0323+342 and PMN J0948+0022, while the presence of a corona is not necessary to explain the observed radiation in B2 0954+25A.

From our results, there is no strong preference of one of the emission region position hypotheses over the other, at least for the datasets that we have consider. However, it is necessary to remark that some of the torus-dominated solutions require large emission regions (e.g. $R_{src} \sim 9.5 \times 10^{17}\,\mathrm{cm}$ in the case of PMN J0948+0022) that would seem hard to reconcile with the distance of the torus ($R_{IR} \sim 10^{18}\,\mathrm{cm}$), and might be a hint of this emission region location hypothesis to be unrealistic. This is an issue that needs to be looked into more detail in the future.

In theory, an emission region located close to the central engine, e.g. our disc-IC and BLR-IC scenario, would be expected to suffer from TeV absorption due to the interaction between the gamma-rays and the soft photons from the innermost part of the AGN. The lack of absorption features in the VHE spectrum of a source would hence point towards a region located farther from the BH, probably at a distance where the torus dominates, e.g. our torus-IC scenario. This, in turn, would be hard to reconcile with the fast variability time-scales seen in blazars, which require the emission region to be small enough and thus close to the engine. TeV emission has

not yet been detected from gamma-loud NLS1s, but this might change once the next generation of IACTs, the Cherenkov Telescope Array (CTA) begins its operation. CTA will lower the energy threshold of the current generation of instruments, which seems encouraging w.r.t. the detection of GeV NLS1 that have so far only been detected mostly during flaring gamma-ray states.

The assumption of external photon fields that remain unchanged between different gamma-ray states could be regarded as a bold supposition. Therefore, we have explored a third scenario where a changing accretion regime would explain the enhanced high energy emission of the source. We tested this hypothesis by applying it to the disc-IC and BLR-IC dominated scenario of PMN J0948+0022. Our results show that a disc featuring an increased mass accretion rate via a larger Eddington ratio value requires minor changes in the electron distribution and a blob located slightly closer to the central engine in order to describe the high-energy emission of the flaring epoch of PMN J0948+0022.

Last, we have investigated whether our multi-component code can describe flaring events at frequencies other than gamma-rays. For that purpose, we have applied the model to an orphan X-ray flare of PMN J0948+0022 both for an emission region within the BLR (disc-BLR-IC dominated scenario) and an emission region outside the BLR (torus-dominated scenario) and again assuming that only the parameters linked to the jet change. The main differences in the model parameters between the gamma-ray flare and the X-ray flare models are denser emission regions located much closer to the central engine during the orphan X-ray flare for both emission region position hypotheses.

Overall, we have shown that our multi-component model can describe the emission from the selected gamma-loud NLS1s both during quiescent and flaring states. All the different scenarios and hypotheses considered throughout the present work can be used as an initial probing tool for our improved multi-component numerical code. The present work opens a path to continue the research to narrow down the most likely hypotheses regarding the model parameters of the studied gamma-loud NLS1s.

The next logical step would be to extend the modeled sample to the remaining gamma-loud NLS1s, to see whether other sources exhibit the same behaviour as the sources of our small subsample. The application of our multi-component model to TeV detected FSRQs is a step that would also be interesting to take, to further explore the differences and similarities between them and gamma-emitting NLS1s. Regarding our numerical code, a further step towards a more detailed modeling of gamma-emitting NLS1s, and sources whose SED requires external photon fields

in general, would be to implement a more complex description of the accretion disc, whose UV excess or BBB was simplified to a multi-temperature black-body emitter in our model. An additional soft-excess component would improve the model description of the soft-excess regime that is observed during certain states such as the intermediate one of PMN J0948+0022.

The study of the gamma-loud NLS1 subsample is getting increasing attention from the astronomy community. Indeed, gamma-loud NLS1s are intrinsically interesting because it was absolutely unexpected to detect gamma-ray emission from objects that supposedly harbored no relativistic jets. This class of AGN features characteristics of both blazars and Seyfert 1 galaxies that might help fine-tuning the unification theory of AGN. What is more, the fact that their central region is unobscured means we can take a peek on components so powerful as the highly efficient accretion disks that reach up to Eddington luminosity levels. Certainly, getting an overall idea of whether NLS1 can only be detected at gamma-rays during flaring activity is crucial for the preparatory phase of the Cherenkov Telescope Array, whose enhanced sensitivity should increase the sample of so far detected gamma-loud NLS1 sources.

Bibliography

[AF09] M. W. B. Anderson and M. D. Filipovic. “Radio Detection of 18 RASS BL Lac Objects”. In: *Serbian Astronomical Journal* 179 (Dec. 2009), pp. 7–17. arXiv: 0907.4214 (cit. on p. 146).

[AS80] J. R. P. Angel and H. S. Stockman. “Optical and infrared polarization of active extragalactic objects”. In: *ARAA* 18 (1980), pp. 321–361 (cit. on p. 29).

[Abd+11] A. A. Abdo et al. “Fermi Large Area Telescope Observations of Markarian 421: The Missing Piece of its Spectral Energy Distribution”. In: *The Astrophysical Journal* 736.2 (2011), p. 131 (cit. on p. 33).

[Ace+15] F. Acero et al. “Fermi Large Area Telescope Third Source Catalog”. In: *Astrophys. J. Suppl.* 218.2 (2015), p. 23. arXiv: 1501.02003 [astro-ph.HE] (cit. on pp. 147, 190, 192).

[Ae13] C. P. Ahn and et al. “VizieR Online Data Catalog: The SDSS Photometric Catalog, Release 9 (Adelman-McCarthy+, 2012)”. In: *VizieR Online Data Catalog* 5139 (Jan. 2013) (cit. on p. 37).

[Aha06] F. et al. for the H.E.S.S. collaboration Aharonian. “Fast Variability of Tera-Electron Volt gamma-rays from the Radio Galaxy M87”. In: *Science* (2006). eprint: http://science.sciencemag.org/content/early/2006/10/26/science.1134408.full.pdf (cit. on p. 17).

[And+13] H Anderhub, M Backes, A Biland, et al. “Design and operation of FACT – the first G-APD Cherenkov telescope”. In: *Journal of Instrumentation* 8.06 (2013), P06008 (cit. on p. 133).

[BD02] M. Böttcher and C. D. Dermer. “An Evolutionary Scenario for Blazar Unification”. In: *ApJ* 564 (Jan. 2002), pp. 86–91. eprint: astro-ph/0106395 (cit. on p. 178).

[BG92] T. A. Boroson and R. F. Green. “The emission-line properties of low-redshift quasi-stellar objects”. In: *ApJS* 80 (May 1992), pp. 109–135 (cit. on p. 34).

[BK79] R. D. Blandford and A. Königl. “Relativistic jets as compact radio sources”. In: *ApJ* 232 (Aug. 1979), pp. 34–48 (cit. on p. 205).

[BM54] W. Baade and R. Minkowski. “Identification of the Radio Sources in Cassiopeia, Cygnus A, and Puppis A.” In: *ApJ* 119 (Jan. 1954), p. 206 (cit. on p. 4).

[BM82] R. D. Blandford and C. F. McKee. “Reverberation mapping of the emission line regions of Seyfert galaxies and quasars”. In: *ApJ* 255 (Apr. 1982), pp. 419–439 (cit. on p. 12).

[BR78] R. D. Blandford and M. J. Rees. “Extended and compact extragalactic radio sources - Interpretation and theory”. In: 17 (Mar. 1978), pp. 265–274 (cit. on p. 6).

[BS12] V. Beckmann and C. Shrader. “The AGN phenomenon: open issues”. In: *Proceedings of “An INTEGRAL view of the high-energy sky (the first 10 years)” - 9th INTEGRAL Workshop and celebration of the 10th anniversary of the launch (INTEGRAL 2012). 15-19 October 2012. Bibliotheque Nationale de France, Paris, France. Published online at <A href=“http://pos.sissa.it/cgi-bin/reader/conf.cgi?confid=176”>http://pos.sissa.it/cgi-bin/reader/conf.cgi?confid=176</A>, id.69*. 2012, p. 69. arXiv: 1302.1397 [astro-ph.HE] (cit. on p. 26).

[BS48] J. G. Bolton and G. J. Stanley. “Variable Source of Radio Frequency Radiation in the Constellation of Cygnus”. In: 161 (1948), pp. 312–313 (cit. on p. 4).

[Ber08] Konrad Bernlöhr. “Simulation of imaging atmospheric Cherenkov telescopes with CORSIKA and sim$_telarray$”. In: *Astroparticle Physics* 30.3 (2008), pp. 149–158 (cit. on p. 57).

[Bla48] P.M.S. Blackett. “Emission spectra of the night sky and aurorae”. In: *Rep. Conf. Gassiot Comm. Phys. Soc.* 34 (1948) (cit. on p. 48).

[CA96] V. Charmandaris and P. N. Appleton. “The Neutral Hydrogen Disk of ARP 10 (=VV 362): A Nonequilibrium Disk Associated with a Galaxy with Rings and Ripples”. In: *ApJ* 460 (Apr. 1996), p. 686. eprint: astro-ph/9510003 (cit. on p. 177).

[CB90] P. S. Coppi and R. D. Blandford. “Reaction rates and energy distributions for elementary processes in relativistic pair plasmas”. In: *MNRAS* 245 (Aug. 1990), pp. 453–507 (cit. on p. 88).

[CD02] A. Cavaliere and V. D’Elia. “The blazar main sequence”. In: *ApJ* 571 (May 2002), pp. 226–233. eprint: astro-ph/0106512 (cit. on p. 29).

[CG99] M. Chiaberge and G. Ghisellini. “Rapid variability in the synchrotron self-Compton model for blazars”. In: *MNRAS* 306 (July 1999), pp. 551–560. eprint: astro-ph/9810263 (cit. on p. 89).

[Che34] P. A. Cherenkov. In: *Dokl. Akad. Nauk SSSR* 2.8 (1934), p. 451 (cit. on p. 46).

[Che37] P. A. Cherenkov. “Visible Radiation Produced by Electrons Moving in a Medium with Velocities Exceeding that of Light”. In: *Physical Review* 52 (1937), pp. 378–379 (cit. on p. 46).

[Cur41] Eve Curie. *Madame Curie*. 1941 (cit. on p. 45).

[D’A+15] F. D’Ammando, M. Orienti, J. Finke, et al. “The most powerful flaring activity from the NLSy1 PMNJ0948+0022”. In: *MNRAS* 446.3 (2015), pp. 2456–2467 (cit. on pp. 204, 205, 231, 233, 234).

[DC11] F. D'Ammando and S. Ciprini. "Fermi LAT detection of a new GeV flare from the radio-loud Narrow-Line Sy1 PMN J0948+0022". In: *The Astronomer's Telegram* 3429 (June 2011) (cit. on p. 203).

[DM09] C. D. Dermer and G. Menon. *High Energy Radiation from Black Holes: Gamma Rays, Cosmic Rays, and Neutrinos*. 2009 (cit. on pp. 98, 101, 104).

[DN06] Mathieu De Naurois. "Analysis methods for atmospheric Cerenkov telescopes". In: *arXiv preprint astro-ph/0607247* (2006) (cit. on p. 70).

[DO13] F. D'Ammando and M. Orienti. "Fermi-LAT detection of a new gamma-ray flare from the NLSy1 PMN J0948+0022". In: *The Astronomer's Telegram* 4694 (Jan. 2013) (cit. on p. 38).

[DS93] C. D. Dermer and R. Schlickeiser. "Model for the High-Energy Emission from Blazars". In: *ApJ* 416 (Oct. 1993), p. 458 (cit. on p. 98).

[Du+16] Pu Du, Kai-Xing Lu, Zhi-Xiang Zhang, et al. "Supermassive Black Holes with High Accretion Rates in Active Galactic Nuclei. V. A New Size–Luminosity Scaling Relation for the Broad-line Region". In: *The Astrophysical Journal* 825.2 (2016), p. 126 (cit. on p. 12).

[Egg+13] Joseph R. Eggen, H. Richard Miller, and Jeremy D. Maune. "The Variable Optical Polarization and Fermi Observations of PMN J0948+0022". In: *The Astrophysical Journal* 773.2 (2013), p. 85 (cit. on p. 203).

[FD10] J. D. Finke and C. D. Dermer. "On the Break in the Fermi-Large Area Telescope Spectrum of 3C 454.3". In: *ApJL* 714 (May 2010), pp. L303–L307. arXiv: 1004.1418 [astro-ph.HE] (cit. on pp. 108, 109).

[FH12] V. F. Hess. "Über Beobachtungen der durchdringenden Strahlung bei sieben Freiballonfahrten". In: *Physikalische Zeitschrift* 13 (Nov. 1912), pp. 1084–1091 (cit. on p. 63).

[Fos11] Luigi Foschini. "Accretion and jet power in active galactic nuclei". In: *Research in Astronomy and Astrophysics* 11.11 (2011), p. 1266 (cit. on p. 177).

[GD04] M. Gierliński and C. Done. "Is the soft excess in active galactic nuclei real?" In: *MNRAS* 349 (Mar. 2004), pp. L7–L11. eprint: astro-ph/0312271 (cit. on p. 11).

[GH05] J. E. Greene and L. C. Ho. "Estimating Black Hole Masses in Active Galaxies Using the Hα Emission Line". In: *ApJ* 630 (Sept. 2005), pp. 122–129. eprint: astro-ph/0508335 (cit. on p. 176).

[GJ53] W. Galbraith and J. V. Jelley. "Light Pulses from the Night Sky associated with Cosmic Rays". In: 171 (Feb. 1953), pp. 349–350 (cit. on p. 48).

[GM04] D. Grupe and S. Mathur. "M_{BH}-σ Relation for a Complete Sample of Soft X-Ray-selected Active Galactic Nuclei". In: *ApJL* 606 (2004), pp. L41–L44. eprint: astro-ph/0312390 (cit. on p. 34).

[GM63] J. L. Greenstein and T. A. Matthews. "Redshift of the Radio Source 3C 48." In: *AJ* 68 (1963), p. 279 (cit. on p. 5).

[GP94] P. Giommi and P. Padovani. “BL Lac Reunification”. In: *MNRAS* 268 (May 1994), p. L51 (cit. on p. 31).

[GR88] P. W. Guilbert and M. J. Rees. “‘Cold’ material in non-thermal sources”. In: *MNRAS* 233 (July 1988), pp. 475–484 (cit. on p. 10).

[GT09] G. Ghisellini and F. Tavecchio. “Canonical high-power blazars”. In: *MNRAS* 397 (2009), pp. 985–1002. arXiv: 0902.0793 (cit. on pp. 13, 106, 112, 229, 232).

[GT15] G. Ghisellini and F. Tavecchio. “Fermi/LAT broad emission line blazars”. In: *MNRAS* 448 (Apr. 2015), pp. 1060–1077. arXiv: 1501.03504 [astro-ph.HE] (cit. on pp. 30, 123).

[Ghi+17] G. Ghisellini, C. Righi, L. Costamante, and F. Tavecchio. “The Fermi blazar sequence”. In: *Monthly Notices of the Royal Astronomical Society* 469.1 (2017), pp. 255–266. eprint: /oup/backfile/content_public/journal/mnras/469/1/10.1093_mnras_stx806/1/stx806.pdf (cit. on p. 32).

[Gu+15] Minfeng Gu, Yongjun Chen, S. Komossa, et al. “The Radio Properties of Radio-Loud Narrow-Line Seyfert 1 Galaxies on Parsec Scales”. In: *ApJS* 221.1 (2015), p. 3. arXiv: 1509.01889 [astro-ph.GA] (cit. on p. 43).

[HB89] A. Hewitt and G. Burbidge. “A new optical catalog of Quasi-Stellar Objects.” In: *A new optical catalog of QSO (1989)*. 1989 (cit. on p. 134).

[HM91] F. Haardt and L. Maraschi. “A two-phase model for the X-ray emission from Seyfert galaxies”. In: *ApJL* 380 (Oct. 1991), pp. L51–L54 (cit. on p. 11).

[HM93] F. Haardt and L. Maraschi. “X-ray spectra from two-phase accretion disks”. In: *ApJ* 413 (Aug. 1993), pp. 507–517 (cit. on p. 11).

[Hay+15] M. Hayashida, K. Nalewajko, G. M. Madejski, et al. “Rapid Variability of Blazar 3C 279 during Flaring States in 2013-2014 with Joint Fermi-LAT, NuSTAR, Swift, and Ground-Based Multiwavelength Observations”. In: *The Astrophysical Journal* 807.1 (2015), p. 79 (cit. on p. 33).

[Hea89] Oliver Heaviside. “XXXIX. On the electromagnetic effects due to the motion of electrification through a dielectric”. In: *Philosophical Magazine* 27.167 (1889), pp. 324–339. eprint: http://dx.doi.org/10.1080/14786448908628362 (cit. on p. 45).

[Hom12] Daniel C. Homan. “PHYSICAL PROPERTIES OF JETS IN AGN”. In: *International Journal of Modern Physics: Conference Series* 08 (2012), pp. 163–171 (cit. on p. 41).

[JB91a] N. Jackson and I. W. A. Browne. “Optical Properties of Quasars - Part Two - Emission Line Geometry and Radio Properties”. In: *MNRAS* 250 (May 1991), p. 422 (cit. on p. 189).

[JB91b] N. Jackson and I. W. A. Browne. “Optical properties of quasars. I - Observations. II - Emission-line geometry and radio properties”. In: *MNRAS* 250 (May 1991), pp. 414–421 (cit. on p. 189).

[JB91c] N. Jackson and I. W. A. Browne. “Optical properties of quasars. I - Observations. II - Emission-line geometry and radio properties”. In: *MNRAS* 250 (1991), pp. 414–421 (cit. on p. 190).

[KB88] J. H. Krolik and M. C. Begelman. “Molecular tori in Seyfert galaxies - Feeding the monster and hiding it”. In: *ApJ* 329 (1988), pp. 702–711 (cit. on p. 14).

[KW74] E. Y. Khachikian and D. W. Weedman. “An atlas of Seyfert galaxies”. In: *ApJ* 192 (1974), pp. 581–589 (cit. on pp. 18, 34).

[Kov+05] Yuri Y. Kovalev et al. “Sub-milliarcsecond imaging of quasars and active galactic nuclei. 4. Fine scale structure”. In: *Astron. J.* 130 (2005), pp. 2473–2505. arXiv: `astro-ph/0505536 [astro-ph]` (cit. on pp. 43, 189).

[LM05] E. Lorenz and M. Martinez. “High energy astrophysics: The MAGIC telescope”. In: *Astronomy and Geophysics* 46.6 (Dec. 2005), pp. 6.21–6.25 (cit. on p. 133).

[LM83] T.-P. Li and Y.-Q. Ma. “Statistical reliability of gamma-ray line observations”. In: *International Cosmic Ray Conference* 1 (Aug. 1983), pp. 76–79 (cit. on pp. 77, 149, 150).

[LW88] A. P. Lightman and T. R. White. “Effects of cold matter in active galactic nuclei - A broad hump in the X-ray spectra”. In: *ApJ* 335 (Dec. 1988), pp. 57–66 (cit. on p. 10).

[LZ02] F. K. Liu and Y. H. Zhang. “A new list of extra-galactic radio jets”. In: *A&A* 381 (Jan. 2002), pp. 757–760. eprint: `astro-ph/0212477` (cit. on p. 190).

[MB92] K. Mannheim and P. L. Biermann. “Gamma-ray flaring of 3C 279 - A proton-initiated cascade in the jet?” In: *A&A* 253 (Jan. 1992), pp. L21–L24 (cit. on p. 130).

[MJ04] R. J. McLure and M. J. Jarvis. “The relationship between radio luminosity and black hole mass in optically selected quasars”. In: *MNRAS* 353 (Oct. 2004), pp. L45–L49. eprint: `astro-ph/0408203` (cit. on p. 177).

[MM83] R. Morrison and D. McCammon. “Interstellar photoelectric absorption cross sections, 0.03-10 keV”. In: *ApJ* 270 (July 1983), pp. 119–122 (cit. on p. 138).

[MS81] R. L. Moore and H. S. Stockman. “The class of highly polarized quasars - Observations and description”. In: *ApJ* 243 (Jan. 1981), pp. 60–75 (cit. on p. 29).

[MS82] M. A. Malkan and W. L. W. Sargent. “The ultraviolet excess of Seyfert 1 galaxies and quasars”. In: *ApJ* 254 (Mar. 1982), pp. 22–37 (cit. on p. 10).

[MT03] L. Maraschi and F. Tavecchio. “The jet-disk connection and the blazar unification”. In: *ApJ* 593.2 (2003), p. 667 (cit. on p. 29).

[Mal26] L.C.R. Mallet. In: *Acad. Sci. Paris* 183.274 (1926) (cit. on p. 46).

[Mal28] L.C.R. Mallet. In: *Acad. Sci. Paris* 187.222 (1928) (cit. on p. 46).

[Mal29] L.C.R. Mallet. In: *Acad. Sci. Paris* 188.445 (1929) (cit. on p. 46).

[NC55] N. M. Nesterova and A. E. Chudakov. “On the Observation of Cerenkov Radiation Accompanying Broad Atmospheric Showers of Cosmic Rays”. In: *Journal of Experimental and Theoretical Physics* 28 (1955), p. 384 (cit. on p. 48).

[OP85] D. E. Osterbrock and R. W. Pogge. “The spectra of narrow-line Seyfert 1 galaxies”. In: *ApJ* 297 (Oct. 1985), pp. 166–176 (cit. on p. 34).

[PG95] P. Padovani and P. Giommi. “The connection between x-ray- and radio-selected BL Lacertae objects”. In: *ApJ* 444 (May 1995), pp. 567–581. eprint: astro-ph/9412073 (cit. on p. 31).

[PH14] R. D. Parsons and J. A. Hinton. “A Monte Carlo template based analysis for air-Cherenkov arrays”. In: *Astroparticle Physics* 56 (Apr. 2014), pp. 26–34. arXiv: 1403.2993 [astro-ph.IM] (cit. on p. 74).

[PM65] R. M. Price and D. K. Milne. “The Parkes catalogue of radio sources, declination zone -60$\deg to -90\deg$”. In: *Australian Journal of Physics* 18 (1965), p. 329 (cit. on p. 5).

[Rak+17a] Suvendu Rakshit, C. S. Stalin, Hum Chand, and Xue-Guang Zhang. “A Catalog of Narrow Line Seyfert 1 Galaxies from the Sloan Digital Sky Survey Data Release 12”. In: *The Astrophysical Journal Supplement Series* 229.2 (2017), p. 39 (cit. on pp. 35, 180).

[Rak+17b] Suvendu Rakshit, C. S. Stalin, Hum Chand, and Xue-Guang Zhang. “Properties of Narrow line Seyfert 1 galaxies”. In: 2017. arXiv: 1706.00797 [astro-ph.GA] (cit. on p. 35).

[Ros08] Eduardo Ros. “Kinematics of AGN Jets”. In: *J. Phys. Conf. Ser.* 131 (2008), p. 012061. arXiv: 0810.4714 [astro-ph] (cit. on p. 43).

[SH06] L. Saugé and G. Henri. “On the dependence of the spectral parameters on the observational conditions in homogeneous time dependent models of the TeV blazars”. In: *A&A* 454 (July 2006), pp. L1–L4. eprint: astro-ph/0606509 (cit. on p. 89).

[SHC07] Andrew J Smith and the HAWC Collaboration. “HAWC: A next generation all-sky gamma-ray telescope”. In: *Journal of Physics: Conference Series* 60.1 (2007), p. 131 (cit. on p. 134).

[SS73] N. I. Shakura and R. A. Sunyaev. “Black holes in binary systems. Observational appearance.” In: *A&A* 24 (1973), pp. 337–355 (cit. on p. 103).

[TF37] IE Tamm and IM Frank. “Coherent radiation of fast electrons in a medium”. In: *Dokl. Akad. Nauk SSSR*. Vol. 14. 3. 1937, pp. 107–112 (cit. on p. 46).

[TG08] F. Tavecchio and G. Ghisellini. “The spectrum of the broad-line region and the high-energy emission of powerful blazars”. In: *MNRAS* 386 (May 2008), pp. 945–952. arXiv: 0802.0871 (cit. on p. 111).

[TP89] T. J. Turner and K. A. Pounds. “The EXOSAT spectral survey of AGN”. In: *MNRAS* 240 (Oct. 1989), pp. 833–880 (cit. on p. 11).

[TW81] K. E. Turver and T. C. Weekes. “Gamma-rays above 100 GeV”. In: *Philosophical Transactions of the Royal Society of London Series A* 301 (June 1981), pp. 615–628 (cit. on p. 49).

[Tav+14] J. León Tavares, J. Kotilainen, V. Chavushyan, et al. “The Host Galaxy of the Gamma-Ray Narrow-line Seyfert 1 Galaxy 1H 0323+342”. In: *The Astrophysical Journal* 795.1 (2014), p. 58 (cit. on pp. 176, 177).

[UP95] C. M. Urry and P. Padovani. “Unified Schemes for Radio-Loud Active Galactic Nuclei”. In: *PASP* 107 (1995), p. 803. eprint: astro-ph/9506063 (cit. on p. 30).

[Vav34] S. I. Vavilov. In: *Dokl. Akad. Nauk SSSR* 2.8 (1934), p. 457 (cit. on p. 46).

[WT77] T. C. Weekes and K. E. Turver. “Gamma-ray astronomy from 10-100 GeV: A new approach”. In: *Recent Advances in Gamma-Ray Astronomy*. Ed. by R. D. Wills and B. Battrick. Vol. 124. ESA Special Publication. July 1977 (cit. on pp. 49, 61).

[WU02] J.-H. Woo and C. M. Urry. “Active Galactic Nucleus Black Hole Masses and Bolometric Luminosities”. In: *ApJ* 579 (Nov. 2002), pp. 530–544. eprint: astro-ph/0207249 (cit. on p. 189).

[dR09] M. de Naurois and L. Rolland. “A high performance likelihood reconstruction of γ-rays for imaging atmospheric Cherenkov telescopes”. In: *Astroparticle Physics* 32 (Dec. 2009), pp. 231–252. arXiv: 0907.2610 [astro-ph.IM] (cit. on p. 73).

[A.M13] A.M. Hillas. “Evolution of ground-based gamma-ray astronomy from the early days to the Cherenkov Telescope Arrays”. In: *Astroparticle Physics* 43 (2013). Seeing the High-Energy Universe with the Cherenkov Telescope Array - The Science Explored with the CTA, 19 –43 (cit. on p. 51).

[Aba+09] K. N. Abazajian, J. K. Adelman-McCarthy, M. A. Agüeros, et al. “The Seventh Data Release of the Sloan Digital Sky Survey”. In: *ApJS* 182, 543-558 (2009), pp. 543–558. arXiv: 0812.0649 (cit. on p. 190).

[Abb+17] B. P. Abbott, R. Abbott, T. D. Abbott, et al. “Multi-messenger Observations of a Binary Neutron Star Merger”. In: *ApJL* 848, L12 (Oct. 2017), p. L12. arXiv: 1710.05833 [astro-ph.HE] (cit. on p. 267).

[Abd+09a] A. A Abdo et al. “Fermi/Large Area Telescope Discovery of Gamma-Ray Emission from a Relativistic Jet in the Narrow-Line Quasar PMN J0948+0022”. In: *ApJ* 699 (2009), pp. 976–984. arXiv: 0905.4558 [astro-ph.HE] (cit. on p. 36).

[Abd+09b] A. A. Abdo et al. “Fermi/Large Area Telescope Discovery of Gamma-Ray Emission from a Relativistic Jet in the Narrow-Line Quasar PMN J0948+0022”. In: *ApJ* 699 (July 2009), pp. 976–984. arXiv: 0905.4558 [astro-ph.HE] (cit. on pp. 38, 203).

[Abd+09c] A. A. Abdo et al. “Radio-Loud Narrow-Line Seyfert 1 as a New Class of Gamma-Ray Active Galactic Nuclei”. In: *ApJL* 707 (Dec. 2009), pp. L142–L147. arXiv: 0911.3485 [astro-ph.HE] (cit. on pp. 178, 227, 228).

[Abd+10a] A. A. Abdo, M. Ackermann, M. Ajello, et al. “Fermi Large Area Telescope First Source Catalog”. In: *ApJS* 188 (June 2010), pp. 405–436. arXiv: 1002.2280 [astro-ph.HE] (cit. on p. 190).

[Abd+10b] A. A. Abdo, M. Ackermann, I. Agudo, et al. “The Spectral Energy Distribution of Fermi Bright Blazars”. In: *ApJ* 716 (June 2010), pp. 30–70. arXiv: 0912.2040 (cit. on p. 31).

[Abd+16a] H. Abdalla, A. Abramowski, F. Aharonian, et al. “H.E.S.S. Limits on Linelike Dark Matter Signatures in the 100 GeV to 2 TeV Energy Range Close to the Galactic Center”. In: *Physical Review Letters* 117.15, 151302 (2016), p. 151302. arXiv: 1609.08091 [astro-ph.HE] (cit. on p. 268).

[Abd+16b] H. Abdallah, A. Abramowski, F. Aharonian, et al. “Search for Dark Matter Annihilations towards the Inner Galactic Halo from 10 Years of Observations with H.E.S.S.” In: *Physical Review Letters* 117.11, 111301 (2016), p. 111301. arXiv: 1607.08142 [astro-ph.HE] (cit. on p. 268).

[Acc+11] V. A. Acciari et al. “TeV and Multi-wavelength Observations of Mrk 421 in 2006-2008”. In: *ApJ* 738, 25 (Sept. 2011), p. 25. arXiv: 1106.1210 [astro-ph.HE] (cit. on p. 205).

[Ade+06] J. K. Adelman-McCarthy et al. “The Fourth Data Release of the Sloan Digital Sky Survey”. In: *ApJS* 162 (2006), pp. 38–48. eprint: astro-ph/0507711 (cit. on p. 190).

[Ade09] J. K. et al. Adelman-McCarthy. “VizieR Online Data Catalog: The SDSS Photometric Catalog, Release 7 (Adelman-McCarthy+, 2009)”. In: *VizieR Online Data Catalog* 2294 (2009) (cit. on pp. 37, 189).

[Aha+04] F. Aharonian, A. G. Akhperjanian, K.-M. Aye, et al. “Very high energy gamma rays from the direction of Sagittarius A*”. In: *A&A* 425 (Oct. 2004), pp. L13–L17. eprint: astro-ph/0406658 (cit. on p. 66).

[Aha+08] F. Aharonian, A. G. Akhperjanian, U. Barres de Almeida, et al. “Discovery of VHE γ-rays from the high-frequency-peaked BL Lacertae object RGB J0152+017”. In: *A&A* 481 (Apr. 2008), pp. L103–L107. arXiv: 0802.4021 (cit. on p. 95).

[Ahn+12] C. P. Ahn, R. Alexandroff, C. Allende Prieto, et al. “The Ninth Data Release of the Sloan Digital Sky Survey: First Spectroscopic Data from the SDSS-III Baryon Oscillation Spectroscopic Survey”. In: *ApJS* 203, 21 (Dec. 2012), p. 21. arXiv: 1207.7137 [astro-ph.IM] (cit. on p. 203).

[Ang+15] E. Angelakis, L. Fuhrmann, N. Marchili, et al. “Radio jet emission from GeV-emitting narrow-line Seyfert 1 galaxies”. In: *A&A* 575, A55 (2015), A55. arXiv: 1501.02158 [astro-ph.HE] (cit. on p. 35).

[Ant+08] S. Antón, I. W. A. Browne, and M. J. Marchã. “The colour of the narrow line Sy1-blazar 0324+3410”. In: *A&A* 490 (2008), pp. 583–587. arXiv: 0907.2400 (cit. on pp. 36, 176, 177).

[Ant93] R. Antonucci. “Unified models for active galactic nuclei and quasars”. In: *ARAA* 31 (1993), pp. 473–521 (cit. on pp. 18, 26).

[Bal+16a] R. D. Baldi, A. Capetti, A. Robinson, A. Laor, and E. Behar. “Radio-loud Narrow Line Seyfert 1 under a different perspective: a revised black hole mass estimate from optical spectropolarimetry”. In: *MNRAS* 458 (May 2016), pp. L69–L73. arXiv: 1602.02783 (cit. on pp. 34, 177).

[Bal+16b] T. J. Balonek, R. W. Stahlin, K. J. Chapman, et al. “Detection of optical outburst activity in the BL Lac object OT 081 (PKS 1749+096)”. In: *The Astronomer’s Telegram* 9259 (July 2016) (cit. on p. 134).

[Bec+11] Y. Becherini, A. Djannati-Ataï, V. Marandon, M. Punch, and S. Pita. “A new analysis strategy for detection of faint γ-ray sources with Imaging Atmospheric Cherenkov Telescopes”. In: *Astroparticle Physics* 34 (July 2011), pp. 858–870. arXiv: 1104.5359 [astro-ph.HE] (cit. on p. 74).

[Bec+16] J. Becerra Gonzalez, D. Thompson, and Fermi-LAT Collaboration. “Fermi-LAT detection of a GeV gamma-ray flare from the BL Lac object OT 081”. In: *The Astronomer’s Telegram* 9231 (July 2016) (cit. on p. 134).

[Bel78a] A. R. Bell. “The acceleration of cosmic rays in shock fronts. I”. In: *MNRAS* 182 (Jan. 1978), pp. 147–156 (cit. on p. 27).

[Bel78b] A. R. Bell. “The acceleration of cosmic rays in shock fronts. II”. In: *MNRAS* 182 (Feb. 1978), pp. 443–455 (cit. on p. 27).

[Ben+09] M. C. Bentz, J. L. Walsh, A. J. Barth, et al. “The Lick AGN Monitoring Project: Broad-line Region Radii and Black Hole Masses from Reverberation Mapping of Hβ”. In: *ApJ* 705 (Nov. 2009), pp. 199–217. arXiv: 0908.0003 (cit. on p. 12).

[Ber+07] D. Berge, S. Funk, and J. Hinton. “Background modelling in very-high-energy γ-ray astronomy”. In: *A&A* 466 (May 2007), pp. 1219–1229. eprint: astro-ph/0610959 (cit. on p. 76).

[Bha+14] S. Bhattacharyya, H. Bhatt, N. Bhatt, and K. K. Singh. “The XMM-Newton view of the radio-loud narrow-line Seyfert 1 galaxy PMN J0948+0022”. In: *MNRAS* 440 (May 2014), pp. 106–118. arXiv: 1301.1150 [astro-ph.HE] (cit. on p. 204).

[Bol+49] J. G. Bolton, G. J. Stanley, and O. B. Slee. “1949, Positions of Three Discrete Sources of Galactic Radio-Frequency Radiation”. In: *Classics in Radio Astronomy*. Ed. by W. T. Sullivan III. 1949, p. 239 (cit. on p. 4).

[Bol+64] J. G. Bolton, F. F. Gardner, and M. B. Mackey. “The Parkes catalogue of radio sources, declination zone -20$\mathrm{deg}\,to-60\mathrm{deg}$”. In: *Australian Journal of Physics* 17 (1964), p. 340 (cit. on p. 5).

[Bol+96] T. Boller, W. N. Brandt, and H. Fink. “Soft X-ray properties of narrow-line Seyfert 1 galaxies.” In: *A&A* 305 (Jan. 1996), p. 53. eprint: astro-ph/9504093 (cit. on p. 34).

[Bol48] J. G. Bolton. “Discrete Sources of Galactic Radio Frequency Noise”. In: 162 (1948), pp. 141–142 (cit. on p. 4).

[Bot+13] M. Bottcher, A. Reimer, and H. Zhang. “Leptonic and Hadronic Modeling of Fermi-Detected Blazars. Spectral Energy Distribution Modeling and High-Energy Polarization Predictions”. In: *European Physical Journal Web of Conferences*. Vol. 61. European Physical Journal Web of Conferences. Dec. 2013, p. 05003 (cit. on p. 130).

[Bou+08] T. Boutelier, G. Henri, and P. O. Petrucci. “Time dependent modelisation of TeV blazars by a stratified jet model”. In: *SF2A-2008*. Ed. by C. Charbonnel, F. Combes, and R. Samadi. Nov. 2008, p. 179. arXiv: 0810.0221 (cit. on p. 89).

[Bra+93] H. V. Bradt, R. E. Rothschild, and J. H. Swank. “X-ray timing explorer mission”. In: *A&AS* 97 (Jan. 1993), pp. 355–360 (cit. on p. 147).

[Bre+16] J. Bregeon, M. Compin, S. Rivoire, M. Sanguillon, and G. Vasileiadis. “An elastic lidar system for the H.E.S.S. Experiment”. In: *Nuclear Instruments and Methods in Physics Research A* 819 (May 2016), pp. 60–66. arXiv: 1512.02441 [astro-ph.IM] (cit. on p. 68).

[Bur+05] D. N. Burrows, J. E. Hill, J. A. Nousek, et al. “The Swift X-Ray Telescope”. In: 120 (Oct. 2005), pp. 165–195. eprint: astro-ph/0508071 (cit. on pp. 135, 146, 159).

[Cac+14] A. Caccianiga, S. Antón, L. Ballo, et al. “SDSS J143244.91+301435.3: a link between radio-loud narrow-line Seyfert 1 galaxies and compact steep-spectrum radio sources?” In: *MNRAS* 441 (2014), pp. 172–186. arXiv: 1403.3229 (cit. on p. 36).

[Cal+11] G. Calderone, L. Foschini, G. Ghisellini, et al. “γ-ray variability of radio-loud narrow-line Seyfert 1 galaxies”. In: *MNRAS* 413 (June 2011), pp. 2365–2370. arXiv: 1101.1265 [astro-ph.HE] (cit. on p. 38).

[Cal+12] G. Calderone, G. Ghisellini, M. Colpi, and M. Dotti. “B2 0954+25A: a typical Fermi blazar or a γ-ray loud Narrow Line Seyfert 1”. In: *MNRAS* 424 (2012), pp. 3081–3093. arXiv: 1202.3790 [astro-ph.HE] (cit. on pp. 189, 191, 192, 197, 229–231, 234).

[Cal+13] G. Calderone, G. Ghisellini, M. Colpi, and M. Dotti. “Black hole mass estimate for a sample of radio-loud narrow-line Seyfert 1 galaxies”. In: *MNRAS* 431 (May 2013), pp. 210–239. arXiv: 1212.1181 (cit. on pp. 34, 177).

[Cel+97] A. Celotti, P. Padovani, and G. Ghisellini. “Jets and accretion processes in active galactic nuclei: further clues”. In: *MNRAS* 286 (Apr. 1997), pp. 415–424. eprint: astro-ph/9611111 (cit. on p. 227).

[Cer+13a] M. Cerruti, C. Boisson, and A. Zech. “Constraining the parameter space of the one-zone synchrotron-self-Compton model for GeV-TeV detected BL Lacertae objects”. In: *A&A* 558, A47 (Oct. 2013), A47. arXiv: 1305.4597 [astro-ph.HE] (cit. on pp. 92, 168, 170).

[Cer+13b] M. Cerruti, C. D. Dermer, B. Lott, C. Boisson, and A. Zech. “Gamma-Ray Blazars near Equipartition and the Origin of the GeV Spectral Break in 3C 454.3”. In: *ApJL* 771, L4 (July 2013), p. L4. arXiv: 1305.4159 [astro-ph.HE] (cit. on p. 107).

[Cer+15] M. Cerruti, A. Zech, C. Boisson, and S. Inoue. “A hadronic origin for ultra-high-frequency-peaked BL Lac objects”. In: *MNRAS* 448 (Mar. 2015), pp. 910–927. arXiv: 1411.5968 [astro-ph.HE] (cit. on p. 130).

[Cer+17] M. Cerruti, A. Zech, G. Emery, and D. Guarin. “Hadronic modeling of TeV AGN: Gammas and neutrinos”. In: *6th International Symposium on High Energy Gamma-Ray Astronomy*. Vol. 1792. American Institute of Physics Conference Series. Jan. 2017, p. 050027. arXiv: 1610.00255 [astro-ph.HE] (cit. on p. 132).

[Chu+63] A. E. Chudakov, V. L. Dadykin, V. I. Zatsepin, and N. M. Nesterova. “On the high energy photons from local sources”. In: *International Cosmic Ray Conference* 4 (1963), p. 199 (cit. on p. 48).

[Cip+16] S. Ciprini, J. B. Gonzalez, G. Pivato, and D. J. Thompson. “Fermi and Swift observations of correlated outburst activity from the BL Lac object OT 081 (PKS 1749+096)”. In: *The Astronomer’s Telegram* 9260 (July 2016) (cit. on p. 135).

[Coc60] G. Cocconi. “An air shower telescope and the detection of 10^{12} eV photon sources”. In: *International Cosmic Ray Conference* 2 (1960), p. 309 (cit. on p. 48).

[Coh+07] A. S. Cohen, W. M. Lane, W. D. Cotton, et al. “The VLA Low-Frequency Sky Survey”. In: *AJ* 134 (2007), pp. 1245–1262. arXiv: 0706.1191 (cit. on pp. 40, 189).

[D’A+12] F. D’Ammando, M. Orienti, J. Finke, and Fermi-LAT Collaboration. “To be or not to be a blazar. The case of the narrow-line Seyfert 1 SBS 0846+513”. In: *American Institute of Physics Conference Series*. Ed. by F. A. Aharonian, W. Hofmann, and F. M. Rieger. Vol. 1505. American Institute of Physics Conference Series. Dec. 2012, pp. 570–573. arXiv: 1210.0546 [astro-ph.HE] (cit. on pp. 41, 227).

[D’A+13] D’Ammando, F., Orienti, M., Finke, J., Larsson, J., and Giroletti, M. “Relativistic jets in narrow-line Seyfert 1 galaxies. New discoveries and open questions”. In: *EPJ Web of Conferences* 61 (2013), p. 05006 (cit. on pp. 35, 203).

[D’A+16] F. D’Ammando, M. Orienti, J. Finke, et al. “The awakening of the γ-ray narrow-line Seyfert 1 galaxy PKS 1502+036”. In: *MNRAS* 463 (2016), pp. 4469–4480. arXiv: 1609.04845 [astro-ph.HE] (cit. on p. 41).

[D’A+17] F. D’Ammando, J. A. Acosta-Pulido, A. Capetti, et al. “Uncovering the host galaxy of the γ-ray-emitting narrow-line Seyfert 1 galaxy FBQS J1644+2619”. In: *MNRAS* 469 (July 2017), pp. L11–L15. arXiv: 1703.07367 (cit. on pp. 36, 177).

[D’A11] F. et al. D’Ammando. “AGILE detection of extreme γ-ray activiry from the blazar PKS 1510-089 during March 2009. Multifrequency analysis”. In: *A&A* 529, A145 (May 2011), A145. arXiV: 1103.3647 (cit. on p. 37).

[D’E+13] V. D’Elia, M. Perri, S. Puccetti, et al. “The seven year Swift-XRT point source catalog (1SWXRT)”. In: *A&A* 551, A142 (Mar. 2013), A142. arXiv: 1302.7113 [astro-ph.IM] (cit. on p. 139).

[Day+66] G. A. Day, A. J. Shimmins, R. D. Ekers, and D. J. Cole. “The Parkes catalogue of radio sources, declination zone $0\deg to +20\deg$”. In: *Australian Journal of Physics* 19 (1966), p. 35 (cit. on p. 5).

[Deo+06] R. P. Deo, D. M. Crenshaw, and S. B. Kraemer. “The Host Galaxies of Narrow-Line Seyfert 1 Galaxies: Nuclear Dust Morphology and Starburst Rings”. In: *AJ* 132 (2006), pp. 321–346. eprint: astro-ph/0603806 (cit. on p. 36).

[Doi+12] A. Doi, H. Nagira, N. Kawakatu, et al. “Kiloparsec-scale Radio Structures in Narrow-line Seyfert 1 Galaxies”. In: *ApJ* 760, 41 (Nov. 2012), p. 41. arXiv: 1210.1303 (cit. on p. 177).

[Don+01] Donato, D., Ghisellini, G., Tagliaferri, G., and Fossati, G. “Hard X-ray properties of blazars*”. In: *A&A* 375.3 (2001), pp. 739–751 (cit. on p. 32).

[Don+12] C. Done, S. W. Davis, C. Jin, O. Blaes, and M. Ward. “Intrinsic disc emission and the soft X-ray excess in active galactic nuclei”. In: *MNRAS* 420 (Mar. 2012), pp. 1848–1860. arXiv: 1107.5429 [astro-ph.HE] (cit. on p. 103).

[Don10] D. Donato. “Fermi LAT detection of a GeV flare from the radio-loud NL Sy1 PMN J0948+0022”. In: *The Astronomer’s Telegram* 2733 (July 2010) (cit. on p. 203).

[Dra+09] A. J. Drake, S. G. Djorgovski, A. Mahabal, et al. “First Results from the Catalina Real-Time Transient Survey”. In: *ApJ* 696 (May 2009), pp. 870–884. arXiv: 0809.1394 (cit. on p. 163).

[Dri+97] M. J. Drinkwater, R. L. Webster, P. J. Francis, et al. “The Parkes Half-Jansky Flat-Spectrum Sample”. In: *MNRAS* 284 (Jan. 1997), pp. 85–125. eprint: astro-ph/9609019 (cit. on p. 134).

[Edg+59] D. O. Edge, J. R. Shakeshaft, W. B. McAdam, J. E. Baldwin, and S. Archer. “A survey of radio sources at a frequency of 159 Mc/s.” In: 68 (1959), pp. 37–60 (cit. on p. 5).

[Elv+92] M. Elvis, D. Plummer, J. Schachter, and G. Fabbiano. “The Einstein Slew Survey”. In: *ApJS* 80 (May 1992), pp. 257–303 (cit. on p. 146).

[Fab+15] A. C. Fabian, A. Lohfink, E. Kara, et al. “Properties of AGN coronae in the NuSTAR era”. In: *MNRAS* 451 (Aug. 2015), pp. 4375–4383. arXiv: 1505.07603 [astro-ph.HE] (cit. on p. 11).

[Fal+03] R. Falomo, J. K. Kotilainen, N. Carangelo, and A. Treves. “Black Hole Masses and the Fundamental Plane of BL Lacertae Objects”. In: *ApJ* 595 (Oct. 2003), pp. 624–630. eprint: astro-ph/0306163 (cit. on p. 31).

[Fat09] E. A. Fath. “The spectra of some spiral nebulae and globular star clusters”. In: *Lick Observatory Bulletin* 5 (1909), pp. 71–77 (cit. on pp. 2, 3).

[Fos+09] L. Foschini, L. Maraschi, F. Tavecchio, et al. “Blazar nuclei in radio-loud narrow-line Seyfert 1?” In: *Advances in Space Research* 43 (Mar. 2009), pp. 889–894. arXiv: 0901.0167 [astro-ph.HE] (cit. on p. 178).

[Fos+11] L. Foschini, G. Ghisellini, Y. Y. Kovalev, et al. “The first gamma-ray outburst of a narrow-line Seyfert 1 galaxy: the case of PMN J0948+0022 in 2010 July”. In: *MNRAS* 413 (May 2011), pp. 1671–1677. arXiv: 1010.4434 [astro-ph.HE] (cit. on p. 203).

[Fos+12] L. Foschini, E. Angelakis, L. Fuhrmann, et al. “Radio-to-γ-ray monitoring of the narrow-line Seyfert 1 galaxy PMN J0948 + 0022 from 2008 to 2011”. In: *A&A* 548, A106 (Dec. 2012), A106. arXiv: 1209.5867 [astro-ph.HE] (cit. on pp. 38, 205, 206, 213, 231–233).

[Fos+98] G. Fossati, L. Maraschi, A. Celotti, A. Comastri, and G. Ghisellini. “A unifying view of the spectral energy distributions of blazars”. In: *MNRAS* 299 (Sept. 1998), pp. 433–448. eprint: astro-ph/9804103 (cit. on p. 32).

[Fos10] L. Foschini. “Continuing GeV activity of the Narrow-Line Seyfert 1 PMN J0948+0022”. In: *The Astronomer’s Telegram* 2752 (July 2010) (cit. on p. 203).

[Fos17] L. Foschini. “What We Talk about When We Talk about Blazars”. In: *Frontiers in Astronomy and Space Science* 4 (2017), p. 6 (cit. on p. 29).

[Fra+08] A. Franceschini, G. Rodighiero, and M. Vaccari. “Extragalactic optical-infrared background radiation, its time evolution and the cosmic photon-photon opacity”. In: *A&A* 487 (Sept. 2008), pp. 837–852. arXiv: 0805.1841 (cit. on pp. 93, 171).

[Fra+91] P. J. Francis, P. C. Hewett, C. B. Foltz, et al. “A high signal-to-noise ratio composite quasar spectrum”. In: *ApJ* 373 (1991), pp. 465–470 (cit. on pp. 23, 107).

[Fuh+16] L. Fuhrmann, V. Karamanavis, S. Komossa, et al. “Inner jet kinematics and the viewing angle towards the γ-ray narrow-line Seyfert 1 galaxy 1H 0323+342”. In: *Research in Astronomy and Astrophysics* 16, 176 (2016), p. 176. arXiv: 1608.03232 [astro-ph.HE] (cit. on pp. 36, 41, 178, 184, 228).

[Ghi+14] G. Ghisellini, F. Tavecchio, L. Maraschi, A. Celotti, and T. Sbarrato. “The power of relativistic jets is larger than the luminosity of their accretion disks”. In: 515 (Nov. 2014), pp. 376–378. arXiv: 1411.5368 [astro-ph.HE] (cit. on p. 36).

[Ghi+98] G. Ghisellini, A. Celotti, G. Fossati, L. Maraschi, and A. Comastri. “A theoretical unifying scheme for gamma-ray bright blazars”. In: *MNRAS* 301 (1998), pp. 451–468. eprint: astro-ph/9807317 (cit. on p. 29).

[Goo89] R. W. Goodrich. “Spectropolarimetry of ’narrow-line’ Seyfert 1 galaxies”. In: *ApJ* 342 (July 1989), pp. 224–234 (cit. on p. 34).

[Gou79] R. J. Gould. “Compton and synchrotron processes in spherically-symmetric non-thermal sources”. In: *A&A* 76 (July 1979), pp. 306–311 (cit. on p. 88).

[Gre+06] J. E. Greene, L. C. Ho, and J. S. Ulvestad. “The Radio Quiescence of Active Galaxies with High Accretion Rates”. In: *ApJ* 636 (Jan. 2006), pp. 56–62. eprint: astro-ph/0509198 (cit. on p. 177).

[Gre+08] J. Greiner, W. Bornemann, C. Clemens, et al. “GRONDa 7-Channel Imager”. In: *PASP* 120 (Apr. 2008), p. 405. arXiv: 0801.4801 (cit. on p. 147).

[H.E+12] H.E.S.S. Collaboration, Abramowski, A., Acero, F., et al. “A multiwavelength view of the flaring state of PKS2155-304 in 2006”. In: *AA* 539 (2012), A149 (cit. on p. 94).

[H.E+17] H.E.S.S. Collaboration, H. Abdalla, A. Abramowski, et al. “Gamma-ray blazar spectra with H.E.S.S. II mono analysis: The case of <ASTROBJ>PKS 2155-304</ASTROBJ> and <ASTROBJ>PG 1553+113</ASTROBJ>”. In: *A&A* 600, A89 (2017), A89. arXiv: 1612.01843 [astro-ph.HE] (cit. on p. 268).

[H. +16a] H. E. S. S. Collaboration, H. Abdalla, A. Abramowski, et al. “A search for very high-energy flares from the microquasars GRS 1915+105, Circinus X-1, and V4641 Sgr using contemporaneous H.E.S.S. and RXTE observations”. In: *ArXiv e-prints* (2016). arXiv: 1607.04613 [astro-ph.HE] (cit. on p. 269).

[H. +16b] H. E. S. S. Collaboration, H. Abdalla, A. Abramowski, et al. “Deeper H.E.S.S. Observations of Vela Junior (RX J0852.0-4622): Morphology Studies and Resolved Spectroscopy”. In: *ArXiv e-prints* (2016). arXiv: 1611.01863 [astro-ph.HE] (cit. on p. 268).

[H. +16c] H. E. S. S. Collaboration, : H. Abdalla, et al. “H.E.S.S. observations of RX J1713.7-3946 with improved angular and spectral resolution; evidence for gamma-ray emission extending beyond the X-ray emitting shell”. In: *ArXiv e-prints* (2016). arXiv: 1609.08671 [astro-ph.HE] (cit. on p. 268).

[H. +16d] H. E. S. S. Collaboration, H. Abdalla, A. Abramowski, et al. “The supernova remnant W49B as seen with H.E.S.S. and Fermi-LAT”. In: *ArXiv e-prints* (2016). arXiv: 1609.00600 [astro-ph.HE] (cit. on p. 268).

[H. +17a] H. E. S. S. Collaboration, : H. Abdalla, et al. “Characterising the VHE diffuse emission in the central 200 parsecs of our Galaxy with H.E.S.S”. In: *ArXiv e-prints* (June 2017). arXiv: 1706.04535 [astro-ph.HE] (cit. on p. 268).

[H. +17b] H. E. S. S. Collaboration, H. Abdalla, A. Abramowski, et al. “Characterizing the γ-ray long-term variability of PKS 2155-304 with H.E.S.S. and Fermi-LAT”. In: *A&A* 598, A39 (2017), A39. arXiv: 1610.03311 [astro-ph.HE] (cit. on p. 268).

[H. +17c] H. E. S. S. Collaboration, : H. Abdalla, et al. “Contributions of the High Energy Stereoscopic System (H.E.S.S.) to the 35th International Cosmic Ray Conference (ICRC), Busan, Korea”. In: *ArXiv e-prints* (Sept. 2017). arXiv: 1709.06442 [astro-ph.HE] (cit. on p. 268).

[H. +17d] H. E. S. S. Collaboration, H. Abdalla, A. Abramowski, et al. “First limits on the very-high energy gamma-ray afterglow emission of a fast radio burst. H.E.S.S. observations of FRB 150418”. In: *A&A* 597, A115 (2017), A115. arXiv: 1611.09209 [astro-ph.HE] (cit. on p. 268).

[H. +17e] H. E. S. S. Collaboration, : H. Abdalla, et al. “Measurement of the EBL spectral energy distribution using the VHE gamma-ray spectra of H.E.S.S. blazars”. In: *ArXiv e-prints* (July 2017). arXiv: 1707.06090 [astro-ph.HE] (cit. on pp. 93, 267).

[H. +17f] H. E. S. S. Collaboration, : H. Abdalla, et al. “Systematic search for very-high-energy gamma-ray emission from bow shocks of runaway stars”. In: *ArXiv e-prints* (2017). arXiv: 1705.02263 [astro-ph.HE] (cit. on p. 268).

[H. +17g] H. E. S. S. Collaboration, : H. Abdalla, et al. “TeV gamma-ray observations of the binary neutron star merger GW170817 with H.E.S.S”. In: *ArXiv e-prints* (Oct. 2017). arXiv: 1710.05862 [astro-ph.HE] (cit. on p. 267).

[H. +17h] H. E. S. S. Collaboration, : H. Abdalla, et al. “The population of TeV pulsar wind nebulae in the H.E.S.S. Galactic Plane Survey”. In: *ArXiv e-prints* (2017). arXiv: 1702.08280 [astro-ph.HE] (cit. on p. 268).

[HES+08] HESS Collaboration, F. Aharonian, A. G. Akhperjanian, U. Barres de Almeida, and et al. “Upper limits from HESS active galactic nuclei observations in 2005-2007”. In: *A&A* 478 (Feb. 2008), pp. 387–393. arXiv: 0711.3196 (cit. on p. 145).

[HES+13] HESS Collaboration, A. Abramowski, F. Acero, et al. “HESS and Fermi-LAT discovery of γ-rays from the blazar 1ES 1312-423”. In: *MNRAS* 434 (Sept. 2013), pp. 1889–1901. arXiv: 1306.3186 [astro-ph.HE] (cit. on p. 146).

[Han58] R. Hanbury Brown. “Galactic and extra-galactic radio frequency radiation due to sources other than the thermal and 21-cm emission of the interstellar gas”. In: *Comparison of the Large-Scale Structure of the Galactic System with that of Other Stellar Systems*. Ed. by N. G. Roman. Vol. 5. IAU Symposium. 1958, p. 37 (cit. on p. 5).

[Hei54] W. Heitler. *Quantum theory of radiation*. 1954 (cit. on p. 53).

[Her+15] O. Hervet, C. Boisson, and H. Sol. “Linking radio and gamma-ray emission in Ap Librae”. In: *A&A* 578, A69 (June 2015), A69. arXiv: 1503.01377 [astro-ph.HE] (cit. on pp. 125, 127).

[Hey+46] J. S. Hey, S. J. Parsons, and J. W. Phillips. “Fluctuations in Cosmic Radiation at Radio-Frequencies”. In: 158 (1946), p. 234 (cit. on p. 4).

[Hil85] A. M. Hillas. “Cerenkov light images of EAS produced by primary gamma”. In: *International Cosmic Ray Conference* 3 (Aug. 1985) (cit. on pp. 49, 70).

[Ho+93] L. C. Ho, A. V. Filippenko, and W. L. W. Sargent. “A Search for Low-Luminosity AGNs in a Complete Sample of Nearby Galaxies”. In: *American Astronomical Society Meeting Abstracts #182*. Vol. 25. Bulletin of the American Astronomical Society. May 1993, p. 817 (cit. on p. 19).

[Ho02] L. C. Ho. “On the Relationship between Radio Emission and Black Hole Mass in Galactic Nuclei”. In: *ApJ* 564 (Jan. 2002), pp. 120–132. eprint: astro-ph/0110440 (cit. on p. 34).

[Hub25] E. P. Hubble. “Cepheids in spiral nebulae”. In: *The Observatory* 48 (May 1925), pp. 139–142 (cit. on pp. 2, 3).

[Hub26] E. P. Hubble. “Extragalactic nebulae.” In: *ApJ* 64 (1926) (cit. on p. 2).

[Ito+13] R. Itoh, Y. T. Tanaka, Y. Fukazawa, et al. “Minute-scale Rapid Variability of the Optical Polarization in the Narrow-line Seyfert 1 Galaxy PMN J0948+0022”. In: *ApJL* 775, L26 (Sept. 2013), p. L26. arXiv: 1308.4478 [astro-ph.HE] (cit. on p. 203).

[Jaf+93] W. Jaffe, H. C. Ford, L. Ferrarese, F. van den Bosch, and R. W. O’Connell. “A large nuclear accretion disk in the active galaxy NGC4261”. In: 364 (1993), pp. 213–215 (cit. on p. 14).

[Jah+96] K. Jahoda, J. H. Swank, A. B. Giles, et al. “In-orbit performance and calibration of the Rossi X-ray Timing Explorer (RXTE) Proportional Counter Array (PCA)”. In: *EUV, X-Ray, and Gamma-Ray Instrumentation for Astronomy VII*. Ed. by O. H. Siegmund and M. A. Gummin. Vol. 2808. Oct. 1996, pp. 59–70 (cit. on p. 155).

[Jia+12] N. Jiang, H.-Y. Zhou, L. C. Ho, et al. “Rapid Infrared Variability of Three Radio-loud Narrow-line Seyfert 1 Galaxies: A View from the Wide-field Infrared Survey Explorer”. In: *ApJL* 759, L31 (Nov. 2012), p. L31. arXiv: 1210.2800 [astro-ph.HE] (cit. on p. 228).

[Jon+09] D. H. Jones, M. A. Read, W. Saunders, et al. “The 6dF Galaxy Survey: final redshift release (DR3) and southern large-scale structures”. In: *MNRAS* 399 (Oct. 2009), pp. 683–698. arXiv: 0903.5451 (cit. on pp. 146, 170, 237).

[Kar+17] V. Karamanavis, E. Angelakis, S. Komossa, et al. “Radio and gamma-ray loud narrow-line Seyfert 1 galaxies in the spotlight”. In: *ArXiv e-prints* (2017). arXiv: 1701.09111 [astro-ph.HE] (cit. on p. 178).

[Kar15] V. Karamanavis. “Zooming into γ-ray loud galactic nuclei: broadband emission and structure dynamics of the blazar PKS 1502+106 and the narrow-line Seyfert 1 1H 0323+342”. PhD thesis. Max-Planck-Institut für Radioastronomie <EMAIL>vkaramanavis@mpifr.de</EMAIL>, 2015 (cit. on p. 178).

[Kas+00] S. Kaspi, P. S. Smith, H. Netzer, et al. “Reverberation Measurements for 17 Quasars and the Size-Mass-Luminosity Relations in Active Galactic Nuclei”. In: *ApJ* 533 (Apr. 2000), pp. 631–649. eprint: astro-ph/9911476 (cit. on p. 12).

[Kat+01] K. Katarzyński, H. Sol, and A. Kus. “The multifrequency emission of Mrk 501. From radio to TeV gamma-rays”. In: *A&A* 367 (Mar. 2001), pp. 809–825 (cit. on pp. 89, 94, 125, 129, 166, 170, 236).

[Kat+03] K. Katarzyński, H. Sol, and A. Kus. “The multifrequency variability of Mrk 421”. In: *A&A* 410 (Oct. 2003), pp. 101–115 (cit. on pp. 125, 126, 129).

[Kee83] W. C. Keel. “Spectroscopic evidence for activity in the nuclei of normal spiral galaxies”. In: *ApJ* 269 (1983), pp. 466–486 (cit. on p. 23).

[Kel+04] K. I. Kellermann, M. L. Lister, D. C. Homan, et al. “Sub-Milliarcsecond Imaging of Quasars and Active Galactic Nuclei. III. Kinematics of Parsec-scale Radio Jets”. In: *ApJ* 609 (2004), pp. 539–563. eprint: astro-ph/0403320 (cit. on p. 190).

[Kel+89] K. I. Kellermann, R. Sramek, M. Schmidt, D. B. Shaffer, and R. Green. “VLA observations of objects in the Palomar Bright Quasar Survey”. In: *AJ* 98 (Oct. 1989), pp. 1195–1207 (cit. on p. 5).

[Ken92] R. C. Kennicutt Jr. “A spectrophotometric atlas of galaxies”. In: *ApJS* 79 (1992), pp. 255–284 (cit. on p. 23).

[Khe+15] B. Khelifi, A. Djannati-Ataï, L. Jouvin, et al. “HAP-Fr, a pipeline of data analysis for the HESS-II experiment”. In: *34th International Cosmic Ray Conference (ICRC2015)*. Vol. 34. International Cosmic Ray Conference. July 2015, p. 837 (cit. on p. 74).

[Kir+98] J. G. Kirk, F. M. Rieger, and A. Mastichiadis. “Particle acceleration and synchrotron emission in blazar jets”. In: *A&A* 333 (May 1998), pp. 452–458. eprint: astro-ph/9801265 (cit. on p. 89).

[Kom+06] S. Komossa, W. Voges, D. Xu, et al. “Radio-loud Narrow-Line Type 1 Quasars”. In: *AJ* 132 (2006), pp. 531–545. eprint: astro-ph/0603680 (cit. on p. 34).

[Kot+98a] J. K. Kotilainen, R. Falomo, and R. Scarpa. “Near-infrared imaging of the host galaxies of flat spectrum radio quasars”. In: *A&A* 332 (1998), pp. 503–513. eprint: astro-ph/9711065 (cit. on p. 36).

[Kot+98b] J. K. Kotilainen, R. Falomo, and R. Scarpa. “The host galaxies of BL Lac objects in the near-infrared”. In: *A&A* 336 (1998), pp. 479–489. eprint: astro-ph/9805295 (cit. on p. 36).

[Kra+01] H. Krawczynski, R. Sambruna, A. Kohnle, et al. “Simultaneous X-Ray and TeV Gamma-Ray Observation of the TeV Blazar Markarian 421 during 2000 February and May”. In: *ApJ* 559 (Sept. 2001), pp. 187–195. eprint: astro-ph/0105331 (cit. on p. 126).

[Kru+11] T. Kruhler, Schady, P., Greiner, J., et al. “Photometric redshifts for gamma-ray burst afterglows from GROND and Swift/UVOT”. In: *AA* 526 (2011), A153 (cit. on p. 164).

[Kue+81] H. Kuehr, A. Witzel, I. I. K. Pauliny-Toth, and U. Nauber. “A catalogue of extragalactic radio sources having flux densities greater than 1 Jy at 5 GHz”. In: *A&AS* 45 (1981), pp. 367–430 (cit. on p. 189).

[Kun+91] H. Kunieda, H. Awaki, K. Koyama, et al. “Rapid Variability of Iron Line from NGC 6814”. In: *Iron Line Diagnostics in X-ray Sources*. Ed. by A. Treves, G. C. Perola, and L. Stella. Vol. 385. Lecture Notes in Physics, Berlin Springer Verlag. 1991, p. 241 (cit. on p. 11).

[Lan+13] M. Landoni, R. Falomo, A. Treves, et al. “ESO Very Large Telescope Optical Spectroscopy of BL Lacertae Objects. IV. New Spectra and Properties of the Full Sample”. In: *AJ* 145, 114 (Apr. 2013), p. 114. arXiv: 1302.2591 (cit. on p. 146).

[Lan+17] H. Landt, M. J. Ward, M. Baloković, et al. “On the black hole mass of the γ-ray emitting narrow-line Seyfert 1 galaxy 1H 0323+342”. In: *MNRAS* 464 (2017), pp. 2565–2576. arXiv: 1609.08002 [astro-ph.HE] (cit. on pp. 103, 176, 177, 181, 221).

[Law+96] C. R. Lawrence, J. R. Zucker, A. C. S. Readhead, et al. “Optical Spectra of a Complete Sample of Radio Sources. I. The Spectra”. In: *ApJS* 107 (1996), p. 541 (cit. on p. 23).

[Lei99] K. M. Leighly. “A Comprehensive Spectral and Variability Study of Narrow-line Seyfert 1 Galaxies Observed by ASCA”. In: *AAS/High Energy Astrophysics Division #4*. Vol. 31. Bulletin of the American Astronomical Society. 1999, p. 724 (cit. on p. 34).

[Lem+06] M. Lemoine-Goumard, B. Degrange, and M. Tluczykont. “Selection and 3D-reconstruction of gamma-ray-induced air showers with a stereoscopic system of atmospheric Cherenkov telescopes”. In: *Astroparticle Physics* 25 (Apr. 2006), pp. 195–211. eprint: astro-ph/0601373 (cit. on p. 72).

[Len+08] J.-P. Lenain, C. Boisson, and H. Sol. “SSC Scenario for Tev Emission from Non-Blazar AGNs”. In: *International Journal of Modern Physics D* 17 (2008), pp. 1577–1584. arXiv: 0712.3075 (cit. on pp. 128, 129).

[Liu+10] H. Liu, J. Wang, Y. Mao, and J. Wei. “Violent Intranight Optical Variability of a Radio-loud Narrow-line Seyfert 1 Galaxy: SDSS J094857.3+002225”. In: *ApJL* 715 (June 2010), pp. L113–L116. arXiv: 1005.0916 [astro-ph.GA] (cit. on p. 203).

[MAG+10] MAGIC Collaboration, J. Aleksić, L. A. Antonelli, et al. “Detection of Very High Energy γ-ray Emission from the Perseus Cluster Head-Tail Galaxy IC 310 by the MAGIC Telescopes”. In: *ApJL* 723 (Nov. 2010), pp. L207–L212. arXiv: 1009.2155 [astro-ph.HE] (cit. on p. 146).

[MAG+17] MAGIC Collaboration, M. L. Ahnen, S. Ansoldi, et al. “Constraints on particle acceleration in SS433/W50 from MAGIC and H.E.S.S. observations”. In: *ArXiv e-prints* (July 2017). arXiv: 1707.03658 [astro-ph.HE] (cit. on p. 268).

[Mad+99] G. M. Madejski, M. Sikora, T. Jaffe, et al. “X-Ray Observations of BL Lacertae during the 1997 Outburst and Association with Quasar-like Characteristics”. In: *ApJ* 521 (Aug. 1999), pp. 145–154 (cit. on p. 29).

[Mal83] M. A. Malkan. “The ultraviolet excess of luminous quasars. II - Evidence for massive accretion disks”. In: *ApJ* 268 (May 1983), pp. 582–590 (cit. on p. 10).

[Man93] K. Mannheim. “The proton blazar”. In: *A&A* 269 (Mar. 1993), pp. 67–76. eprint: astro-ph/9302006 (cit. on p. 130).

[Mar+12] A. P. Marscher, S. G. Jorstad, I. Agudo, N. R. MacDonald, and T. L. Scott. “Relation between Events in the Millimeter-wave Core and Gamma-ray Outbursts in Blazar Jets”. In: *ArXiv e-prints* (Apr. 2012). arXiv: 1204.6707 [astro-ph.HE] (cit. on p. 205).

[Mas+04] E. Massaro, M. Perri, P. Giommi, R. Nesci, and F. Verrecchia. “Log-parabolic spectra and particle acceleration in blazars. II. The BeppoSAX wide band X-ray spectra of Mkn 501”. In: *A&A* 422 (July 2004), pp. 103–111. eprint: astro-ph/0405152 (cit. on pp. 89, 167).

[Mas+09a] E. Massaro, P. Giommi, C. Leto, et al. “Roma-BZCAT: a multifrequency catalogue of blazars”. In: *A&A* 495 (Feb. 2009), pp. 691–696. arXiv: 0810.2206 (cit. on p. 29).

[Mas+09b] E. Massaro, P. Giommi, C. Leto, et al. “Roma-BZCAT: a multifrequency catalogue of blazars”. In: *A&A* 495 (Feb. 2009), pp. 691–696. arXiv: 0810.2206 (cit. on p. 37).

[Mat+90] M. Matsuoka, L. Piro, M. Yamauchi, and T. Murakami. “X-ray spectral variability and complex absorption in the Seyfert 1 galaxies NGC 4051 and MCG -6-30-15”. In: *ApJ* 361 (Oct. 1990), pp. 440–458 (cit. on p. 11).

[Mau+03] T. Mauch, T. Murphy, H. J. Buttery, et al. “SUMSS: a wide-field radio imaging survey of the southern sky - II. The source catalogue”. In: *MNRAS* 342 (July 2003), pp. 1117–1130. eprint: astro-ph/0303188 (cit. on p. 146).

[Mau+13] J. D. Maune, H. R. Miller, and J. R. Eggen. “The Extreme Optical Variability of J0948+0022”. In: *ApJ* 762, 124 (Jan. 2013), p. 124. arXiv: 1211.3082 [astro-ph.HE] (cit. on p. 203).

[Mir16] R. Mirzoyan. “MAGIC detects very high energy gamma-ray emission from the blazar OT 081 (PKS 1749+096, 4C +09.57)”. In: *The Astronomer’s Telegram* 9267 (July 2016) (cit. on p. 135).

[Mor+11] R. Morganti, J. Holt, C. Tadhunter, et al. “PKS 1814-637: a powerful radio-loud AGN in a disk galaxy”. In: *A&A* 535, A97 (Nov. 2011), A97. arXiV: 1109.0630 (cit. on p. 36).

[Mor+57] D. Morris, H. P. Palmer, and A. R. Thompson. “Five radio sources of small angular diameter”. In: *The Observatory* 77 (1957), pp. 103–106 (cit. on p. 5).

[Mor57] P. Morrison. “On the Origins of Cosmic Rays”. In: *Reviews of Modern Physics* 29 (Apr. 1957), pp. 235–243 (cit. on p. 48).

[Mus+93] R. F. Mushotzky, C. Done, and K. A. Pounds. “X-ray spectra and time variability of active galactic nuclei”. In: *ARAA* 31 (1993), pp. 717–761 (cit. on p. 21).

[Nol+12] P. L. Nolan, A. A. Abdo, M. Ackermann, et al. “Fermi Large Area Telescope Second Source Catalog”. In: *ApJS* 199, 31 (Apr. 2012), p. 31. arXiv: 1108.1435 [astro-ph.HE] (cit. on p. 190).

[Oht+07] K. Ohta, K. Aoki, T. Kawaguchi, and G. Kiuchi. “A Bar Fuels a Supermassive Black Hole?: Host Galaxies of Narrow-Line Seyfert 1 Galaxies”. In: *ApJS* 169 (2007), pp. 1–20. eprint: astro-ph/0610355 (cit. on p. 36).

[Ost89] D. E. Osterbrock. “Active galactic nuclei”. In: *Annals of the New York Academy of Sciences* 571 (1989), pp. 99–109 (cit. on p. 34).

[Owe+90] F. N. Owen, C. P. O’Dea, and W. C. Keel. “Long-slit spectroscopy of 3C 31, 3C 75, 3C 465, NGC 1265, and Cygnus A”. In: *ApJ* 352 (1990), pp. 44–54 (cit. on p. 23).

[Pad92] P. Padovani. “Is there a relationship between BL Lacertae objects and flat-spectrum radio quasars?” In: *MNRAS* 257 (Aug. 1992), pp. 404–414 (cit. on p. 30).

[Pal+14] V. S. Paliya, S. Sahayanathan, M. L. Parker, et al. “The Peculiar Radio-loud Narrow Line Seyfert 1 Galaxy 1H 0323+342”. In: *ApJ* 789, 143 (July 2014), p. 143. arXiv: 1405.0715 [astro-ph.HE] (cit. on pp. 178, 179, 181, 183, 227).

[Pet+17] E. Petroff, S. Burke-Spolaor, E. F. Keane, et al. “A polarized fast radio burst at low Galactic latitude”. In: *MNRAS* 469 (Aug. 2017), pp. 4465–4482. arXiv: 1705.02911 [astro-ph.HE] (cit. on p. 268).

[Pet04] B. M. Peterson. “Black hole masses from reverberation measurements”. In: *The Interplay Among Black Holes, Stars and ISM in Galactic Nuclei*. Ed. by T. Storchi-Bergmann, L. C. Ho, and H. R. Schmitt. Vol. 222. IAU Symposium. Nov. 2004, pp. 15–20. eprint: astro-ph/0404539 (cit. on p. 12).

[Pet93] B. M. Peterson. “Reverberation mapping of active galactic nuclei”. In: *PASP* 105 (Mar. 1993), pp. 247–268 (cit. on p. 12).

[Pet98] B. M. Peterson. “Reverberation mapping of active nuclei”. In: *Advances in Space Research* 21 (1998), pp. 57–66 (cit. on p. 12).

[Pic+88] A. J. Pica, A. G. Smith, J. R. Webb, et al. “Long-term optical behavior of 144 compact extragalactic objects - 1969-1988”. In: *AJ* 96 (1988), pp. 1215–1226 (cit. on p. 189).

[Pir+90] L. Piro, M. Yamauchi, and M. Matsuoka. “X-ray spectral signatures of very thick cold matter in the spectra of the Seyfert 1 galaxies NGC 7469 and IC 4329A”. In: *ApJL* 360 (Sept. 1990), pp. L35–L38 (cit. on p. 11).

[Plo+11] R. M. Plotkin, S. Markoff, S. C. Trager, and S. F. Anderson. “Dynamical black hole masses of BL Lac objects from the Sloan Digital Sky Survey”. In: *MNRAS* 413 (May 2011), pp. 805–812. arXiv: 1012.1601 (cit. on p. 31).

[Pog11] R. W. Pogge. “A quarter century of Narrow-Line Sefert 1s”. In: *Narrow-Line Seyfert 1 Galaxies and their Place in the Universe*. 2011, p. 2 (cit. on p. 35).

[Poo+08] T. S. Poole, A. A. Breeveld, M. J. Page, et al. “Photometric calibration of the Swift ultraviolet/optical telescope”. In: *MNRAS* 383 (Jan. 2008), pp. 627–645. eprint: 0708.2259 (cit. on p. 136).

[Pou+90] K. A. Pounds, K. Nandra, G. C. Stewart, I. M. George, and A. C. Fabian. “X-ray reflection from cold matter in the nuclei of active galaxies”. In: 344 (Mar. 1990), p. 132 (cit. on p. 11).

[Pun+92] M. Punch, C. W. Akerlof, M. F. Cawley, et al. “Detection of TeV photons from the active galaxy Markarian 421”. In: 358 (Aug. 1992), p. 477 (cit. on p. 49).

[Rat+96] A. Ratcliffe, T. Shanks, A. Broadbent, et al. “The Durham/UKST Galaxy Redshift Survey - I. Large-scale structure in the Universe”. In: *MNRAS* 281 (Aug. 1996), p. 47 (cit. on p. 146).

[Rau+12] A. Rau, P. Schady, J. Greiner, et al. “BL Lacertae objects beyond redshift 1.3 - UV-to-NIR photometry and photometric redshift for Fermi/LAT blazars”. In: *A&A* 538, A26 (Feb. 2012), A26. arXiv: 1112.0025 (cit. on pp. 147, 163, 164).

[Ree78] M. J. Rees. “Emission from the nuclei of nearby galaxies - Evidence for massive black holes”. In: *Structure and Properties of Nearby Galaxies*. Ed. by E. M. Berkhuijsen and R. Wielebinski. Vol. 77. IAU Symposium. 1978, pp. 237–242 (cit. on p. 7).

[Ree84] M. J. Rees. “Black Hole Models for Active Galactic Nuclei”. In: *ARAA* 22 (1984), pp. 471–506 (cit. on p. 7).

[Rem+93] R. A. Remillard, H. V. D. Bradt, R. J. V. Brissenden, et al. “Twenty-two emission-line AGNs from the HEAO-1 X-ray survey”. In: *AJ* 105 (June 1993), pp. 2079–2089 (cit. on p. 176).

[Rey16] C. S. Reynolds. “Unwrapping the X-ray spectra of active galactic nuclei”. In: *Astronomische Nachrichten* 337 (May 2016), p. 404. arXiv: 1510.07638 [astro-ph.HE] (cit. on p. 11).

[Rey82] S. P. Reynolds. “Theoretical Studies of Compact Radio Sources - Part Two - Inverse-Compton Radiation from Anisotropic Photon and Electron Distributions - General Results and Spectra from Relativistic Flows”. In: *ApJ* 256 (May 1982), p. 38 (cit. on p. 98).

[Rom+05] P. W. A. Roming, T. E. Kennedy, K. O. Mason, et al. “The Swift Ultra-Violet/Optical Telescope”. In: 120 (Oct. 2005), pp. 95–142. eprint: astro-ph/0507413 (cit. on p. 136).

[Rom+09] P. W. A. Roming, T. S. Koch, S. R. Oates, et al. “The First Swift Ultraviolet/Optical Telescope GRB Afterglow Catalog”. In: *ApJ* 690 (Jan. 2009), pp. 163–188. arXiv: 0809.4193 (cit. on p. 161).

[Rov+13] A. C. Rovero, C. Donzelli, H. Muriel, A. Cillis, and A. Pichel. “On the redshift of the gamma-ray blazar PKS 0447-439: Optical spectroscopy using Gemini observations with high S/N ratio”. In: *ArXiv e-prints* (July 2013). arXiv: 1307.6907 [astro-ph.HE] (cit. on p. 134).

[San+10] E. Sani, D. Lutz, G. Risaliti, et al. “Enhanced star formation in narrow-line Seyfert 1 active galactic nuclei revealed by Spitzer”. In: *MNRAS* 403 (2010), pp. 1246–1260. arXiv: 0908.0280 (cit. on p. 36).

[San65] A. Sandage. “The Existence of a Major New Constituent of the Universe: the Quasistellar Galaxies.” In: *ApJ* 141 (May 1965), p. 1560 (cit. on p. 5).

[Sch+00] A. Schwope, G. Hasinger, I. Lehmann, et al. “The ROSAT Bright Survey: II. Catalogue of all high-galactic latitude RASS sources with PSPC countrate CR 0.2 s^{-1}”. In: *Astronomische Nachrichten* 321 (2000), pp. 1–52. eprint: astro-ph/0003039 (cit. on p. 146).

[Sch+17] F. Schüssler, M. Seglar-Arroyo, M. Arrieta, et al. “Target of Opportunity Observations of Blazars with H.E.S.S.” In: *ArXiv e-prints* (Aug. 2017). arXiv: 1708.01083 [astro-ph.HE] (cit. on pp. 134, 141, 142, 236, 268).

[Sch63] M. Schmidt. “3C 273 : A Star-Like Object with Large Red-Shift”. In: *Nature* 197 (1963), p. 1040 (cit. on p. 5).

[Sch65] M. Schmidt. “Large Redshifts of Five Quasi-Stellar Sources.” In: *ApJ* 141 (Apr. 1965), p. 1295 (cit. on p. 134).

[Sey43] C. K. Seyfert. “Nuclear Emission in Spiral Nebulae.” In: *ApJ* 97 (1943), p. 28 (cit. on pp. 3, 4).

[She+11] Y. Shen, G. T. Richards, M. A. Strauss, et al. “A Catalog of Quasar Properties from Sloan Digital Sky Survey Data Release 7”. In: *ApJS* 194, 45 (June 2011), p. 45. arXiv: 1006.5178 [astro-ph.CO] (cit. on p. 189).

[She+96] S. A. Shectman, S. D. Landy, A. Oemler, et al. “The Las Campanas Redshift Survey”. In: *ApJ* 470 (Oct. 1996), p. 172. eprint: astro-ph/9604167 (cit. on p. 146).

[Sik+07] M. Sikora, Ł. Stawarz, and J.-P. Lasota. “Radio Loudness of Active Galactic Nuclei: Observational Facts and Theoretical Implications”. In: *ApJ* 658 (Apr. 2007), pp. 815–828. eprint: astro-ph/0604095 (cit. on p. 178).

[Sik+09] M. Sikora, Ł. Stawarz, R. Moderski, K. Nalewajko, and G. M. Madejski. “Constraining Emission Models of Luminous Blazar Sources”. In: *ApJ* 704 (Oct. 2009), pp. 38–50. arXiv: 0904.1414 [astro-ph.CO] (cit. on p. 103).

[Sin+15] V. Singh, C. H. Ishwara-Chandra, J. Sievers, et al. “Discovery of rare double-lobe radio galaxies hosted in spiral galaxies”. In: *MNRAS* 454 (Dec. 2015), pp. 1556–1572. arXiV: 1509.01559 (cit. on p. 36).

[Skr+06] M. F. Skrutskie, R. M. Cutri, R. Stiening, et al. “The Two Micron All Sky Survey (2MASS)”. In: *AJ* 131 (Feb. 2006), pp. 1163–1183 (cit. on p. 146).

[Sli17] V. M. Slipher. “The spectrum and velocity of the nebula N.G.C. 1068 (M 77)”. In: *Lowell Observatory Bulletin* 3 (1917), pp. 59–62 (cit. on p. 2).

[Smi51] F. G. Smith. “An Accurate Determination of the Positions of Four Radio Stars”. In: 168 (1951), p. 555 (cit. on p. 4).

[Ste+76] W. A. Stein, S. L. Odell, and P. A. Strittmatter. “The BL Lacertae objects”. In: *ARAA* 14 (1976), pp. 173–195 (cit. on p. 29).

[Str+01] L. Strüder, U. Briel, K. Dennerl, et al. “The European Photon Imaging Camera on XMM-Newton: The pn-CCD camera”. In: *A&A* 365 (Jan. 2001), pp. L18–L26 (cit. on p. 204).

[Str+72] P. A. Strittmatter, K. Serkowski, R. Carswell, et al. “Compact Extragalactic Nonthermal Sources”. In: *ApJL* 175 (July 1972), p. L7 (cit. on p. 29).

[Tav+98] F. Tavecchio, L. Maraschi, and G. Ghisellini. “Constraints on the Physical Parameters of TeV Blazars”. In: *ApJ* 509 (Dec. 1998), pp. 608–619. eprint: astro-ph/9809051 (cit. on pp. 91, 167, 169).

[Tel01] R. Telfer. “The EUV Continuum of QSOs and the Ionization of the Intergalactic Medium”. In: *American Astronomical Society Meeting Abstracts*. Vol. 33. Bulletin of the American Astronomical Society. Dec. 2001, p. 1353 (cit. on p. 107).

[Tho+98] H.-C. Thomas, K. Beuermann, K. Reinsch, et al. “Identification of soft high galactic latitude RASS X-ray sources. I. A complete count-rate limited sample”. In: *A&A* 335 (July 1998), pp. 467–478 (cit. on p. 146).

[Tor+05] I. Torniainen, M. Tornikoski, H. Teräsranta, M. F. Aller, and H. D. Aller. “Long term variability of gigahertz-peaked spectrum sources and candidates”. In: *A&A* 435 (2005), pp. 839–856 (cit. on p. 189).

[Tur+01] M. J. L. Turner, A. Abbey, M. Arnaud, et al. “The European Photon Imaging Camera on XMM-Newton: The MOS cameras : The MOS cameras”. In: *A&A* 365 (Jan. 2001), pp. L27–L35. eprint: astro-ph/0011498 (cit. on p. 204).

[Van+01] D. E. Vanden Berk, G. T. Richards, A. Bauer, et al. “Composite Quasar Spectra from the Sloan Digital Sky Survey”. In: *AJ* 122 (Aug. 2001), pp. 549–564. eprint: astro-ph/0105231 (cit. on p. 107).

[Ver+04] M.-P. Veron-Cetty, M. Joly, and P. Véron. “The unusual emission line spectrum of I Zw 1”. In: *A&A* 417 (2004), pp. 515–525. eprint: astro-ph/0312654 (cit. on p. 34).

[Vet+98] G. Vettolani, E. Zucca, R. Merighi, et al. “The ESO Slice Project (ESP) galaxy redshift survey. III. The sample”. In: *A&AS* 130 (June 1998), pp. 323–332. eprint: astro-ph/9805195 (cit. on p. 146).

[Waj+14] K. Wajima, K. Fujisawa, M. Hayashida, et al. “Short-term Radio Variability and Parsec-scale Structure in a Gamma-Ray Narrow-line Seyfert 1 Galaxy 1H 0323+342”. In: *ApJ* 781, 75 (2014), p. 75. arXiv: 1312.3118 (cit. on pp. 38, 177).

[Wan+16] J. Wang, Y. Xu, D. W. Xu, and J. Y. Wei. “Powerful Radio Emission from Low-mass Supermassive Black Holes Favors Disk-like Bulges”. In: *ApJL* 833, L2 (Dec. 2016), p. L2. arXiv: 1611.04283 (cit. on p. 177).

[Wee03] T. C. Weekes. “VERITAS: the next generation very high energy gamma-ray telescope.” In: *American Astronomical Society Meeting Abstracts*. Vol. 35. Bulletin of the American Astronomical Society. Dec. 2003, p. 1372 (cit. on p. 134).

[Wil+02] R. J. Williams, R. W. Pogge, and S. Mathur. “Narrow-line Seyfert 1 Galaxies from the Sloan Digital Sky Survey Early Data Release”. In: *AJ* 124 (Dec. 2002), pp. 3042–3049. eprint: astro-ph/0208211 (cit. on p. 203).

[Wil+13] R. Willingale, R. L. C. Starling, A. P. Beardmore, N. R. Tanvir, and P. T. O’Brien. “Calibration of X-ray absorption in our Galaxy”. In: *MNRAS* 431 (May 2013), pp. 394–404. arXiv: 1303.0843 [astro-ph.HE] (cit. on pp. 138, 193).

[Wil+92] B. J. Wills, D. Wills, M. Breger, R. R. J. Antonucci, and R. Barvainis. “A survey for high optical polarization in quasars with core-dominant radio structure - Is there a beamed optical continuum?” In: *ApJ* 398 (1992), pp. 454–475 (cit. on p. 189).

[Woo+84] K. S. Wood, J. F. Meekins, D. J. Yentis, et al. “The HEAO A-1 X-ray source catalog”. In: *ApJS* 56 (Dec. 1984), pp. 507–649 (cit. on p. 176).

[Wri+10] E. L. Wright, P. R. M. Eisenhardt, A. K. Mainzer, et al. “The Wide-field Infrared Survey Explorer (WISE): Mission Description and Initial On-orbit Performance”. In: *AJ* 140, 1868-1881 (2010), pp. 1868–1881. arXiv: 1008.0031 [astro-ph.IM] (cit. on p. 146).

[Yao+15] S. Yao, W. Yuan, S. Komossa, et al. “The γ-Ray Detected Narrow-line Seyfert 1 Galaxy 1H 0323+342: Swift Monitoring and Suzaku Spectroscopy”. In: *AJ* 150, 23 (July 2015), p. 23. arXiv: 1505.01269 [astro-ph.HE] (cit. on pp. 179, 227, 228).

[Yon+08] Yonehara, A., Hirashita, H., and Richter, P. “Origin of chromatic features in multiple quasars* - Variability, dust, or microlensing”. In: *AA* 478.1 (2008), pp. 95–109 (cit. on p. 78).

[Yua+08] W. Yuan, H. Y. Zhou, S. Komossa, et al. “A Population of Radio-Loud Narrow-Line Seyfert 1 Galaxies with Blazar-Like Properties?” In: *ApJ* 685, 801-827 (2008), pp. 801–827. arXiv: 0806.3755 (cit. on pp. 34, 36).

[Zec+17] Zech, A., Cerruti, M., and Mazin, D. “Expected signatures from hadronic emission processes in the TeV spectra of BL Lacertae objects”. In: *AA* 602 (2017), A25 (cit. on pp. 130, 131).

[Zho+03] H.-Y. Zhou, T.-G. Wang, X.-B. Dong, Y.-Y. Zhou, and C. Li. “SDSS J094857.3+002225: A Very Radio Loud, Narrow-Line Quasar with Relativistic Jets?” In: *ApJ* 584 (2003), pp. 147–152 (cit. on pp. 203, 204).

[Zho+06] H. Zhou, T. Wang, W. Yuan, et al. “A Comprehensive Study of 2000 Narrow Line Seyfert 1 Galaxies from the Sloan Digital Sky Survey. I. The Sample”. In: *ApJS* 166 (2006), pp. 128–153. eprint: astro-ph/0603759 (cit. on p. 37).

[Zho+07] H. Zhou, T. Wang, W. Yuan, et al. “A Narrow-Line Seyfert 1-Blazar Composite Nucleus in 2MASX J0324+3410”. In: *ApJL* 658 (2007), pp. L13–L16. eprint: astro-ph/0702329 (cit. on pp. 36, 37, 176–178).

Appendix
List of publications

Papers in preparation:

- Arrieta-Lobo, M.; Lefaucheur J. and Pita, S. for the HESS collaboration: "VHE gamma-ray discovery and multi-wavelength study of the blazar 1ES 2322−409 ". Currently undergoing internal HESS review.

Conference Proceedings:

- Arrieta-Lobo, M.; Boisson, C. and Zech, A.: "Modeling the broad-band emission from the gamma-ray emitting Narrow-Line Seyfert-1 galaxies 1H 0323+342 and B2 0954+25A". Proceeding from the "Quasars at all Cosmic Epochs" conference. Currently under review.

Co-author:

- "TeV gamma-ray observations of the binary neutron star merger GW170817 with H.E.S.S [H. +17g]

- "Multi-messenger Observations of a Binary Neutron Star Merger [Abb+17]

- "Measurement of the EBL spectral energy distribution using the VHE gamma-ray spectra of H.E.S.S. blazars [H. +17e]

- ”Contributions of the High Energy Stereoscopic System (H.E.S.S.) to the 35th International Cosmic Ray Conference (ICRC), Busan, Korea [H. +17c]

- “A polarized fast radio burst at low Galactic latitude [Pet+17]

- ”Target of Opportunity Observations of Blazars with H.E.S.S. [Sch+17]

- “Constraints on particle acceleration in SS433/W50 from MAGIC and H.E.S.S. observations [MAG+17]

- ”Characterising the VHE diffuse emission in the central 200 parsecs of our Galaxy with H.E.S.S. [H. +17a]

- “Systematic search for very-high-energy gamma-ray emission from bow shocks of runaway stars [H. +17f]

- ”Gamma-ray blazar spectra with H.E.S.S. II mono analysis: The case of PKS 2155-304 and PG 1553+113 [H.E+17]

- “The population of TeV pulsar wind nebulae in the H.E.S.S. Galactic Plane Survey [H. +17h]

- ”Characterizing the γ-ray long-term variability of PKS 2155-304 with H.E.S.S. and Fermi-LAT [H. +17b]

- “First limits on the very-high energy gamma-ray afterglow emission of a fast radio burst. H.E.S.S. observations of FRB 150418 [H. +17d]

- ”Deeper H.E.S.S. Observations of Vela Junior (RX J0852.0-4622): Morphology Studies and Resolved Spectroscopy [H. +16b]

- “H.E.S.S. Limits on Linelike Dark Matter Signatures in the 100 GeV to 2 TeV Energy Range Close to the Galactic Center [Abd+16a]

- ”Search for Dark Matter Annihilations towards the Inner Galactic Halo from 10 Years of Observations with H.E.S.S. [Abd+16b]

- “H.E.S.S. observations of RX J1713.7-3946 with improved angular and spectral resolution; evidence for gamma-ray emission extending beyond the X-ray emitting shell [H. +16c]

- ”The supernova remnant W49B as seen with H.E.S.S. and Fermi-LAT [H. +16d]

• “A search for very high-energy flares from the microquasars GRS 1915+105, Circinus X-1, and V4641 Sgr using contemporaneous H.E.S.S. and RXTE observations [H. +16a]

Colophon

This thesis was written using the `cleanthesis` latex package by Ricardo Langner.

Résumé

Ce manuscrit de thèse present l'étude des processus d'émission de deux types de noyaux actifs de galaxie détectés aux rayons gamma: des blazars vues au TeV et des Narrow Line Seyfert 1s (NLS1s) détectés au GeV.

La distribution spectrale d'énergie des blazars peut être décrite en général par des modèles 'one-zone synchrotron self-Compton'. Ce modèle a été appliqué au blazar 1ES 2322−409 qui fut premièrement detecté au TeV par l'expérience HESS.

Des composantes externes comme le tore, le disque d'accretion, la couronne X ou la 'Broad Line Region' (BLR) sont necessaires pour expliquer la radiation observé dans des NLS1 qui émettent des rayons gamma. Un modèle numérique qui considère ces champs des photons externes a été developée. Ce modéle explique l'émission observée et la transition entre des états bas et des états d'emission augmentée pour trois NLS1 vues au regime gamma: 1H 0323+342, B2 0954+25A et PMN J0948+0022.

Mots Clés

Noyaux Actifs de Galaxie, Astrophysique des Hautes Energies, Experience HESS, Modelisation, Blazars, NLS1

Abstract

This thesis manuscript presents the study of the emission processes of two types of gamma-emitting active galactic nuclei: TeV-detected blazars and GeV-detected Narrow Line Seyfert 1s (NLS1s).

The Spectral Energy Distribution (SED) of TeV blazars can in general be well described by simple one-zone synchrotron self-Compton models. Such model has been applied to the blazar 1ES 2322−409 that was first detected at TeV by the HESS collaboration.

Additional external photon fields such as the obscuring torus, the accretion disc, the X-ray corona or the Broad Line Region (BLR) are necessary to describe the observed radiation and broad-band SED of gamma-emitting NLS1. A numerical model that takes into account emission from these external fields has been developed. The model explains the observed emission and the transition from quiescent to gamma-ray flaring states of three gamma-emitting NLS1s: 1H 0323+342, B2 0954+25A and PMN J0948+0022.

Keywords

Active Galactic Nuclei, High Energy Astrophysics, HESS Experiment, Modeling, Blazars,
NLS1